Geotechnical Characterization of Sediments from Hydrate Ridge, Cascadia Continental Margin

by

Brian B. Tan

Bachelor of Science in Civil Engineering (2001)
University of the Philippines

Submitted to the Department of Civil and Environmental Engineering
in Partial Fulfillment of the Requirements for the Degree of
Master of Science in Civil and Environmental Engineering

at the

Massachusetts Institute of Technology
March 2004

© 2004 Massachusetts Institute of Technology
All Rights Reserved

Signature of Author.....
Department of Civil and Environmental Engineering
March 19, 2004

Certified by .....
John T. Germaine
Principal Research Associate
Thesis Supervisor

Accepted by .....
Heidi Nepf
Chairman Departmental Committee on Graduate Studies

GEOTECHNICAL CHARACTERIZATION OF SEDIMENTS FROM HYDRATE RIDGE, CASCADIA CONTINENTAL MARGIN

by

BRIAN B. TAN

Submitted to the Department of Civil and Environmental Engineering on March 19, 2004 in partial fulfillment of the requirements for the degree of Master of Science in Civil and Environmental Engineering

ABSTRACT

Eight whole core sediment samples were obtained from ODP Site 1244, Hydrate Ridge, Cascadia Continental Margin with the goal of understanding the stress history, consolidation behavior and strength characteristics of the soil. Hydrate Ridge is located in an accretionary margin setting. Furthermore, these samples are known to be within the gas hydrate stability zone, with the exception of the deepest sample, which was in the free gas zone. A series of Constant Rate of Strain Consolidation (CRSC) and Ko-Consolidated Undrained triaxial (CKoU) tests were performed in order to study the behavior. In addition, Atterberg limits and x-ray diffraction were performed in order to better classify the material.

One of the key issues regarding this soil is the level of disturbance imparted during sampling and transportation. Evidence of the disturbance are cracks and voids in x-rays, as well as highly rounded compression curves. The Terzaghi et al (1996) and Lunne et al (1997) soil quality criteria rate the soil as D to E and poor to very poor. A new criterion comparing the initial loading to the reload cycle shows that soil quality varies, but has no pattern with depth. Nonetheless, due to the limited amount of good quality soil, highly disturbed samples and trimmings from previous tests were resedimented to produce better quality specimens for consolidation and strength testing.

Conventional application of the strain energy method yielded high preconsolidation pressures that indicate the soil is normally to overconsolidated ($1<OCR<8$). An alternative method used to estimate the pre-consolidation stress based on the in-situ void ratio and extrapolation of the virgin consolidation curve predicts that samples shallower than 33 mbsf are near normally consolidated ($OCR\sim1.2$) whereas deeper sediments are underconsolidated ($OCR<1$). However, analysis of the stress path history from a horizontally-oriented CRSC sample gives evidence that the in-situ horizontal effective stress is greater than the vertical effective stress. This analysis provides an upper and lower bound factor that is applied to the strain energy preconsolidation pressure. The result is a reduced preconsolidation pressure that indicates the soil is underconsolidated ($0.2<OCR<0.8$). The in-situ hydraulic conductivity (k_o) is found to vary between $1.5x10^{-7}$ to $3x10^{-8}$ cm/s with no trend with depth. The compression ratio (C_c) ranges from 0.473 to 0.704 with an average of 0.600. C_c is fairly constant up to a depth of 79 mbsf, after which, C_c decreases.

The triaxial tests have revealed that the site may be divided into two layers, with the shallow layer extending up to 20.3 mbsf and the deep layer extending below 20.3 mbsf. In addition, the resedimented specimens exhibited behavior similar to the specimens from the shallow layer. The average normalized undrained strength for the shallow and deep layers are 0.35 and 0.31 respectively. The average friction angle in triaxial compression for the shallow layer is 36^o and 33^o for the deep layer. The results of the laboratory tests were used to determine the SHANSEP parameters of the soil, which, when combined with the stress history at the site, gives the strength profile of the site. Finally, the input parameters for the MIT E-3 soil model were estimated, which will allow further study of the behavior of the soil.

Acknowledgements

I would like to thank the Arnold Schoettler Fellowship and the MIT Presidential Fellowship for providing financial support during my first year at MIT. I would also like to thank the Ocean Drilling Program Leg 204 Scientific Party for providing financial support during my second year, and for providing whole core soil samples.

To my thesis supervisor, Dr. John Germaine, for the wonderful insight and guidance, for the direction, for the brilliant ideas, for the patience, for the understanding, for the personal insight and support, for the inspiration.

To my adviser, Prof. Peter Flemings, for the spark and initiative, for the guidance and motivation, for the words of encouragement, for the funding.

To my professors, Prof. Herbert Einstein, Dr. Lucy Jen, Prof. Charles Ladd, Prof. Andrew Whittle, for the knowledge and wisdom, for the wealth of experience, for the support and advice, for the respect.

To my friends, Alice, Carolyn, and Sheila, for the short conversations in the hallway, for the location of free food, for the reduction of red tape, for the lack of bureaucracy.

To the geotechs, Karim, Louis, Patrick, Madhu, Matt, Kartal, Maria, Eng Sew, Jian Yong, Jed, Patrick, Isabella, Yun, Chu, Anamika, Tae Young, Art, Fernando, and Adonis, for the friendship, for the fun dinners and outings, for the answers to tough questions, for the laughs during the good and bad times.

To my lunch buddies, Francois, Pong, Joon, Sang Yoon, for the noontime meals, for the bonds of friendship, for the help in the time of need, for the unique humor and wit, for the honest and accurate advice, for the wonderful, unforgettably humorous conversations.

To my good friends, buddies, and compatriots, Louie and Val, for the smooth transition to US life, for the help and knowledge of the city of Boston, for the bonds of friendship, for the companionship, for the great, simple, unpretentious, humble, caring personalities.

To my UP friends, for the friendship through thick and thin, for the eastwood gimiks, for the stories and the chismis, for the tambayan and Besa days, for the love and support, for the unforgettable and fun college life.

To my Xavier and ICA friends, for the FGs, for the team destiny, for the yahoo messenger chats, for the wonderful and enjoyable homecomings, for the feeling of not wanting to go back to the US, for the gimiks and basketball, for the love and support, for the bonds of true and everlasting friendship.

To my loving father, David, for the inspiration, for the genes, for the knowledge, for the pride, for the stature, for the gift life.

To my loving mother, Tessie, for being the best mother a son could have, for the support with every decision, for the love and comfort, for the happiness and peace, for the gift of life, the feeling of love and the knowledge of caring.

To my loving sister, Kathy, for being a wonderful roommate, for the love, for the Sunday laundry, for the food, for the advice and caring, for the understanding of shortcomings and accepting me for who I am.

And most of all, to my loving girlfriend, Loline, for the support amidst everything, for the love no matter what, for the meaning to the madness, for the glimpse of the future, for the purpose, for the gift of a life worth living.

Table of Contents

List of Tables

List of Figures

List of Symbols

Symbol	Definition
APC	Advance piston corer
BBC	Boston blue cay
BSR	Bottom simulating reflector
CKoUC	K_o-consolidated undrained compression triaxial test
CKoUE	K_o-consolidated undrained compression triaxial test
CRS	Constant rate of strain
CRSC	Constant rate of strain consolidation test
FGZ	Free gas zone
GHSZ	Gas hydrate stability zone
LVDT	Linear variable differential transformer
LWD	Logging while drilling
MAD	Moisture and density
NC	Normally consolidated
OC	Overconsolidated
OCR	Overconsolidation ratio
ODP	Ocean drilling program
PVC	Pressure volume controller
SD	Standard deviation
SHANSEP	Stress history and normalized strength soil engineering properties
TX	Triaxial
A	A-parameter
B	B-value
C_c	Compression index
C_r	Recompression index
c_v	Coefficient of consolidation
G_s	Specific gravity
e_c	Consolidation void ratio
e_i	Initial void ratio
I_l	Liquidity index
I_p	Plasticity index
K	Lateral stress ratio
K_c	Consolidation lateral stress ratio
K_o	In-situ lateral stress ratio
k	Hydraulic conductivity
k_o	In-situ hydraulic conductivity
LoI	Loss on ignition
m	m parameter in SHANSEP equation
p’	Average effective stress
q	Shear stress
S	S parameter in SHANSEP equation

S_i	Initial saturation
t_s	Time for secondary compression
u_b	Back pressure
w_c	Water content
w_l	Liquid limit
w_n	Natural water content
w_p	Plastic limit
Δu_e	Excess pore pressure
Δu_s	Shear induced pore pressure
$\delta\varepsilon/\delta t$	Strain rate
ε_a	Axial strain
ε_{vol}	Volumetric strain
γ_t	Total unit weight
ϕ	Friction angle
σ'_i	Initial effective stress

Chapter 1: Introduction

Gas hydrates, when in stable form, are solid, ice-like substances composed of a methane molecule surrounded by a cage of water molecules. Gas hydrates have been found in the pore space of offshore sediments. When conditions arise that lead to the instability of gas hydrates, they dissociate into water and gas causing a sudden and dramatic decrease in strength of the soil. It is therefore believed that these substances have been linked to a number of failure mechanisms such as slope failure and well-collapse. Furthermore, on an environmental note, dissociation of gas hydrates has been linked to the increase in global temperatures. Hence, there is a considerable interest in the scientific and business community to develop a more comprehensive understanding of the geologic setting of gas hydrate saturated sediments. The purpose of this research is to gain an understanding of the geotechnical properties of the site, in order to provide answers to some of the questions surrounding gas hydrate research.

In the year 2002, the Ocean Drilling Program (ODP) set out for the coast of Oregon on a scientific expedition focused on understanding the biogeochemical factors that control the distribution and concentration of gas hydrates. ODP Leg 204 was devoted to the study of Hydrate Ridge, Cascadia Continental Margin, off the coast of Oregon. A total of nine sites were investigated within the area. Eight whole core samples totaling 8.5 feet that were obtained from Hydrate Ridge were brought to the MIT geotechnical laboratory to perform experiments with the following goals in mind:

1) Determine the consolidation and strength properties of the soil such as the compression and recompression index, hydraulic conductivity, undrained strength, friction angle, and modulus.
2) Determine the stress history profile at the site, keeping in mind that Hydrate Ridge is located in an accretionary margin setting and may be under passive loading.
3) Estimate the SHANSEP parameters for the site as a means of determining the strength profile.
4) Obtain the input parameters for a complex soil model, specifically, the MIT E-3 soil model developed by Whittle (1987) using the “best-fit” parameter method proposed by Korchaiyapruk (2000).

The consolidation properties were determined from the results of Constant Rate of Strain Consolidation (CRSC) on both intact and resedimented samples. The strength properties were measured from the results of Ko-Consolidated Undrained (CKoU) Triaxial tests.

This thesis is divided into seven chapters, with the first and the last being the introduction and the conclusion, respectively.

The second chapter focuses on the characteristics and properties of gas hydrates. In this chapter, the origin of gas hydrate research, as well as the formation of gas hydrates in-situ is discussed. Also discusses are the effects and issues related to gas hydrates. In addition, a brief introduction to sample disturbance is tackled. This chapter also talks about the SHANSEP and recompression triaxial techniques, as well as the casagrande and strain energy method for determining the preconsolidation pressure.

The third chapter gives an overview of the Hydrate Ridge site and describes in detail ODP Leg 204. It also discusses the various in-situ and shipboard tests that are performed by the ODP. Also found in this chapter is an overview of the laboratory testing program.

The fourth chapter describes the various laboratory tests and gives the test procedures for each laboratory test. Also explained in this chapter are the theories behind the laboratory tests and the equations used to analyze the results of each test.

The fifth chapter provides the results of the laboratory tests.

The sixth chapter discusses the interpretation of the laboratory test results. Found in this chapter are the estimated stress history and strength profile, as well as the SHANSEP and MIT E-3 parameters. In addition, the effect of sample disturbance on the results of the laboratory tests shall be discussed. And more importantly, a discussion into the stress path history of the shallow samples will be included in order to properly determine the stress history of the site.

It is hoped that this study will prove useful for other scientists working with soil from Hydrate Ridge.

Chapter 2: Background

Soil extracted from Hydrate Ridge, Cascadia Continental Margin, USA, was brought to the MIT geotechnical laboratory in order to understand the behavior and determine the geotechnical properties of the Hydrate Ridge soil. Details of the Ocean Drilling Program (ODP) Leg that obtained this soil will be discussed in Chapter 3. The significance of the Hydrate Ridge soil is that it was located within the Gas Hydrate Stability Zone. This chapter will give an introduction to gas hydrates and focus on the aspects and characteristics of gas hydrates that are significant to this research. Furthermore, this chapter will discuss the issue of sample disturbance, which affects the results of experiments in general and specifically to the Hydrate Ridge soil.

2.1 Gas Hydrates

The main feature of Hydrate Ridge is the presence of gas hydrates in the pore space of the sediments. As such, it is important to gain an understanding of the characteristics of gas hydrates. This section focuses on what are gas hydrates, how they are formed, and its uses and implications.

2.1.1. What are Gas Hydrates?

Gas hydrates are solid, ice-like substances made up of water and gas (see Figure 2.1). They were first discovered by Humphrey Davy in 1811. Davy noticed that when a mixture of chlorine and water-cooled, a solid, ice-like substance was formed. In the 1820's, John Faraday was able to successfully recreate Davy's experiments. These experiments gave birth to a new class of associative compounds which we now call gas hydrates.

Gas hydrates are classified as clathrates, which are compounds formed by the inclusion of "guest" molecules of one type into the crystal lattice of a "host" molecule. Gas hydrates refer to clathrates whose host molecule is water and guest molecules are gases. The term "natural gas hydrates" is used to indicate gas hydrates that occur naturally, as opposed to those hydrates that are synthesized in laboratories, and contain "natural gas", which is defined by the oil industry to be the gaseous phase of petroleum (Hunt, 1996).

The most common type of natural gas hydrate on Earth is methane hydrate (Kvenvolden, 2000). This type of hydrate has methane as the guest molecule in the crystal lattice of water. Table 2.1 gives the properties of methane hydrate (Pellenbarg and Max, 2000). Between the late-80's and mid-90's, a number of scientists have made estimates of the amount of methane in gas hydrates worldwide. These estimates range from as little as $1x10^{15}$ m^3 to as much as $115x10^{15}$ m^3, with a consensus value of $21x10^{15}$ m^3 (Kvenvolden, 2000). A new study suggests that the best estimate of gas hydrate volume given the current knowledge is in the range of $1x10^{15}$ m^3 to $5x10^{15}$ m^3 (Milkov, 2003). Regardless of the exact number, it can be seen that the amount of methane found in hydrates is quite large. If it is assumed that the energy density of gas hydrate is $6.50x10^6$ Btu/m^3 (see Table 2.1), gas hydrates can produce $6.50x10^{21}$ to $3.25x10^{22}$ Btu. In the year 2001, the world dry natural gas consumption was estimated to be $9.31x10^{16}$ Btu (EIA, 2001). It can be seen from this statistic that the worldwide gas hydrate volume should be enough to provide natural gas energy for the next 70,000 years.

2.1.2. How are Gas Hydrates Formed?

Water and gas that is near saturation are the two ingredients necessary in the formation of hydrates. However, gas hydrates will not form by simply mixing these two ingredients. They will only form and remain stable under low temperatures and high pressures. When gas hydrates are exposed to high temperatures or low pressures, they dissociate into free gas and water. As such, the only areas where natural gas hydrates can be found are in permafrost regions and deep oceanic sediments on the continental slope and rise. Figure 2.2 shows the phase diagram for a pure water and pure methane system. The boundary between free methane gas and methane hydrate is shown, as well as the boundary between ice and water. The hydrate-gas phase boundary shifts to the left with the addition of NaCl and N_2, and shifts to the right with the addition of CO_2, C_2H_6, H_2S, and C_3H_6.

Figure 2.3 shows an arbitrary depth-temperature curve for an oceanic setting, which is where Hydrate Ridge is located. As shown in the figure, the phase boundary increases with depth. This increase with depth corresponds to the pressure increase due to increasing water pressure. The thermal gradient on the other hand slowly decreases when in water, until the water-sediment boundary is reached. Below this boundary, the geothermal gradient causes temperatures to increase. The region wherein the thermal gradient is to the left of the phase

boundary is called the Gas Hydrate Stability Zone (GHSZ). In this zone, the pressure is high enough to meet the pressure requirement for hydrate stability while the temperature remains below the limiting temperature. The GHSZ ends when the effect of the geothermal gradient causes the temperature to increase beyond the phase boundary, allowing free gas and water to exist as separate components. As such, the zone below the GHSZ is referred to as the Free Gas Zone (FGZ). The Bottom Simulating Reflector (BSR) marks the base of the GHSZ (see Figure 2.4). The location of the BSR is found when a reverse in the polarity of the reflected seismic signal occurs during a seismic survey. In many cases, gas hydrate is concentrated near the BSR.

2.1.3. Why Do We Study Gas Hydrates?

Gas hydrates, when in solid "ice-like" form, are believed to be strong and very stable. In fact, during the formation of gas hydrates in soil wherein gas hydrates replace water in pores, the shear strength of the soil increases while porosity and permeability decreases. This results in an overall increase in the strength and stability of the sediment. However, strength and stability problems arise when events that lead to the dissociation of the gas hydrate occur. During dissolution of gas hydrates, the shear strength decreases as porosity suddenly increases, resulting in a sudden decrease in strength and stability. Furthermore, if gas saturation is exceeded, hydrate decomposition causes gas bubbles to be produced causing a decrease of the strength even further. More importantly, there is a corresponding increase in pore pressure within the sediment due to the release of methane gas in the pore space. This results in a net decrease in effective stress of the sediment.

2.1.3.1. Well-Casing Failure

The parties most immediately affected by the problems associated with gas hydrate dissociation are the oil companies. In order to extract oil from beneath the ocean floor, oil companies drill wells deep into the oceanic crust (~6km). A steel casing, about 0.25" thick, is used to stabilize the walls of the wells. In turn, the casing relies on the strength of the surrounding soil to provide lateral support and prevent buckling. The cost of installing one of these wells is in the order of hundreds of millions of dollars. As such, each well is expected to extract a large volume of oil and gas over a fairly long service life in order to recoup the installation cost. The presence of gas hydrates in the soil layers through which the wells are

driven pose a significant problem in the stability and integrity of these wells (Kvenvolden, 1999). The reason for this instability is that when hot gases are pumped through the well, the surrounding soil heats up, causing the gas hydrates to dissociate. The dissociation leaves the once strong soil layer weak and incapable of supporting the well wall, causing buckling or collapse of the well (see Figure 2.5). There have been incidents wherein the casing walls have collapsed, rendering the well useless and ruining a multi-million dollar investment. By understanding the behavior of hydrate-saturated sediments, it may be possible to design well-casings that would not collapse and fail when the gas hydrates dissociate, without having to spend more than is necessary.

2.1.3.2. Underwater Slope Failures

Another major problem associated with the dissociation of gas hydrates is its effect on the stability of underwater slopes. Slope instability is a commonly encountered, very well studied problem in geotechnical engineering. Generally, slopes fail as a result of stresses being applied to the slope that exceed the strength of the soil that makes up the slope. Furthermore, if there exists a layer whose strength is much lower than the surrounding soil, the probability that the slope will fail greatly increases. In fact, the failure arc for the slope will almost always pass through this weak layer.

In a number of underwater slope failures, the weak layer can be attributed to the presence of a layer of dissociated gas hydrates (see Figure 2.6). It is important to note that the release of overburden due to slope failures may lead to further dissociation of gas hydrate, which may then lead to more slope failures. A number of authors have linked slope failures to the dissociation of gas hydrate (e.g. Summerhayes et al., 1979; Embley, 1980; Carpenter, 1981; Cashman and Popenoe, 1985; Paull et al., 1991; Rothwell et al., 1998; Nisbet and Piper, 1998; Cherkis et al., 1999). Their observations are based on the occurrence of BSRs in the region of the slope failures.

One very well-documented slope failure attributed to the dissociation of gas hydrates is the Storegga Slide on the Norwegian Continental Margin. The Storrega Slide is 290km long and extends over 800km down slope. The slide is believed to have been caused by 3 separate slope failures (Bugge et al., 1987 & 1988). The first two slope failures were believed to have occurred during the late Pleistocene period, while the third slide known to have caused an 11m high

tsunami over the Norwegian coast (Bondevik et al., 1997). A BSR has been found in the region around the Storrega Slide, suggesting that the failure of the slope is linked to the dissociation of gas hydrates. Furthermore, the base of the failure surface was found to be coincident with the base of the GHSZ prior to the slope failure (Paull et al., 2000).

2.1.3.3. Sinking of Ships

Another interesting subject is the linking of the dissociation of gas hydrates to the sinking of ships. A study by May and Monaghan (2003) has linked the sinking of some ships to the eruption of gas as a result of the dissociation of gas hydrates. Their study focuses on the effect of a small number of large methane gas bubbles on the stability of passing ships. The result of their research is that a small number of large methane gas bubbles may result in waves and troughs that cause ships to become unstable and ultimately sink. Research into the effect of a large number of small methane gas bubbles was performed by Denardo, Pringle, and DeGrace (2001). Their research states that the methane bubbles may reduce the density of the fluid below the ship causing it to lose buoyancy and sink.

2.1.3.4. Greenhouse Effect

On a more global scale, the dissociation of gas hydrate has a dramatic impact on the environment. As was mentioned earlier, the most common gas contained in gas hydrate is methane, which unfortunately is a greenhouse gas. Therefore, when gas hydrates dissociate into their components, methane is released into the environment. Should the gas escape into the atmosphere, it could aid in the greenhouse effect, which is responsible for the increase in global temperatures.

It is believed that a drop in the sea-level of about 120m during the last glacial period has reduced the hydrostatic pressure to such a level that would lower the GHSZ by about 20m in the lower latitudes (Dillon and Payll, 1983). The net effect of this lowering is dissociation of gas hydrates causing methane to be released into the environment, and more importantly, weakening the underlying sediment (see Figure 2.6). As was discussed earlier, this could lead to slope failures and slumps. This may result in the release of a significant amount of trapped methane gas into the environment (Haq, 2000).

Conversely, a rise in sea level in the arctic regions may lead to the dissociation of gas hydrates, as a result of warm water raising the temperature in hydrate saturated sediments (USGS, 2003). Figure 2.7 describes this behavior.

2.1.3.5. Potential Energy Source

Nevertheless, though there are many harmful consequences associated with gas hydrates, there is a known benefit linked to this voluminous resource. Gas hydrates comprise more than 50% of the organic carbon in the Earth's reservoirs (see Figure 2.8). What this means is gas hydrates are a potential source of energy with voluminous quantities over the world, even more than fossil fuels. Furthermore, methane exists in voluminous amounts over the world as gas hydrate deposits. This is important because methane is a natural gas and hence a vital source of energy. Therefore, in order to take advantage of this resource, it is essential that a method for mining these gas hydrates be developed without causing any adverse effects to the environment.

2.2 Sample Disturbance

Sample disturbance refers to the changes in chemical and mechanical characteristics that result from the process of removing intact material from the in situ state. Sample disturbance is one of the most commonly faced yet least quantified issues in geotechnical laboratory testing. It is an issue that cannot be overlooked as it greatly affects the results of laboratory tests, most importantly the consolidation and strength tests.

Though sample disturbance affects the results of laboratory experiments, it cannot be totally eliminated, only minimized. As such, it is important to understand the effect of disturbance on the results of laboratory tests. Generally, sample disturbance causes an increase in strain to the plastic zone and results in an unclear transition between the elastic and plastic state (Lunne et al, 1997). Furthermore, sample disturbance causes a decrease in strength and stiffness during undrained shearing. A good discussion on sampling disturbance effects in clay can be found in the paper by Santagata and Germaine (2002).

2.2.1. Causes of Sample Disturbance

The process of soil sampling involves a long process that comprises a number of stages. From drilling the borehole to extruding the sample, sample disturbance can occur as a result of a multitude of reasons.

2.2.1.1. Stress Relief Due to Drilling

Prior to sampling, drilling is performed to reach the desired sampling depth. Because of the removal of the overburden, the locked-in shear stress is released, possibly causing failure in undrained extension. This event imparts a significant amount of sample disturbance to the in-situ soil. To prevent this from occurring, a heavy weight drilling mud is used to apply stress on the hole.

2.2.1.2. Method of Sampling

The method of sampling greatly affects the amount of disturbance imparted on the obtained sample. The most common type of sampling involves hammering a split-spoon sampler into the ground. The difficulty with this sampling method is that the walls of the sampler are thick relative to the diameter of the sample. Furthermore, the sampler is not lowered gently into the ground; rather, the sampler is hammered into the ground. Hence, the resulting disturbance level is significantly high, leading to unreliable laboratory test results.

The preferred method of sampling involves the use of a push-piston sampler. The push-piston sampler is very well studied and has been proven to minimize the amount of disturbance (Santagata, 2002; Ladd, 1991; Baligh, 1985). An advantage of the push-piston over the split-spoon is that the push-piston is slowly pushed into the soil rather than hammered. However, the most important advantage of the push-piston sampler over the split-spoon sampler involves the area ratio of the sampler, i.e., the ratio of the diameter of the sampler to the wall thickness. Figure 2.9 shows the effect of the area ratio on the amount of strain that the centerline element experiences. It can be seen from the figure that as the thickness decreases, i.e., the area ratio increases, the amount of strain experienced by the centerline element decreases (Baligh, 1985). This results in an overall lowering of the sampling disturbance and an increase in soil quality.

Data for the area ratio of the sampler used by ODP was not available. As an estimate, the thickness of the plastic tube that contains the soil was measured. The thickness of the sampler was assumed to be equal to this thickness. As a result, the B was calculated to be 77.4mm and the t was calculated as 5.4mm. The resulting area ratio is 14.33. Based on Figure 2.9, the maximum vertical strain experienced by the centerline element of the soil during sampling was 3% in compression and extension. This is a very high strain, especially when considering that most normally consolidated soils fail at 0.5% to 1% strain.

2.2.1.3. Transportation of Tube Samples

Improper handling of the sampling tubes during storage and transportation are a major cause of disturbance. Once the sampling tubes have been brought on board the drilling ship, they must be stored in a manner as to prevent further disturbance. ASTM D4220 prescribes the proper method of handling, storage and transportation of tube samples in order to minimize the amount of disturbance.

2.2.1.4. Test Specimen Preparation

Proper specimen preparation is vital in preserving the quality of the soil. Improper specimen preparation and handling can lead to misleading results. Section 4.1 discusses how the specimens were prepared in order to minimize sample disturbance.

2.2.2. Effect of Sample Disturbance on Consolidation Results

Sample disturbance has a significant effect on the results of consolidation tests. The effect of disturbance is most visibly seen on the log-stress vs. strain consolidation curve. Figure 2.10 compares the consolidation curves of one of the Hydrate Ridge samples and a Maine silt specimen which is known to have low sample disturbance. The quality of the Hydrate Ridge samples can be evaluated by looking at the following characteristics of the consolidation curves:

1) *Slope of initial loading*. For good quality samples such as the Maine silt samples, the slope of the initial loading is similar to the slope of the unload cycle of the same OCR. The Hydrate Ridge samples have initial loading slopes that are much steeper than the slope of the unload cycle, thus indicating the poorness of the sample quality.
2) *Transition between over and normally consolidated state*. It can be seen in Figure 2.10 that the transition between the over and normally consolidated state, i.e., the transition from the elastic to plastic state, is well defined for the Maine silt sample. This characterizes a good quality sample. The Hydrate Ridge sample on the other hand, does not exhibit a clear transition point, which is indicative of the poorness of the sample quality.
3) *Strain to plastic state*. The strain to the plastic state should be small for good quality samples, as shown in Figure 2.10 wherein the strain to the plastic state for the Maine silt was approximately 1.5%. The Hydrate Ridge sample on the other hand had a

strain to the plastic state of >10%. Sample quality indices are available that classify the quality of the sample based on the strain to the plastic state. These indices are described in detail below.

The effect of sample disturbance on the consolidation properties is as follows:

1) *Decrease in compression index* (C_c): The measured slope of the virgin compression line decreases as a result of poorly defined transition between the over and normally consolidated state.
2) *Increase in initial recompression index* (C_r): For disturbed samples, the slope of the initial C_r is generally higher than the C_r for an unload-reload cycle of the same OCR. This increase in measured slope is a result of softening of the initial elastic zone.
3) *Preconsolidation pressure* (σ'_p): If the dominating disturbance mechanism is the decrease in effective stress at constant water content, the preconsolidation pressure is increasingly overestimated with increasing disturbance (see Figure 2.11a). However, if the dominating disturbance mechanism is the rearrangement of the soil's structure, the slope of the virgin compression line is lowered causing an underestimation of the preconsolidation pressure (see Figure 2.11b). As a result, disturbance can increase or decrease the estimated preconsolidation pressure of a soil, depending on the dominating mechanism involved (Santagata, 2002).

2.2.3. Sample Quality Indices

Terzaghi et al (1996) established criteria for classifying the quality of soil samples. Their criterion is based on the suggestion of Andresen and Kolstad (1979) that the magnitude of the volumetric strain required to reach the in-situ stress in a consolidation test is a good measure of soil quality. Table 2.2 gives the criteria suggested by Terzaghi et al. They also mention that this criteria is valid for cohesive soils with an OCR less than 3 to 5.

Lunne et al (1997) proposed a new criterion for quantifying sample disturbance. They based their criterion on the four quantitative requirements listed by Okumura (1971) for parameters to be used in the evaluation of sample quality. These are requirements are:

1) Easy to determine for the perfectly undisturbed conditions.
2) Regularly variable with disturbance, regardless of the depth of extraction, the stress system experienced, and the soil type.

3) Sensitive to change due to disturbance.
4) Easily and accurately measured.

They concluded that the first requirement is not possible because it is difficult to know the parameters for an undisturbed sample. They went on to conclude that the measurement of $\Delta e/\Delta e_o$ in a consolidation test would best satisfy the other three requirements. $\Delta e/e_o$ refers to the change in the pore volume divided by the initial pore volume at the in-situ stress. Table 2.3 gives the soil quality criteria established by Lunne et al.

2.2.4. Determining the Preconsolidation Pressure

One of the most important parameters in geotechnical engineering is the preconsolidation pressure. This parameter gives the value of the maximum past pressure, and hence gives an indication of whether the soil is normally or overconsolidated.

2.2.4.1. Casagrande Graphical Method

The most commonly used method for determining the preconsolidation pressure is the Casagrande graphical method (Casagrande, 1936). The advantage of this method is it is quick and easy to perform. The drawback however is that it is a highly subjective method and requires experience to accurately predict the preconsolidation pressure. Furthermore, the Casagrande method was difficult to apply to the Hydrate Ridge samples. The reason for this is that the transition between the elastic and plastic state was not well-defined for all the samples. Hence, the casagrande method was not performed for the samples.

2.2.4.2. Strain Energy Method

A more objective method in determining the preconsolidation pressure is the Strain Energy method (Becker et al, 1987). The strain energy is defined as the summation of the product of an increment in strain by the average stress over that increment. The preconsolidation pressure is predicted as follows:

1) The strain energy is plotted versus effective stress.
2) A line tangent to the initial portion of the graph is drawn.
3) A line tangent to the latter straight portion of the curve is drawn.
4) The intersection between these two lines is the preconsolidation pressure (see Figure 2.12).

For tests wherein the unload-reload cycle was performed before the virgin compression line had been reached, the data points corresponding to the unload-reload cycle had to be removed. The reason for this was that the unload-reload cycle causes an upward shift in the strain energy curve.

2.2.5. Developing the Site Profile

One of the purposes of this research is to develop the stress history and strength profile at the site. With this in mind, it is necessary to obtain accurate measurements of consolidation and strength properties. The consolidation properties are measured using the Constant Rate of Strain Consolidation (CRSC) test. The consolidation property pertinent to the development of the site profile is the preconsolidation pressure.

The strength properties are measured using the Ko-Consolidated Undrained (CKoU) triaxial test. The strength property relevant to the development of the site profile is the undrained strength of the soil. The triaxial test is not as simple as placing the soil in the triaxial cell and loading it until failure. The soil specimen must first be consolidated to a known stress state. Over the years, two techniques have been developed to be able to obtain the proper strength properties: recompression and SHANSEP.

2.2.5.1. Recompression Technique

The recompression technique was developed by the Norwegian Geotechnical Institute. This technique involves consolidation of the specimen to the in-situ effective stress (see Figure 2.13). Once the consolidation has been reached, the sample is sheared undrained. The weakness of this technique is that it is susceptible to the effects of sample disturbance. As seen from the figure, if the specimen has undergone a significant amount of sample disturbance, the void ratio at the consolidation stress will be significantly different from the void ratio at the in-situ condition. This results in a measured strength that is significantly different from in-situ.

This technique is not recommended for normally consolidated soils as the undrained strength will be overestimated (Ladd, 1991). However, this method is recommended for highly structured soils because it keeps the structure intact, assuming it was not disturbed by sample disturbance. Also, recompression is suggested for good quality block samples because the

amount of disturbance for this type of sampling is usually minimal. Bjerrum (1973) presents a detailed explanation of the recompression technique and the rationale behind the test.

The strength profile of the site may be developed using this technique by testing soil samples from each depth. The difficulty in doing this with the Hydrate Ridge soil lies in the unknown initial stress state and large strain to overburden stress of the soil, as well as the limited amount of soil samples.

2.2.5.2. SHANSEP Technique

The stress history and normalized soil engineering properties (SHANSEP) technique, as described by Ladd and Foott (1974), was developed as a means of reducing the effects of sample disturbance on the measured strength parameters. The SHANSEP technique is predicated on the assumption that soils of the same mineralogical composition will exhibit uniform strength parameters when normalized to the vertical consolidation stress. This assumption has been confirmed by numerous studies into the normalized behavior of cohesive soils (Santagata, 2002; Sinfield, 1994; de la Beaumelle, 1991; Ladd, 1991)

The SHANSEP technique is performed by consolidating the soil well into the normally consolidated region (see Figure 2.13). Once consolidated to the normally consolidated state, the sample is sheared undrained in order to obtain the normally consolidated normalized undrained strength. If the overconsolidated normalized undrained strength is desired, the sample is unloaded to the desired stress state after consolidation to the normally consolidated state. Once in the desired overconsolidated stress state, the sample is sheared undrained.

The purpose of consolidating well into the normally consolidated region is to minimize the effect of disturbance. It is believed that destructuring of the sample by consolidation to the normally consolidated state will remove the effects imparted by sample disturbance. Furthermore, since it is established that a soil does exhibit normalized behavior, the strength at any depth can be obtained by using the SHANSEP equation:

$$\frac{S_u}{\sigma'_{vc}} = S(OCR)^m \tag{2.1}$$

where S_u is the undrained strength, σ'_{vc} is the vertical effective consolidation stress, and OCR is the overconsolidation ratio. The parameters S and m are called the SHANSEP parameters. S is the value of the normalized undrained strength for a normally consolidated soil, while m is the

factor that gives the normalized undrained strength for overconsolidated soil. The S and m parameters are determined experimentally through a series of SHANSEP triaxial tests. The minimum required tests to obtain the S and m parameters are two normally consolidated SHANSEP triaxial tests and one overconsolidated SHANSEP triaxial test. The two normally consolidated tests are used to verify whether the soil exhibits normalized parameters and obtain the S parameter, while the overconsolidated test is used to obtain the m parameter.

Using equation 2.1 and the appropriate S and m values, the strength profile can be formed by running a series of consolidation tests throughout the depth profile in order to give the OCR at different depths.

The advantage of the SHANSEP technique over the recompression technique is that the issue of sample disturbance is addressed in the SHANSEP technique. It is critical for the development of the strength profile that the sample disturbance present in the Hydrate Ridge soil be minimized or eliminated. More importantly, the SHANSEP technique will allow for the use of resedimented samples, which will be discussed in detail in Section 4.1.2. This aspect is beneficial to this research due to the limited amount of soil. Another advantage of the SHANSEP technique is that it gives a measure of the lateral stress ratio, K_o, which is otherwise difficult to measure in standard consolidation tests.

However, the disadvantage of the SHANSEP technique is that it should not be used with highly structured soil, since consolidation to the normally consolidated state removes whatever structure was intrinsic to the soil. Also, this test technique is difficult to perform and time consuming compared to the recompression test.

A comparison between the SHANSEP and recompression technique was conducted by de la Beaumelle (1991) and Estabrook (1991). The results of their studies have shown that the recompression technique results in a higher S estimate for triaxial compression, and a higher m estimate for triaxial extension. Furthermore, recompression exhibits lower strain to failure, especially in triaxial extension.

2.3 References

Andresen, A., and Kolstad, P. (1979). "The NGI 54-mm Samplers for Undisturbed Sampling of Clays and Representative Sampling of Coarser Material." *The Art and Science of Geotechnical Engineering*, Englewood Cliffs, N. J., Prentice Hall, 206-220

ASTM (2003). *Annual Book of ASTM Standards,* vol. 04.08, *Soil and Rock (I).* Standard no. D4220-95(2003), "Standard Practices for Preserving and Transporting Soil Samples." West Conshohocken, Pa., 539-549

Baligh, M. M. (1985). "The Strain Path Method." *Journal of Geotechnical Engineering*, ASCE, 111(9), 1108-1136.

Becker, D. E., Crooks, J. H. A., Been, K., and Jefferies, M. G. (1987). "Work as a Criterion for Determining In Situ and Yield Stress in Clays." *Canadian Geotechnical Journal*, 24(4), 549-564

Bohrmann, G., Trehu A. M., et. al. (2002). *Proc. ODP Initial Reports*, 204, Ocean Drilling Program, Texas A&M University, College Station, Texas

Bondevik, S., Svendsen, J. I., Johsen, G., Mangerud, J., and Kaland, P. E. (1997). "The Storegga Tsunami Along the Norwegian Coast, Its Age and Run-up," *Boreas*, 26, 29-53

Bugge, T., Belderson, R. H., and Kenyon, N. H. (1988). "The Storegga Slide," *Phil. Transactions of the Royal Society of London*, 325, 357-388

Carpenter, G. (1981). "Coincident Sediment Slump/Clathrate Complexes on the US Atlantic Continental Slope," *Geo-Marine Letters*, 1, 29-32

Cashman, K. V. and Popenoe, P. (1985). "Slumping and Shallow Faulting Related to the Presence of Salt on the Continental Slope and Rise Off North Carolina," *Marine and Petroleum Geology*, 2, 260-272

Centre for Gas Hydrate Research (2004). Available from World Wide Web: http://www.pet.hw.ac.uk/research/hydrate/hydrates_where.html

Cherkis, N. Z., Max, M. D., Vogt, P. R., Crane, K., Midthassel, A., and Sundvor, E. (1999). "Large-Scale Mass Wasting on the North Spitsbergen Continental Margin, Arctic Ocean" in: Gardiner, J., Vogt, P., and Crane, K. (eds), *Mass Wasting in the Arctic*, Geomarine Letters Special Issue 19, 131-142

Collett, T. (2003). "Geologic Characterization of the Eileen and Tarn Gas Hydrate Accumulations on the North Slope of Alaska," *DoE Office of Fossil Energy Methane Hydrate R&D Conference*. Available from World Wide Web: http://www.netl.doe.gov/scng/hydrate/conference_pdfs/JIP_Collett_Northslope.pdf

De L Beaumelle, A. (1991). "Evaluation of SHANSEP Strength-Deformation Properties of Undisturbed Boston Blue Clay from Automated Triaxial Testing," S. M. thesis, Dept. of Civil Engineering, MIT, Cambridge, MA.

Denardo, B., Pringle, L., DeGrace, C. (2001). "When Do Bubbles Cause a Floating Body to Sink." *American Journal of Physics,* 69, 1064-1072

EIA (2001). "World Dry Natural Gas Consumption (Btu) 1992-2001" Available from World Wide Web: http://www.eia.doe.gov/emeu/iea/tablee3.html

Embley, R. W. (1980). "The Role of Mass Transport in the Distribution and Character of Deep-Ocean Sediments with Special Reference to the North Atlantic", *Marine Geology*, 38, 28-50

Estabrook, A. H. (1991). "Comparison of Recompression and SHANSEP Strength-Deformation of Undisturbed Boston Blue Clay from Automated Triaxial Testing," S. M. thesis, Dept. of Civil Engineering, MIT, Cambridge, MA.

Haq, B. U. (2000). "Climactic Impact of Natural Gas Hydrate," in: Max, M.D. (ed.). *Natural Gas Hydrate in Oceanic and Permafrost Environments*, Kulwer Academic Publishers, Netherlands, 137-148.

Kvenvolden, K. A. (1998). "A Primer on the Geological Occurrence of Gas Hydrate.," in: Henriet, J.-P. & Meinert, J. (eds.). *Gas Hydrates: Relevance to World Margin Stability and Climate Change*, Geological Society, London, Special Publications, 137, 9-30

Kvenvolden, K. A. (1999). "Potential Effects of Gas Hydrates on Human Welfare," *Proceedings National Academy of Sciences Colloqium*, USA, 96, 3420-3426

Kvenvolden, K. A. (2000). "Natural Gas Hydrate: Introduction and History of Discovery," in: Max, M.D. (ed.). *Natural Gas Hydrate in Oceanic and Permafrost Environments*, Kulwer Academic Publishers, Netherlands, 9-16.

Ladd, C. C., and Foott, R. (1974). "New Design Procedure for Stability of Soft Clays," *Journal of Geotechnical Engineering*, 100(7), 763-786.

Ladd, C. C. (1991). "Stability Evaluation During Staged Construction," *Journal of Geotechnical Engineering*, 117(4), 537-615.

Lunne, T., Berre, T., And Strandvik, S. (1997). "Sample Disturbance Effects in Soft Low Plastic Norwegian Clay," in: *Almeida (ed.) Recent Developments in Soil and Pavement Mechanics,* Balkema, Rotterdam, 81-102

May, D. A., Monaghan, J. J. (2003). "Can a Single Bubble Sink a Ship," *American Journal of Physics*, 71(9), 842-850.

Milkov, A. V. (2003). "How and Why the Global Estimates of Hydrate-Bound Gas in Marine Sediments Decreased Over the Last Thirty Years, and What This Means for Resources and Global Change Evaluations," *Eos Trans. AGU*, 84(46), Fall Meeting Supplement, Abstract OS42C-01.

Nisbet, E. G., and Piper, D. J. W. (1998). "Giant Submarine Landslides," *Nature*, 392, 329-330

Okumara, T. (1971). "The Variation of Mechanical Properties of Clay Samples Depending on Its Degree of Disturbance." *Proc. Spec. Session on Quality in Soil Sampling, 4th Asian Conference*, ISSMFE, Bangkok, 73-81

Paull, C. K., Usserl III, W., and Dillon, W. P. (2000). "Potential Role of Gas Hydrate Decomposition in Generating Submarine Slope Failures," in: Max, M.D. (ed.). *Natural Gas Hydrate in Oceanic and Permafrost Environments*, Kulwer Academic Publishers, Netherlands, 149-156.

Paull, C. K. (1991). "Is the Extent of Glaciation Limiter by Marine Gas Hydrates?," *Geophysical Research Letters*, 18, 432-434

Pellenbarg, R. E., Max, M. D. (2000). "Introduction, Physical Properties, and Natural Occurrences of Hydrate," in: Max, M.D. (ed.). *Natural Gas Hydrate in Oceanic and Permafrost Environments*, Kulwer Academic Publishers, Netherlands, 1-8.

Rothwell, R. G., Thomson, J., and Kohler, G. (1998). "Low Sea-Level Emplacement of a Very Large Late Pleistocene Megaturbidite in the Western Mediterranean Sea," *Nature*, 392, 377-380.

Santagata, M. C., and Germaine, J. T. (2002). "Sampling Disturbance Effects in Normally Consolidated Clays." *Journal of Geotechnical and Geoenvironmental Engineering*, 128(12), 997-1006

Sinfield, J. V. (1994). "An Experimental Investigation of Sampling Disturbance Effects in Resedimented Boston Blue Clay." S. M. thesis, Dept. of Civil and Environmental Engineering, MIT, Cambridge, MA.

Summerhayes, C. P., Bornhold, B. D. & Embley, R. W. (1979). "Surficial Slides and Slumps on the Continental Slope and Rise of South West Africa: A Reconnaissance Study", *Marine Geology*, 31, 265-277.

USGS (2003). Available from World Wide Web: http://walrus.wr.usgs.gov/resources/hydrate.html

Bulk Density	0.912 g/cm^3
Poisson's Ratio	0.33
Bulk Modulus @ 272 K	5.6 MPa
Shear Modulus @ 272 K	2.4 MPa
Energy Density	6,497,909 btu/m^3
Dielectric Constant @ 273 K	~58
Heat of Fusion	54-57 kJ/mol

Table 2.1: Properties of methane hydrates (Pellenbarg and Max, 2000)

Volumetric Strain (%)	Specimen Quality Designation
<1	A
1-2	B
2-4	C
4-8	D
>8	E

Table 2.2: Criteria for evaluating sample quality (Terzaghi et al, 1996)

Overconsolidation Ratio	$\Delta e/e_o$			
	Very Good to Excellent (VGE)	Good to Fair (GF)	Poor (P)	Very Poor (VP)
1-2	<0.04	0.04-0.07	0.07-0.14	>0.14
2-4	<0.03	0.03-0.05	0.05-0.10	>0.10

Table 2.3: Criteria for evaluating sample quality (Lunne et al, 1997)

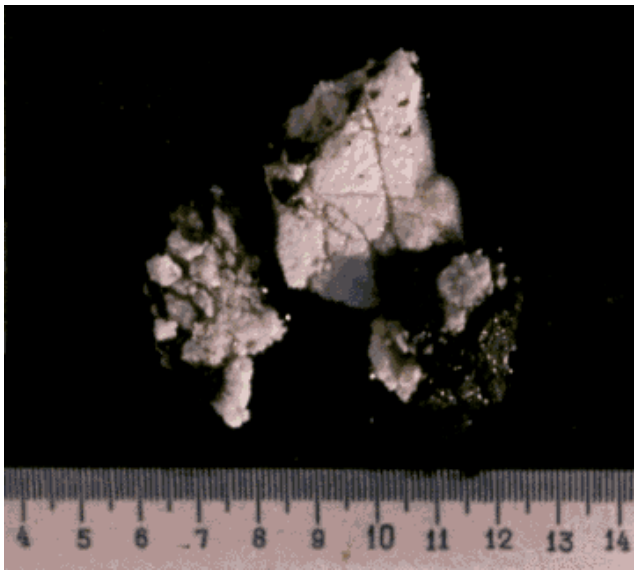

Figure 2.1: Methane gas hydrate (*USGS, 2003*)

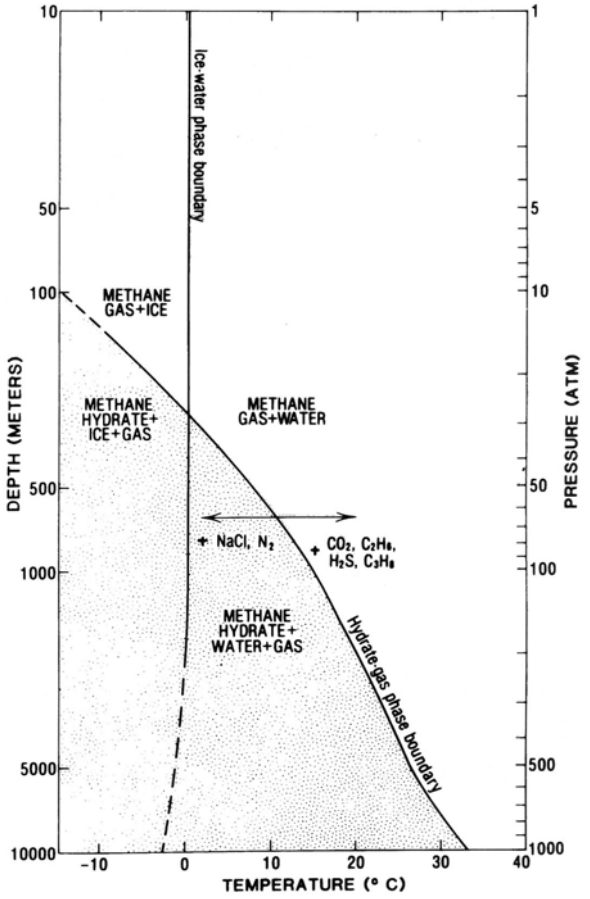

Figure 2.2: Phase diagram of a pure water and pure methane system (*Kvenvolden, 1998*)

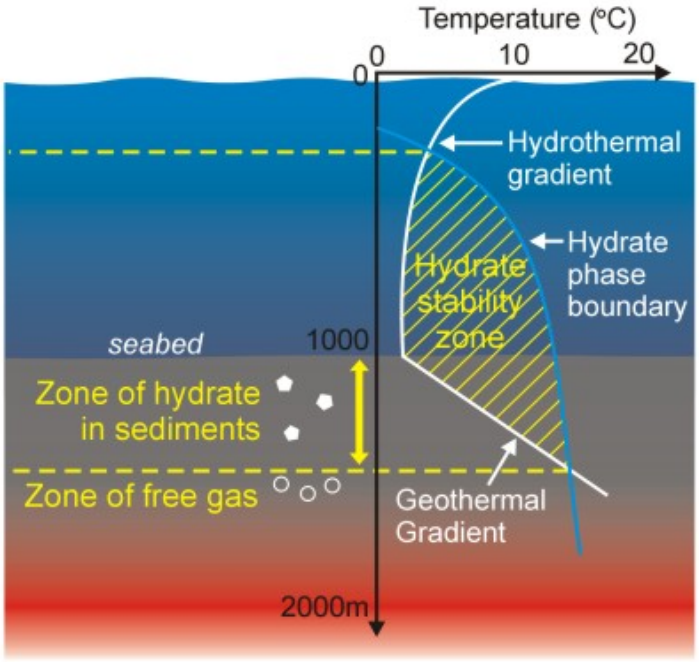

Figure 2.3: Arbitrary depth-temperature curve for oceanic methane hydrate stability (*Centre for Gas Hydrate Research, 2004*)

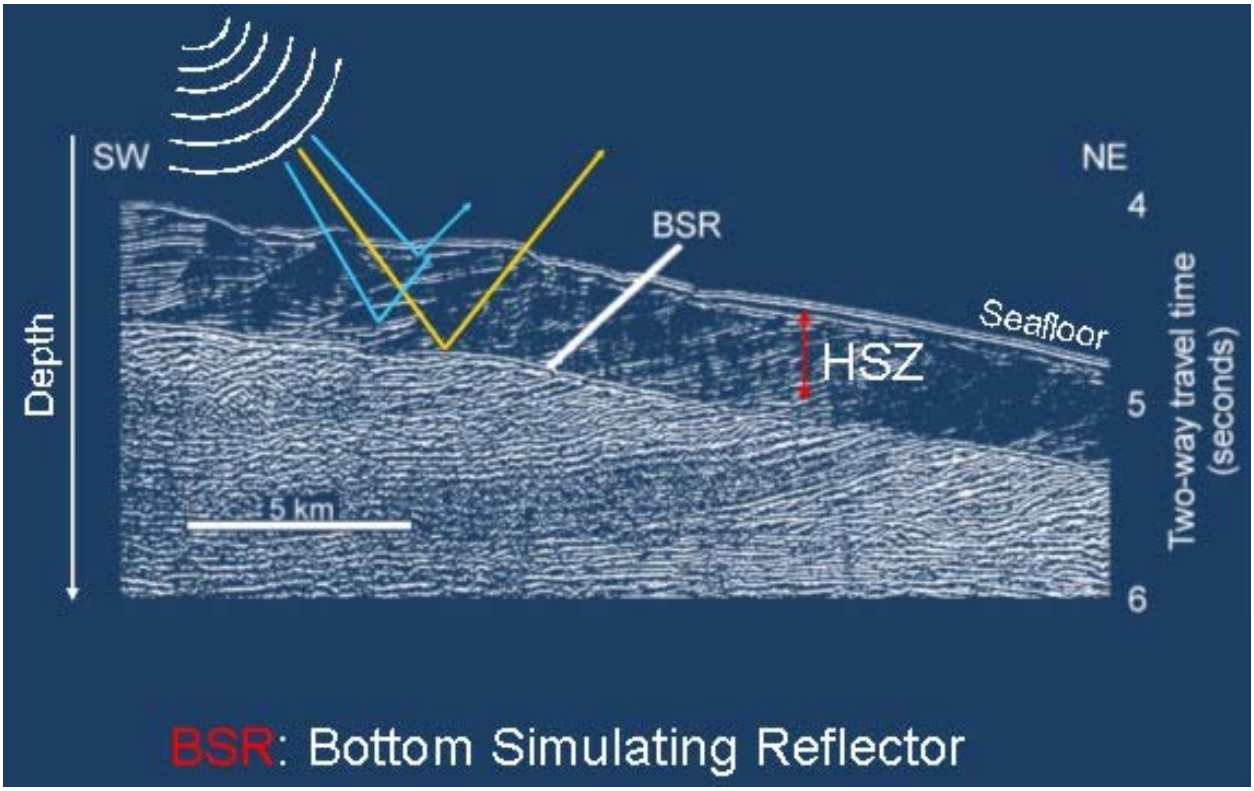

Figure 2.4: Bottom simulating reflector (BSR) (*Centre for Gas Hydrate Research, 2004*)

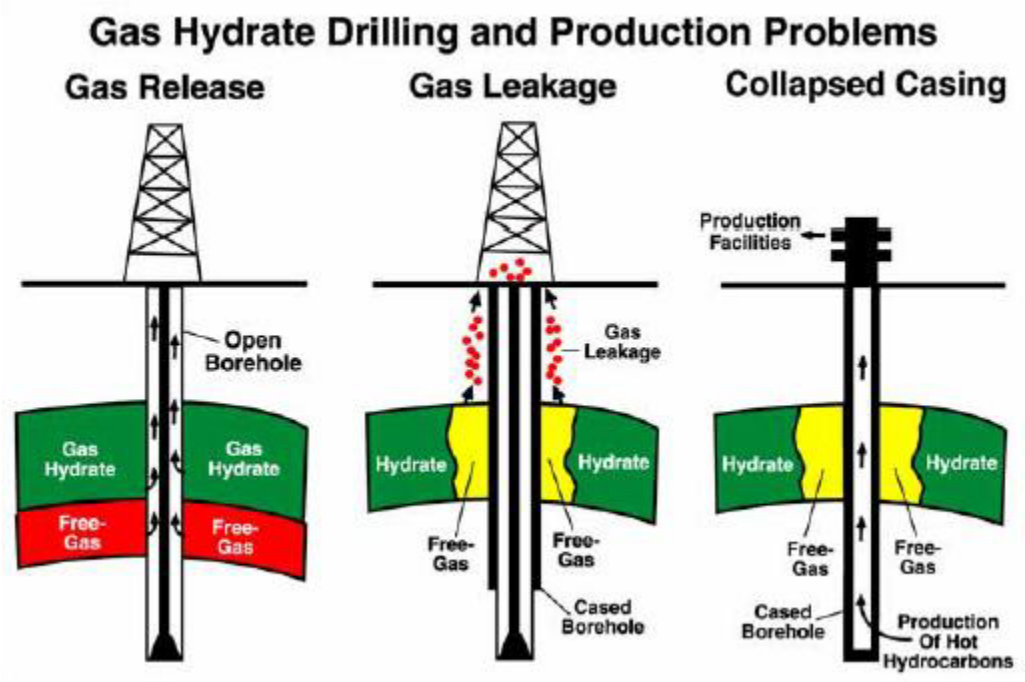

Figure 2.5: Well casing collapse due to hydrate dissociation (*Collett, 2003*)

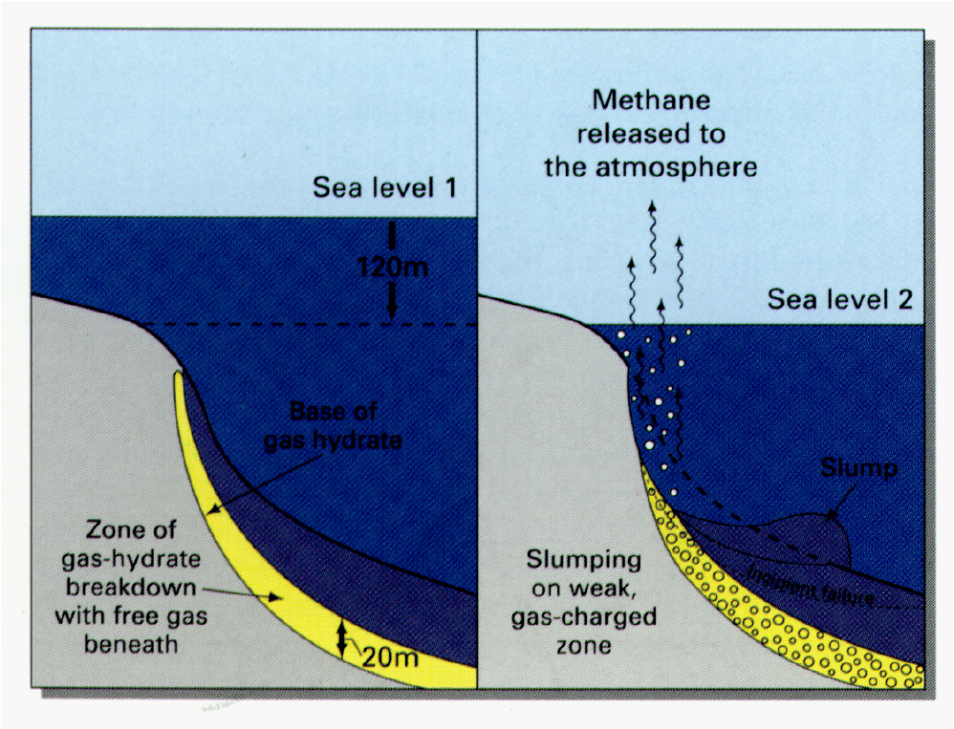

Figure 2.6: Slope failure due to hydrate dissociation (*USGS, 1992*)

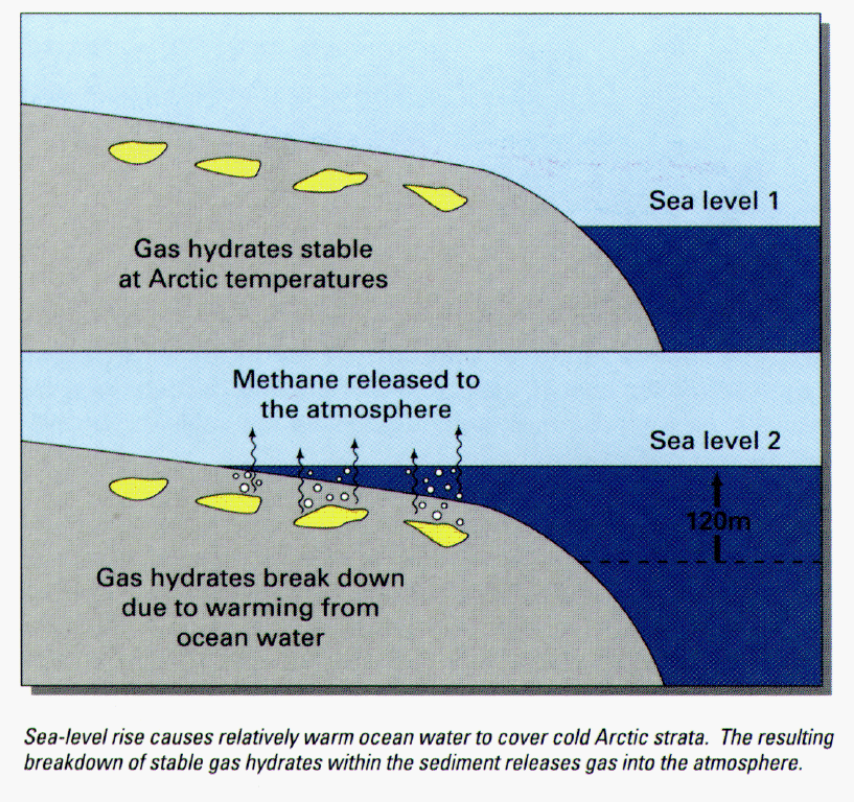

Sea-level rise causes relatively warm ocean water to cover cold Arctic strata. The resulting breakdown of stable gas hydrates within the sediment releases gas into the atmosphere.

Figure 2.7: Methane release due to hydrate dissociation (*USGS, 1992*)

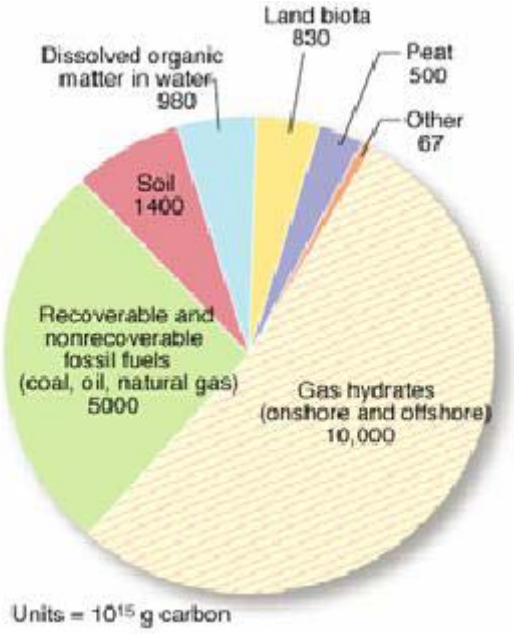

Figure 2.8: Distribution of organic carbon in Earth's reservoirs (*Collett, 2003*)

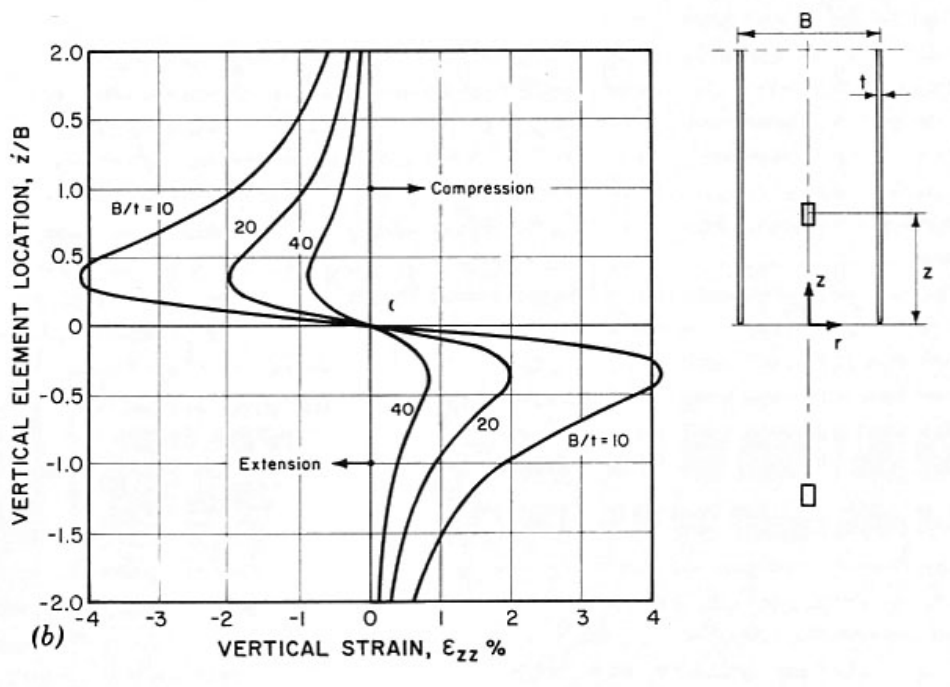

Figure 2.9: Effect of area ratio of centerline element strain path (*Baligh, 1985*)

Slope of initial loading

- For good quality samples, slope of initial loading is very similar to slope of unload cycle to same OCR
- For the Hydrate Ridge soil, slope of initial loading is much steeper than slope of unload-reload cycle

Transition between over and normally consolidated state

- For good quality samples, transition should be clear and marked by short curved portion
- For the Hydrate Ridge soil, there is no clear transition point and curve is very rounded

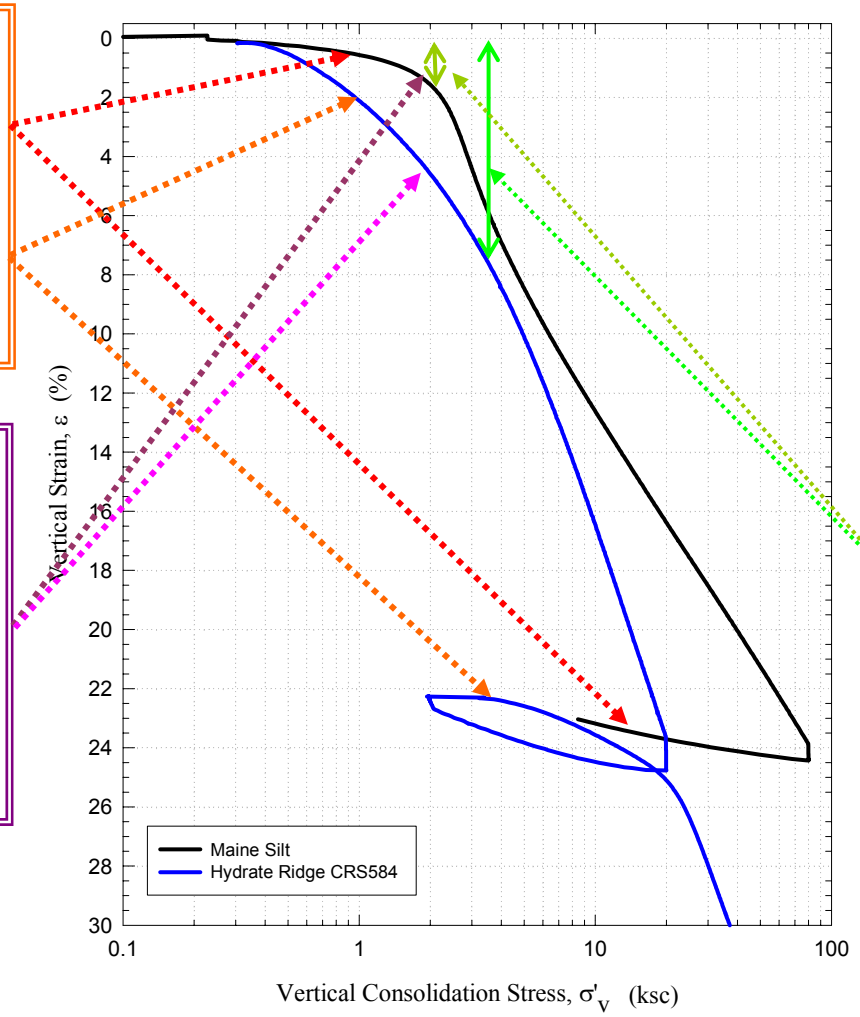

ε to plastic state

- For good quality samples, ε to reach plastic zone is in the range of 1% to 2%
- Based on soil quality classification by Terzaghi, Peck and Mesri (1996), Hydrate Ridge soil classifies mostly as class C to E
- Based on soil quality classification by NGI (1997), Hydrate Ridge soil classifies mostly as Poor to Very Poor

Figure 2.10: Evaluation of sample quality

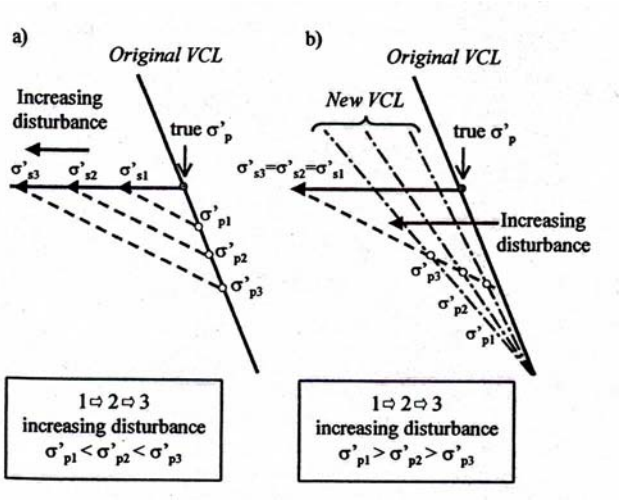

Figure 2.11: (a) Effect of decreasing effective stress on preconsolidation pressure, (b) effect of decreasing VCL slope on preconsolidation pressure (Santagata, 2002)

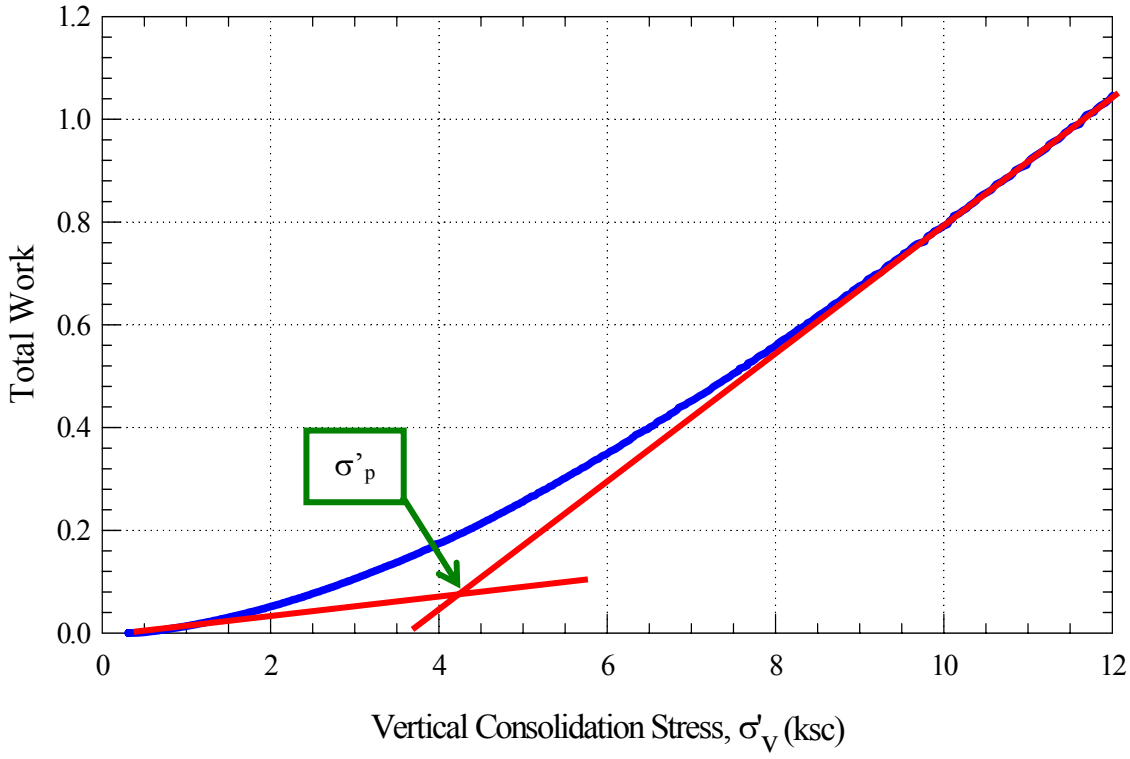

Figure 2.12: Strain energy method for estimating the preconsolidation pressure

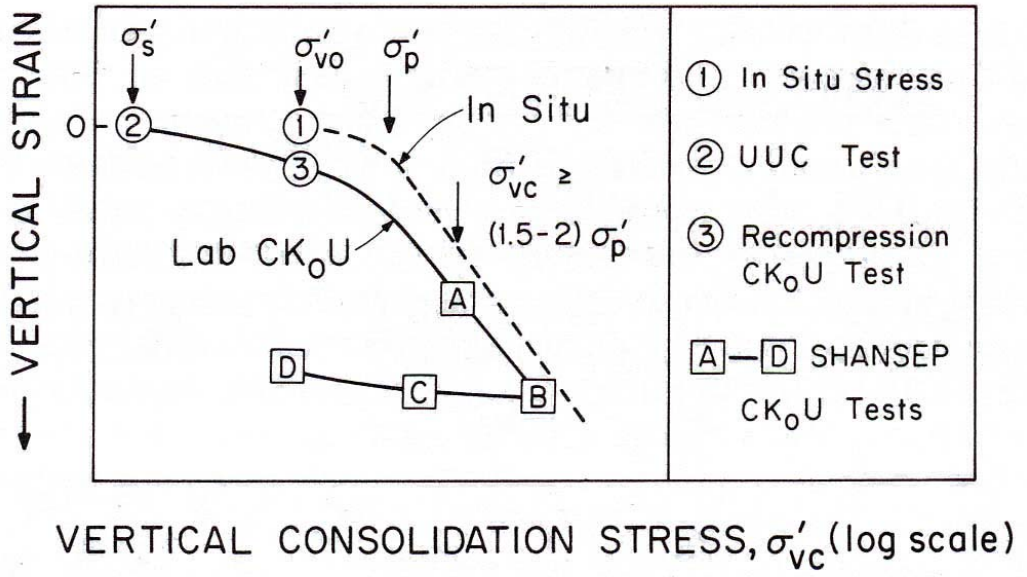

Figure 2.13: Recompression and SHANSEP consolidation techniques for CK_oU tests (*Ladd, 1986*)

Chapter 3: Overview of Hydrate Ridge Soil

This chapter will discuss the details of ODP Leg 204, which was a Leg devoted to the study of the distribution and concentration of gas hydrates in an accretionary ridge setting. Also to be discussed is the method of sample preparation for both intact and remolded specimens. Finally, the last part of this chapter will talk address the laboratory testing program for the Hydrate Ridge soil.

3.1 Description of Hydrate Ridge

In July 2002, the Ocean Drilling Program (ODP) set off on a two month long cruise (Leg 204) to study the biogeochemical factors controlling the distribution and concentration of gas hydrates in an accretionary margin, specifically, Hydrate Ridge, Cascadia Continental Margin. This region is located of the coast of Oregon, in the Pacific Northwest USA (see Figure 3.1A and B).

Hydrate Ridge is a 25 km long and 15 km wide ridge in the Cascadia accretionary complex formed by the subduction of the Juan de Fuca plate beneath North America (see Figure 3.2A), which is subducting at an average rate of 4.5 cm/year (*Bohrmann and Trehu, 2002*). Large volumes of sandy and silty turbidites can be found on the subducting plate. Hydrate Ridge is characterized by a northern and southern peak, with a minimum depth of 600 m and 800 m, respectively (see Figure 3.2B). Furthermore, there exists a strong, well-marked bottom-simulating reflector (BSR). Interestingly, the southern region of Hydrate Ridge contains an abundance of hydrate at the seafloor near the summit. Also, vents located on the northern and southern peaks of Hydrate Ridge have been observed to discharge violent streams of methane gas.

A total of 9 sites, Sites 1244 to 1252, were cored and logged during ODP Leg 204. The samples brought to MIT for laboratory testing were obtained from Site 1244 (see Figure 3.2C).

3.1.1. Site 1244 Holes B and C

ODP Site 1244 is located in 890 meters of water, ~3 km NE of the southern summit of hydrate ridge (see Figure 3.2B and C). 3-D seismic data has shown that the BSR occurs at a

depth of ~125 mbsf (see Figure 3.3). As such, the region above ~125 mbsf is the gas hydrate stability zone (GHSZ), while the region below ~125 mbsf is the free gas zone (FGZ). Furthermore, the seafloor temperature and pressure are well within the range for gas hydrate stability, which implies that gas hydrates can exist within the region above the BSR (see Figure 3.4).

Six holes were drilled at the site, with coring performed on five of the six holes. Hole 1244A was abandoned as the first core overshot and a mudline was not recorded. Hole 1244B was abandoned at 53.1 mbsf due to a disconnection of one of the tools. Hole 1244C was drilled from the seafloor down to 334 mbsf. Hole 1244D was drilled from the seafloor down to 380 mbsf. This hole was devoted to wireline and seismic measurements. Hole 1244E was drilled from the seafloor down to 136 mbsf. This hole was devoted to geochemistry, hydrates, and microbiology testing. Hole 1244F was drilled from the seafloor down to 24 mbsf. The purpose of this hole was for high resolution microbiological sampling.

The site is divided into three Lithostratigraphic Units. Lithostratigraphic Unit I is composed of dark greenish gray clay, with scattered thin layers of silty clay and fine silt. The age of this Unit is 0.27 Ma. The depths of Unit I are as follows: Hole 1244A: 0-9.99 mbsf; Hole 1244B: 0-54.08 mbsf; Hole 1244C: 0-69.00 mbsf; Hole 1244E: 0-77.60 mbsf; and Hole 1244F: 0-23.10 mbsf. Lithostratigraphic Unit II is composed of dark greenish gray silty clay and contains more very fine sand interbedding than Unit I. This age of this Unit ranges from 0.27 to 1.6 Ma. The depths of Unit II are as follows: Hole 1244C: 69.00-245.00 mbsf and Hole 1244E: 77.60-140.79 mbsf. This implies that the BSR is located in Unit II. Lithostratigraphic Unit III is composed of hard, indurated, dark greenish gray silty clay and clayey silt with scattered glauconite sand layers. The distinction between Unit II and Unit III is based on the lack of sulfide precipitates, bioturbation, and silt layers in Unit III. Furthermore, Unit III has a higher state of lithification. The age of this Unit is ~1.6 Ma.

3.1.2. Gas Hydrate Concentration Within Holes 1244B and 1244C

When gas hydrates dissociate, fresh water is dispersed into the pore fluid causing a "freshening effect" of the interstitial water. Therefore, the presence of gas hydrates may be estimated by measuring the chlorinity in the interstitial water of the soil. Drops in the chlorinity of the interstitial water would indicate the presence of gas hydrates. By establishing a "no-

hydrate" chlorinity content, the regions in the GHSZ that may have gas hydrates can be ascertained.

For site 1244 (see Figure 3.5), the chlorine content stays constant above 75 mbsf. Furthermore, from 75 to 300 mbsf, the chlorine content decreases linearly at a rate of ~0.35 mM/m. This linear decrease suggests diffusion of pore fluid whose concentration is 540mM at 70 mbsf, with low salinity fluids in the accretionary wedge. The interstitial water chlorinity data at site 1244 shows sudden drops in the chlorinity at certain regions in the GHSZ. A more detailed explanation of the gas hydrate occurrence estimation can be found in the ODP Leg 204 Initial Report.

3.1.3. Downhole Logging

The ocean drilling program employs two methods to obtain the physical, chemical and structural properties of a deposit in-situ. These two methods are logging-while-drilling (LWD) and wireline logging.

3.1.3.1. Logging-While-Drilling

In LWD, in-situ properties are measured during drilling of the hole through the use of tools attached to the bottomhole assembly of the drillstring, right above the drill bit. However, there is no real-time communication between the LWD tools and the surface. Data are recorded in downhole memory devices, which are then downloaded once the tools have been brought back to the ship. The advantage of LWD is that properties are measured immediately, with little to no formation invasion or wellbore alteration. The ODP employs three LWD tools to obtain in-situ properties:

1) Azimuthal Density Neutron (ADN): This tool provides neutron porosity and bulk density data to determine porosity and lithology of the site. Photoelectric factor measurements are used to improve these nuclear measurements. The tool is said to be azimuthal as it supplies porosity and density information as a function of borehole azimuth. Furthermore, porosity and density information are given for the full 360^{o} as a result of rotation of the tool's sensors. If used together with the Power Pulse tool (MWD), estimates of the in-situ effective stress can be determined. Figure 3.6 shows a schematic of the ADN tool.

2) Compensated Dual Resistivity (CDR): Two receivers measure the phase shift and signal attenuation of a 2-MHz electromagnetic wave emitted by the tool. Interpretation of these data will result in information about the stratigraphy and structural geology of the site.

3) Resistivity-at-the-Bit (RAB): This tool uses a gamma ray emitter and a scintillation gamma ray detector to provide lateral resistivity measurements. A full, 360^{o} image of the borehole can be acquired with the aid of an azimuthal positioning system. Figure 3.7 shows a schematic of the RAB tool and Figure 3.8 shows a sample image produced by RAB data.

Figure 3.9 shows the bulk density of the soil as measured by LWD, while Figure 3.10 shows the thermal neutron porosity and nuclear magnetic resonance porosity.

3.1.3.2. Wireline Logging

The second method used by ODP to determine in-situ properties is called wireline logging. In this method, logging tools are lowered into the borehole on a wireline cable after the coring has been performed. The ODP uses two types of standard toolstrings:

1) Triple Combo: Also known as the geophysical toolstring, this combination of tools will provide density, resistivity, porosity, gamma radiation, and hole size. This toolstring is comprised of the Accelerator Porosity Sonde (APS), Phasor Induction Tool (DITE), and Hostile Environment Litho-Density Sonde (HLDS). Figure 3.11 shows a schematic of the triple combo toolstring.

2) Formation MicroScanner: This toolstring provides high resolution images of the variations in borehole microsenstivity. Included in this toolstring is the General Purpose Inclinometer Tool (GPIT), which allows for orientation of the microsenstivity measurements in the borehole. Also included in this toolstring are the Dipole Sonic Imager (DSI) and Natural Gamma-Ray Tool (NGT).

The ODP also uses a series of specialty toolstrings, but these are beyond the scope of this research. Further information regarding these toolstrings may be found on the ODP website.

Figure 3.12 gives the bulk density as measured by wireline, while Figure 3.13 gives the APS porosity.

For this research, the LWD and wireline in-situ void ratios were used in the interpretation of consolidation results. This interpretation will be discussed in Section 6.2.2.

3.1.4. Shipboard Tests

The ODP performs a series of shipboard geotechnical laboratory tests once the drilled cores are extracted and brought back to the surface. The advantage in immediately conducting the laboratory tests onboard is that the soil has yet to be greatly affected by handling during transportation and storage. Furthermore, the loss of moisture is minimal. Shipboard tests include Gamma-Ray Densiometry, Magnetic Susceptibility, Natural Gamma Radiation, P-Wave Velocity, Thermal Conductivity, and Spectral Reflectance Coloriometry. However, the shipboard laboratory tests that are most significant to this research are the moisture and density (MAD) test and the shear strength tests.

3.1.4.1. Moisture and Density Test

The moisture of the soil is obtained by taking the mass of an 8 cm^3 sample before and after drying for 24 hours in a 110 ^oC convection oven. The bulk density of the soil is obtained by measuring the mass of a specimen and then dividing by its dry volume plus pore-water volume. The dry volume is measured by the ODP by using a helium displacement gas pycnometer. The gas pycnometer method is based on the ideal gas law, whereby the volume of a specimen is measured by recording the change in volume in the system when a change in pressure is introduced. The pore-water volume is calculated by dividing the pore-water mass by the pore-water density. The ODP assumes a pore-water density of 1.024 g/cm^3. The pore-water mass is measured by subtracting the dry mass from the bulk mass, and then divided by 1-s, where s is the pore-water salinity. The ODP assumes a pore-water salinity of 0.035.

Once the moisture and bulk density have been measured, the grain density, dry density, porosity, and void ratio can be measured accordingly. Studies by the ODP have shown that expansion of solids can be neglected and the error introduced by expansion of pore water is negligible compared to the analytical error in calculating the bulk density. Furthermore, fractures induced by the escape of gas do not affect the MAD measured porosity, unlike porosity derived from methods such as gamma ray attenuation. The reason for this is that the method relies solely on the mass and volume of the solid and liquid phases. In addition, the ODP uses a

seawater salinity of 35 g/L, a seawater density of 1.024 g/cm^3, and an average seawater salt density of 2.20 g/cm^3. A more detailed explanation of the MAD method can be found in chapter 2 of ODP Technical Note No. 26.

Figure 3.14 and Figure 3.15 give the MAD void ratio and water content for Site 1244 Hole B and C, respectively.

3.1.4.2. Undrained Shear Strength Tests

The undrained shear strength of the soil is measured onboard using three different pieces of equipment: torvane, pocket penetrometer, and automated vane shear. The torvane is a small device that is pushed into the soil and manually twisted until failure (see Figure 3.16). The handle of the torvane has a gauge that reads the shear strength of the soil. However, the torvane has a quick failure rate and thus may overestimate the measured undrained shear strength. However, because of the significant amount of sample disturbance, the measured strength tends to be underestimated.

The pocket penetrometer is a handheld device that is pushed into the soil up to a specified distance (see Figure 3.17). A scale along the shaft measures the unconfined compressive strength, which is twice the shear strength. The results of the pocket penetrometer are also not accurate and tend to overestimate the undrained shear strength because of the fast shearing rate. However, as with the torvane, the measured strength in this case tends to be underestimated because of the significant amount of sample disturbance.

The automated vane shear employs a four-bladed vane connected to a small motor (see Figure 3.18). The vane is inserted into the soil and rotated by the motor at a rate of 90^o/min while the measuring the torque. The maximum torque required to rotate the soil is used to calculate the undrained shear strength. However, like the torvane, the resulting undrained shear strength may be overestimated due to the quick shearing rate. More detailed explanations of these three shipboard methods used by the ODP to obtain the undrained shear strength can be found in chapter 7 of ODP Technical Note No. 26.

For Site 1244, the only strength test that was performed was the torvane test. Figure 3.19 plots the results of the torvane test with depth.

3.2 Whole Core Samples Provided to MIT

Eight whole core sections taken between 5.7 and 136 mbsf were delivered to MIT for consolidation and strength testing. Table 3.1 gives a list of the whole core sections. The samples are dark greenish gray interspersed with medium greenish gray layers (see Figure 3.20). This difference in color within the sample may be the result of sample oxidation while in the tube.

Samples 1H-4WR (5.7 mbsf) and 3H-3WR (20.3 mbsf) are located in the GHSZ, but it is unclear whether or not these samples do contain gas hydrates. Samples 4H-6WR (32.98 mbsf), 6H-8WR (52.81 mbsf), 8H-7WR (70.88 mbsf), 9H-5WR (79.05 mbsf), and 13H-3WR (114.20 mbsf) are located within the GHSZ and are known to contain gas hydrates. Sample 17H-3WR (135.55 mbsf) is located below the BSR, in the free gas zone (FGZ). Figure 3.21 shows where these samples are located relative to the GHSZ and FGZ.

Upon arrival at MIT, all of the tubes were x-rayed in the MIT geotechnical laboratory x-ray facility. The x-ray procedure is similar to ASTM D4452. The purpose of radiography is to be able to visually assess the sample quality, as well as detect and locate cracks and inclusions inside the soil. Furthermore, radiography reflects changes in soil density and type. This will allow selection of good quality samples for testing in order to minimize the effects of sample disturbance. The x-rays show that tubes 1H-4WR, 4H-6WR, and 17H-3WR have minimal sample disturbance, while tubes 3H-3WR, 6H-8WR, 8H-7WR, 9H-5WR, and 13H-3WR have a significant amount of sample disturbance. Prints of the tube x-ray negatives can be found in Appendix A. Once the tubes have been x-rayed, a log is prepared for each tube. The tube log contains a description of the soil and locations of any cracks or inclusions. These logs also show the various tests performed on samples from each tube, as well as their location relative to the tube length. Complete tube logs can be found in Appendix B. The selection and preparation of laboratory specimens is discussed in detail in Section 4.1.1. After tube x-raying, the samples are stored in a refrigerator set at 4^{o}C.

3.3 Overview Laboratory Testing Program

As was mentioned earlier, the goal of this research is to gain knowledge of the properties and characteristics of the Hydrate Ridge soil. Hence, a suite of laboratory tests were performed to achieve this goal. Table 3.2 gives a summary of all the laboratory tests that were performed at the MIT geotechnical laboratory. The succeeding chapters present the details of each test, as

well as the results. Sections 4.2 and 4.3 present index tests and mineralogy. Section 4.4 presents consolidation tests, specifically, the Constant Rate of Strain Consolidation (CRSC) test. Section 4.5 talks about strength tests, in particular, the Ko-Consolidated Undrained Triaxial (CKoU) test.

3.3.1. Index and Mineralogy Testing Program

Atterberg limits were performed on material from each core location. One liquid limit test was performed an oven-dried sample to see the effect of oven-drying on the measured liquid limit. Furthermore, loss on ignition was performed on samples from each tube. Also, particle size analysis was performed on only one sample.

X-ray diffraction on samples prepared using the random powder method was performed on three samples from different depths. X-ray diffraction on calcite-treated random powder samples were performed on six samples. Lastly, x-ray diffraction on the clay fraction using the random powder method was performed on three samples from different depths.

3.3.2. Consolidation Testing Program

A total of twenty CRSC tests were conducted on the Hydrate Ridge soil. Of the twenty tests, eight were standard-diameter-intact specimens of which two encountered testing problems, nine were small-diameter-intact specimens, two were standard-diameter-resedimented specimens, and one was standard-diameter-remolded. Of the nine small-diameter-intact specimens, one was conducted on a horizontally-oriented specimen. Table 3.3 gives a summary of all CRSC tests that were performed.

3.3.3. Strength Testing Program

A total of ten CKoU tests were conducted on the Hydrate Ridge soil. All of the tests were SHANSEP tests, the details of which will be described in the next chapter. Eight of the ten tests were Ko-consolidated into the normally consolidated zone to at least 10% strain and then sheared in compression. Of these eight, three were sheared in extension after more than 3% shearing in compression. One of the ten tests was Ko-consolidated to 10% strain, unloaded to an OCR of 2, and then sheared in compression. The last of the ten tests was Ko-consolidated to 10% strain then sheared in extension. Of the ten tests, three were performed on resedimented

samples, one was performed on a remolded sample, while the other six were performed on intact samples. Table 3.4 gives a summary of all the CKoU tests that were conducted.

3.4 References

ASTM (2003). *Annual Book of ASTM Standards,* vol. 04.08, *Soil and Rock (I).* Standard no. D4452-85(2002), "Standard Methods for X-Ray Radiography of Soil Samples," West Conshohocken, Pa., 686-699

Blum, P., (1997). "Physical properties handbook: a guide to the shipboard measurement of physical properties of deep-sea cores." *ODP Tech. Note,* 26 [Online]. Available from World Wide Web: http://www-odp.tamu.edu/publications/tnotes/tn26/INDEX.HTM

Bohrmann, G., Trehu A. M., et. Al. (2002). *Proc. ODP Initial Reports*, 204, Ocean Drilling Program, Texas A&M University, College Station, Texas

Earth Book (1987). Esselte Map Service, Sweden

Germaine, J. T. (1982). "Development of the Directional Shear Cell for Measuring Cross-Anisotropic Clay Properties." Sc. D. thesis, Dept. of Civil Engineering, MIT, Cambridge, MA.

Hunt, J.M. (1996). *Petroleum Geochemistry and Geology*, 2nd ed., W.H. Freeman, San Francisco, California

Kvenvolden, K.A. (2000). "Natural Gas Hydrate: Introduction and History of Discovery." in: *Max, M.D. (ed.). Natural Gas Hydrate in Oceanic and Permafrost Environments,* Kulwer Academic Publishers, Netherlands, 9-16.

Ocean Drilling Program (2004). "ODP Logging Manual." Available from World Wide Web: http://www.ldeo.columbia.edu/BRG/ODP/LOGGING/MANUAL/Media_D/index2.html

Ocean Drilling Program (2004). "ODP Logging Tools." Available from World Wide Web: http://www.ldeo.columbia.edu/BRG/ODP/LOGGING/TOOLS/tools.html

Site	Hole	Section		Depth to top of section (mbsf)	Interval (cm)	Lithographic Unit	Hydrate Zone
1244	B	1H	4WR	5.70	120-150	I	GHSZ
1244	B	3H	3WR	20.30	120-150	I	GHSZ
1244	B	4H	6WR	32.98	120-150	I	GHSZ
1244	B	6H	8WR	52.81	0-30	I	GHSZ
1244	C	8H	7WR	70.88	45-75	II	GHSZ
1244	C	9H	5WR	79.05	105-135	II	GHSZ
1244	C	13H	3WR	114.20	120-150	II	GHSZ
1244	C	17H	3WR	135.55	65-109	II	FGZ

Table 3.1: Whole core sections delivered to MIT for consolidation and strength testing

Tube	Depth (mbsf)	Index Tests			X-ray Diff			CRSC		Triaxial Shear		
					RP	RP CT	RP CF			NC		OC
		AL	LoI	PSA				St	Sm	CKoUC	CKoUE	CKoUC
1H-4WR	5.70	1	1						1,1[c]	1[a]		
3H-3WR	20.30	1	1			1		1	1	1		
4H-6WR	32.98	1	1		1	1	1	1	1	1[a], 1[b]		
6H-8WR	52.81	1	1			1		2	1			
8H-7WR	70.88	1	1		1	1	1	1	1			
9H-5WR	79.05	1	1						1	1[a]		
13H-3WR	114.20	1	1	1	1	1	1	2	1			
17H-3WR	135.55	1	1			1		1	1	1[b]		
Remolded		1						1		1		
Resedimented								2		1	1	1

AL: Atterberg Limits
CF: Clay Fraction
CKoUC: Ko-Consolidated Undrained Compression
CKoUE: Ko-Consolidated Undrained Extension
CT: Calcite Treated
LoI: Loss on Ignition
NC: Normally Consolidated
OC: Over Consolidated
PSA: Particle Size Analysis
RP: Random Powder (XRD)
Sm: Small Diameter
St: Standard Diameter

[a]: Compression then Extension
[b]: High Pressure Cell
[c]: Horizontal sample

Table 3.2: Summary table of all tests conducted on Hydrate Ridge soil

Test Name	Tube	Location (mbsf)	Remarks
CRS491	13H-3WR	115.654	Standard Diameter
CRS493	13H-3WR	115.603	Standard Diameter
CRS495	17H-3WR	136.556	Standard Diameter
CRS497	3H-3WR	21.779	Standard Diameter
CRS499	Resedimented 17H-3WR		Standard Diameter
CRS504	8H-7WR	71.609	Standard Diameter
CRS506	6H-8WR	52.861	Standard Diameter Error during test
CRS508	4H-6WR	34.205	Standard Diameter
CRS509	6H-8WR	53.089	Error at 21000s Standard Diameter
CRS511	Resedimented 6H-8WR		Standard Diameter
CRS563	4H-6WR	34.332	Small Diameter
CRS564	17H-3WR	136.467	Small Diameter
CRS567	13H-3WR	115.413	Small Diameter
CRS569	9H-5WR	80.113	Small Diameter
CRS577	Remolded Mixed		Standard Diameter
CRS578	8H-7WR	71.355	Small Diameter
CRS580	1H-4WR	6.938	Small Diameter
CRS584	6H-8WR	52.886	Small Diameter
CRS585	3H-3WR	21.513	Small Diameter
CRS608	1H-4WR	6.976	Small Diameter Horizontal

Table 3.3: Summary of CRSC testing

Test Name	Tube	Location (mbsf)	Test Type	OCR	Remarks
TX635	4H-6WR	34.383	CKoUC	1	High pressure cell
TX636	17H-3WR	136.403	CKoUC	1	High pressure cell
TX641	Remolded*		CKoUC	1	
TX642	3H-3WR	21.627	CKoUC	1	
TX643	1H-4WR	7.141	CKoUC	1	Compression to 8.5% then extension
TX644	Resedimented*		CKoUC	1	Compression to 5.5% then extension With radial filter strips
TX645	4H-6WR	34.269	CKoUC	1	Compression to 4% then extension
TX646	9H-5WR	80.252	CKoUC	1	Compression to 9% then extension
TX647	Resedimented*		CKoUC	2	
TX650	Resedimented*		CKoUE	1	

*Remolded and resedimented specimens were taken from various samples

Table 3.4: Summary of CKoU testing

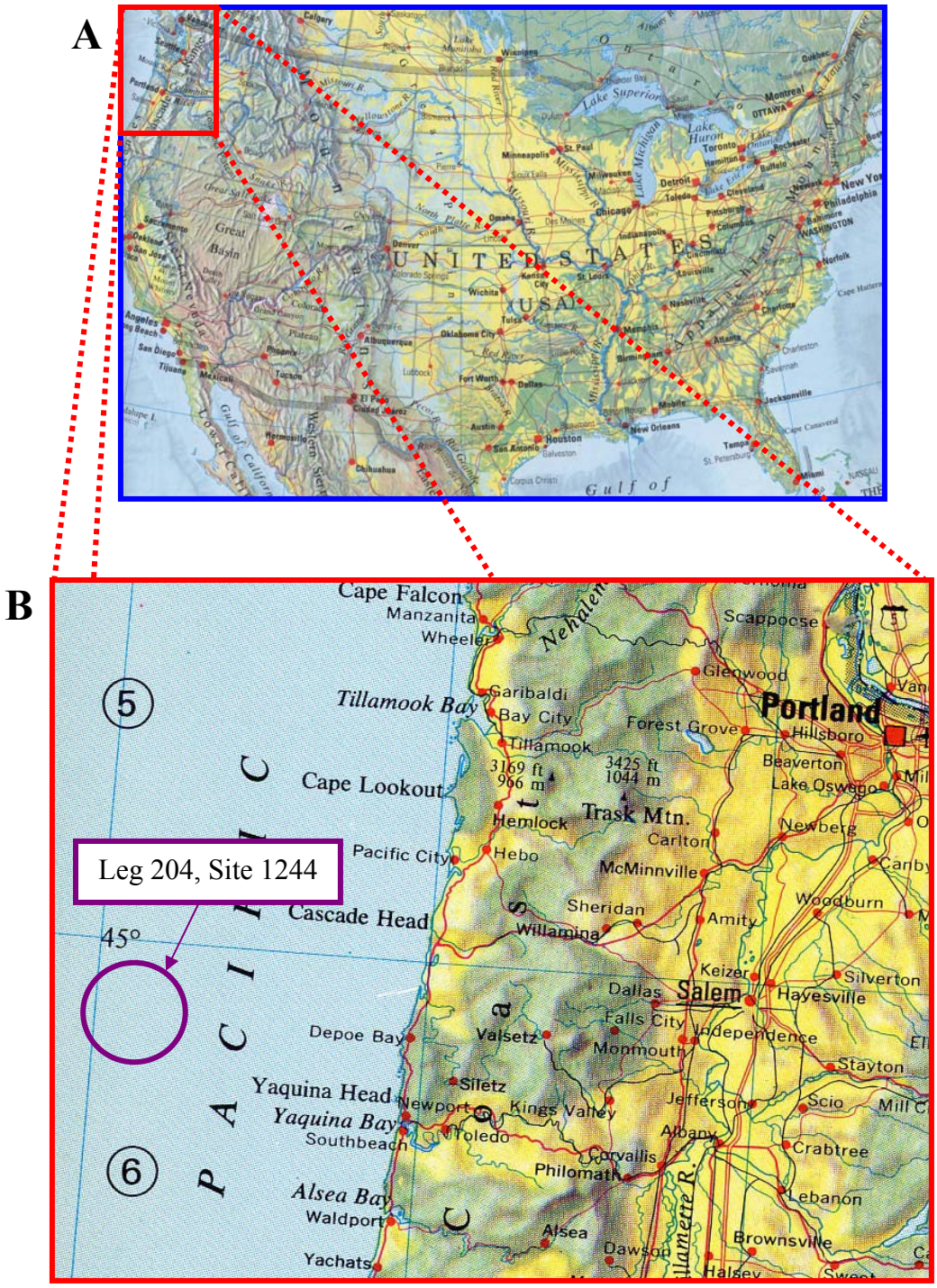

Figure 3.1: (A) Map of USA, (B) Location of Leg 204, Site 1244 (*Earth Book, 1987)*

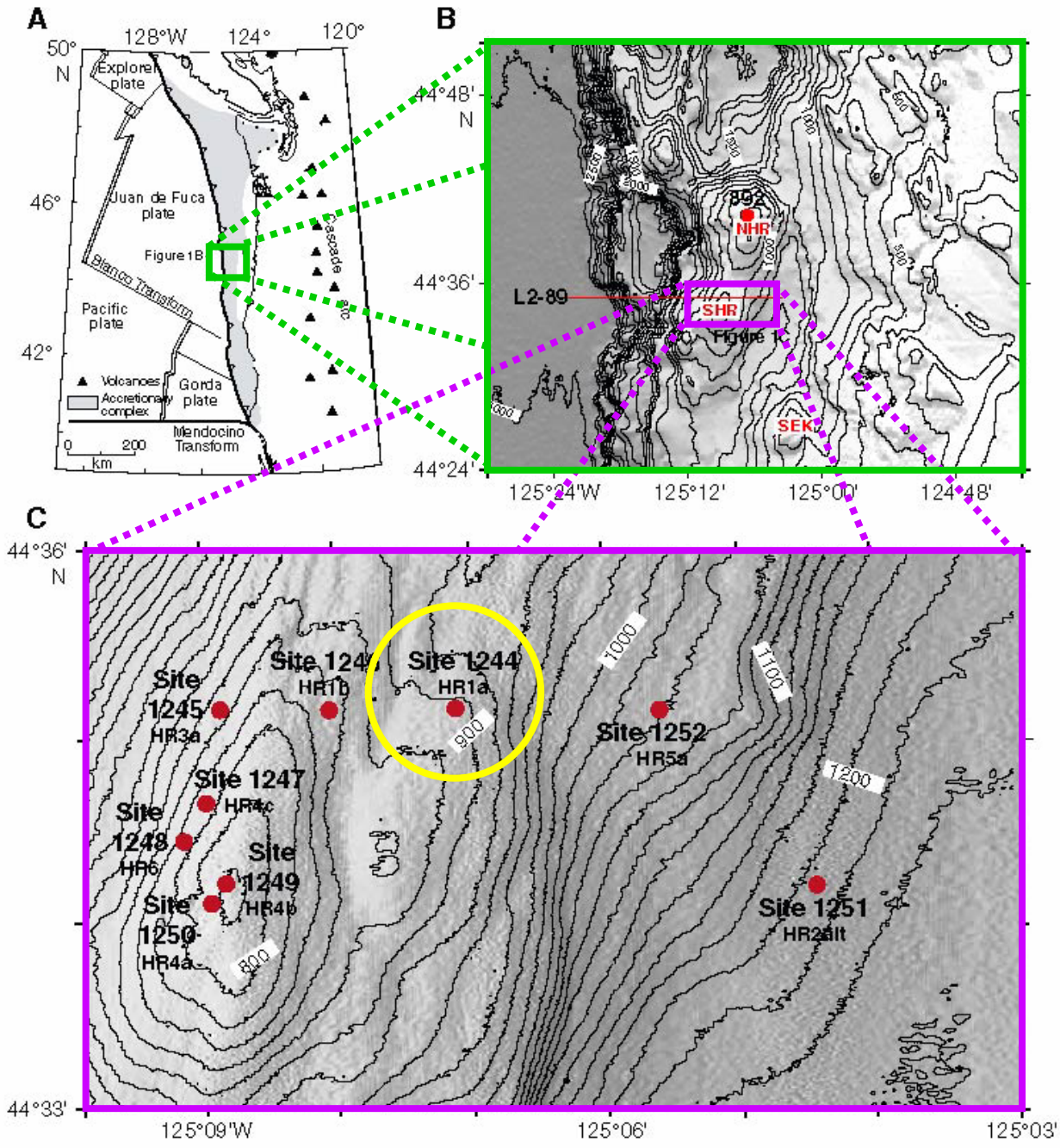

Figure 3.2: (A) Location of Cascadia Continental Margin, (B) Location of Hydrate Ridge, (C) ODP Leg 204, Site 1244 (*Bohrmann and Trehu, 2002)*

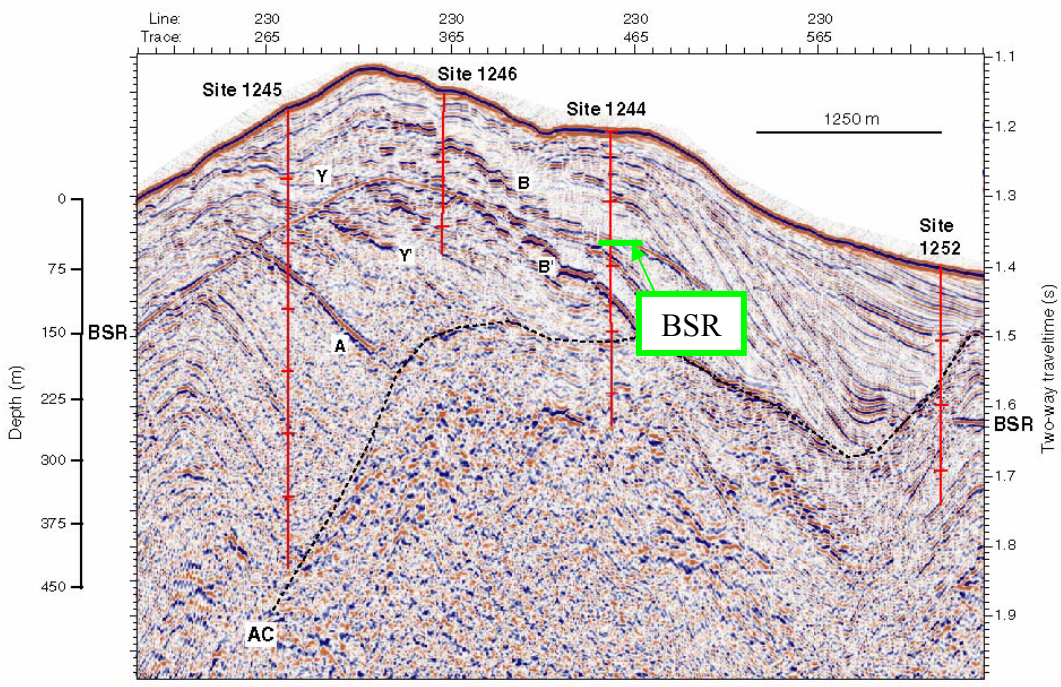

Figure 3.3: Bottom simulating reflector for Site 1244 (*Bohrmann and Trehu, 2002)*

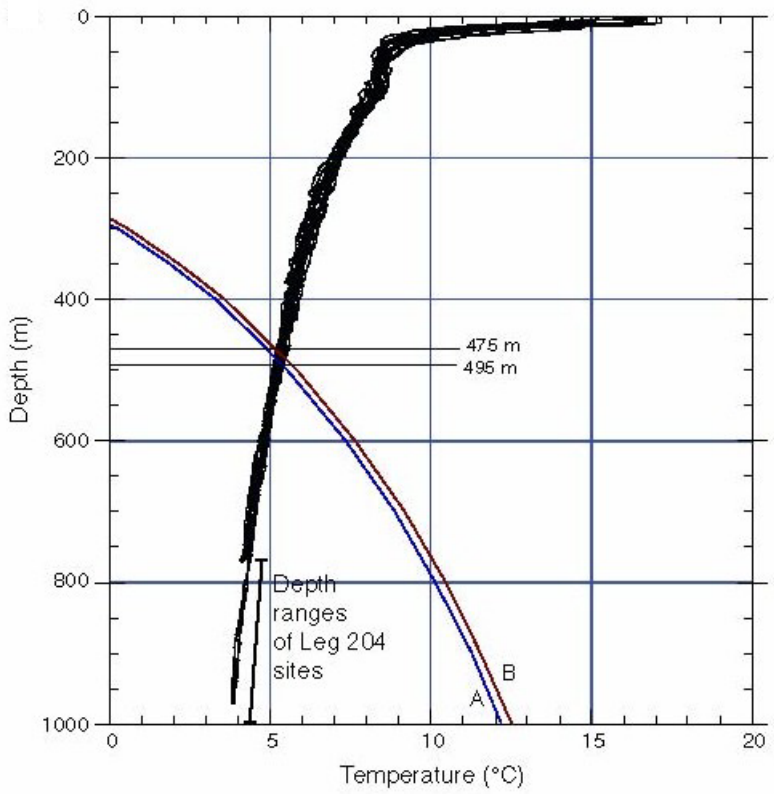

Figure 3.4: Stability boundary for pure methane hydrate (*Bohrmann and Trehu, 2002*)

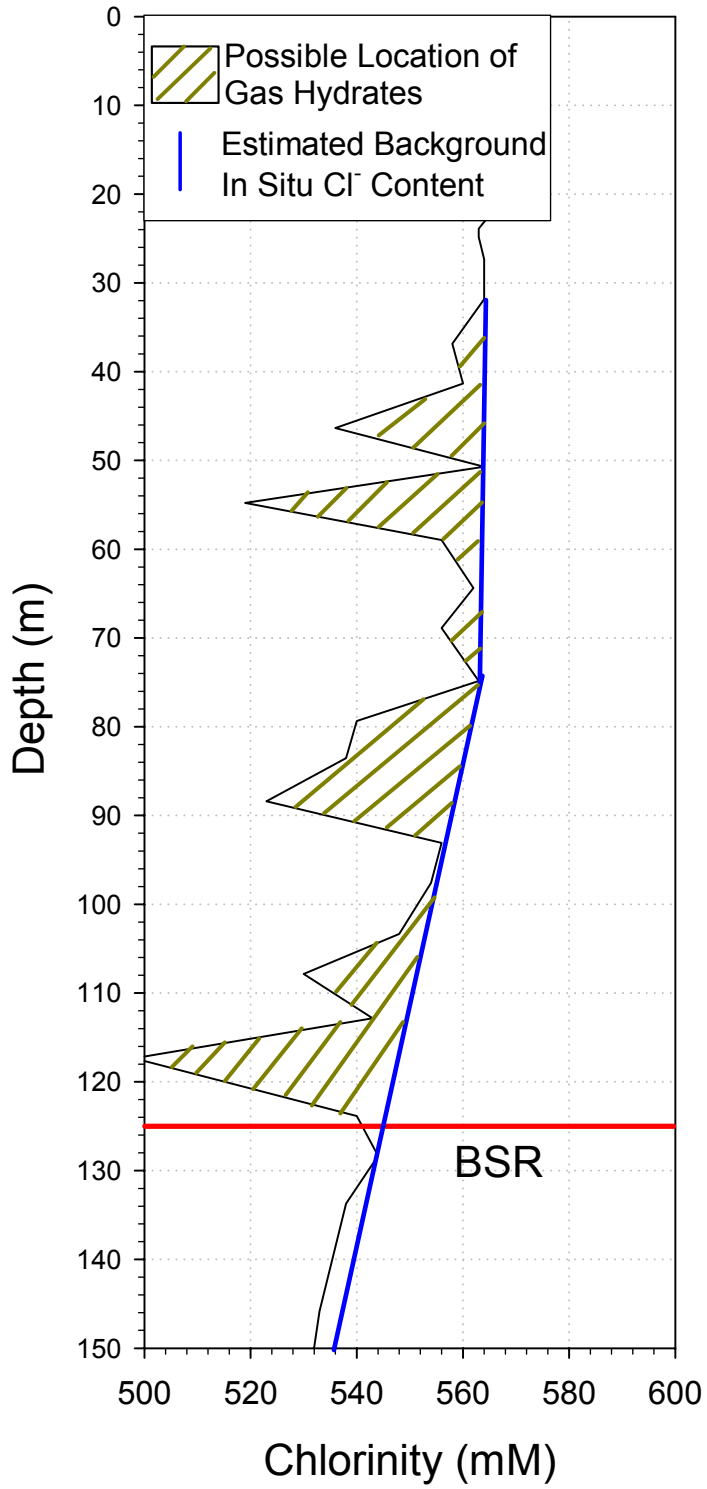

Figure 3.5: Pore water chlorinity as an indication of presence of gas hydrates (*Bohrmann and Trehu, 2002*)

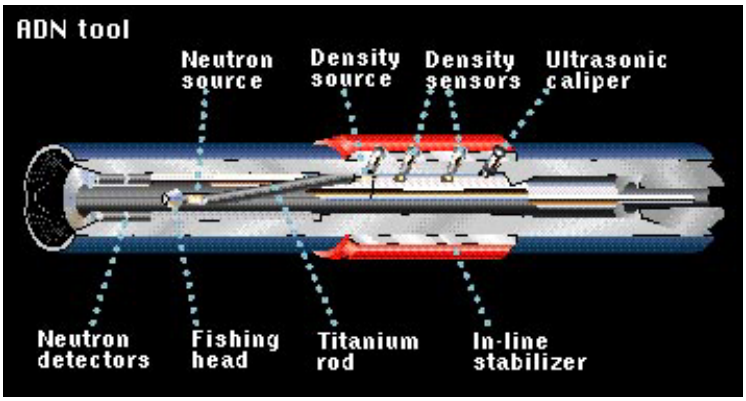

Figure 3.6: Azimuthal Density Neutron tool (*ODP, 2004*)

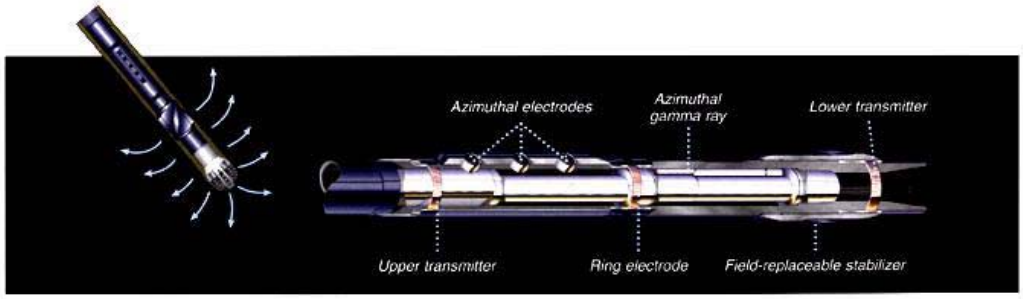

Figure 3.7: Resistivity-at-the-Bit tool (*ODP, 2004*)

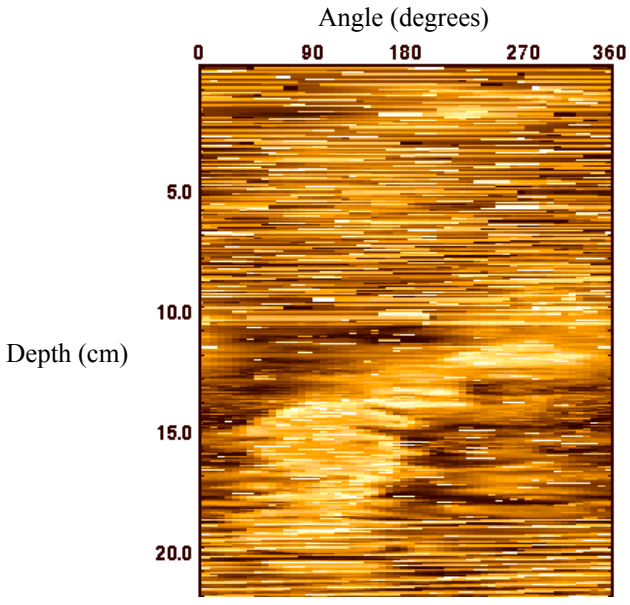

Figure 3.8: Sample RAB image (*Bohrmann and Trehu, 2002*)

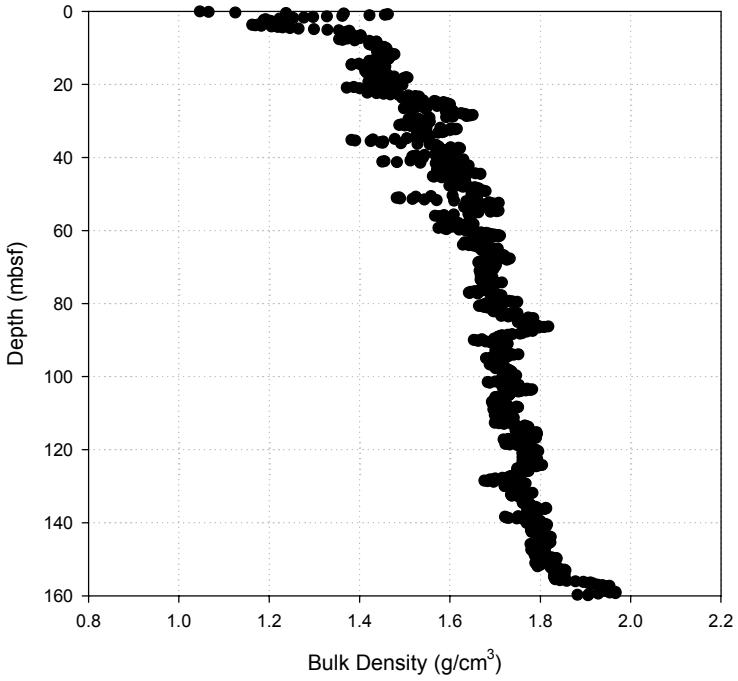

Figure 3.9: Bulk density as measured from LWD (*Bohrmann and Trehu, 2002*)

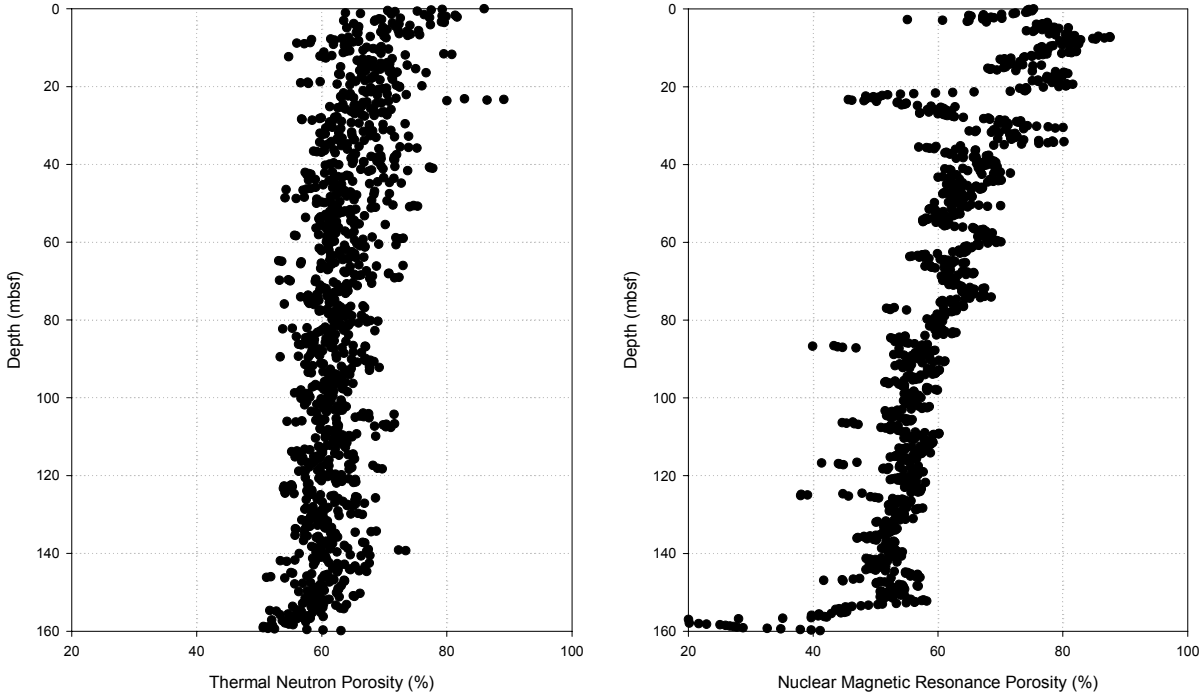

Figure 3.10: Thermal neutron and NMR porosity from LWD (*Bohrmann and Trehu, 2002*)

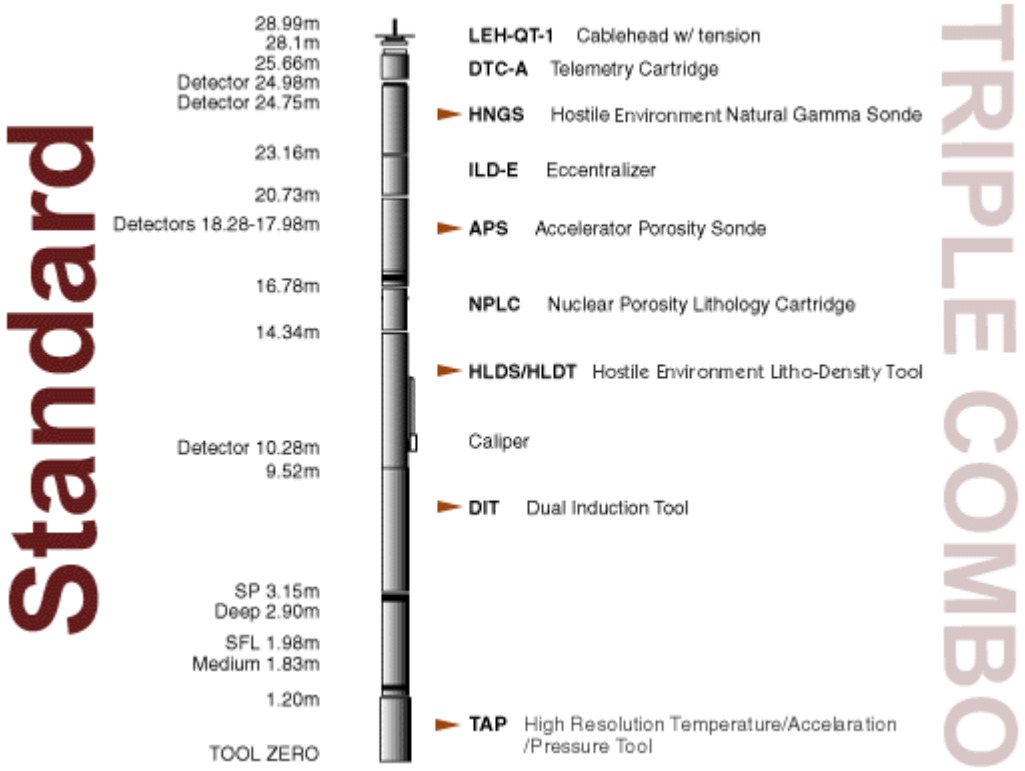

Figure 3.11: Triple combo wireline toolstring (*ODP, 2004*)

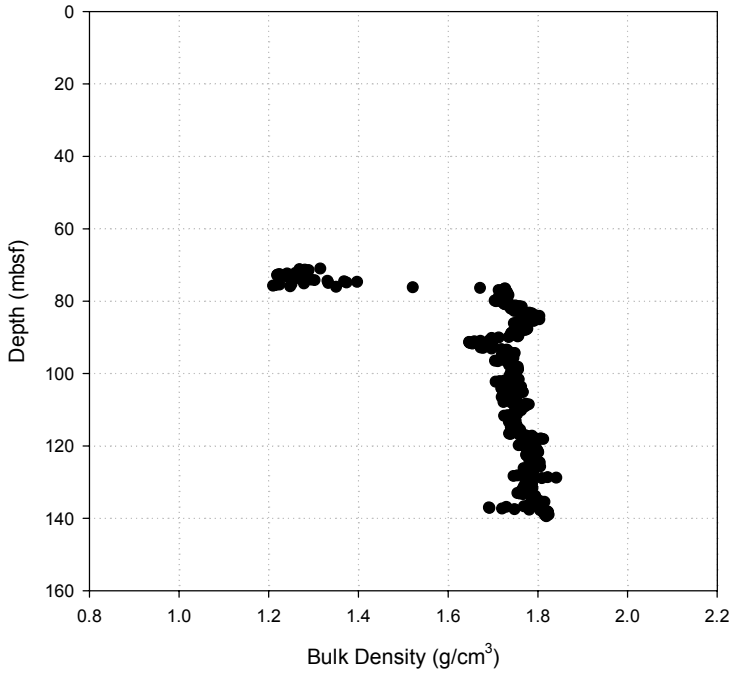

Figure 3.12: Bulk density as measured by wireline (*Bohrmann and Trehu, 2002*)

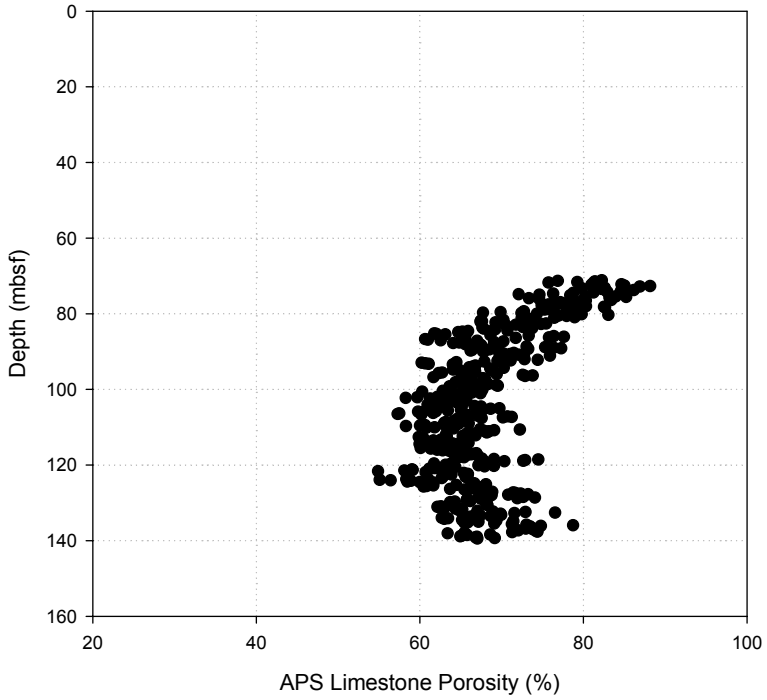

Figure 3.13: APS limestone porosity as measured by wireline (*Bohrmann and Trehu, 2002*)

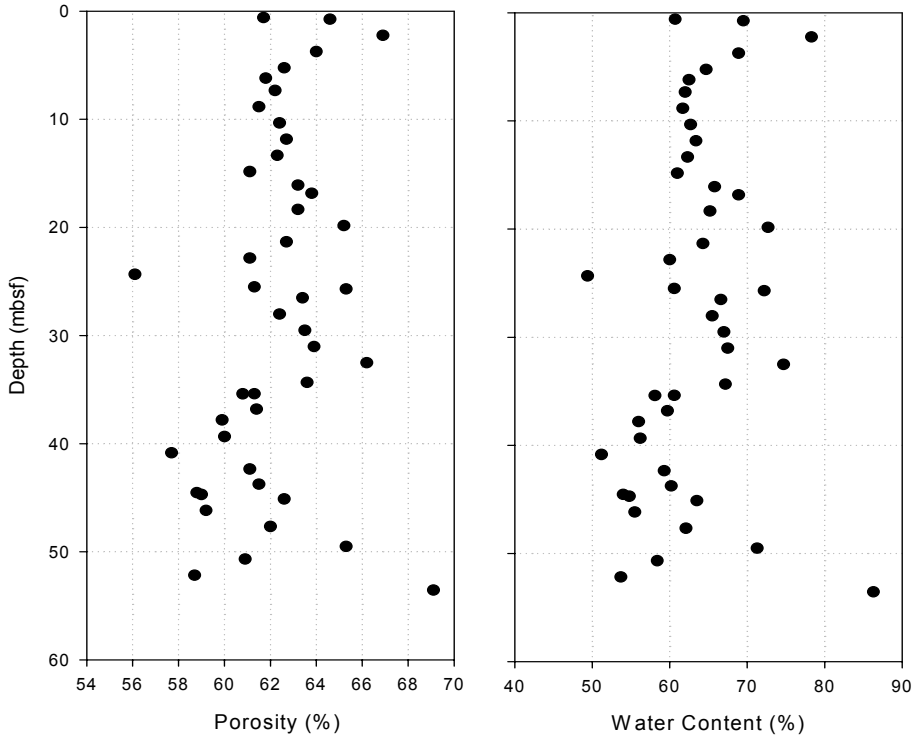

Figure 3.14: MAD porosity and water content for Site 1244 Hole B (*Bohrmann and Trehu, 2002*)

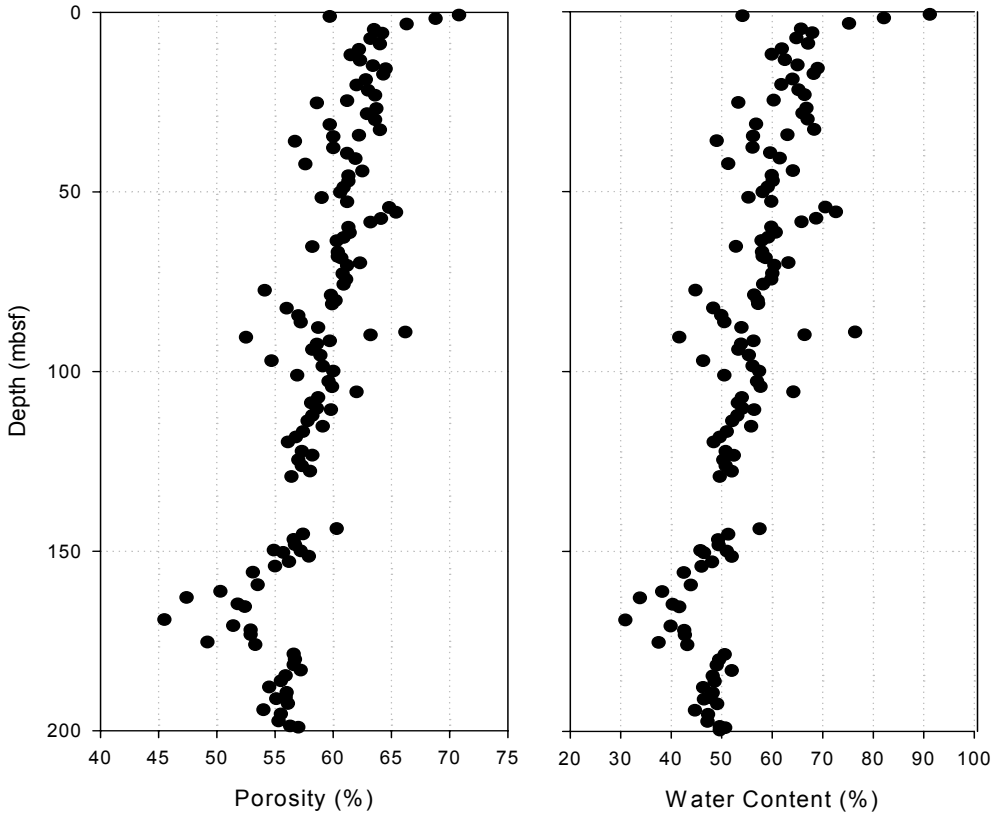

Figure 3.15: MAD porosity and water content for Site 1244 Hole C (*Bohrmann and Trehu, 2002*)

Figure 3.16: Torvane device

Figure 3.17: Pocket penetrometer device

Figure 3.18: Automated vane shear

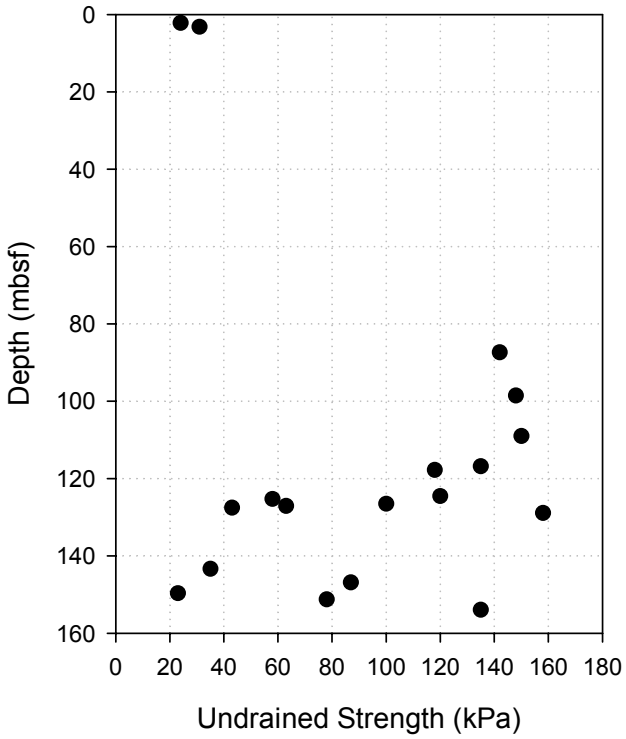

Figure 3.19: Torvane undrained strength for Site 1244 Hole C (*Bohrmann and Trehu, 2002*)

Figure 3.20: Color of hydrate ridge soil

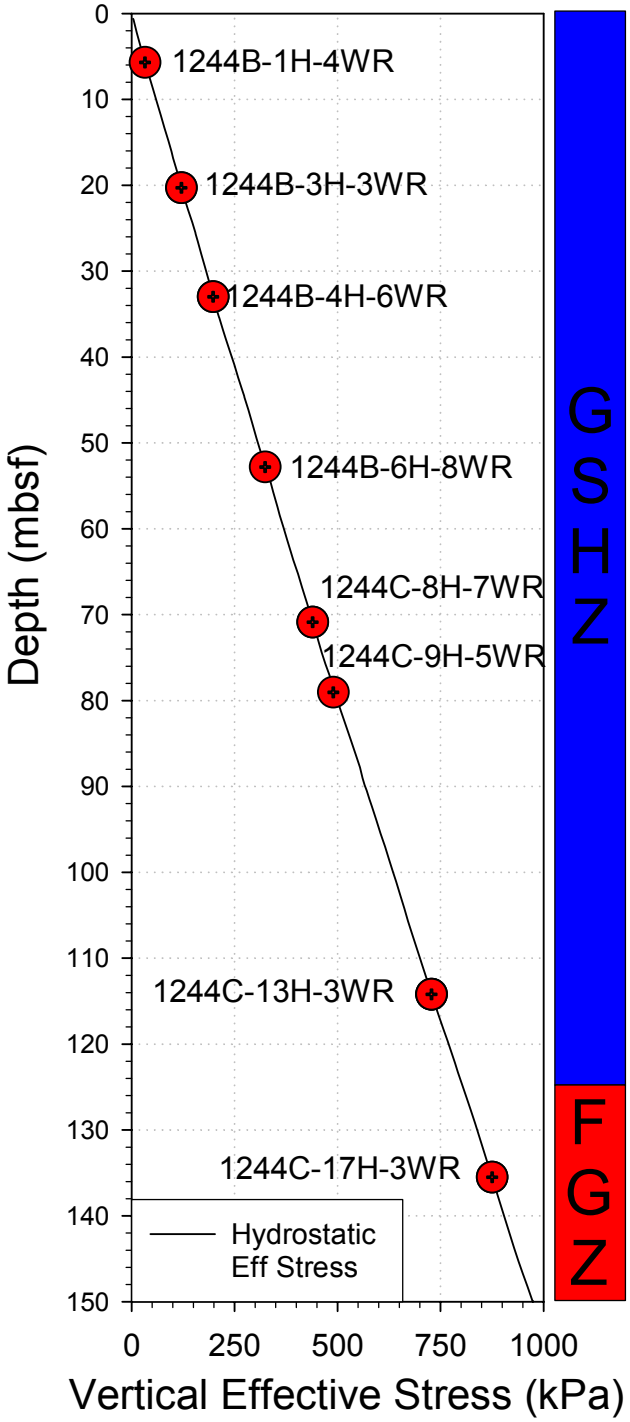

Figure 3.21: Location and in-situ vertical effective stress of MIT whole core samples

Chapter 4: Laboratory Testing Methodology

Geotechnical laboratory tests are performed to determine the geotechnical characteristics of the soil such as compressibility and strength. This chapter focuses on how the various geotechnical laboratory tests are performed. The results of these tests are presented in Chapter 5.

4.1 Sample Preparation

One of the most important steps in performing a laboratory geotechnical experiment is proper sample preparation. The goal of proper sample preparation is to minimize disturbance and obtain control of the dimensions and stresses. This section discusses the standard trimming practices of the MIT geotechnical laboratory and how remolded and resedimented specimens are prepared.

4.1.1. Selection and Preparation of Intact Specimens

The first step in the selection process is to check the soil quality from the tube x-rays. Once a sample with the best quality soil is selected, the tube is cut above and below that location. The soil is then extruded by first inserting a piano wire between the tube and the soil, and slowly running the piano wire around the inside perimeter of the tube. The purpose of this process is to debond the soil from the tube to allow for easy extrusion and minimize sample disturbance. Now that the soil and tube are debonded, the soil may be slowly pushed out of tube. The extruded soil may now be trimmed depending on what type of test will be conducted.

For consolidation tests, the soil is placed in a trimming jig that lowers the consolidation ring into the soil (see Figure 4.1). The consolidation ring has a cutting edge to allow the ring to cut into the soil. Consequently, to prevent additional disturbance, excess soil is slowly trimmed off from around the perimeter and the ring is pushed into the soil in small increments.

For strength tests, the soil is first trimmed down in a miter box using a wire saw, until the radius is about 0.75 cm greater than the final radius. The specimen is then placed in a trimming jig (see Figure 4.2) and trimmed using a wire saw (see Figure 4.3), along the coarse side of the jig first and then finally on the fine side. Then, the ends are cut to desired height of the specimen, which is usually 3”. The ends are finished with a thin blade to ensure a flat, smooth surface.

4.1.2. Preparation of Remolded and Resedimented Specimens

Because of the limited amount of intact, good quality soil available for testing, a number of tests were conducted on laboratory reconstituted specimens. Remolded specimens were prepared by first mixing together trimmings left over from sample preparation and highly disturbed soil that could not be used for intact sample testing. The soil is then allowed to air dry until the water content is about 40%. For consolidation tests, the soil is pressed into the consolidation ring, making sure that the soil is tightly packed into the ring. For strength tests, the soil is placed in a mold that has the same dimensions of a triaxial test specimen (see Figure 4.4). The soil is slowly packed, making sure that it is placed tightly in the mold and there are no voids. The results of the tests performed on remolded specimens can be found in Section 5.3 and 5.4. However, the results show that preparing the soil in this manner does not produce results similar to that of tests on intact specimens, especially in undrained shearing. Possible reasons for this are that the molding water content is too low and the molded soil fabric is different from the intact fabric. Preparing the soil at a higher water content is possible, but makes test setup too difficult. As such, an alternative method for preparing remolded specimens with a high water content was employed. This method, called resedimentation, is similar to the process used to prepare Resedimented Boston Blue Clay (Germaine, 1982).

The soil for resedimentation is prepared by mixing trimmings from previous tests and soil deemed unsuitable for intact sample testing in a blender with water to turn it into a slurry. The slurry is then thickened by placing it in a 100 ^{o}C oven and removing it every hour for about five minutes in order to stir and let it to cool. This process of stirring and cooling the soil ensures the soil is only thickened and not fully dried. Once the slurry has thickened, it is ready for bench consolidation. For consolidation tests, the slurry is placed in the consolidation ring and tested immediately. For strength tests, the slurry is first scooped in a tall oedometer ring (see Figure 4.5). The slurry must be slowly scooped into the ring to prevent the formation of air pockets and voids. Then, the slurry is incrementally loaded until the vertical effective stress reaches approximately 500 kPa. A load-increment ratio of 1 was used, with each load being maintained for at least 24 hours to ensure the completion of primary consolidation. Once 500 kPa has been achieved, the load is reduced until an OCR of 4 is reached. Figure 4.6 shows a specimen being resedimented. The sample is then extruded and trimmed as an undisturbed sample. The results of tests performed on resedimented specimens can be found in Section 5.3 and 5.4. The results

show that resedimentation exhibits similar behavior to intact specimens, especially in undrained shearing.

4.2 Index Tests

Index tests are performed to give the basic properties of a particular soil. These properties are also used in the classification of the soil based on classification standards. Index tests consist of a suite of laboratory tests that is comprised of the atterberg limit test, particle size analysis, and specific gravity analysis. This section discusses the different theories behind index tests, as well as how they are conducted.

4.2.1. Atterberg Limits

The water content of a cohesive soil affects its consistency and behavior. Albert Atterberg (1911) defined three boundaries that differentiate the four behavior states of a cohesive soil. These boundaries are:

- *Liquid Limit:* change between the liquid and plastic state
- *Plastic Limit:* change between the plastic and semisolid state
- *Shrinkage Limit:* change between the semisolid and solid state

The range over which a soil behaves plastically, i.e. the difference between the liquid limit and the plastic limit, is defined as its plasticity. The Atterberg Limits tests were conducted in accordance with ASTM D4318.

The liquid limit was obtained by placing the soil in a casagrande cup, grooving the soil with ASTM groove tool, and counting the number of blows necessary to close the groove by 1/2". The water content at 25 blows is the liquid limit. The plastic limit is the water content of a soil when rolled until crumbling occurs at a diameter of 1/8". The results of the atterberg limits can be found in Section 5.1.1.

4.2.2. Loss on Ignition

When the atterberg limits were performed on an oven-dried sample, there was a significant decrease in the liquid limit. Hence, it was deemed necessary to quantify the loss on ignition of the soil. The test was performed by placing a small amount (~5 grams) of oven-dried samples in a muffle furnace at 440^{o}C for 24 hours. The resulting change in mass indicated the amount of loss on ignition. The test was conducted in accordance with ASTM D2974.

The results of the loss on ignition test can be found in Section 5.1.2.

4.2.3. Particle Size Analysis

Particle size analysis is used to determine the distribution of particle size for the soil. The first step in determining the particle size distribution is to separate the coarse-grained material from the fine-grained. This is accomplished by separating the soil on a #200 sieve (0.076mm), with the soil passing the #200 sieve classified as fine-grained, and the soil retained on the #200 sieve classified as coarse-grained. For the coarse-grained particles, the size distribution is determined using sieves of various sizes and calculating the percentage of soil retained on each sieve. For the fine-grained particles, the particle size distribution is determined by performing the hydrometer test. The soil is prepared by mixing with water and 5g of sodium hexametaphosphate, which acts as a dispersant. The mixture is then thoroughly blended in order to break interparticle flocs. The slurry is then placed in a volumetric flask, which in turn is placed in a water bath to maintain a fairly constant temperature. A hydrometer is then placed in the volumetric flask and the readings recorded at a geometrically increasing time schedule. The particle size distribution can then be measured using Stokes' Law. The test was performed in accordance with ASTM D422.

The results of the particle size analysis can be found in Section 5.1.3.

4.3 Mineralogy

Having knowledge of the presence of certain clay minerals may suggest an explanation of certain soil behavioral issues. As such, it is very helpful to have the mineralogical make-up of a particular soil.

The soil mineralogy can be identified using a technique called X-ray diffraction and a machine called an X-ray diffractometer. This technique is used as a tool for mineralogical analysis of the soil's clay fraction by determining the spacing between atomic planes. The spacing is determined by recording the angle at which an incident ray produces a diffracted ray and applying Bragg's law. To identify clay minerals using X-ray diffraction, samples may be prepared in two ways: random powder or oriented clay aggregates. For this research, only random powder testing was conducted. Once the samples were prepared, they were sent to the MIT x-ray diffraction testing facility. The facility uses a Rigaku Rotaflex 180mm diffractometer

with a graphite diffracted beam monochromator, using CuKα (λ=1.5418Å). Normally, the diffractometer is rotated between 4^o and 56^o.

In random powder sample preparation, 1 gram of oven-dried soil is finely ground using a sapphire crystal mortar and pestle. The soil is ground until it completely passes through a #325 sieve (45 μm). Once the soil has passed through the sieve, it must be thoroughly mixed to prevent any bias in the results.

In order to eliminate the effect of calcium carbonate on the results of the tests, calcite treated random powder samples were also prepared. The calcite was removed by mixing 20ml of 1N HCl with 2g of soil in a sealed container while using a calibrated pressure transducer to obtain the %wt of $CaCO_3$. The calcite removal was in accordance with ASTM 4373.

As the results in Section 5.2 have shown, there is a significant amount of non-clay particles. As such, random powder x-ray diffraction was performed on only the clay-sized fraction. The clay-sized fraction was separated by sedimentation in a volumetric flask. Sedimentation was performed by mixing the soil into a slurry and placing it in a flask filled with water having a pH level of 9. The soil was then allowed to sediment in the flask for 48 hours. The sedimentation time was determined from the settlement time of the clay-sized particles during the particle size analysis test.

The results of the x-ray diffraction tests can be found in Section 5.2.

4.4 Consolidation Testing

Consolidation tests are performed in order to determine the consolidation properties of a soil and stress history of the site. Consolidation properties include the compression and recompression ratio, coefficient of consolidation, time to end of primary consolidation, hydraulic conductivity, and the rate of secondary compression. In addition, the preconsolidation pressure may be estimated allowing the stress history of the site to be established. This section discusses consolidation testing and the results of a series of Constant Rate of Strain Consolidation (CRSC) tests.

4.4.1. Constant Rate of Strain Consolidation

The conventional consolidation testing practice involves performing a 24-hr incremental oedometer test with a load-increment ratio equal to one. The disadvantages to using this test are

that the consolidation curve is not well-defined, there are relatively few points to define the compression curve, the data points do not correspond to the end-of-primary consolidation, and it is time consuming.

In 1971, Wissa et al developed a rigorous solution for the constant rate of strain consolidation process, extending the approximate solution developed by Smith and Wahls in 1969. This led to the development of a more efficient consolidation test known as the Constant Rate of Strain Consolidation (CRSC).

CRSC, as the name suggests, involves the application of a constant rate of strain on the soil sample while measuring the vertical stress at the top and the pore pressure at the base of the specimen. Digital data acquisition allows for continuous data collection, which in turn captures the complete curvature of the consolidation curve. The advantage of this test over the incremental oedometer is that the CRSC test is relatively rapid, easily automated, and gives a well-defined end-of-primary consolidation curve, hydraulic conductivity, strain energy, and coefficient of consolidation data. The drawback to the CRSC test is that it does not give secondary compression data.

4.4.2. MIT CRSC Setup

Figure 4.7 and Figure 4.8 show a schematic and a picture of the computer controlled CRSC testing apparatus used in the MIT geotechnical laboratory. The apparatus consists of

1) a Trautwein CRS cell consisting of a loading piston riding through a low friction linear bearing and rolling diaphragm seal (see Figure 4.9);
2) a Wykeham Farrance screw driven load frame for axial loading;
3) a pressure-volume controller (PVC) to allow for back pressure saturation;
4) 2 motors driving the load frame and the PVC, and the motor controllers and drivers;
5) an externally-mounted shear beam load cell to measure axial load, an LVDT mounted on the loading piston to measure external axial strain, 2 pressure transducers to measure base pore pressure and cell pressure;
6) a temperature controlled housing that maintains temperature at $25 \pm 0.2\ ^{o}C$;
7) a personal computer responsible for automated control throughout the test;

8) and the central data acquisition system based on a PC interfaced with a Hewlett Packard 3497A data acquisition unit

The standard CRSC specimen has a diameter of about 6 cm and a height of about 2.35 cm. For a specimen of this size, the maximum vertical effective stress that can be applied is 25 kgf/cm^2. Because of the rounded shape of the compression curve and high in-situ effective stress of the Hydrate Ridge soil, it was necessary to apply much higher vertical effective stresses. As such, a specimen ring with a diameter of 3.54 cm was fabricated here at MIT to allow for a maximum of 80 kgf/cm^2. To maintain the same aspect ratio with the standard CRSC specimen, the height of the smaller sample was limited to 1.26 cm. Figure 4.10 shows the standard and small diameter CRSC specimen rings.

4.4.3. MIT CRSC Test Methodology

The MIT geotechnical laboratory has developed a standard method for performing CRSC tests. In addition, ASTM D4186 was used as a guideline in conducting CRSC tests.

The CRSC test can be divided into three stages. The first stage of the test involves sample preparation, which was discussed in Section 4.1. After the sample is trimmed into the CRSC ring, it is carefully placed in the CRSC cell. The CRSC cell is then filled with water and tightly sealed with the piston locked in place.

The second stage of the test is the back pressure saturation stage. The purpose of back pressure saturation is to ensure all the air bubbles go into solution. In this stage, a small effective stress is applied such that there is minimal to no change in axial strain. For the Hydrate Ridge soil, the applied effective stress ranges from 0.05 to 0.4 kgf/cm^2. Then, while maintaining the same effective stress, the axial stress and cell pressure are increased in increments of 1 kgf/cm^2 until the cell pressure reaches 4 kgf/cm^2.

The third stage of the test is the consolidation itself. All of the tests were run at a strain rate of 0.5 %/hr. The strain rate was selected such that the maximum value of the pore pressure ratio does not exceed 4%. In addition, an unload-reload cycle to an OCR of 10 was introduced in all tests. For the standard-diameter and small-diameter samples, the maximum vertical effective stress that was applied ranged from 20 to 25 kgf/cm^2 and 80 kgf/cm^2 respectively. Prior to the unload-reload cycle and after the maximum vertical effective stress was reached, the stress was held constant to allow dissipation of excess pore pressure and allow for some secondary

compression. The hold stress portion was held for 6 hours for the standard diameter sample, and at least 12 hours for the small diameter sample.

4.4.4. MIT CRSC Data Analysis

The raw data recorded by the data acquisition system is converted to meaningful engineering data using a reduction program developed here at MIT by Dr. John Germaine. As was mentioned earlier, the data acquisition system records the vertical force, pore pressure, cell pressure and axial displacement. Once the reduction program has converted the raw data to these measurements, a series of equations are used to obtain the various CRSC data such as the effective stress, void ratio, hydraulic conductivity, and coefficient of consolidation. The equations that were used are as follows:

$$\sigma'_v = \sigma_v - \frac{2}{3} \cdot \Delta u_b \tag{4.1}$$

$$k = \frac{\dot{\varepsilon} \cdot H^2 \cdot \gamma_w}{2 \cdot \Delta u_b} \tag{4.2}$$

$$c_v = \frac{H^2}{2 \cdot \Delta u_b} \left(\frac{\Delta \sigma_v}{\Delta t} \right) \tag{4.3}$$

$$Strain\ Energy = \frac{\sigma_i + \sigma_{i-1}}{2} \cdot Ln \left(\frac{1 - \varepsilon_{i-1}}{1 - \varepsilon_i} \right) \tag{4.4}$$

To reduce the effect of system noise in the result of the strain rate, ε/hr, the strain is averaged over a range of 0.3% strain. This averaged strain rate is then used in the calculation of the hydraulic conductivity. To obtain a smoother c_v curve, the pore pressure is averaged using a 3 point moving window, i.e., average between data point, data point after, and data point before.

The results of the CRSC tests can be found in Section 5.3.

4.5 Strength Testing

The shear strength of soil is one of the most important properties in geotechnical engineering, yet it is one of the most difficult properties to accurately determine. In the laboratory, the shear strength can be determined by conducting a triaxial test. In this test, a soil specimen is loaded until failure is reached, while at the same time measuring both the load and the strain throughout the test. The triaxial test was developed in large part by Bishop and Henkel

(1957). Their book has become a classic reference for triaxial testing. Bishop and Henkel describe three types of triaxial tests that are routinely carried out:

1) Unconsolidated Undrained (UU): The UU test involves loading the specimen under a constant rate of strain, while measuring the load and axial displacement. The loading rate is quite fast, and failure is usually reached in minutes. It is important to note that consolidation is not performed prior to shearing. This is a serious drawback, as the soil is sheared at an unknown effective stress. Further drawbacks to this type of test are a lack of pore pressure measurement and a high rate of shearing. All of these drawbacks lead to misleading values of strength, which may err on either the safe or unsafe side. Hence, this test is highly not recommended.
2) Consolidated Drained (CD): The CD test involves two stages: consolidation and shearing. In the first stage, the soil is consolidated to a desired stress state. In conventional practice, consolidation is done isotropically. For best results however, it is suggested that consolidation be done one-dimensionally. Once consolidation is finished, the specimen is sheared while allowing drainage of pore fluid. Furthermore, the specimen is sheared slowly so as to prevent excess pore pressures from developing. This test provides a measure of the friction envelope but not the undrained strength.
3) Consolidated Undrained (CU): The CU test involves two stages: consolidation and shearing. Like in the CD test, the soil is consolidated. At MIT, the specimen is consolidated one-dimensionally, until the desired stress state is reached. The difference between the CU and CD test lies in the drainage condition during shearing. In the CU test, the specimen is sheared without drainage, thus allowing pore pressures to develop. The pore pressure, together with the total vertical stress, is used to compute for the vertical effective stress and hence the undrained shear stress and shearing stress path.

4.5.1. Ko-Consolidated Undrained Triaxial Test

The Ko-Consolidated Undrained (CKoU) Triaxial Shear test determines the undrained strength of the soil after it has been consolidated one-dimensionally to a predetermined stress

state. In the early days of triaxial testing, specimens were consolidated isotropically, as manual one-dimensional consolidation proved to be much too tedious and difficult. The downside of isotropic consolidation is that the undrained strength is generally overestimated because the shearing does not start from the correct state of stress. Hence, the measured strength is not safe for use in geotechnical design. However, with the advent of computer-controlled tests, one-dimensionally consolidated specimens have become feasible, allowing a more accurate measurement of undrained strength.

4.5.2. MIT Triaxial Shear Test Setup

Figure 4.11 and Figure 4.12 show a schematic and a picture of the computer controlled Triaxial Shear testing apparatus used in the MIT geotechnical laboratory. The apparatus consists of the following components:

1) a triaxial chamber consisting of a Lexan cell, internal posts, fixed top cap, and loading piston riding through a low friction linear bearing, and an o-ring seal (see Figure 4.13);
2) a Wykeham Farrance screw driven load frame for axial loading;
3) 2 pressure-volume controllers (PVC) to regulate cell and back pressure, as well as pore volume change (see Figure 4.14);
4) 2 motors driving the load frame and the PVC, and the motor controllers and drivers;
5) an internally-mounted shear beam load cell to measure axial load, an LVDT mounted on the loading piston to measure external axial strain, 2 pore pressure transducers to measure pore pressure and cell pressure, an LVDT to mounted on the PVC to measure volume change;
6) a temperature controlled housing that maintains temperature at $25 \pm 0.2\ ^{o}C$;
7) a personal computer responsible for automated control throughout the test;
8) and the central data acquisition system based on a PC interfaced with a Hewlett Packard 3497A data acquisition unit

The maximum cell pressure that can be applied to this system is 15 kgf/cm^2. The maximum load that can be applied to this system is limited by the capacity of the load cell being

used, which is typically 500 lbs. This maximum load translates to a maximum total stress about 23 kgf/cm^2.

For high-pressure tests, the chamber is replaced with a solid steel cell with an internally-mounted flat-plate load cell and a free top cap (see Figure 4.15). The maximum cell pressure that can be applied to this system is about 120 kgf/cm^2. The maximum load is limited to 2000 lbs, as this is the limit of the load cell. The maximum pressure that can be applied by the PVCs is 1500 psi.

4.5.3. MIT Ko-Consolidated Undrained Triaxial Test Methodology

The MIT geotechnical laboratory has developed a standard method for performing CKoU tests. This test can be divided into four stages. The first stage of the test involves sample preparation, which was discussed in Section 4.1. After the sample is trimmed down to the size of a triaxial specimen, it is placed on the triaxial base, with a nylon filter fabric and porous stone placed on both ends. No side drains were used during the tests. Two thin, impermeable membranes are rolled over the soil and sealed with 3 o-rings each at the top cap and bottom base. The cell is then filled with silicon oil and tightly sealed.

The second stage of the test is the back pressure saturation stage. The purpose of back pressure saturation is to ensure the soil is fully saturated by applying enough pressure to dissolve all the remaining air bubbles in the soil. In this stage, a small effective stress is applied such that there is minimal to no change in axial strain. For the Hydrate Ridge soil, the applied effective stress ranges from 0.1 to 0.2 kgf/cm^2. Then, while maintaining the same effective stress, the axial stress and cell pressure are increased by an increment of 0.5 kgf/cm^2. At the end of each increment, the B-value is measured to determine the level of saturation. The axial stress and cell pressure are increased incrementally until the measured B-value is 1.00 ± 0.02, which indicates complete saturation, or until the back pressure reaches 3 kgf/cm^2.

The third stage of the test is the K_o-consolidation stage. In K_o-consolidation, the sample is consolidated one-dimensionally, i.e., no radial strain. K_o-consolidation is achieved by applying a constant rate of axial deformation and adjusting the cell pressure such that the volumetric strain and axial strain remain equal. After consolidation, the stresses are held for 24 hours to dissipate excess pore pressure. There are two types of consolidation that can be performed, as discussed in Section 2.2.5.

The MIT geotechnical laboratory employs the SHANSEP testing technique, which was developed by Ladd and Foott (1974) as a means of reducing the effects of sample disturbance on the measured strength parameters. This is accomplished by consolidating the soil well into the normally consolidated region (see Figure 2.13). Ladd recommends consolidating the specimen to more than 1.5-2 times the preconsolidation pressure. For practical purposes, historical data has shown that consolidation to 10% strain is sufficient in eliminating the effects of sample disturbance. It must be noted that the SHANSEP technique is predicated on the belief that soils of the same mineralogical composition will exhibit the same strength parameters when normalized to the vertical consolidation stress. After consolidation, the specimen is allowed to undergo secondary compression for 24 hours, by holding the vertical, cell, and pore pressures constant.

The final stage of the test is the undrained shearing stage. Once the specimen has undergone 24 hours of secondary compression, a leak check is performed by closing the drainage valves for 30 minutes. During this time, the back pressure should remain constant. After the leak check, the specimen is sheared with the drainage lines closed. The specimen is sheared at 0.5%/hr until a distinct failure plane has developed or 10% strain has been reached.

4.5.4. MIT CKoU Triaxial Test Data Analysis

Similar to the CRSC test, the raw data recorded by the data acquisition system is processed using a reduction program developed by Dr. John Germaine. The data acquisition system records the vertical force, pore pressure, cell pressure, volume change, and axial deformation. The following equations were used to calculate the various CKoU triaxial data:

$$\sigma'_v = \sigma_v - \Delta u_b \tag{4.5}$$

$$K_o = \frac{\sigma'_h}{\sigma'_v} \tag{4.6}$$

$$Strain\ Energy = \frac{\sigma_i + \sigma_{i-1}}{2} \cdot Ln\left(\frac{1-\varepsilon_{i-1}}{1-\varepsilon_i}\right) \tag{4.7}$$

$$q = \frac{\sigma'_v - \sigma'_h}{2} \tag{4.8}$$

$$p' = \frac{\sigma'_v + \sigma'_h}{2} \tag{4.9}$$

$$E_u = \frac{2q}{\Delta\varepsilon} \tag{4.10}$$

The results of the CKoU tests can be found in Section 5.4.

4.6 References

ASTM (2003). *Annual Book of ASTM Standards,* vol. 04.08, *Soil and Rock (I).* Standard no. D422-63(2002), "Standard Test Methods for Particle-Size Analysis of Soils," West Conshohocken, Pa., 10-17

ASTM (2003). *Annual Book of ASTM Standards,* vol. 04.08, *Soil and Rock (I).* Standard no. D854-02, "Standard Test Method for Specific Gravity of Soils," West Conshohocken, Pa., 93-99

ASTM (2003). *Annual Book of ASTM Standards,* vol. 04.08, *Soil and Rock (I).* Standard no. D2974-00, "Standard Test Methods for Moisture, Ash, and Organic Matter of Peat and Other Organic Soils," West Conshohocken, Pa., 330-333

ASTM (2003). *Annual Book of ASTM Standards,* vol. 04.08, *Soil and Rock (I).* Standard no. D4186-89(1998), "Standard Test Method for One-Dimensional Consolidation Properties of Soils Using Controlled-Strain Loading," West Conshohocken, Pa., 530-535

ASTM (2003). *Annual Book of ASTM Standards,* vol. 04.08, *Soil and Rock (I).* Standard no. D4318-00, "Standard Test Methods for Liquid Limit, Plastic Limit, and Plasticity Index of Soils," West Conshohocken, Pa., 582-595

ASTM (2003). *Annual Book of ASTM Standards,* vol. 04.08, *Soil and Rock (I).* Standard no. D4373-02, "Standard Test Method for Rapid Determination of Carbonate Content of Soils," West Conshohocken, Pa., ----

ASTM (2003). *Annual Book of ASTM Standards,* vol. 04.08, *Soil and Rock (I).* Standard no. D4767-02, "Standard Test Method for Consolidated undrained Triaxial Compression Test for Cohesive Soils," West Conshohocken, Pa., 911-934

Atterberg, A. (1911). "The Behavior of Clays with Water, Their Limits of Plasticity and Their Degrees of Plasticity," *Kungliga Lantbruksakademiens Handlingar och Tidskrift*, 50(2), 132-158

Becker, D. E., Crooks, J. H. A., Been, K., and Jefferies, M. G. (1987). "Work as a Criterion for Determining In Situ and Yield Stress in Clays." *Canadian Geotechnical Journal*, 24(4), 549-564

Bishop, A. W., and Henkel, D. J. (1962) *The Measurement of Soil Properties in the Triaxial Test,* 2nd ed., Edward Arnold, London

Bjerrum, L. (1973). "Problems of Soil Mechanics and Construction on Soft Clays: SOA Report." *Proc. 8th International Conference on Soil Mechanics and Foundation Engineering*, Moscow, USSR, 3, 111-159

Casagrande, A. (1932). "Research of the Atterberg Limits of Soils." *Public Roads*, 3, 121-130 & 136.

Casagrande, A. (1936) "The Determination of the Preconsolidation Load and Its Practical Significance." *Proceedings of the First International Conference on Soil Mechanics and Foundation Engineering*, Cambridge, MA, Vol. 3, 60-64

Germaine, J. T. (1982). "Development of the Directional Shear Cell for Measuring Cross-Anisotropic Clay Properties." Sc. D. thesis, Dept. of Civil Engineering, MIT, Cambridge, MA.

Ladd, C. C., and Foott, R. (1974). "New Design Procedure for Stability of Soft Clays." *Journal of Geotechnical Engineering*, 100(7), 763-786.

Ladd, C. C. (1991). "Stability Evaluation During Staged Construction." *Journal of Geotechnical Engineering*, 117(4), 537-615.

Smith, R. E., and Wahls, H. E. (1969). "Consolidation Under Constant Rate of Strain." *Journal of Soil Mechanics and Foundations Division*, ASCE, 95(2), 519-539.

Wissa, A. E. Z., Christian, J. T., Davis, E. H., and Heiberg, S. (1971). "Consolidation Testing at Constant Rate of Strain." *Journal of Soil Mechanics and Foundations Division,* ASCE, 97(10), 1393-141.

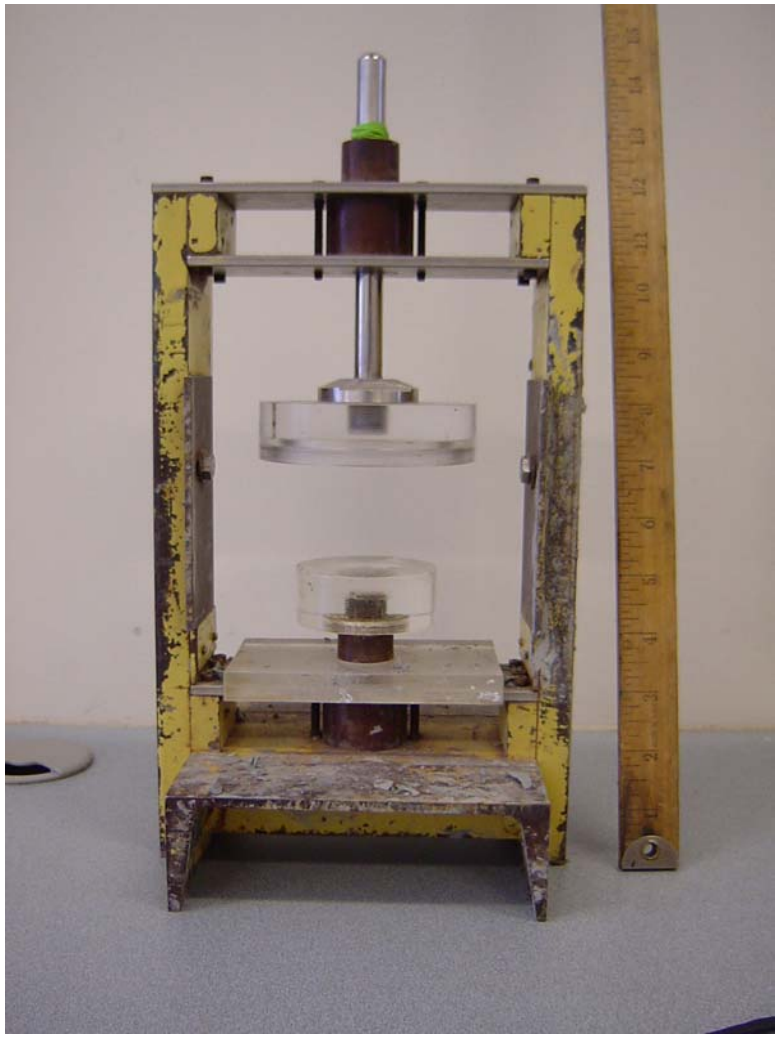

Figure 4.1: CRS specimen trimming jig

Figure 4.2: Triaxial specimen trimming jig

Figure 4.3: Wire saw used for trimming specimens

Figure 4.4: Mold for remolded triaxial specimens

Figure 4.5: Mold for resedimented triaxial specimens

Figure 4.6: Resedimentation process

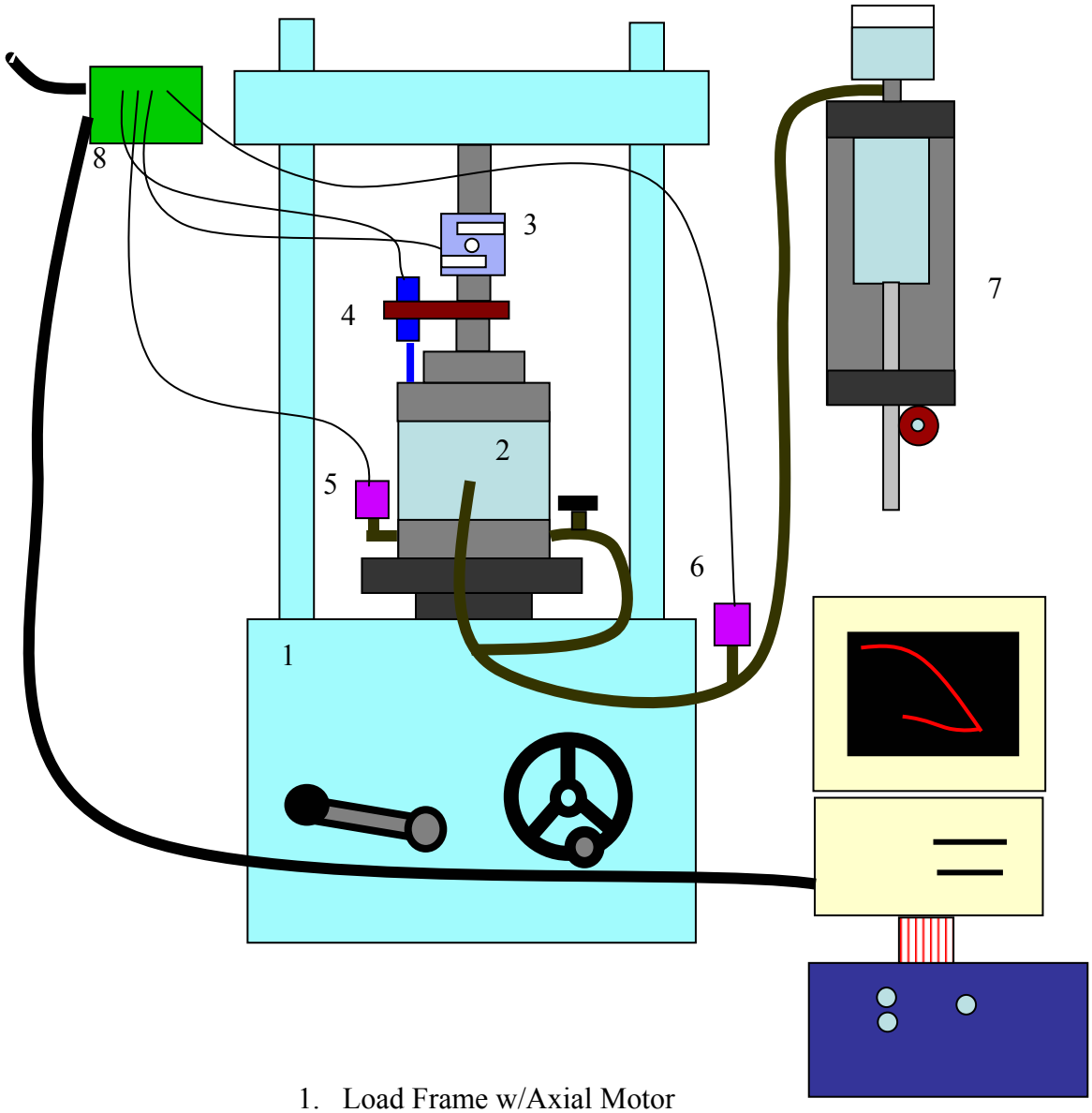

1. Load Frame w/Axial Motor
2. Trautwein CRS Cell
3. Shear Beam Load Cell
4. Axial Displacement Transducer
5. Bottom Pore Pressure Transducer
6. Cell Pressure Transducer
7. Pressure-Volume Controller w/PVC Motor
8. Transducer Box to HP3497A Data Acquisition System
9. IBM PC Compatible and Control Box

Figure 4.7: Schematic of MIT CRSC setup

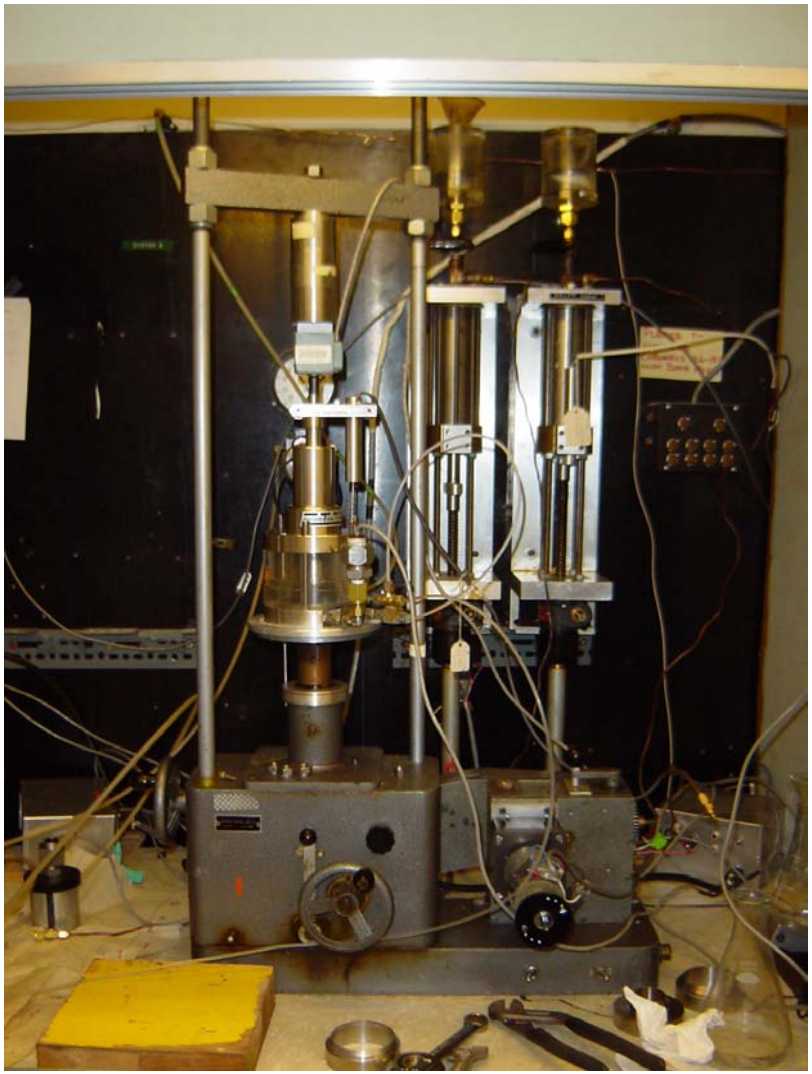

Figure 4.8: Picture of MIT CRSC setup

Figure 4.9: Trautwein CRSC cell

Figure 4.10: Standard diameter CRSC ring (left), Small diameter CRSC ring (right)

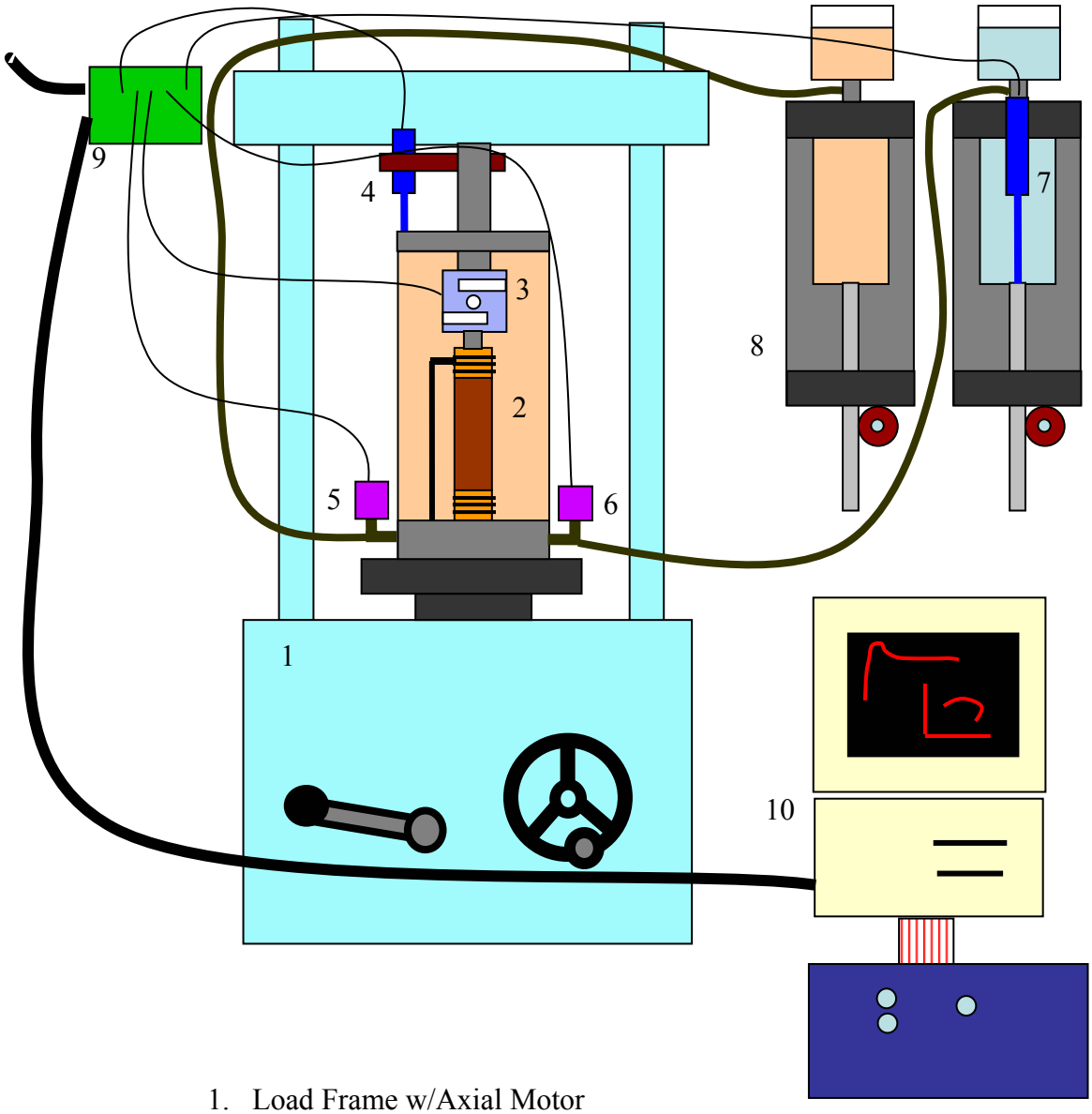

1. Load Frame w/Axial Motor
2. Triaxial Chamber with Internal Posts and Fixed Top Cap Filled with Silicon Oil
3. Internal Shear Beam Load Cell
4. External Axial Displacement Transducer
5. Cell Pressure Transducer
6. Pore Pressure Transducer
7. Volume Change Transducer
8. 2 Pressure-Volume Controllers w/PVC Motors
9. Transducer Box to HP3497A Data Acquisition System
10. IBM PC Compatible and Control Box

Figure 4.11: Schematic of MIT triaxial shear setup

Figure 4.12: Picture of MIT triaxial shear test setup

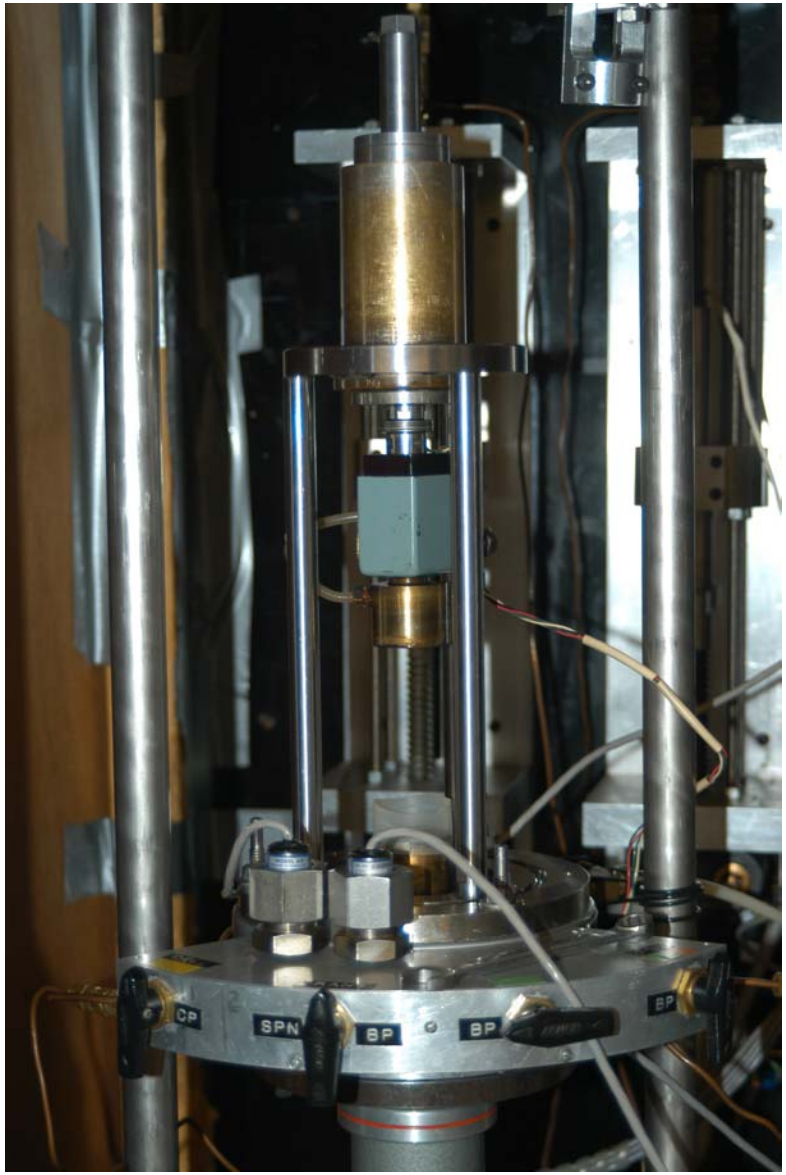

Figure 4.13: MIT triaxial chamber (w/o Lexan cell)

Figure 4.14: Cell pressure volume controller (left), pore pressure volume controller (right)

Figure 4.15: High pressure triaxial cell

Chapter 5: Laboratory Testing Results

In Chapter 4, the details of the laboratory tests performed on the Hydrate Ridge soil were discussed. This chapter focuses purely on the results of these tests. The interpretation and discussion of these results can be found in the next chapter. Table 3.2 gives a summary of the tests that were conducted and their location with depth.

5.1 Index Tests

5.1.1. Atterberg Limits

Atterberg limits were performed on 8 undisturbed samples and 1 oven-dried sample (see Table 5.1). Interestingly, performing atterberg limits on an oven-dried sample dramatically decreases the liquid limit.

To determine a soil's classification based on the USCS (ASTM D2487), the results of the atterberg limit tests are plotted on a plasticity chart (see Figure 5.1). From this chart, a cohesive soil is said to have high plasticity if it has a liquid limit greater than 50%, and low plasticity if the liquid limit is less than 50%. Furthermore, the soil is said to be predominantly clay if it plots above the A-line, and mostly silt if it plots below the A-line. Based on this chart, the Hydrate Ridge soil classifies as an MH or OH. Furthermore, analysis reveals that the soil classifies as MH and not OH because the ratio of the oven-dried liquid limit to the undisturbed liquid limit is greater than 75%. But in general, there is little variation in the atterberg limits, suggesting the soil consists of the same basic material.

5.1.2. Loss on Ignition

Loss on ignition was measured on 8 samples in accordance with ASTM D2974. The change in weight divided by the original weight is the amount of loss on ignition. Table 5.1 gives the results of this test. The loss on ignition is consistent with depth and relatively large.

5.1.3. Particle Size Analysis

Figure 5.2 gives the particle size distribution curve for the Hydrate Ridge soil at 1244C-13H-3WR. Though the hydrometer does identify the silt and clay particle distribution, it must be emphasized that the test classifies the soil based on particle size and not on behavior. It is

entirely possible to have silt-sized clay minerals and clay-sized non-clay particles. As such, the result of the hydrometer test was deemed non-critical, and hence, only one test was run. Details of the particle-size analysis test can be found in Section 4.2.3.

The distribution curve shows that the soil contains 50% clay size. Together with the plasticity index, the resulting activity is close to 1. This result is typical of the clay mineral Illite.

5.2 Mineralogy

The specimens prepared using the random powder preparation is shown in Table 3.1. The x-ray diffractometer was rotated between a 2θ of 6^o and 56^o. Figure 5.3, Figure 5.4 and Figure 5.5 show the results of x-ray diffraction on the three random powder samples. Table 5.2 identifies the peaks of the XRD traces and the corresponding minerals.

Table 3.2 gives a list of the specimens used in calcite-treated random powder preparation. Table 5.1 gives the calcium carbonate content of the soil. Figure 5.6, Figure 5.7, and Figure 5.8 show the results of calcite-treated random powder testing. Table 5.3 gives the peaks and corresponding minerals for the calcite-treated XRD traces.

The results of the two random powder series have shown that there is a significant amount of non-clay particles. In order to better identify the clay-sized particles, x-ray diffraction was performed on random powder samples containing only the clay-sized fraction of the soil. Table 3.2 shows the samples that were tested using this preparation technique. Figure 5.9, Figure 5.10, and Figure 5.11 show the results of x-ray diffraction on the clay-sized fraction random powder samples. Table 5.4 shows the peaks and corresponding minerals for the clay-sized XRD random powder samples.

5.3 Consolidation Testing

5.3.1. Summary of CRSC Results

Table 5.5 gives a summary of the details and conditions of each CRSC test. An insert at the end of Table 5.5 gives the meaning of each parameter. Figure 5.12 and Figure 5.13 show the CRSC consolidation curves in e-logσ'_v space for intact and remolded specimens respectively, while Figure 5.14 and Figure 5.15 show the consolidation curves in ε-logσ'_v space. Also, Figure 5.16 shows the hydraulic conductivity curves for the intact specimens, while Figure 5.17

shows the hydraulic conductivity curves for the remolded specimens. Details of the CRSC test can be found in Section 4.4.

5.3.2. Consolidation Properties

Figure 5.18 to Figure 5.35 show the consolidation curve in both e-logσ'_v and ε-logσ'_v, normalized excess pore pressure, coefficient of consolidation (c_v), strain energy, and hydraulic conductivity (k) for each CRSC test.

Consolidation properties such as the compression index, recompression index, and in-situ hydraulic conductivity can be found in Table 5.5. The compression index refers to the slope of the normally consolidated portion of the compression curve while in e-logσ'_v space. The recompression index refers to the slope of the unload-reload portion of the curve while in e-logσ'_v space. It must be noted that the recompression index varies with the amount of unloading that occurs. As such, the quoted recompression indexes are for unloading to an OCR of 10. The in-situ hydraulic conductivity is obtained by extrapolating the hydraulic conductivity to the in-situ void ratio.

5.4 Strength Testing

5.4.1. Summary of CKoU Results

Table 5.6 gives the details and conditions of each CKoU triaxial for the consolidation stage of the test. Included in this table is the B-value, which is used to test the degree of saturation of the sample. A sample with a B-value of 100 $\pm$ 2 means that it has been fully saturated after the back pressure saturation stage. Also found in this table are the applied effective stress during saturation (σ'_i) and the applied back pressure at the end of back pressure saturation. An insert at the end of Table 5.6 gives the meaning of each parameter referred to in the table.

Table 5.7 gives the details and conditions for the undrained shearing stage of each test. Found in this table are the preshear void ratio (e_c), lateral stress ratio (K_c), and vertical consolidation stress (σ'_{vc}). An insert at the end of Table 5.7 gives the meaning of each parameter in the tables.

Figure 5.36 and Figure 5.37 show the consolidation curves for all CKoU tests in e-logσ'_v and ε-logσ'_v space, respectively. Figure 5.38 shows the variation of K, the lateral stress ratio, with the consolidation stress. Figure 5.39, Figure 5.40, Figure 5.41, Figure 5.42 and Figure 5.43 give a summary of the normalized shear stress vs. strain, normalized shear stress vs. strain (compression only), normalized shearing stress path, friction angle vs. strain, and secant modulus vs. strain, respectively, for all the CKoU tests. Figure 5.44 shows the variation of the normalized undrained strength and friction angle with depth. Details of the CKoU test can be found in Section 4.5.

5.4.2. Triaxial Consolidation and Strength Properties

Figure 5.45 to Figure 5.64 show the consolidation and undrained shearing results for each triaxial test. The odd-numbered figures show the consolidation results including the consolidation curve in e-logσ'_v and ε-logσ'_v space, lateral stress ratio, strain energy, and stress path for each test. The even-numbered figures show the undrained shearing results including the normalized shear stress vs. strain, normalized excess pore pressure and shear induced pore pressure, normalized secant modulus, friction angle, and normalized stress path for each test.

The consolidation properties for each test can be found in Table 5.6. These properties include the compression index (C_c), preconsolidation pressure (σ'_p), and the strain rate (ε_a/hr). Also included are the consolidation stress (σ'_{vc}) and consolidation lateral stress ratio (K_c), which refer to the effective stress and lateral stress ratio at the end of consolidation. The time for secondary compression (t_s) refers to the amount of time that the specimen was held under constant stress at the end of consolidation. Finally, certain consolidation properties are given at the maximum stress condition and at the preshear condition. For normally consolidated specimens, the maximum stress condition is the preshear condition, hence these consolidation properties are the same. For overconsolidated specimens, the maximum stress condition differs from the preshear condition, hence certain consolidation properties will be different.

The strength properties can be found in Table 5.6. The properties are given for both the case when maximum shear occurs and when maximum obliquity or the end of shearing is reached. Obliquity refers to the ratio of the normalized shear stress to the normalized mean effective stress (q/p'). Incidentally, maximum obliquity also occurs when the friction angle is the greatest. Properties included in this table are the axial strain (ε_a), normalized shear stress

(q/σ'_{vc}), normalized mean effective stress (p'/σ'_{vc}), friction angle (ϕ), and the obliquity (q/p'). Also included in the table are the normalized excess pore pressure ($\Delta u_e/\sigma'_{vc}$) and the normalized shear induced pore pressure ($\Delta u_s/\sigma'_{vc}$). Lastly, the A-parameter is included, which describes the angle in stress space between the consolidation and failure point. It must be noted that for tests TX643, TX644, TX645, and TX646 shearing in extension was performed after shearing in compression.

Sample	Depth (mbsf)	w_n (%)	w_l (%)	w_p (%)	I_p (%)	I_l (%)	LoI (%)	$CaCO_3$ Content (% wt)
1H-4WR	6.925	59.90	71	32	39	72	5.89	
3H-3WR	21.754	63.80	82	37	45	60	4.55	1.297
4H-6WR	34.205	62.70	87	42	45	46	5.18	1.253
6H-8WR	53.064	60.05	85	38	47	47	4.93	2.357
8H-7WR	71.584	58.10	86	40	46	39	5.87	2.090
9H-5WR	80.125	54.40	83	38	45	36	7.27	
13H-3WR	115.629	47.27	81	39	42	20	5.19	5.812
13H-3WR	115.527	ovendried	64	39	25			
17H-3WR	136.530	48.85	77	35	42	33	4.68	2.928

I_l: Liquidity Index
I_p: Plasticity Index
LoI: Loss on Ignition
w_l: Liquid Limit
w_n: Natural Water Content
w_p: Plastic Limit

Table 5.1: Summary of atterberg limit, organic matter content, and calcite content tests

1244B-4H-6WR			1244C-8H-7WR			1244C-13H-3WR		
2θ	**d/n**	**Mineral**	**2θ**	**d/n**	**Mineral**	**2θ**	**d/n**	**Mineral**
6.28	14.07	*Chlorite*	6.26	14.12	*Chlorite*	6.28	14.07	*Chlorite*
8.88	9.96	*Illite*	8.90	9.94	*Illite*	8.88	9.96	*Illite*
10.52	8.41	*Hornblende*	10.52	8.41	*Hornblende*	10.48	8.44	*Hornblende*
12.52	7.07	*Kaolinite*	12.54	7.06	*Kaolinite*	12.52	7.07	*Kaolinite*
13.88	6.38	*Feldspar*	13.88	6.38	*Feldspar*	13.86	6.39	*Feldspar*
17.78	4.99	*Illite*	17.84	4.97	*Illite*	17.78	4.99	*Illite*
18.82	4.72	*Chlorite*	18.84	4.71	*Chlorite*	18.82	4.72	*Chlorite*
19.84	4.47	*Illite*	19.86	4.47	*Illite*	19.82	4.48	*Illite*
20.88	4.25	*Quartz*	20.88	4.25	*Quartz*	20.86	4.26	*Quartz*
22.04	4.03	*Feldspar*	22.06	4.03	*Feldspar*	22.02	4.04	*Feldspar*
23.04	3.86	*Calcite*	23.00	3.87	*Calcite*	23.04	3.86	*Calcite*
23.60	3.77	*Feldspar*	23.60	3.77	*Feldspar*	23.56	3.78	*Feldspar*
24.28	3.67	*Feldspar*	24.32	3.66	*Feldspar*	24.26	3.67	*Feldspar*
25.20	3.53	*Chlorite*	25.16	3.54	*Chlorite*	25.16	3.54	*Chlorite*
26.66	3.34	*Quartz*	26.66	3.34	*Quartz*	26.66	3.34	*Quartz*
27.96	3.19	*Illite*	27.94	3.19	*Illite*	27.96	3.19	*Illite*
29.42	3.04	*Calcite*	29.42	3.04	*Calcite*	29.40	3.04	*Calcite*
29.86	2.99	*Feldspar*	29.86	2.99	*Feldspar*	29.80	3.00	*Feldspar*
30.54	2.93	*Feldspar*	30.48	2.93	*Feldspar*	30.48	2.93	*Feldspar*
31.72	2.82	*Calcite*	31.50	2.84	*Calcite*	31.44	2.85	*Calcite*
33.02	2.71	*Marcasite*	33.00	2.71	*Marcasite*	33.06	2.71	*Marcasite*
34.50	2.60	*Chlorite*	34.54	2.60	*Chlorite*	34.46	2.60	*Chlorite*
35.06	2.56	*Chlorite*	35.04	2.56	*Chlorite*	34.98	2.57	*Chlorite*
35.94	2.50	*Calcite*	35.98	2.50	*Calcite*	35.96	2.50	*Calcite*
36.56	2.46	*Quartz*	36.56	2.46	*Quartz*	36.54	2.46	*Quartz*
37.60	2.39	*Kaolinite*	37.62	2.39	*Kaolinite*	37.60	2.39	*Kaolinite*
39.48	2.28	*Quartz*	39.48	2.28	*Quartz*	39.46	2.28	*Quartz*
40.32	2.24	*Quartz*	40.30	2.24	*Quartz*	40.30	2.24	*Quartz*
42.46	2.13	*Quartz*	42.46	2.13	*Quartz*	42.46	2.13	*Quartz*
45.46	2.00	*Illite*	45.46	2.00	*Illite*	43.16	2.10	*Calcite*
45.84	1.98	*Feldspar*	45.84	1.98	*Feldspar*	45.46	2.00	*Illite*
50.16	1.82	*Quartz*	50.16	1.82	*Quartz*	45.76	1.98	*Feldspar*
54.86	1.67	*Quartz*	54.90	1.67	*Quartz*	47.52	1.91	*Calcite*
			55.32	1.66	*Quartz*	48.50	1.88	*Feldspar*
						50.14	1.82	*Quartz*
						50.76	1.80	*Calcite*
						54.88	1.67	*Quartz*

Table 5.2: XRD random powder sample peaks and equivalent minerals

1244B-3H-3WR			1244B-4H-6WR			1244B-6H-8WR		
2θ	**d/n**	**Mineral**	**2θ**	**d/n**	**Mineral**	**2θ**	**d/n**	**Mineral**
6.26	14.12	*Chlorite*	6.22	14.21	*Chlorite*	6.26	14.12	*Chlorite*
8.9	9.94	*Illite*	8.84	10.00	*Illite*	8.84	10.00	*Illite*
10.52	8.41	*Hornblende*	10.52	8.41	*Hornblende*	10.48	8.44	*Hornblende*
12.54	7.06	*Kaolinite*	12.48	7.09	*Kaolinite*	12.52	7.07	*Kaolinite*
13.82	6.41	*Feldspar*	13.82	6.41	*Feldspar*	13.84	6.40	*Feldspar*
14.64	6.05	*Chlorite*	14.64	6.05	*Chlorite*	14.64	6.05	*Chlorite*
17.86	4.97	*Illite*	17.74	5.00	*Illite*	17.78	4.99	*Illite*
18.8	4.72	*Chlorite*	18.8	4.72	*Chlorite*	18.76	4.73	*Chlorite*
19.88	4.47	*Illite*	19.78	4.49	*Illite*	19.8	4.48	*Illite*
20.88	4.25	*Quartz*	20.84	4.26	*Quartz*	20.86	4.26	*Quartz*
22.04	4.03	*Feldspar*	21.98	4.04	*Feldspar*	22.02	4.04	*Feldspar*
23.04	3.86	*Feldspar*	22.98	3.87	*Feldspar*	23.02	3.86	*Feldspar*
23.64	3.76	*Feldspar*	23.6	3.77	*Feldspar*	23.54	3.78	*Feldspar*
24.32	3.66	*Feldspar*	24.26	3.67	*Feldspar*	24.28	3.67	*Feldspar*
25.18	3.54	*Chlorite*	25.16	3.54	*Chlorite*	25.16	3.54	*Chlorite*
25.54	3.49	*Kaolinite*	25.50	3.50	*Kaolinite*	25.54	3.49	*Kaolinite*
26.64	3.35	*Quartz*	26.6	3.35	*Quartz*	26.62	3.35	*Quartz*
27.98	3.19	*Feldspar*	27.92	3.20	*Feldspar*	27.94	3.19	*Feldspar*
29.82	3.00	*Feldspar*	29.88	2.99	*Feldspar*	29.88	2.99	*Feldspar*
30.44	2.94	*Feldspar*	30.38	2.94	*Feldspar*	30.46	2.93	*Feldspar*
31.72	2.82	*Chlorite*	31.68	2.82	*Chlorite*	31.72	2.82	*Chlorite*
32.96	2.72	*Carbonite*	32.96	2.72	*Carbonate*	32.98	2.72	*Carbonate*
34.50	2.60	*Chlorite*	34.54	2.60	*Chlorite*	34.46	2.60	*Chlorite*
35.06	2.56	*Illite*	35.04	2.56	*Illite*	34.96	2.57	*Illite*
36.52	2.46	*Quartz*	36.52	2.46	*Quartz*	36.54	2.46	*Quartz*
37.74	2.38	*Kaolinite*	37.74	2.38	*Kaolinite*	37.7	2.39	*Kaolinite*
38.36	2.35	*Kaolinite*	38.38	2.35	*Kaolinite*	38.4	2.34	*Kaolinite*
39.5	2.28	*Quartz*	39.42	2.29	*Quartz*	39.48	2.28	*Quartz*
40.3	2.24	*Quartz*	40.26	2.24	*Quartz*	40.26	2.24	*Quartz*
42.44	2.13	*Quartz*	42.4	2.13	*Quartz*	42.44	2.13	*Quartz*
45.46	2.00	*Illite*	45.4	2.00	*Illite*	45.42	2.00	*Illite*
45.84	1.98	*Feldspar*	45.84	1.98	*Feldspar*	45.84	1.98	*Feldspar*
49.2	1.85	*Carbonate*	49.18	1.85	*Carbonate*	49.2	1.85	*Carbonate*
50.14	1.82	*Quartz*	50.1	1.82	*Quartz*	50.14	1.82	*Quartz*
50.76	1.80	*Calcite*	50.74	1.80	*Calcite*	50.74	1.80	*Calcite*
54.88	1.67	*Quartz*	54.88	1.67	*Quartz*	54.88	1.67	*Quartz*
55.30	1.66	*Quartz*	55.32	1.66	*Quartz*	55.30	1.66	*Quartz*

Table 5.3: Calcite-treated XRD random powder sample peaks and equivalent minerals

1244C-8H-7WR			1244C-13H-3WR			1244C-17H-3WR		
2θ	**d/n**	**Mineral**	**2θ**	**d/n**	**Mineral**	**2θ**	**d/n**	**Mineral**
6.24	14.16	*Chlorite*	6.24	14.16	*Chlorite*	6.28	14.07	*Chlorite*
8.86	9.98	*Illite*	8.84	10.00	*Illite*	8.88	9.96	*Illite*
10.52	8.41	*Hornblende*	10.52	8.41	*Hornblende*	10.48	8.44	*Hornblende*
12.48	7.09	*Kaolinite*	12.48	7.09	*Kaolinite*	12.52	7.07	*Kaolinite*
13.84	6.40	*Feldspar*	13.80	6.42	*Feldspar*	13.86	6.39	*Feldspar*
14.64	6.05	*Chlorite*	14.64	6.05	*Chlorite*	14.64	6.05	*Chlorite*
17.80	4.98	*Illite*	17.82	4.98	*Illite*	17.76	4.99	*Illite*
18.80	4.72	*Chlorite*	18.78	4.72	*Chlorite*	18.82	4.72	*Chlorite*
19.80	4.48	*Illite*	19.72	4.50	*Illite*	19.86	4.47	*Illite*
20.84	4.26	*Quartz*	20.82	4.27	*Quartz*	20.88	4.25	*Quartz*
22.00	4.04	*Feldspar*	22.00	4.04	*Feldspar*	22.04	4.03	*Feldspar*
22.94	3.88	*Feldspar*	23.02	3.87	*Feldspar*	23.06	3.86	*Feldspar*
23.54	3.78	*Feldspar*	23.58	3.77	*Feldspar*	23.64	3.76	*Feldspar*
24.26	3.67	*Feldspar*	24.26	3.67	*Feldspar*	24.30	3.66	*Feldspar*
25.16	3.54	*Chlorite*	25.12	3.54	*Chlorite*	25.16	3.54	*Chlorite*
25.52	3.49	*Kaolinite*	25.54	3.49	*Kaolinite*	25.54	3.49	*Kaolinite*
26.60	3.35	*Quartz*	26.60	3.35	*Quartz*	26.60	3.35	*Quartz*
27.94	3.19	*Feldspar*	27.92	3.20	*Feldspar*	27.98	3.19	*Feldspar*
29.82	3.00	*Feldspar*	29.84	2.99	*Feldspar*	29.82	3.00	*Feldspar*
30.50	2.93	*Feldspar*	30.42	2.94	*Feldspar*	30.10	2.97	*Feldspar*
31.66	2.83	*Chlorite*	31.64	2.83	*Chlorite*	30.46	2.93	*Feldspar*
32.98	2.72	*Marcasite*	34.60	2.59	*Chlorite*	31.74	2.82	*Chlorite*
34.50	2.60	*Chlorite*	34.54	2.60	*Chlorite*	34.46	2.60	*Chlorite*
35.00	2.56	*Illite*	34.98	2.57	*Illite*	34.58	2.59	*Chlorite*
36.50	2.46	*Quartz*	36.50	2.46	*Quartz*	35.02	2.56	*Illite*
37.66	2.39	*Kaolinite*	37.70	2.39	*Kaolinite*	36.52	2.46	*Quartz*
38.30	2.35	*Kaolinite*	39.42	2.29	*Kaolinite*	37.68	2.39	*Kaolinite*
39.44	2.28	*Quartz*	40.28	2.24	*Quartz*	39.48	2.28	*Quartz*
40.28	2.24	*Quartz*	42.48	2.13	*Quartz*	40.30	2.24	*Quartz*
42.44	2.13	*Quartz*	45.40	2.00	*Illite*	42.48	2.13	*Quartz*
45.40	2.00	*Illite*	50.08	1.82	*Quartz*	45.46	2.00	*Illite*
45.82	1.98	*Feldspar*	45.82	1.98	*Feldspar*	45.82	1.98	*Feldspar*
49.22	1.85	*Carbonate*	49.2	1.85	*Carbonate*	49.18	1.85	*Carbonate*
50.12	1.82	*Quartz*	50.14	1.82	*Quartz*	50.14	1.82	*Quartz*
50.78	1.80	*Calcite*	50.78	1.80	*Calcite*	50.76	1.80	*Calcite*
54.88	1.67	*Quartz*	54.88	1.67	*Quartz*	54.88	1.67	*Quartz*
55.30	1.66	*Quartz*	55.32	1.66	*Quartz*	55.30	1.66	*Quartz*

Table 5.3: Calcite-treated XRD random powder sample peaks and equivalent minerals (con't)

1244B-4H-6WR			1244B-8H-7WR			1244C-13H-3WR		
2θ	**d/n**	**Mineral**	**2θ**	**d/n**	**Mineral**	**2θ**	**d/n**	**Mineral**
12.42	7.13	*Kaolinite*	12.5	7.08	*Kaolinite*	12.42	7.13	*Kaolinite*
14.64	6.05	*Chlorite*	19.84	4.47	*Illite*	19.84	4.47	*Illite*
18.1	4.90	*Illite*	20.88	4.25	*Quartz*	20.94	4.24	*Quartz*
19.78	4.49	*Illite*	22	4.04	*Feldspar*	22	4.04	*Feldspar*
20.28	4.38	*Kaolinite*	23.08	3.85	*Feldspar*	23.14	3.84	*Feldspar*
20.82	4.27	*Quartz*	26.62	3.35	*Quartz*	23.62	3.77	*Feldspar*
21.94	4.05	*Feldspar*	27.30	3.27	*Feldspar*	25.18	3.54	*Chlorite*
23.06	3.86	*Feldspar*	27.9	3.20	*Mica*	26.64	3.35	*Quartz*
26.64	3.35	*Quartz*	29.38	3.04	*Calcite*	27.32	3.26	*Feldspar*
27.36	3.26	*Feldspar*	31.66	2.83	*Chlorite*	29.5	3.03	*Calcite*
29.4	3.04	*Calcite*	35	2.56	*Chlorite*	30.66	2.92	*Feldspar*
30.64	2.92	*Feldspar*	36.02	2.49	*Kaolinite*	31.68	2.82	*Chlorite*
31.66	2.83	*Chlorite*	39.46	2.28	*Quartz*	36.08	2.49	*Kaolinite*
35.02	2.56	*Chlorite*	43.3	2.09	*Calcite*	39.54	2.28	*Quartz*
36.1	2.49	*Kaolinite*	44.78	2.02	*Illite*	40.54	2.23	*Illite*
39.48	2.28	*Quartz*	45.4	2.00	*Illite*	43.3	2.09	*Calcite*
43.36	2.09	*Calcite*	47.36	1.92	*Calcite*	44.78	2.02	*Illite*
44.78	2.02	*Illite*	47.54	1.91	*Calcite*	45.42	2.00	*Illite*
45.4	2.00	*Illite*	48.54	1.88	*Feldspar*	47.38	1.92	*Calcite*
47.58	1.91	*Calcite*	50.12	1.82	*Quartz*	47.64	1.91	*Calcite*
48.6	1.87	*Calcite*	50.54	1.81	*Quartz*	48.72	1.87	*Calcite*
49.04	1.86	*Calcite*	53.84	1.70	*Quartz*	50.28	1.81	*Quartz*
53.82	1.70	*Quartz*				53.84	1.70	*Quartz*

Table 5.4: Clay-sized fraction XRD random powder sample peaks and equivalent minerals

Spec. Location		Index Tests		Specimen Data		Test Conditions		Consolidation Properties		Remarks
Test #	Depth	w_c	w_p	w_n	e_i			C_c		
Boring	(mbsf)	SD	w_l	I_p	S_i (%)	u_b	$\delta\varepsilon/\delta t$	C_r	k_o	
Sample	Markers	# obs		γ_t	G_s	(ksc)	(%/hr)		(cm/s)	
CRS 580	6.938	59.9	32	63.56	1.566			0.544		
1244B		1.2	71	39	104.8	4.00	0.5	0.047	1.5E-07	Small Diameter
1H-4WR	A-B	4.0		1.646	2.58					
CRS 608	6.976	56.1	32	58.00	1.418			0.476		
1244B		1.4	71	39	105.6	4.00	0.5	0.035		Small Diameter
3H-3WR	8.5-9.5	3.0		1.688	2.58					Horizontal Spec
CRS 497	21.779	63.8	37	64.00	1.608			0.646		
1244B		0.2	82	45	102.5	4.00	0.5	0.044	9.5E-08	
3H-3WR	1-2	2.0		1.619	2.58					
CRS 585	21.513	60.0	37	59.32	1.459			0.534		
1244B		2.7	82	45	104.7	4.00	0.5	0.059	1.0E-07	Small Diameter
3H-3WR	B-C	4.0		1.668	2.58					
CRS 508	34.205	63.3	42	63.78	1.659			0.693		
1244B		1.2	87	45	100.8	4.00	0.5	0.053	8.5E-08	
4H-6WR	A-C	2.0		1.615	2.62					
CRS 563	34.332	62.1	42	66.69	1.715			0.704		
1244B		0.5	87	45	101.9	4.00	0.5	0.063	1.0E-07	Small Diameter
4H-6WR	5.5-6.5	4.0		1.609	2.62					
CRS 511	52.81		38		3.214			0.566		
1244B			85	47	102.9	4.00	0.5	0.050		Resedimented
6H-8WR	0-2			1.4	2.59					
CRS 584	52.886	63.1	38	66.53	1.667			0.599		
1244C		0.5	85	47	103.5	4.00	0.5	0.062	1.4E-07	Small Diameter
6H-8WR		4.0		1.620	2.59					
CRS 504	71.609	58.1	40	58.32	1.532			0.633		
1244C		0.6	86	46	99.4	4.00	0.5	0.043	6.5E-08	
8H-7WR	0-1.5	2.0		1.632	2.61					
CRS 578	71.355	57.4	40	61.05	1.573			0.672		
1244C		0.4	86	46	101.3	4.00	0.5	0.049	8.5E-08	Small Diameter
8H-7WR	A.5-C	4.0		1.634	2.61					
CRS 569	80.113	54.4	38	57.24	1.510			0.658		
1244C		1.0	83	45	100.0	4.00	0.5	0.058	1.3E-07	Small Diameter
9H-5WR	B-C	4.0		1.653	2.64					

a) Markers - Location within tube b) Stresses in kg/cm^2 c) 1 kg/cm^2 = 98.06 kPa d) Water Contents in %

Table 5.5: CRSC test conditions and consolidation properties

Spec. Location		Index Tests		Specimen Data		Test Conditions		Consolidation Properties		Remarks
Test #	Depth	w_c	w_p	w_n	e_i			C_c		
Boring	(mbsf)	SD	w_l	I_p	S_i (%)	u_b	$\delta\varepsilon/\delta t$	C_r	k_o	
Sample	Markers	# obs		γ_t	G_s	(ksc)	(%/hr)		(cm/s)	
CRS 491	115.654	49.9	39	50.75	1.402			0.560		
1244C		0.0	81	42	95.3	4.00	0.5	0.037	7.0E-08	
13H-3WR	1.5-2.5	2.0		1.652	2.63					
CRS 493	115.603	47.8	39	51.34	1.414			0.535		
1244C		1.5	81	42	95.6	4.00	0.5	0.064	1.0E-07	
13H-3WR	3.5-4.5	2.0		1.651	2.63					
CRS 567	115.413	54.4	39	57.24	1.510			0.658		
1244C		0.8	81	42	100.0	4.00	0.5	0.058	1.3E-07	Small Diameter
13H-3WR	B-C	4.0		1.653	2.64					
CRS 495	136.556	49.8	35	50.52	1.377			0.435		
1244C		0.2	77	43	98.8	4.00	0.5	0.051	7.0E-08	
17H-3WR	3.5-4.5	2.0		1.704	2.69					
CRS 499	135.55		35		2.744			0.519		
1244C			77	43	101.7	4.00	0.5	0.057		Resedimented
17H-3WR	0-3			1.464	2.69					
CRS 564	136.467	47.9	35	46.68	1.229			0.453		
1244C		2.4	77	43	102.2	5.00	0.5	0.060	3.0E-08	Small Diameter
17H-3WR	7-8	4.0		1.771	2.69					
CRS 577		49.2			1.364			0.340		
Mixed		1.0			101.6	4.00	0.5	0.041		Remolded
Sample		4.0		1.724	2.69					

a) Markers - Location within tube b) Stresses in kg/cm^2 c) 1 kg/cm^2 = 98.06 kPa d) Water Contents in %

Index Tests		Specimen Data	
w_c	water content	w_n	natural water content
w_p	plastic limit	e_i	initial void ratio
w_l	liquid limit	I_p	plasticity index
SD	standard deviation	S_i	initial saturation
#obs	number of observations	γ_t	total unit weight
		G_s	specific gravity
Conditions		**Consolidation**	
u_b	back pressure	C_c	compression index
$\delta\varepsilon/\delta t$	strain rate	C_r	recompression index
		k_o	in situ hydraulic conductivity

Table 5.5: CRSC test conditions and consolidation properties (con't)

Spec. Location		Index Tests		Specimen Data		Conditions			Consolidation Results					
									General		@ Max Stress		@ Preshear	
Test #	Depth	w_c	w_p	w_n	e_i	σ'_i	u_b	B	σ'_p	Cc	ε_a	σ'_{vm}	ε_a	σ'_{vc}
Boring		SD	w_l	I_p	S_i						ε_{vol}	K_c	ε_{vol}	OCR
Sample	Markers	# obs		γ_t	G_s	ε_a		ε_{vol}	ε_a/hr			t_s	K_c	t_s
TX 643	7.141	58.0	32	58.99	1.458	0.19	3.32	99	1.73	0.496	10.45	3.34	10.45	3.34
1244B		1.66	71	39	104.52						10.50	0.464	10.50	1.00
1H-4WR		4		1.671	2.58	0.32		-1.12	0.20			~24	0.464	~24
TX 642	21.627	63.6	37	64.52	1.595	0.18	3.50	98	2.78	0.601	11.72	4.61	11.72	4.61
1244B		1.2	82	45	104.19						11.90	0.454	11.90	1.00
3H-3WR		3		1.633	2.58	0.23		-1.00	0.20			~34	0.454	~34
TX 635	34.383	64.5	42	65.22	1.624	1.17	7.00	103	5.02	0.691	22.63	22.95	22.63	22.95
1244B		0.7	87	45	105.30						22.79	0.566	22.79	1.00
4H-6WR		4		1.651	2.62	0.33		-6.08	0.20			~51	0.566	~51
TX 645	34.269	61.8	42	63.80	1.686	0.21	3.30	99	4.35	0.712	15.91	8.56	15.91	8.56
1244B		0.6	87	45	99.17						16.12	0.503	16.12	1.00
4H-6WR		4		1.598	2.62	0.45		-3.01	0.20			~23	0.503	~23
TX 646	80.252	49.7	38	54.18	1.477	0.25	2.96	98	8.04	0.698	16.95	16.30	16.95	16.30
1244B		0.5	83	45	96.76						17.13	0.506	17.13	1.00
9H-5WR		3		1.642	2.64	0.42		-4.78	0.20			~28	0.506	~28
TX 636	136.403	49.1	35	49.34	1.181	1.29	7.84	98	-	0.448	23.12	42.20	23.12	42.20
1244C		1.9	77	43	110.71						23.55	0.520	23.55	1.00
17H-3WR		4		1.814	2.65	-3.40		-0.92	0.20			~31	0.520	~31
TX 641		34.0		34.00	0.914	0.32	3.18	99	-	0.200	8.88	10.40	8.88	10.40
Remolded		0.1			98.54						9.07	0.454	9.07	1.00
		2		1.855	2.65	0.33		-3.35	0.20			~37	0.454	~37
TX 644		70.1		70.20	1.853	0.09	3.50	98	-	0.462	10.81	1.11	10.81	1.11
Resedimented		0.6			101.94						10.86	0.457	10.86	1.00
		3		1.605	2.69	0.44		-1.15	0.20			~24	0.457	~24

Table 5.6: CKoU test conditions and results for consolidation stage

Spec. Location		Index Tests		Specimen Data		Conditions			Consolidation Results					
									General		@ Max Stress		@ Preshear	
Test #	Depth	w_c	w_p	w_n	e_i	σ'_i	u_b	B	σ'_p	Cc	ε_a	σ'_{vm}	ε_a	σ'_{vc}
Boring		SD	w_l	I_p	S_i						ε_{vol}	K_c	ε_{vol}	OCR
Sample	Markers	# obs		γ_t	G_s	ε_a		ε_{vol}	ε_a/hr			t_s	K_c	t_s
TX 647		58.1		58.81	1.631	0.14	2.86	105	-	0.384	10.93	1.73	10.54	0.86
Resedimented		1.1			97.06						11.00	0.491	10.64	2.00
		3		1.625	2.69	0.58		-0.5	0.20			~25	0.666	~24
TX 650		71.2		70.56	1.918	0.12	3.31	98	-	0.469	10.93	0.58	10.93	0.58
Resedimented		1.5			99.00						11.06	0.514	11.06	1.00
		3		1.573	2.69	0.26		-0.26	0.20			~40	0.514	~40

a) Marker location in tube
b) Stresses in kg/cm^2
c) 1 kg/cm^2 = 98.06 kPa
d) Depth in Feet
e) Time in hours
f) Water content, limits, saturation, strain, and B value in %
g) density in gm/cm^3

Index Tests		Specimen Data	
w_c	water content of trimmings	w_n	natural water content
w_p	plastic limit	e_i	initial void ratio
w_l	liquid limit	I_p	plasticity index
SD	standard deviation	S_i	initial saturation
#obs	number of observations	γ_t	total unit weight
		G_s	specific gravity
Conditions		**Consolidation**	
σ'_i	initial effective stress	σ'_p	preconsolidation pressure
u_b	back pressure	C_c	compression index
B	B-value	ε_a/hr	strain rate
ε_a	axial strain @ σ'_i	σ'_{vm}	maximum consolidation stress
ε_{vol}	volumetric strain for saturation	K_c	consolidation lateral stress ratio
		t_s	time for secondary compression
		OCR	overconsolidation ratio
		σ'_{vc}	consolidation stress
		ε_a	axial strain
		ε_{vol}	volumetric strain

Table 5.6: CKoU test conditions and results for consolidation stage (con't)

Specimen Location		Specimen Data		Conditions			At Max Shear			At Max Obliquity		
Test #	Depth	w_n	e_i		e_c	σ'_{vc}	ε_a	$\Delta u_e/\sigma'_{vc}$	q/p'	ε_a	$\Delta u_e/\sigma'_{vc}$	q/p'
Boring		I_p	S_i					$\Delta u_s/\sigma'_{vc}$	ϕ'		$\Delta u_s/\sigma'_{vc}$	ϕ'
Sample	Markers	γ_t	G_s	ε_a/hr	K_c	OCR	q/σ'_{vc}	p'/σ'_{vc}	A	q/σ'_{vc}	p'/σ'_{vc}	A
TX 643	7.141	58.99	1.458		1.20	3.34	1.63	0.160	0.530	7.44	0.226	0.577
1244B		39	104.5					0.111	32.0		0.190	35.3
1H-4WR		1.671	2.58	0.5	0.464	1.00	0.343	0.647	1.091	0.325	0.563	2.03
TX 643		58.99	1.458		1.20	3.34	-6.44	0.010	-0.798	-6.44	0.010	-0.798
Second shear		39	104.5					0.325	-53.1		0.325	-53.1
		1.671	2.58	0.5	0.464	1.00	-0.201	0.252		-0.201	0.252	
TX 642	21.627	64.52	1.595		1.29	4.61	0.86	0.124	0.513	7.18	0.234	0.589
1244B		45	104.2					0.075	30.9		0.207	36.1
3H-3WR		1.633	2.58	0.5	0.454	1.00	0.347	0.676	0.837	0.314	0.533	2.85
TX 635	34.383	65.22	1.624		1.02	22.95	1.56	0.201	0.467	10.39	0.333	0.554
1244B		45	105.3					0.137	27.8		0.290	33.6
4H-6WR		1.651	2.62	0.5	0.566	1.00	0.314	0.673	1.06	0.282	0.509	2.63
TX 645	34.269	63.80	1.686		1.25	8.56	1.25	0.171	0.490	4.03	0.254	0.553
1244B		45	99.2					0.123	29.4		0.215	33.6
4H-6WR		1.598	2.62	0.5	0.503	1.00	0.319	0.651	1.19	0.307	0.555	2.15
TX 645		63.80	1.686		1.25	8.56	-12.15	-0.052	-0.716	-12.15	-0.052	-0.716
Second shear		45	99.2					0.267	-45.3		0.267	-45.3
		1.598	2.62	0.5	0.503	1.00	-0.232	0.324		-0.232	0.324	
TX 646	80.252	54.18	1.477		1.05	16.30	0.97	0.132	0.454	8.88	0.273	0.536
1244C		45	96.8					0.091	27.0		0.260	32.4
9H-5WR		1.642	2.64	0.5	0.506	1.00	0.309	0.681	1.07	0.267	0.498	6.72
TX 646		54.18	1.477		1.05	16.30	-4.66	0.081	-0.646	-4.66	0.081	-0.646
Second shear		45	96.8					0.357	-40.1		0.357	-40.1
		1.642	2.64	0.5	0.506	1.00	-0.166	0.257		-0.166	0.257	

Table 5.7: CKoU test conditions and results for undrained shearing stage

Specimen Location		Specimen Data		Conditions			At Max Shear			At Max Obliquity		
Test #	Depth	w_n	e_i		e_c	σ'_{vc}	ε_a	$\Delta u_e/\sigma'_{vc}$	q/p'	ε_a	$\Delta u_e/\sigma'_{vc}$	q/p'
Boring		I_p	S_i					$\Delta u_s/\sigma'_{vc}$	ϕ'		$\Delta u_s/\sigma'_{vc}$	ϕ'
Sample	Markers	γ_t	G_s	ε_a/hr	K_c	OCR	q/σ'_{vc}	p'/σ'_{vc}	A	q/σ'_{vc}	p'/σ'_{vc}	A
TX 636	135.5	49.34	1.686		0.68	42.20	1.73	0.188	0.426	7.87	0.286	0.450
1244C		43	99.2					0.136	25.2		0.266	26.7
17H-3WR		1.598	2.62	0.5	0.520	1.00	0.289	0.679	1.21	0.240	0.533	4.83
TX 641		34.00	0.914		0.74	10.40	10.30	0.124	0.522	6.00	0.168	0.535
Remolded			98.5					0.000	31.4		0.061	32.4
		1.855	2.65	0.5	0.519	1.00	0.427	0.818	0.33	0.400	0.748	0.53
TX 644		70.20	1.853		1.54	1.11	0.47	0.104	0.491	5.69	0.243	0.598
Resedimented			101.9					0.049	29.42		0.202	36.7
		1.605	2.69	0.5	0.457	1.00	0.348	0.709	0.63	0.329	0.550	1.94
TX 644		70.20	1.853		1.54	1.11	-10.41	-0.025	-1.157	-10.41	-0.025	-1.157
Second Shear			101.9					0.334	-		0.334	-
		1.605	2.69	0.5	0.457	1.00	-0.258	0.223		-0.258	0.223	
TX 647		58.81	1.631		1.35	0.86	9.07	0.271	0.627	8.29	0.275	0.630
Resedimented			97.1					-0.072	38.83		-0.066	39.05
		1.625	2.69	0.5	0.666	2.00	0.663	1.058	0.261	0.662	1.051	0.267
TX 650		70.56	1.918		1.60	0.58	-12.31	-0.042	-1.063	-12.31	-0.042	-1.063
Resedimented			99.0					0.310	-		0.310	-
		1.573	2.69	-0.5	0.514	1.00	-0.286	0.269	0.037	-0.286	0.269	0.037

a) Marker location in tube

b) Stresses in kg/cm^2

c) 1 kg/cm^2 = 2048 psf

d) Depth in Meters

e) Time in hours

f) Water content, saturation, and strain in %

Specimen Data				Conditions				Undrained Shearing			
w_n	water content	e_i	initial void ratio	e_c	shearing void ratio	ε_a/hr	strain rate	q/σ'_{vc}	shear stress	p'/σ'_{vc}	mean stress
I_p	plasticity index	S_i	initial saturation	OCR	overconsolidation ratio	K_c	lateral stress ratio	$\Delta u_e/\sigma'_{vc}$	excess pore pressure	$\Delta u_s/\sigma'_{vc}$	shear induced pore pressure
γ_t	total unit weight	G_s	specific gravity	σ'_{vc}	consolidation stress			ε_a	axial strain	ϕ'	friction angle

Table 5.7: CKoU test conditions and results for undrained shearing stage (con't)

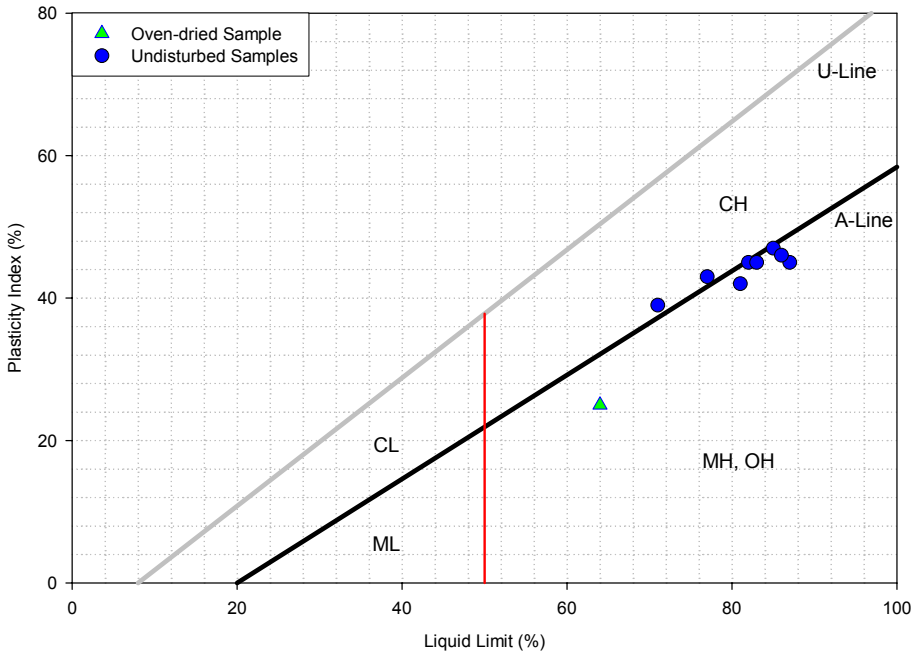

Figure 5.1: Plasticity chart showing the results of atterberg limit tests on undisturbed and oven-dried samples

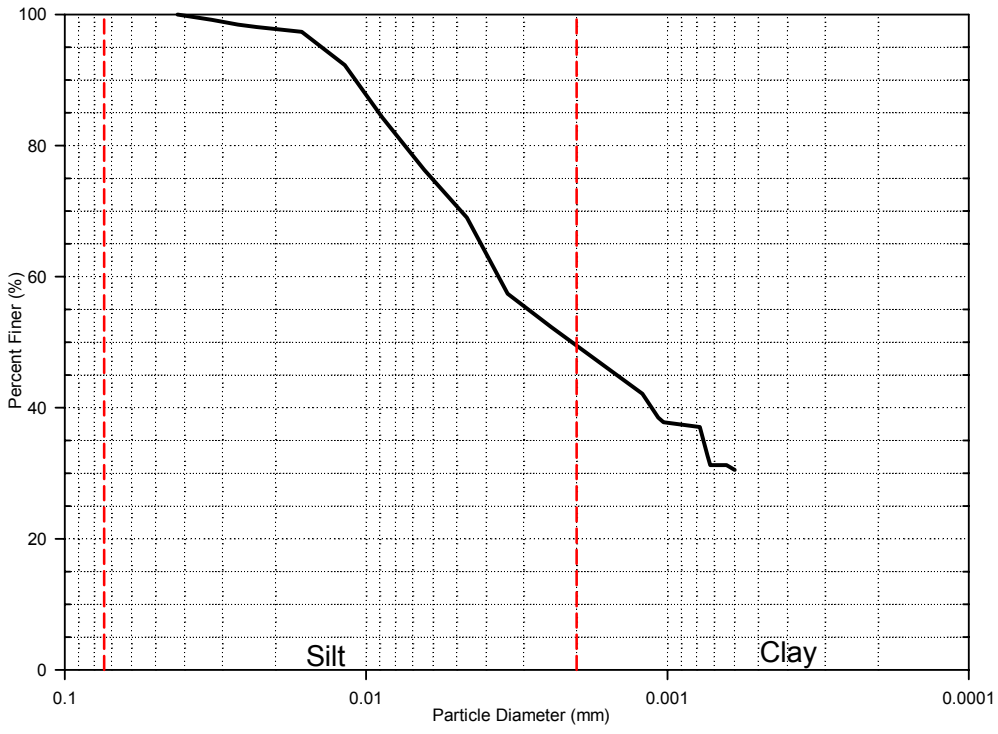

Figure 5.2: Particle size distribution curve for Hydrate Ridge soil

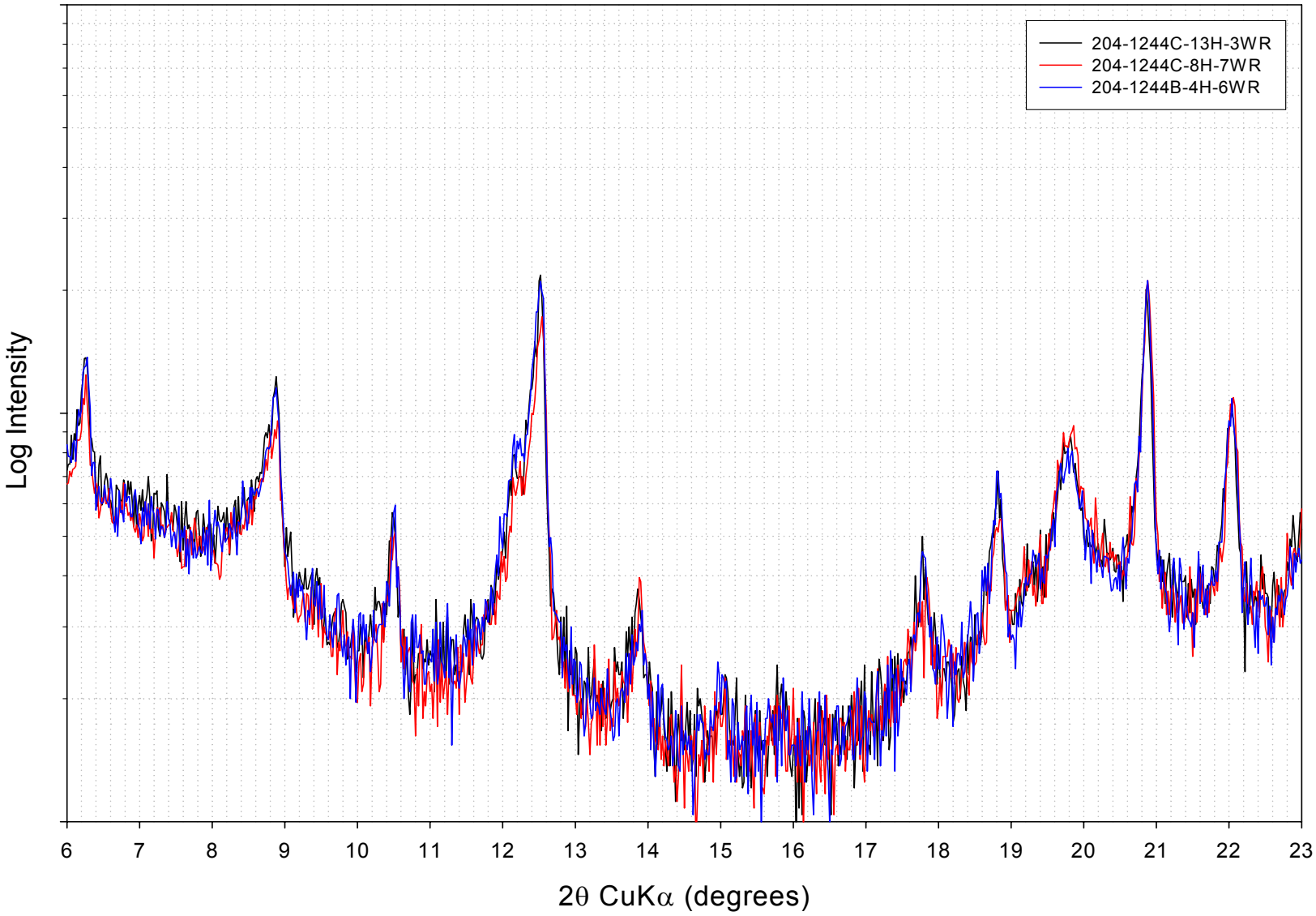

Figure 5.3: X-ray diffraction on random powder sample 2θ = 6° to 23°

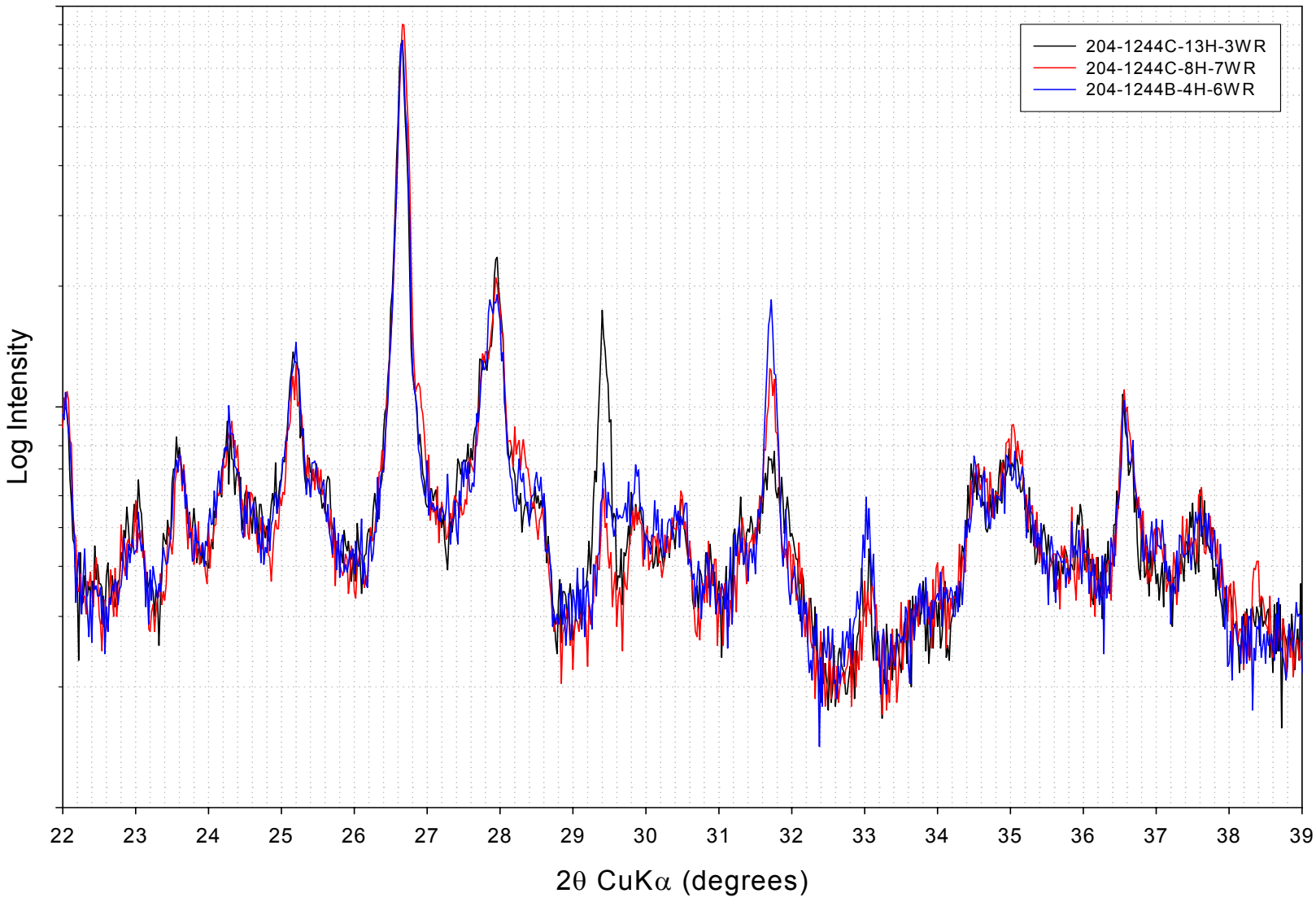

Figure 5.4: X-ray diffraction on random powder sample 2θ = 22° to 39°

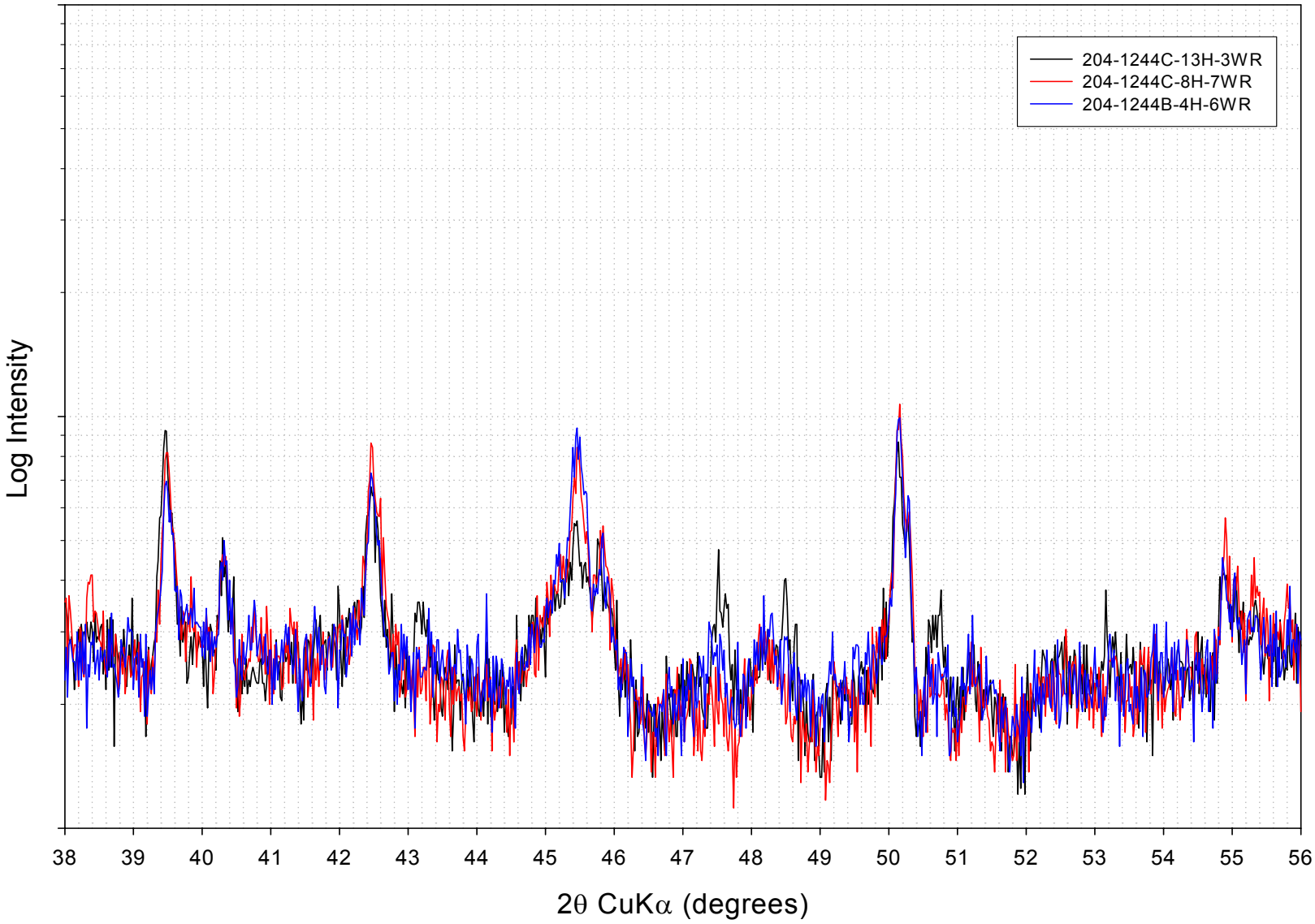

Figure 5.5: X-ray diffraction on random powder sample 2θ = 38° to 56°

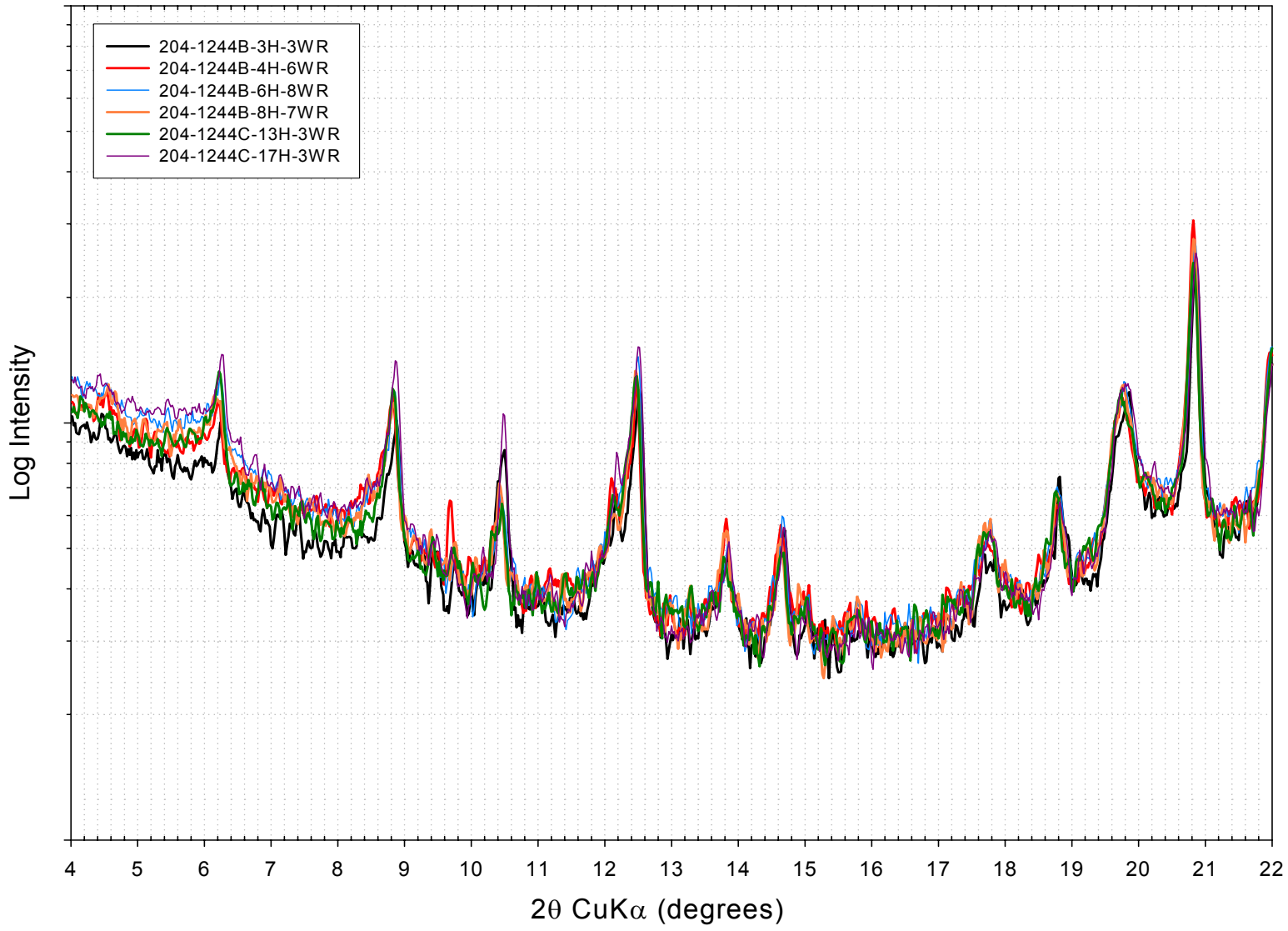

Figure 5.6: X-ray diffraction on calcite-treated random powder sample $2\theta = 4^{o}$ to 22^{o}

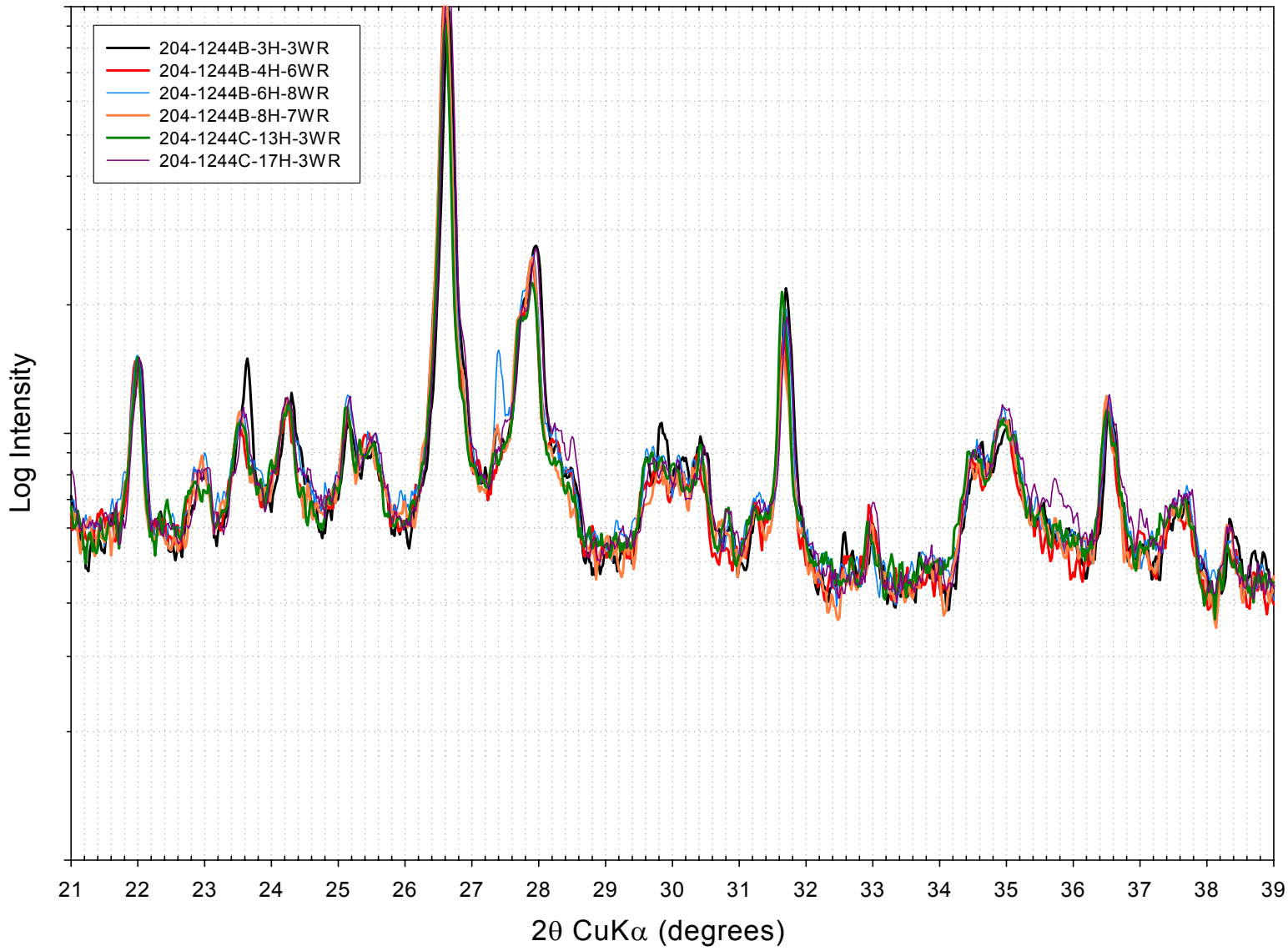

Figure 5.7: X-ray diffraction on calcite-treated random powder sample 2θ = 21° to 39°

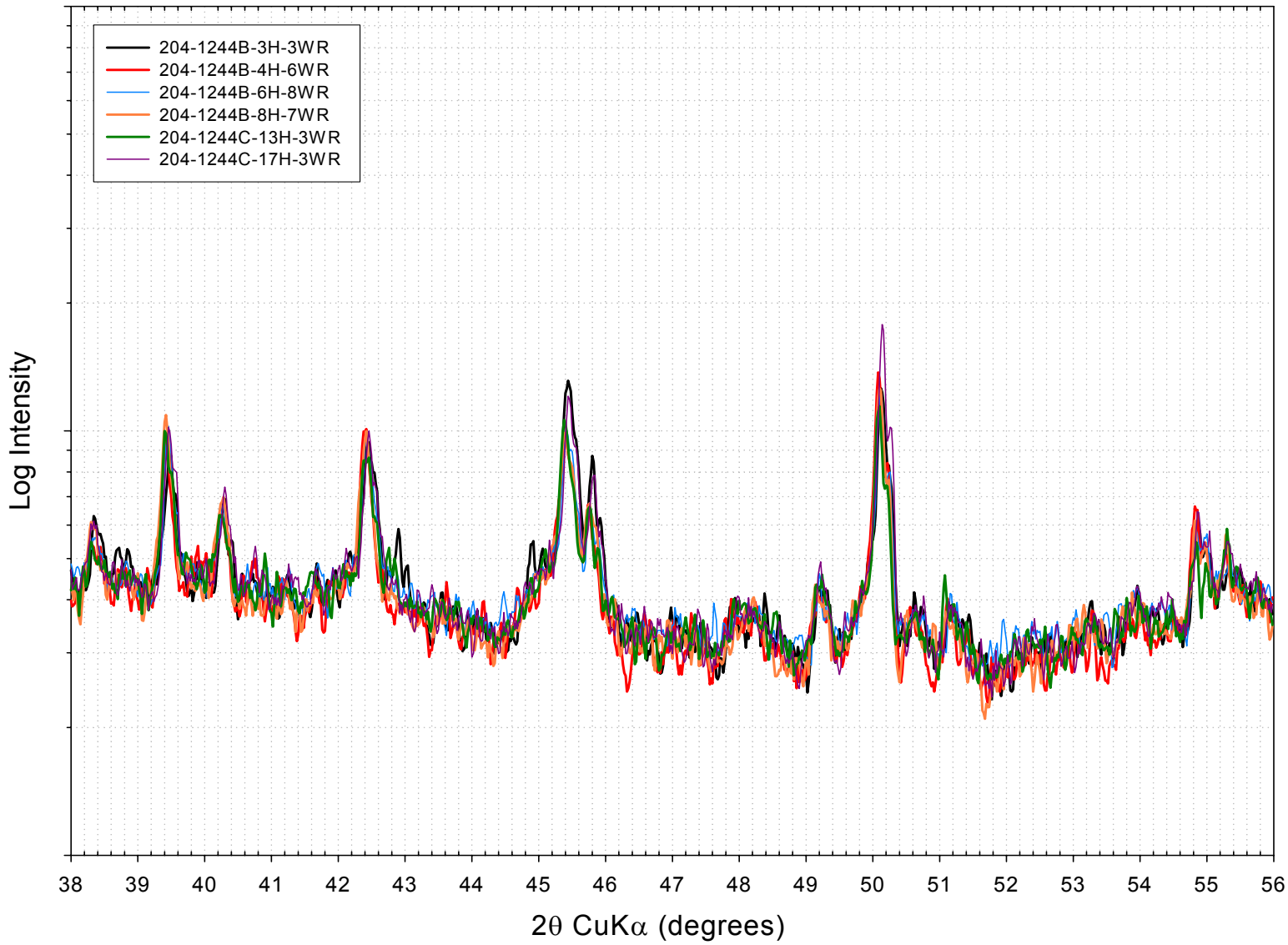

Figure 5.8: X-ray diffraction on calcite-treated random powder sample 2θ = 38° to 56°

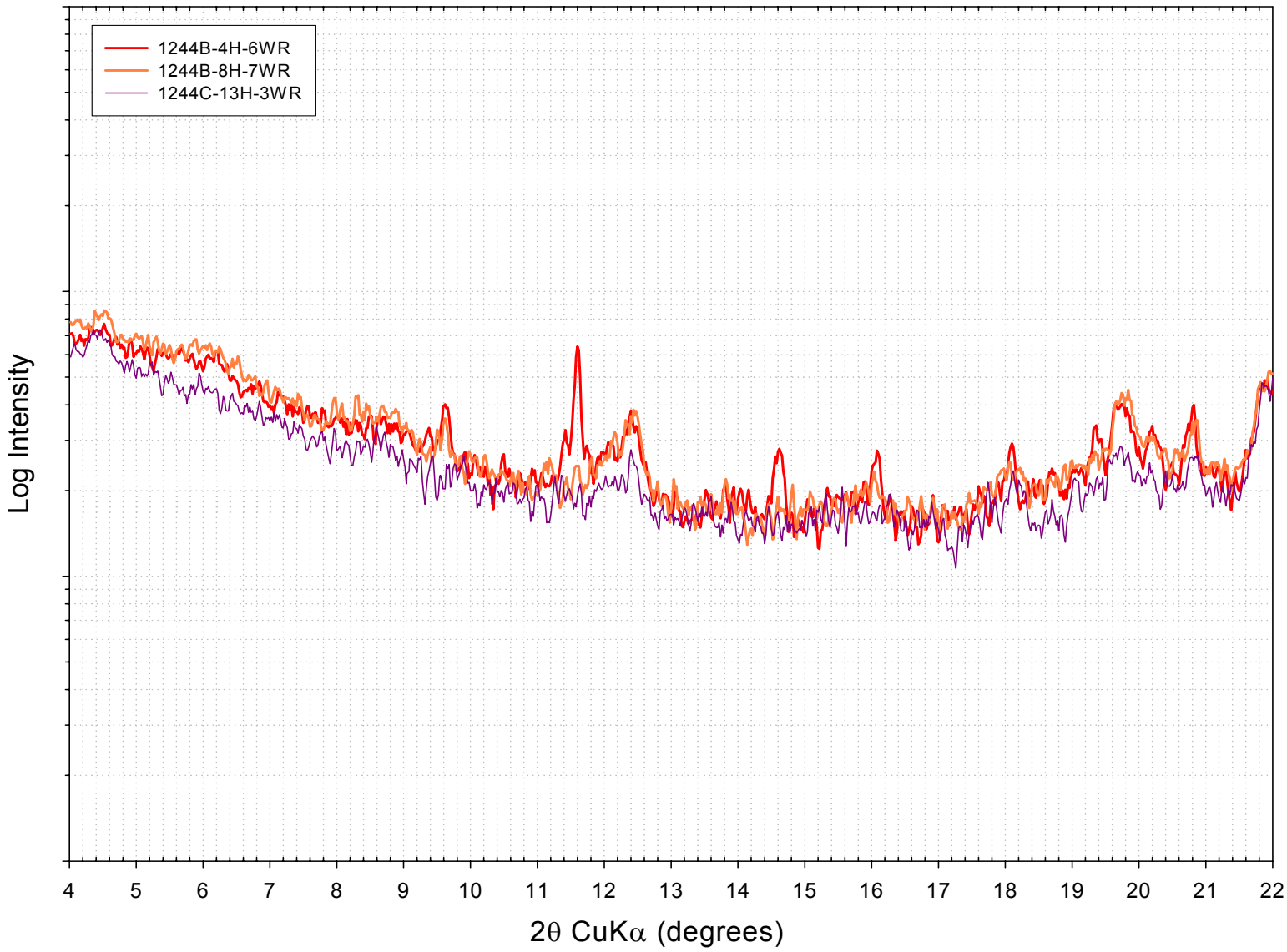

Figure 5.9: X-ray diffraction on clay-fraction random powder sample 2θ = 4° to 22°

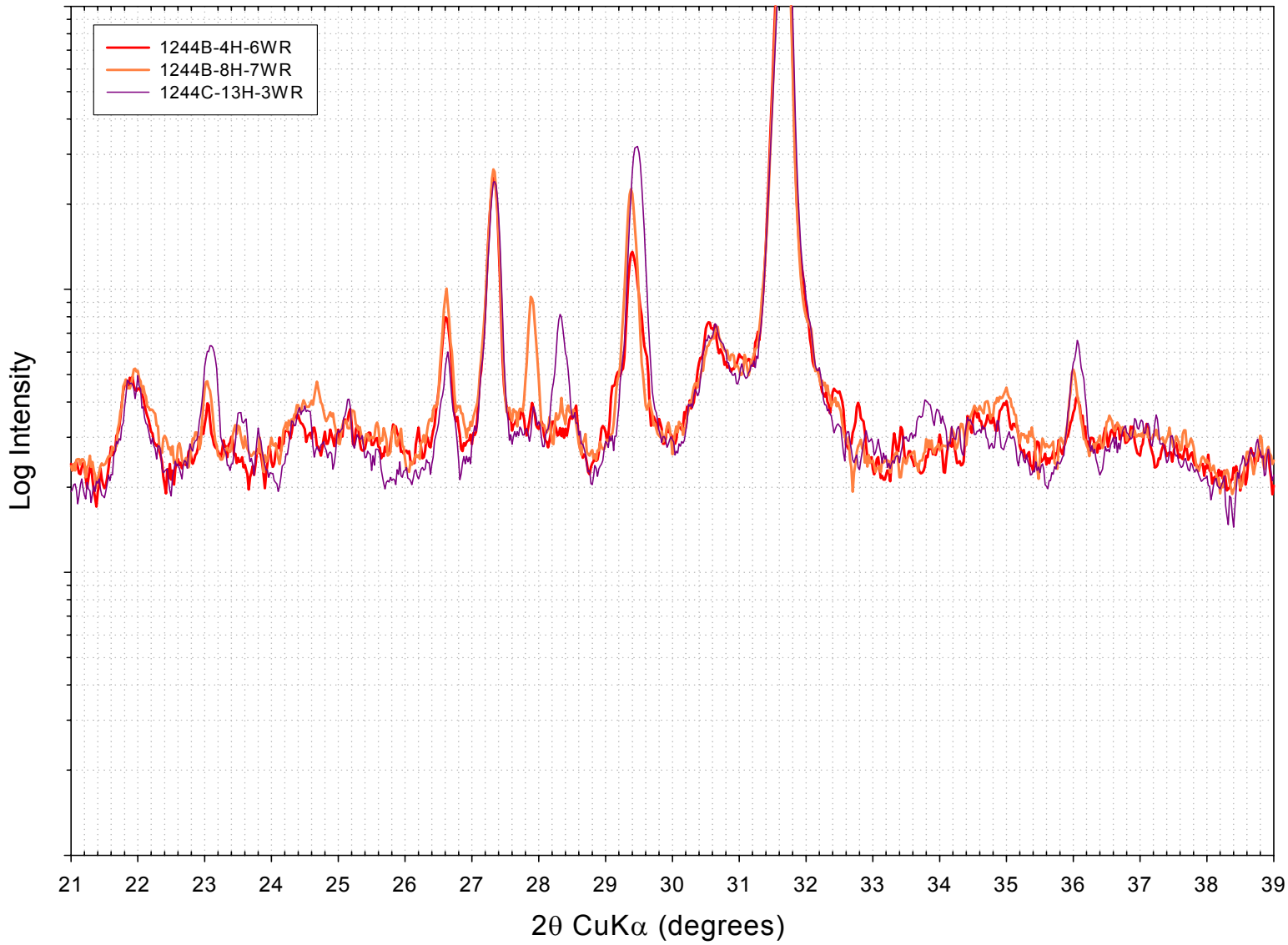

Figure 5.10: X-ray diffraction on clay-fraction random powder sample 2θ = 21° to 39°

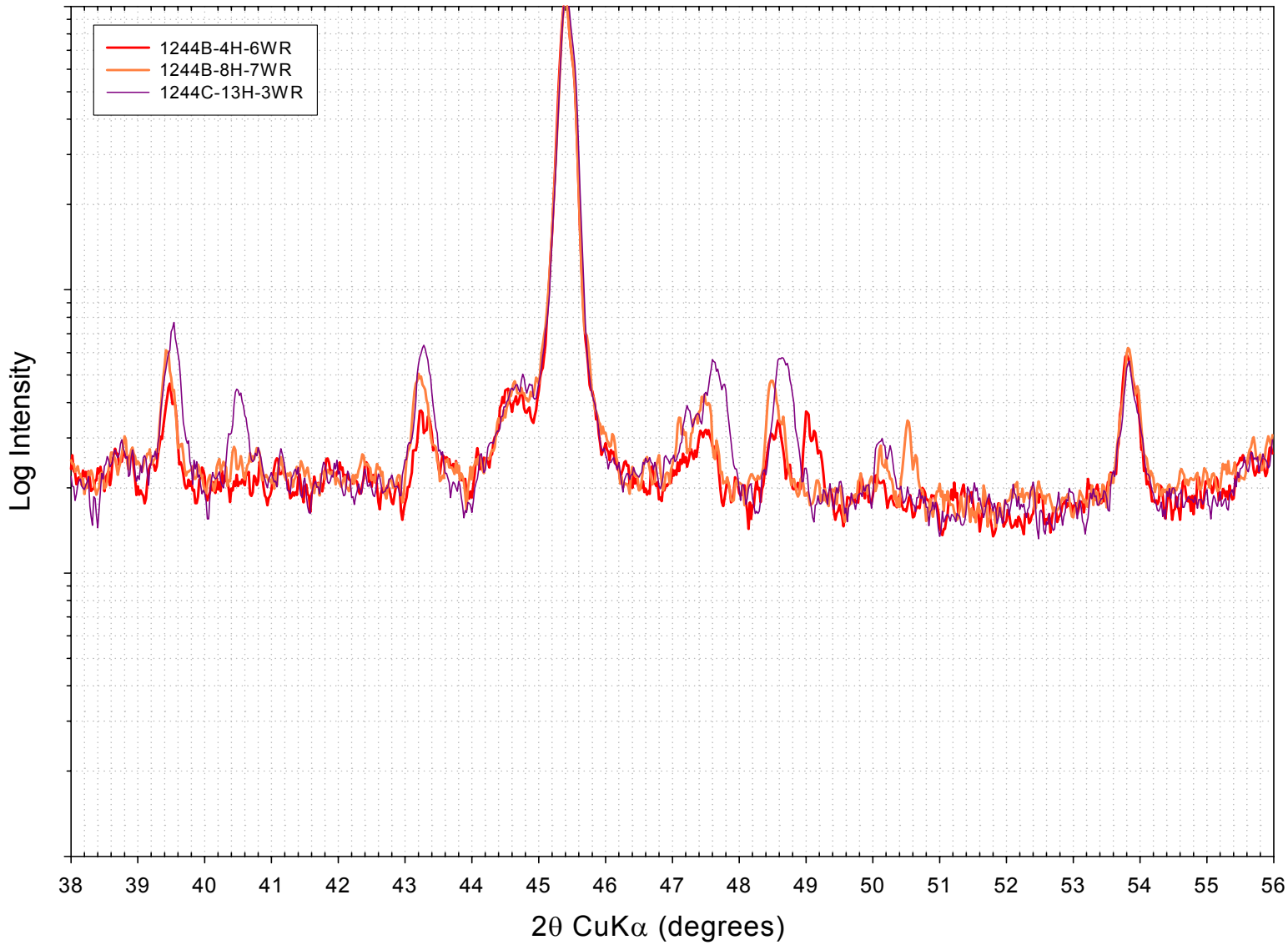

Figure 5.11: X-ray diffraction on clay-fraction random powder sample 2θ = 38° to 56°

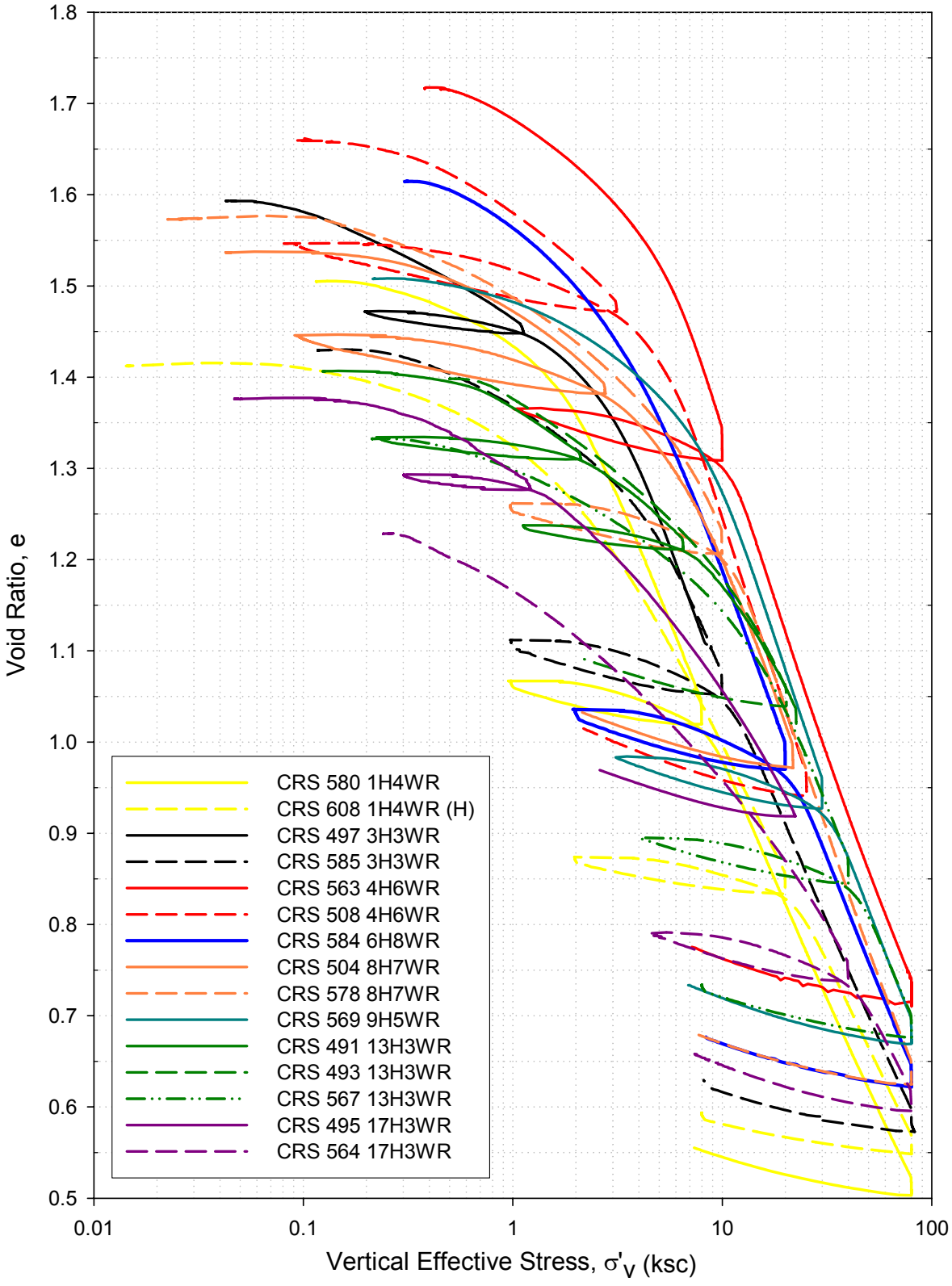

Figure 5.12: Summary of consolidation curves for intact specimens in e-logσ'_v space

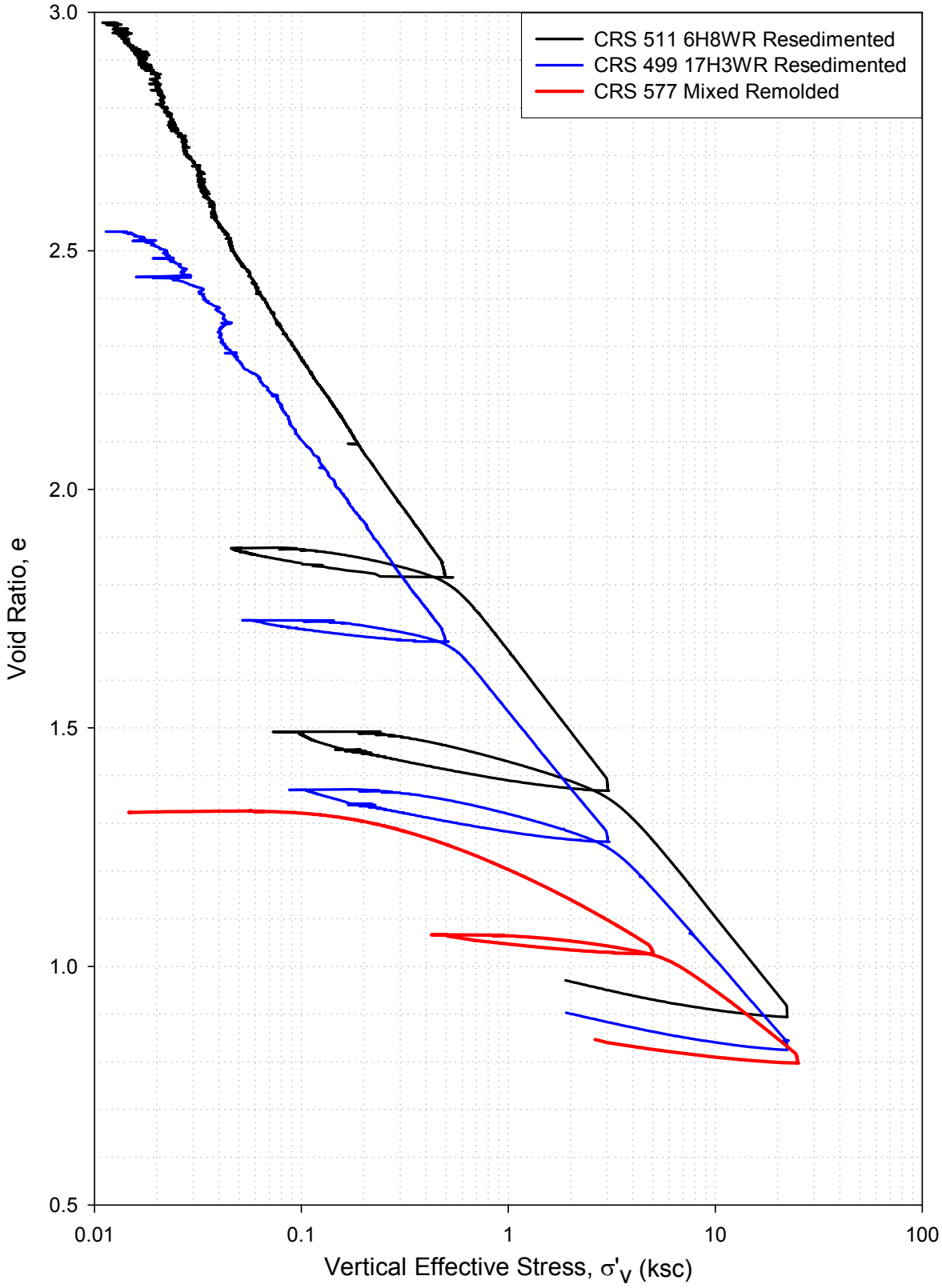

Figure 5.13: Summary of consolidation curves for remolded specimens in e-logσ'_v space

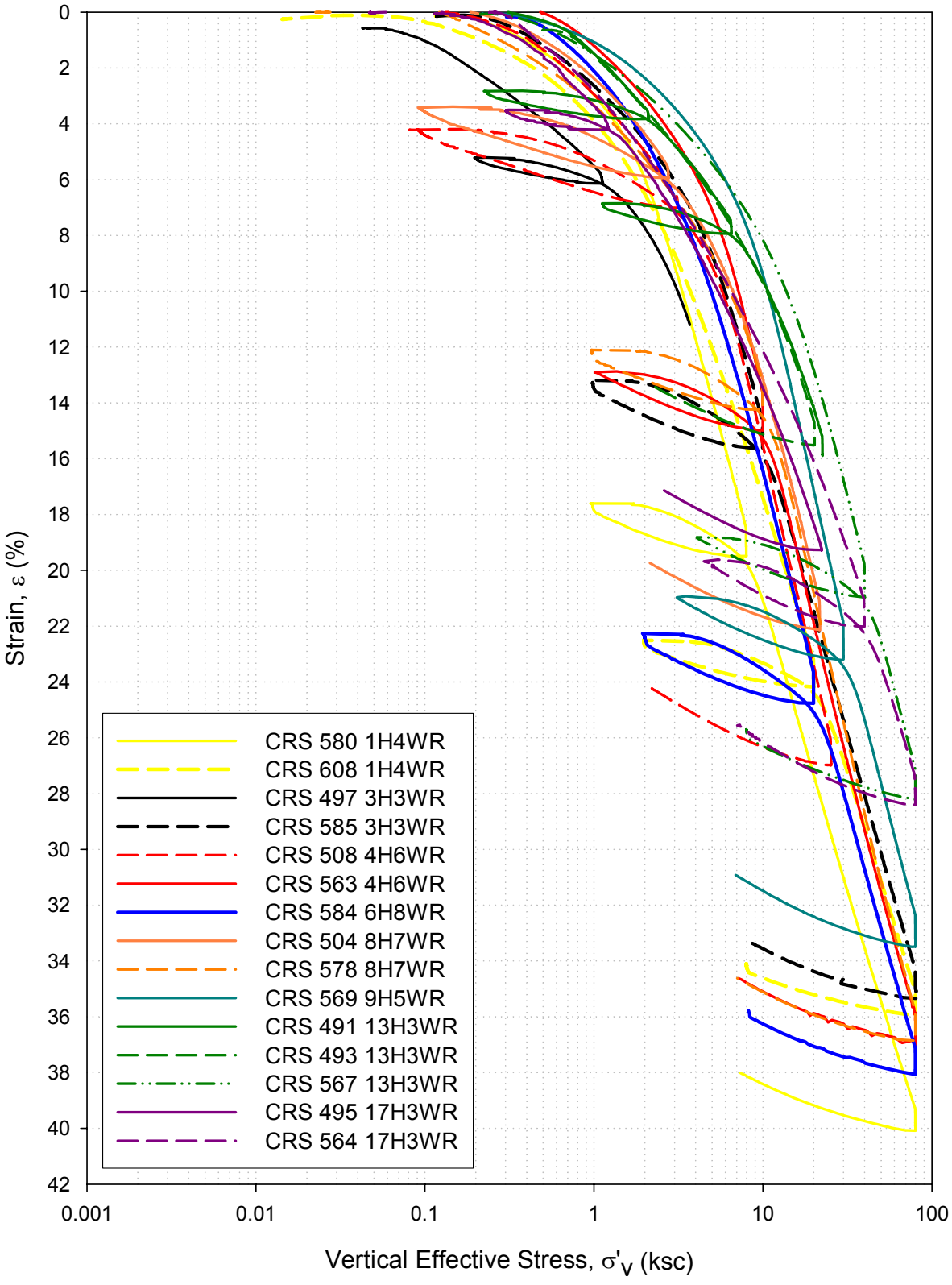

Figure 5.14: Summary of consolidation curves for intact specimens in ε-logσ'_v space

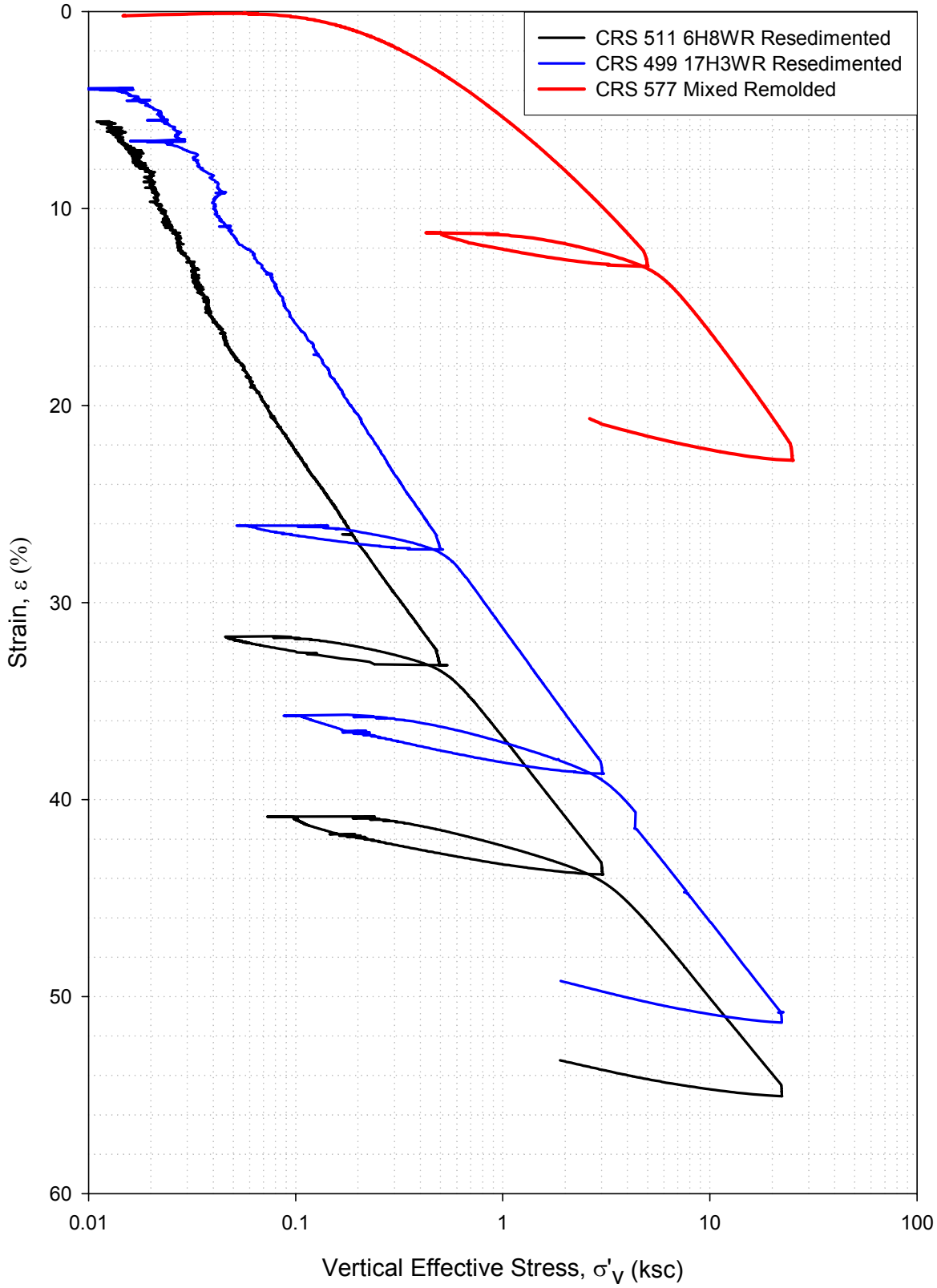

Figure 5.15: Summary of consolidation curves for remolded specimens in ε–logσ'$_v$ space

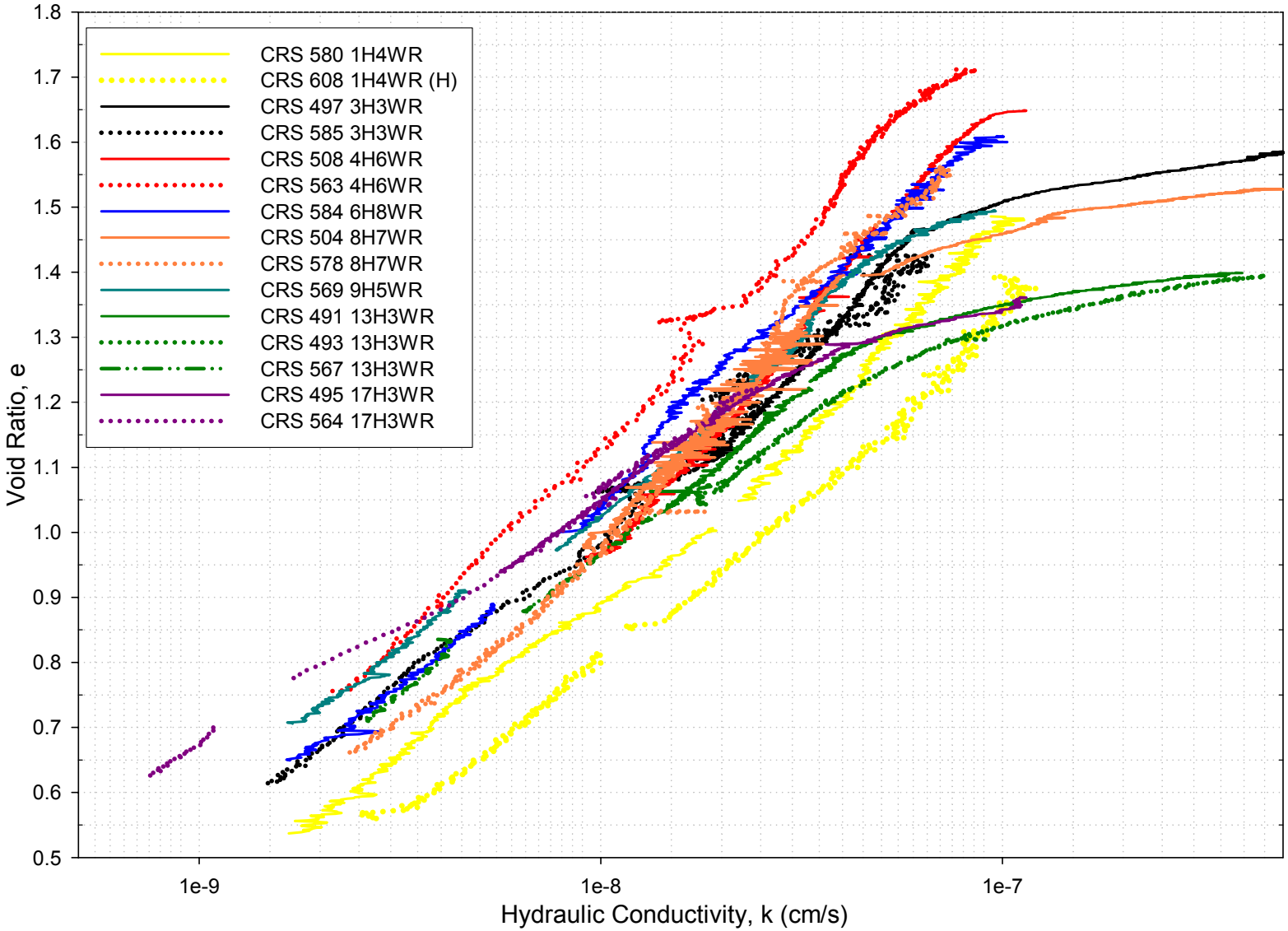

Figure 5.16: Summary of hydraulic conductivity curves for intact specimens

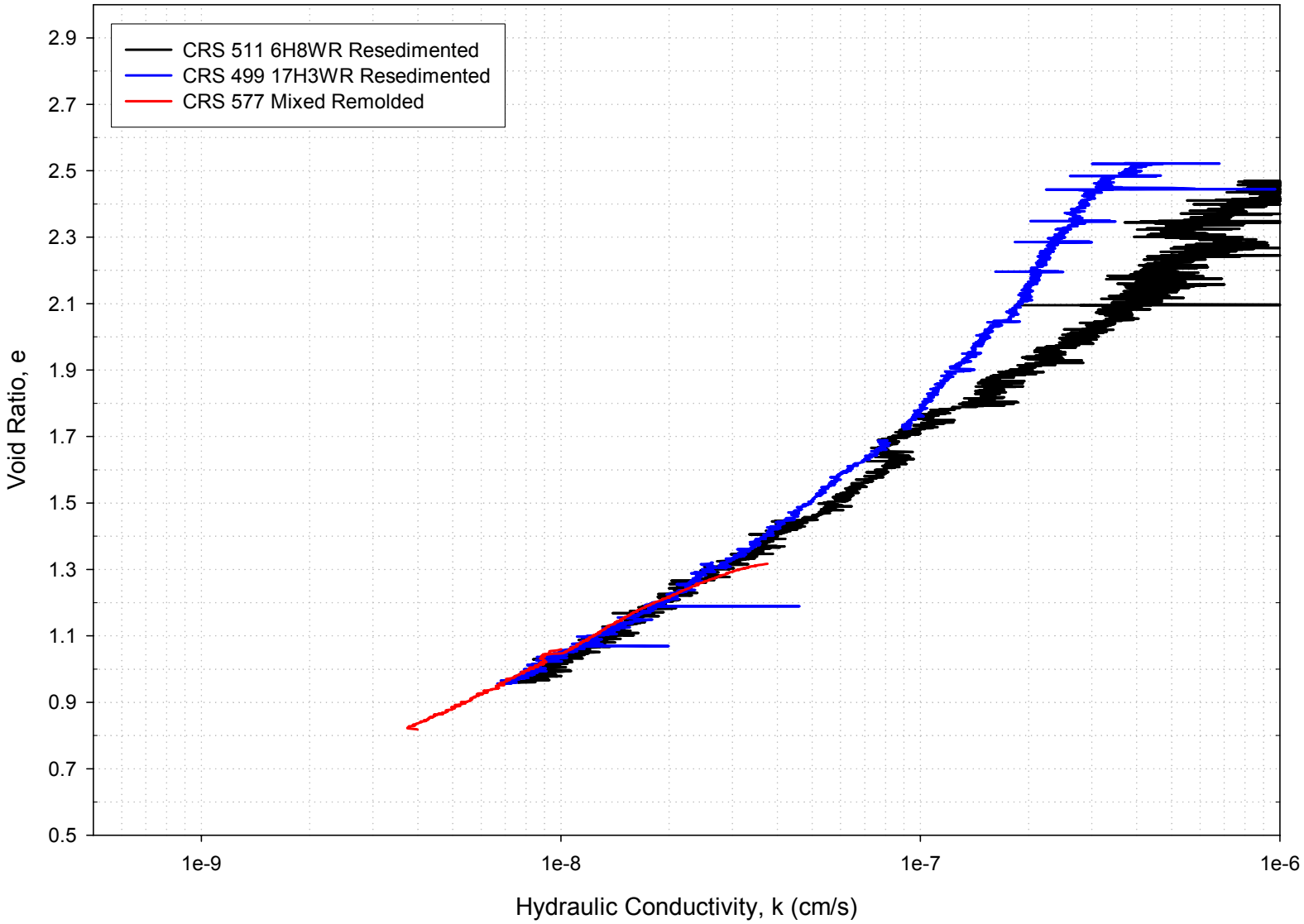

Figure 5.17: Summary of hydraulic conductivity curves for remolded specimens

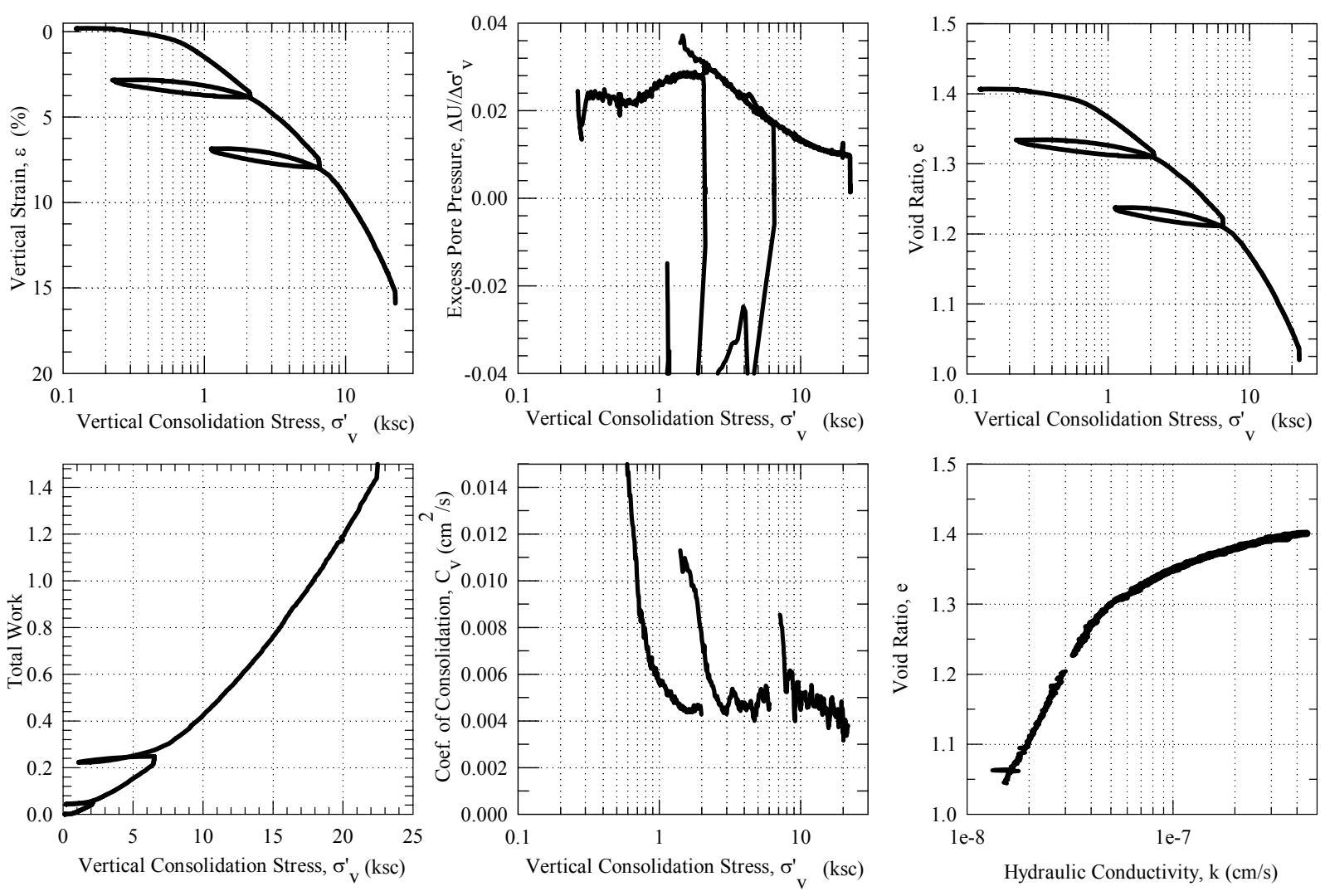

Figure 5.18: CRS 491

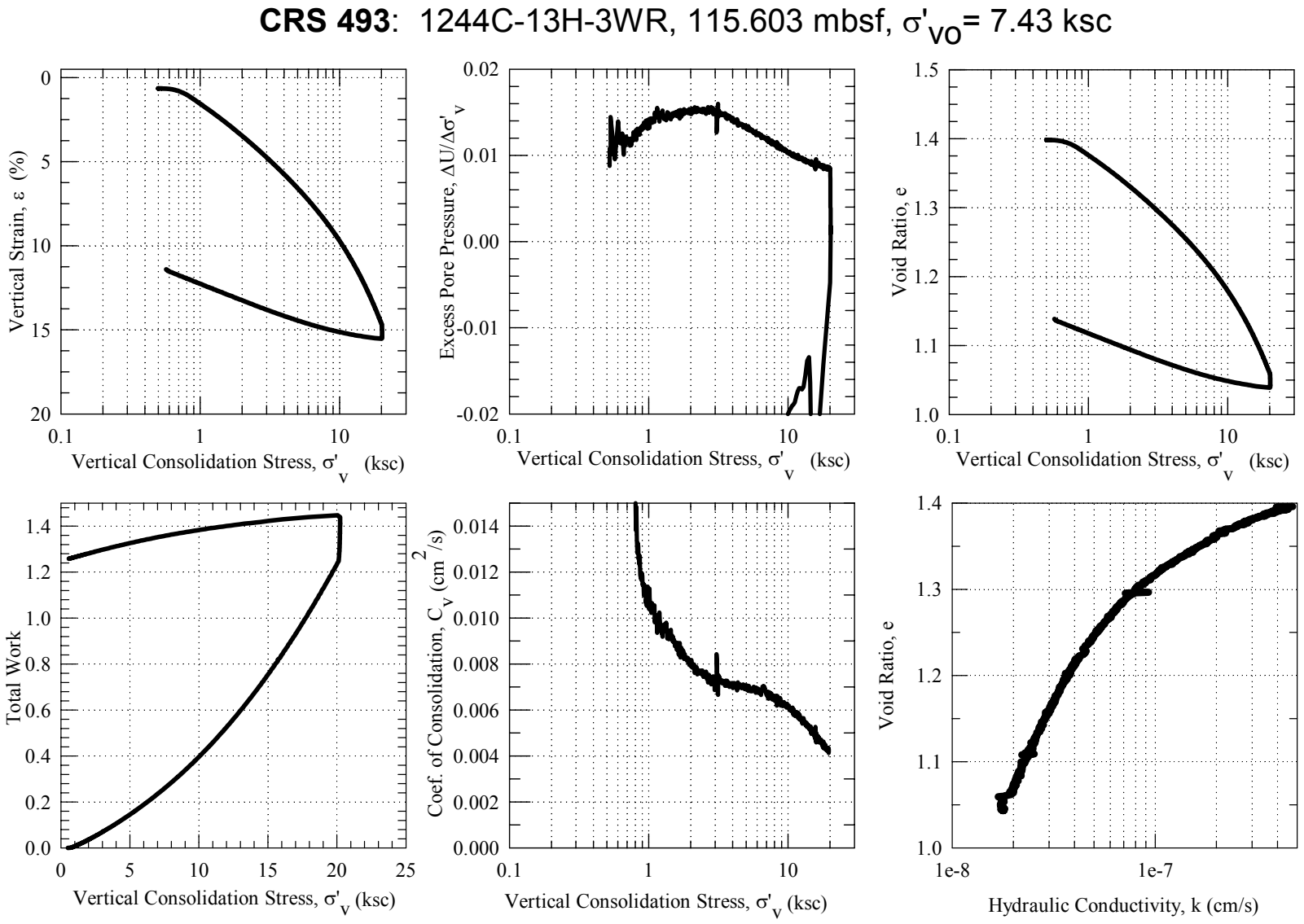

Figure 5.19: CRS 493

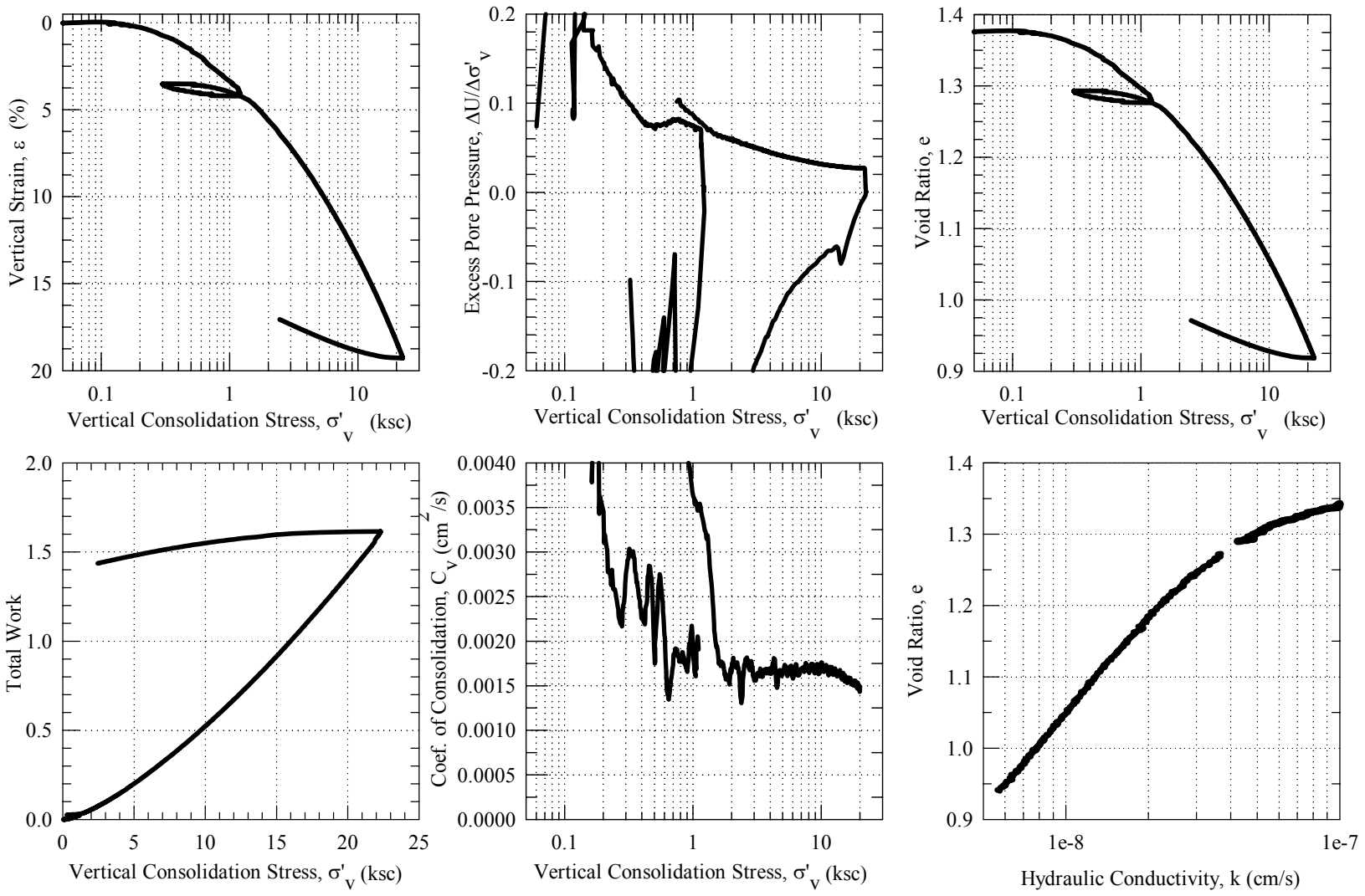

Figure 5.20: CRS 495

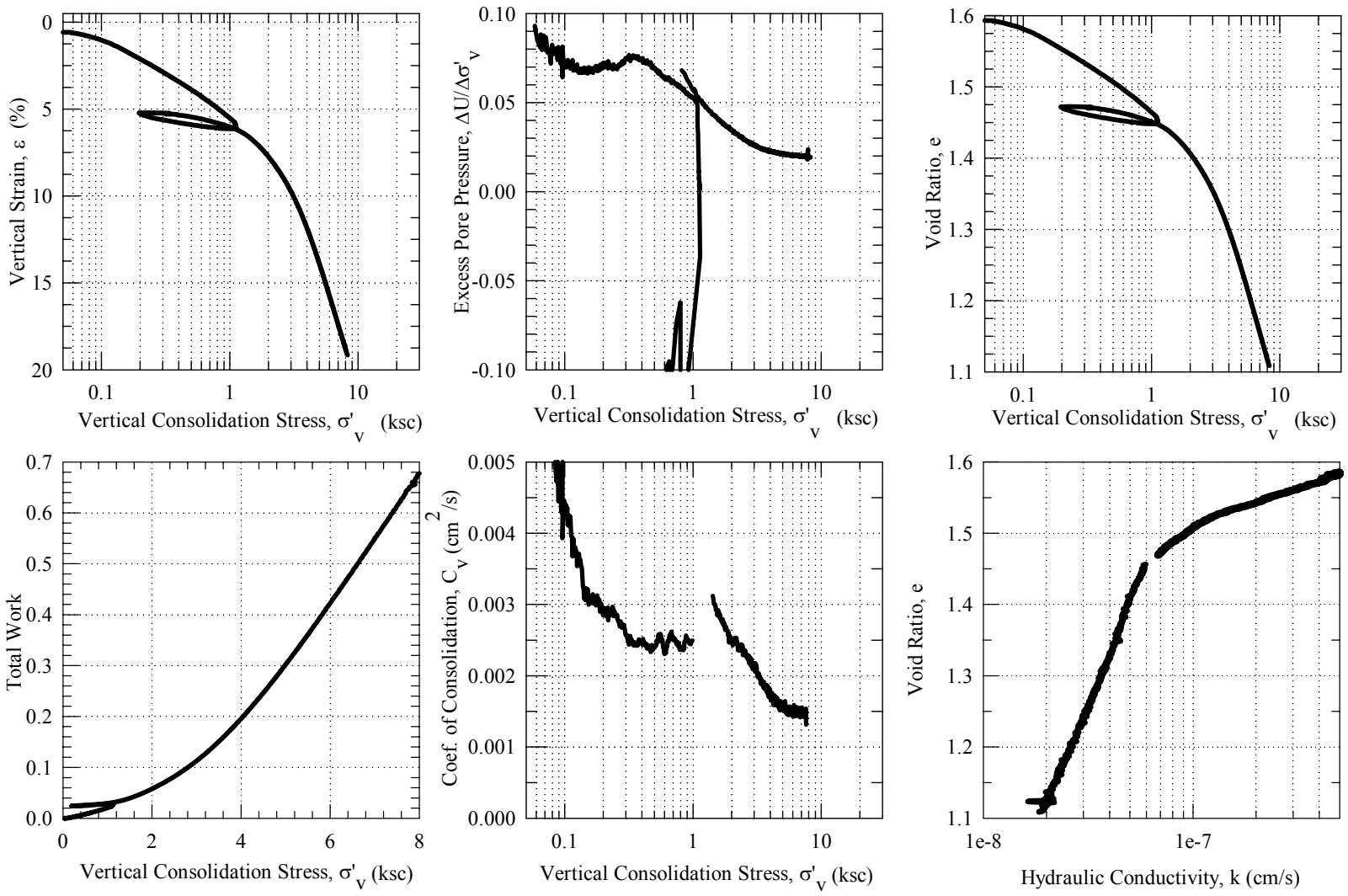

Figure 5.21: CRS 497

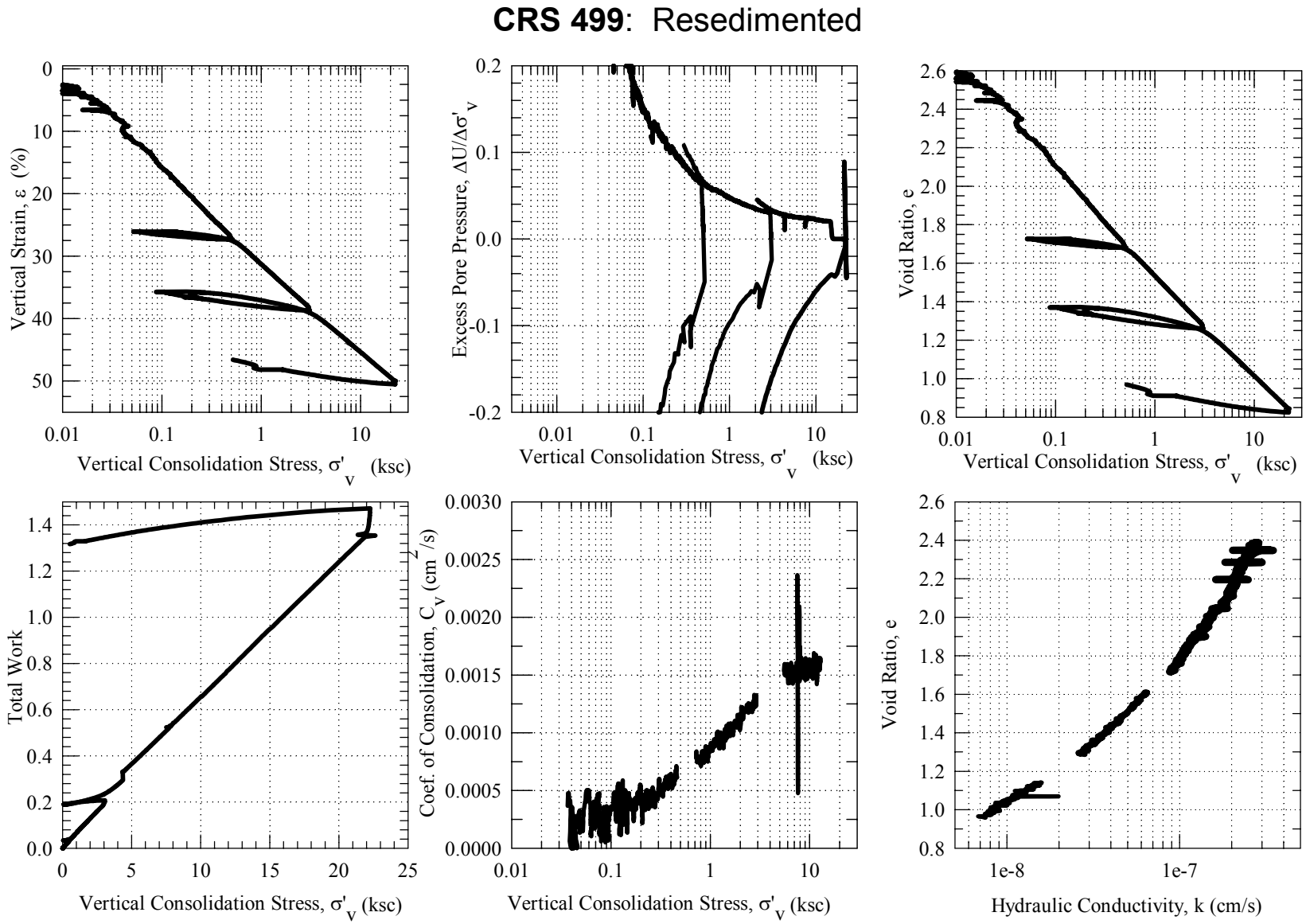

Figure 5.22: CRS 499

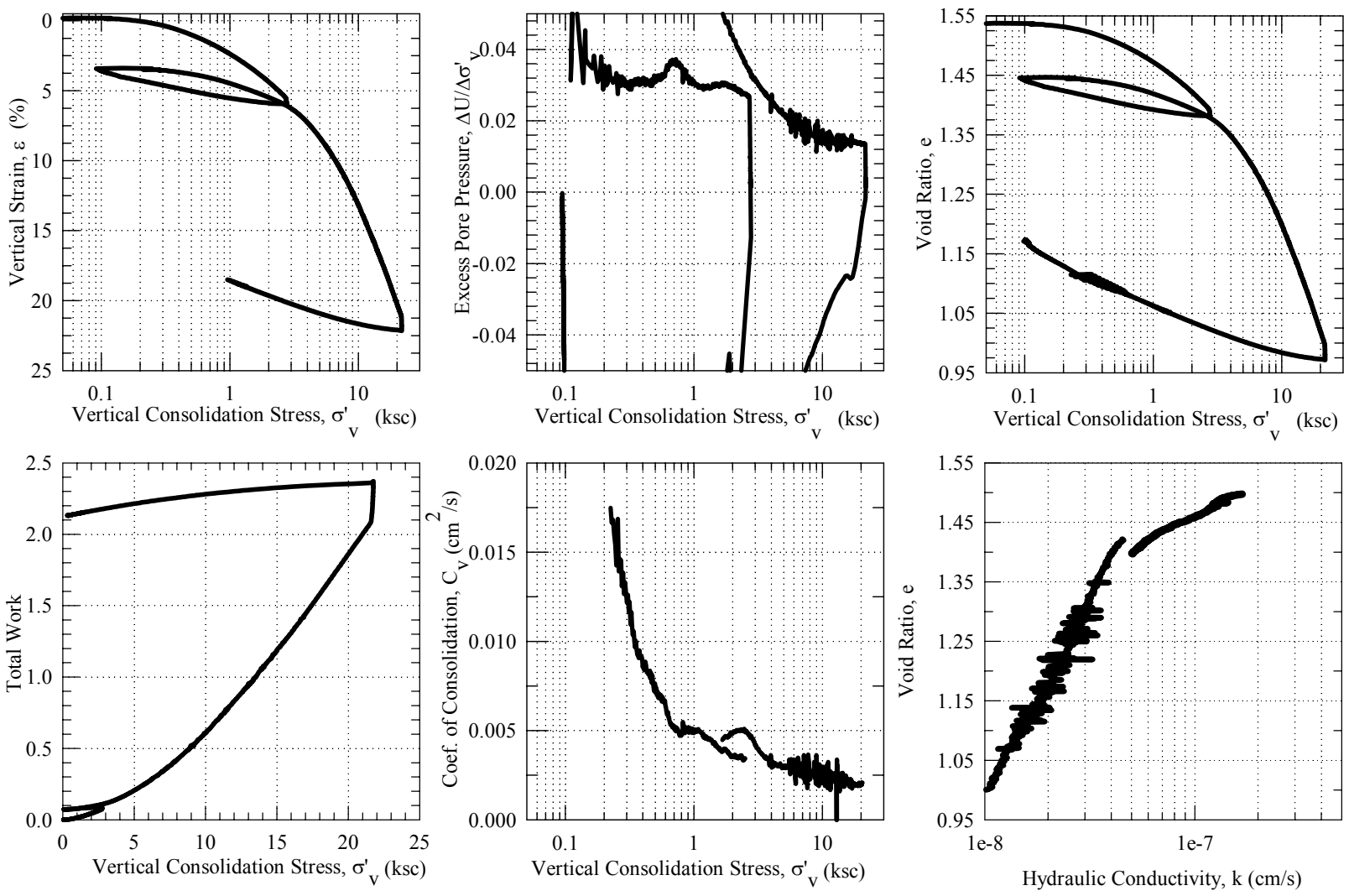

Figure 5.23: CRS 504

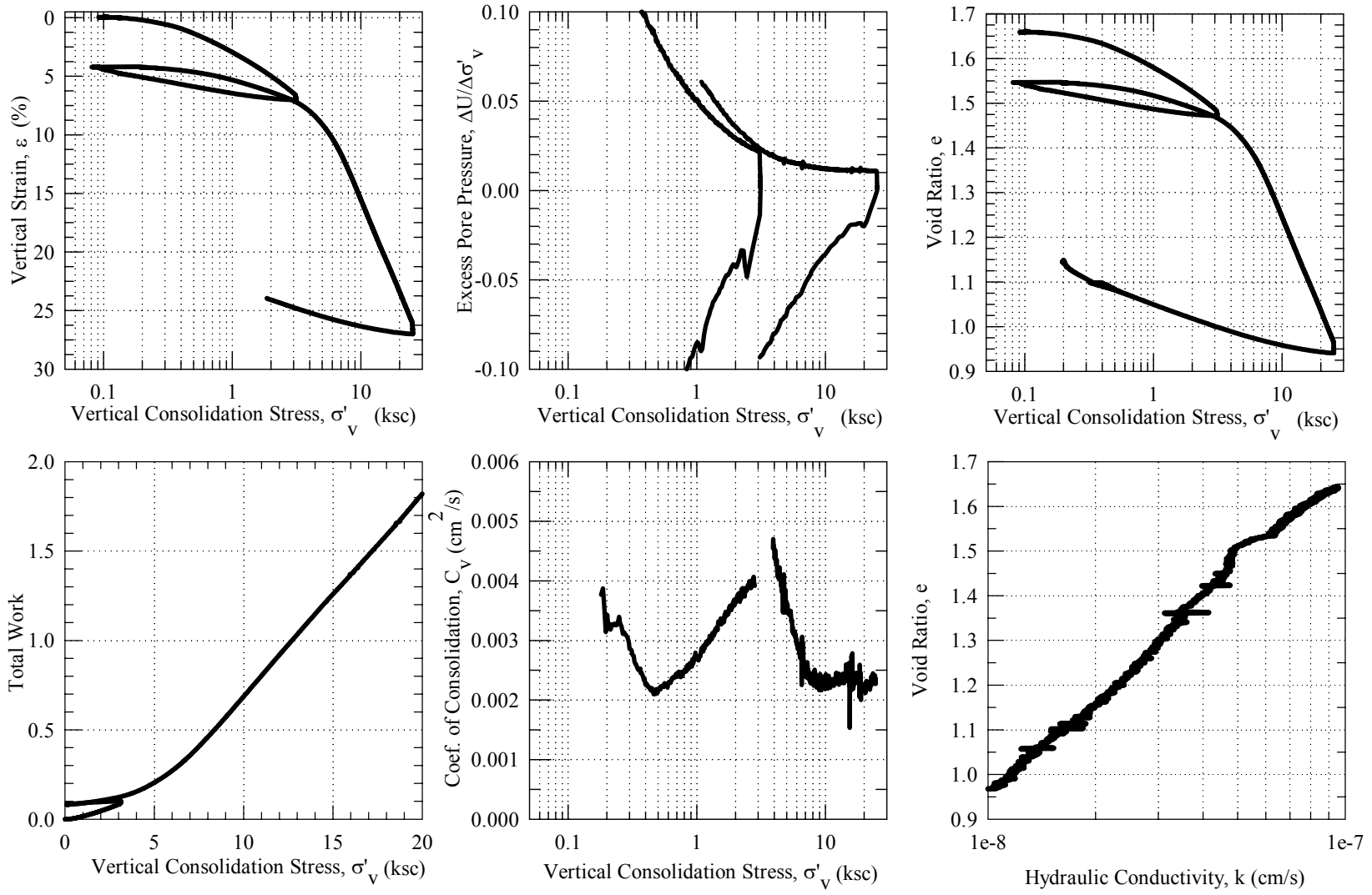

Figure 5.24: CRS 508

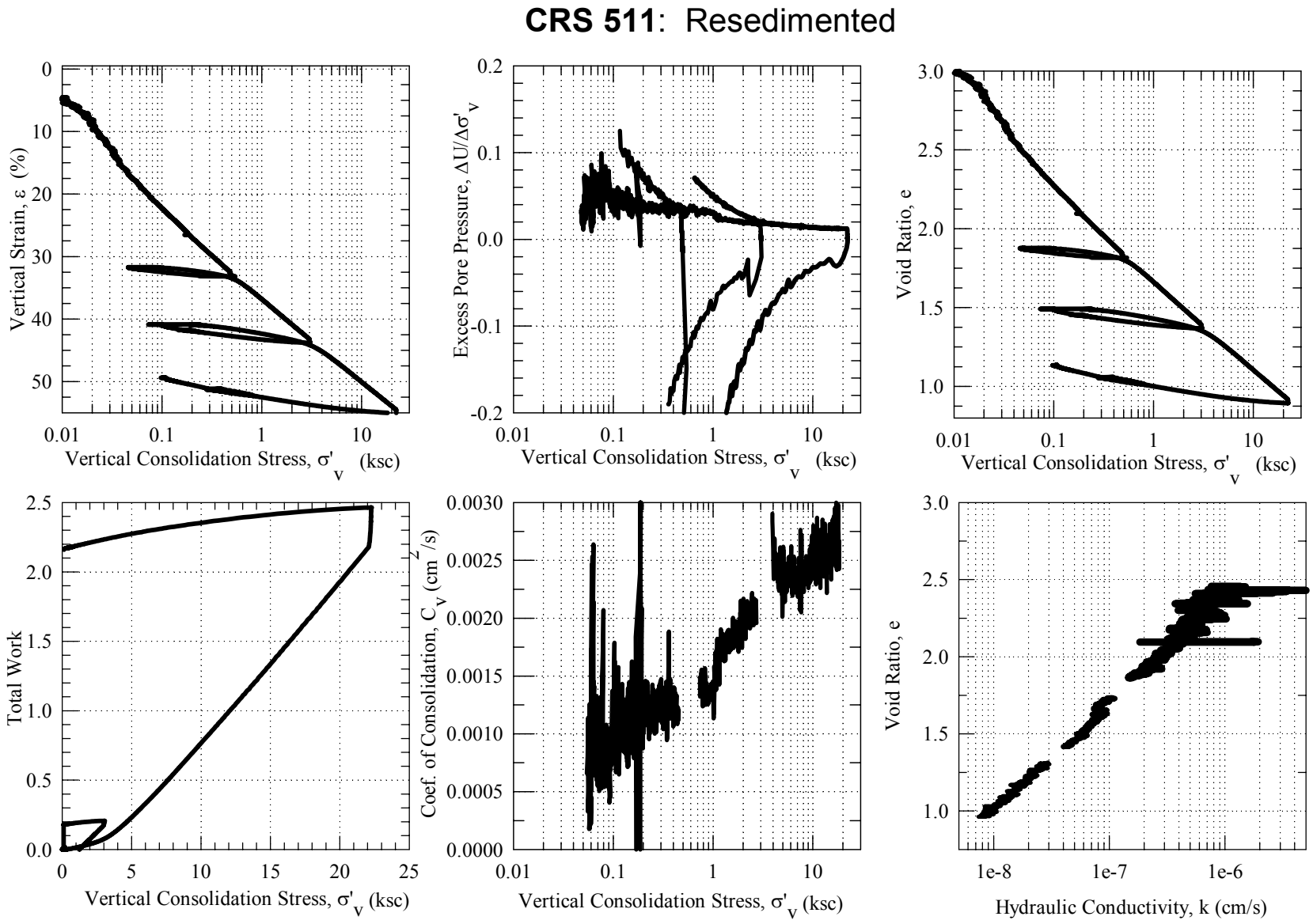

Figure 5.25: CRS 511

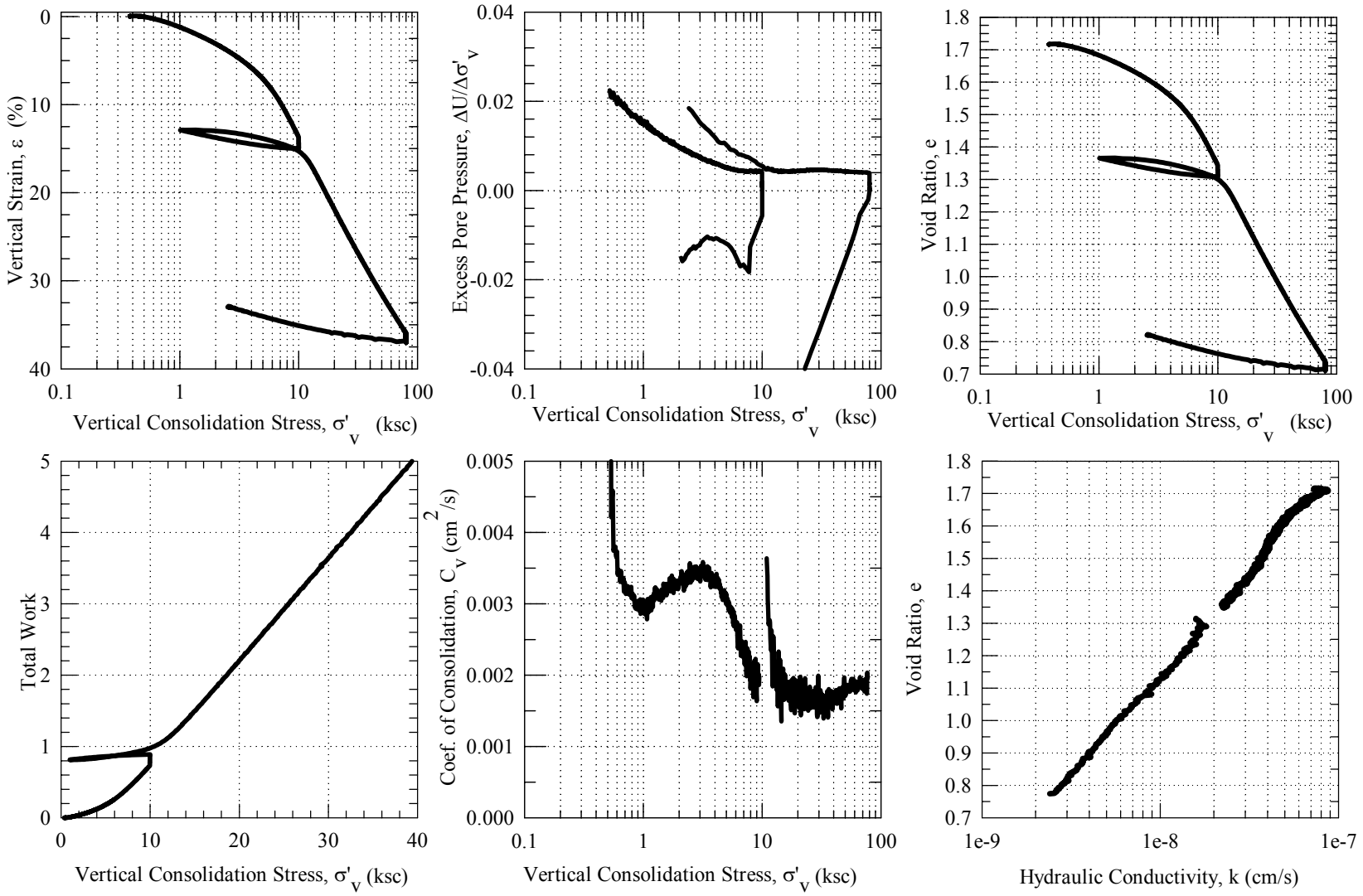

Figure 5.26: CRS 563

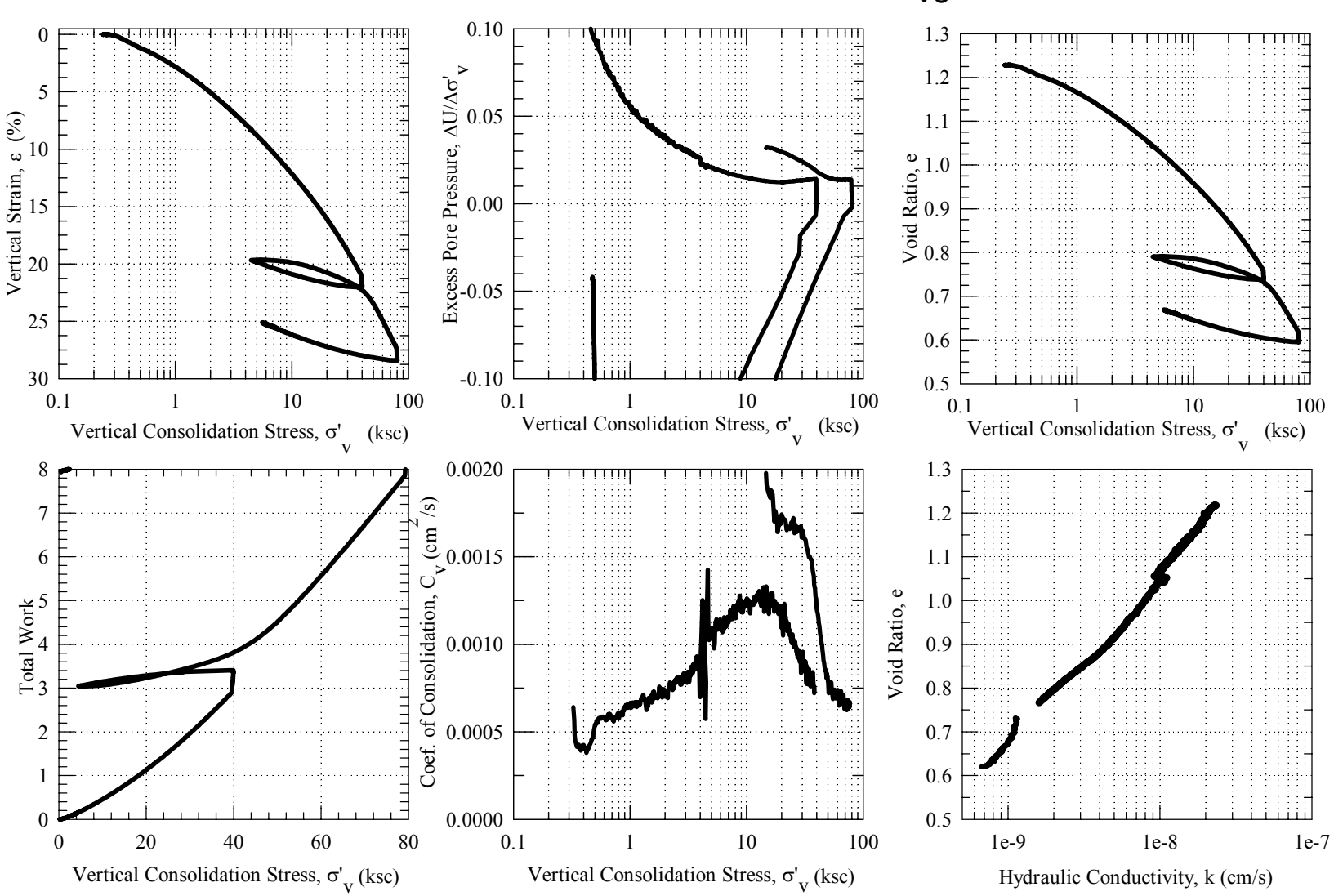

Figure 5.27: CRS 564

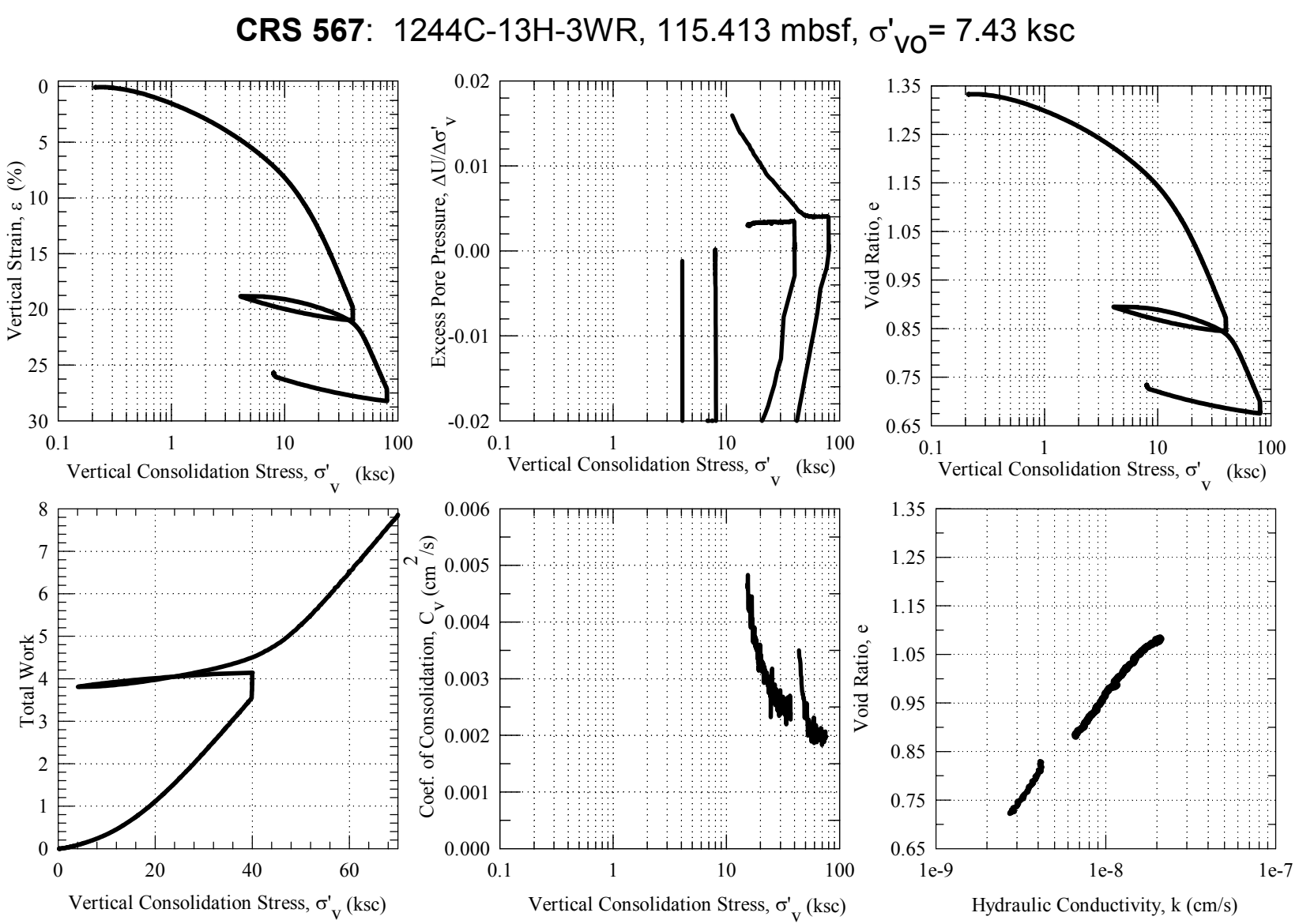

Figure 5.28: CRS 567

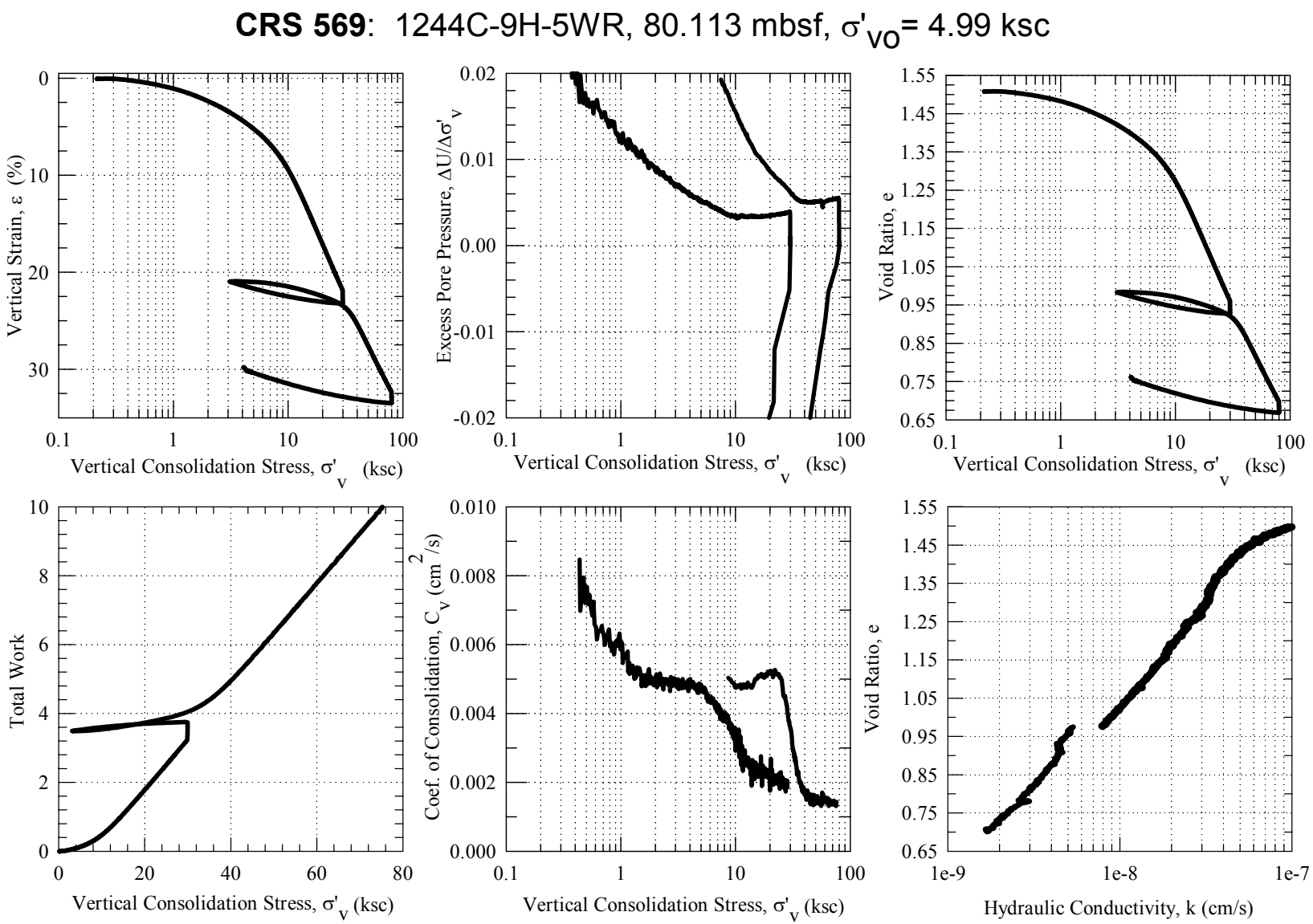

Figure 5.29: CRS 569

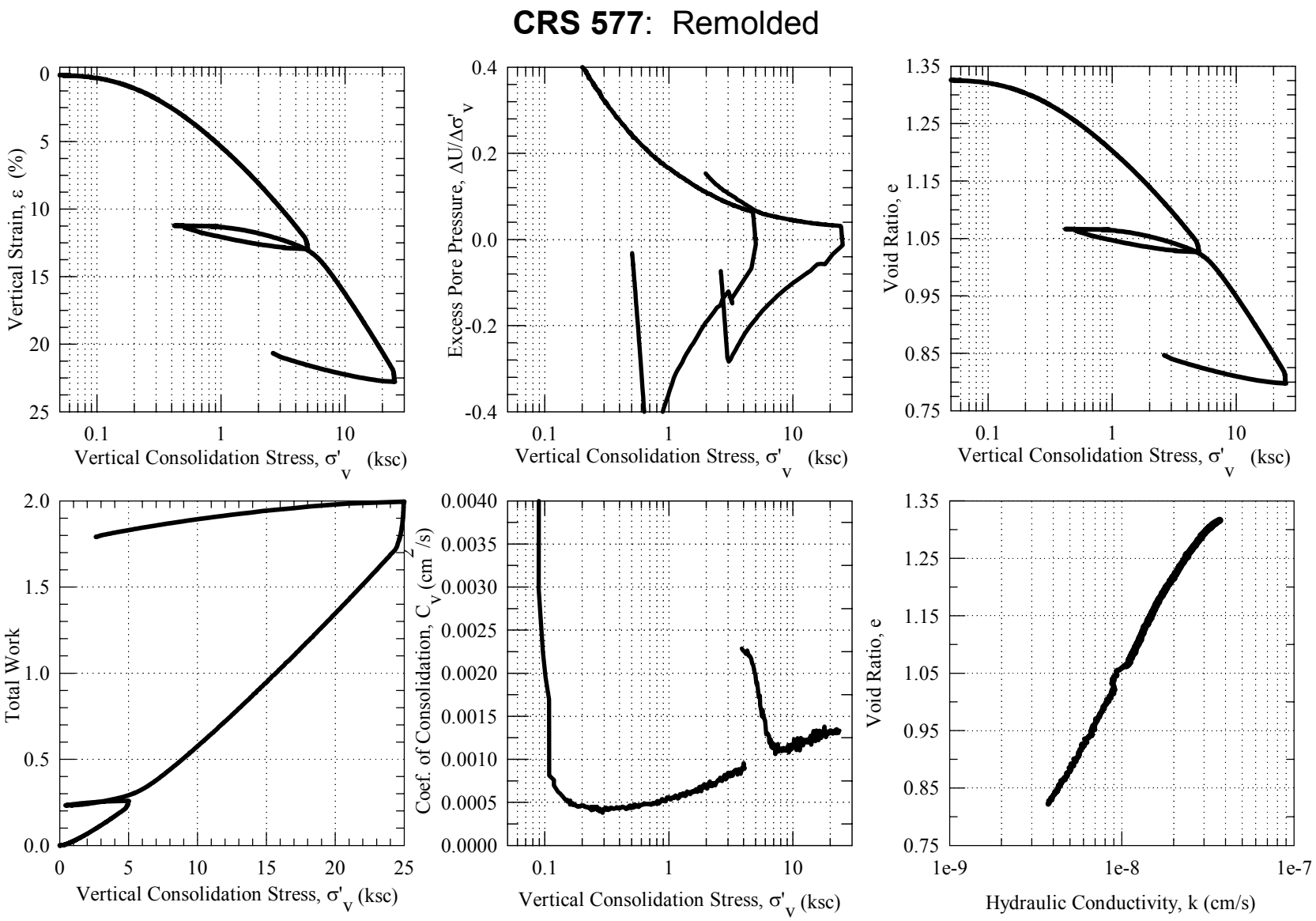

Figure 5.30: CRS 577

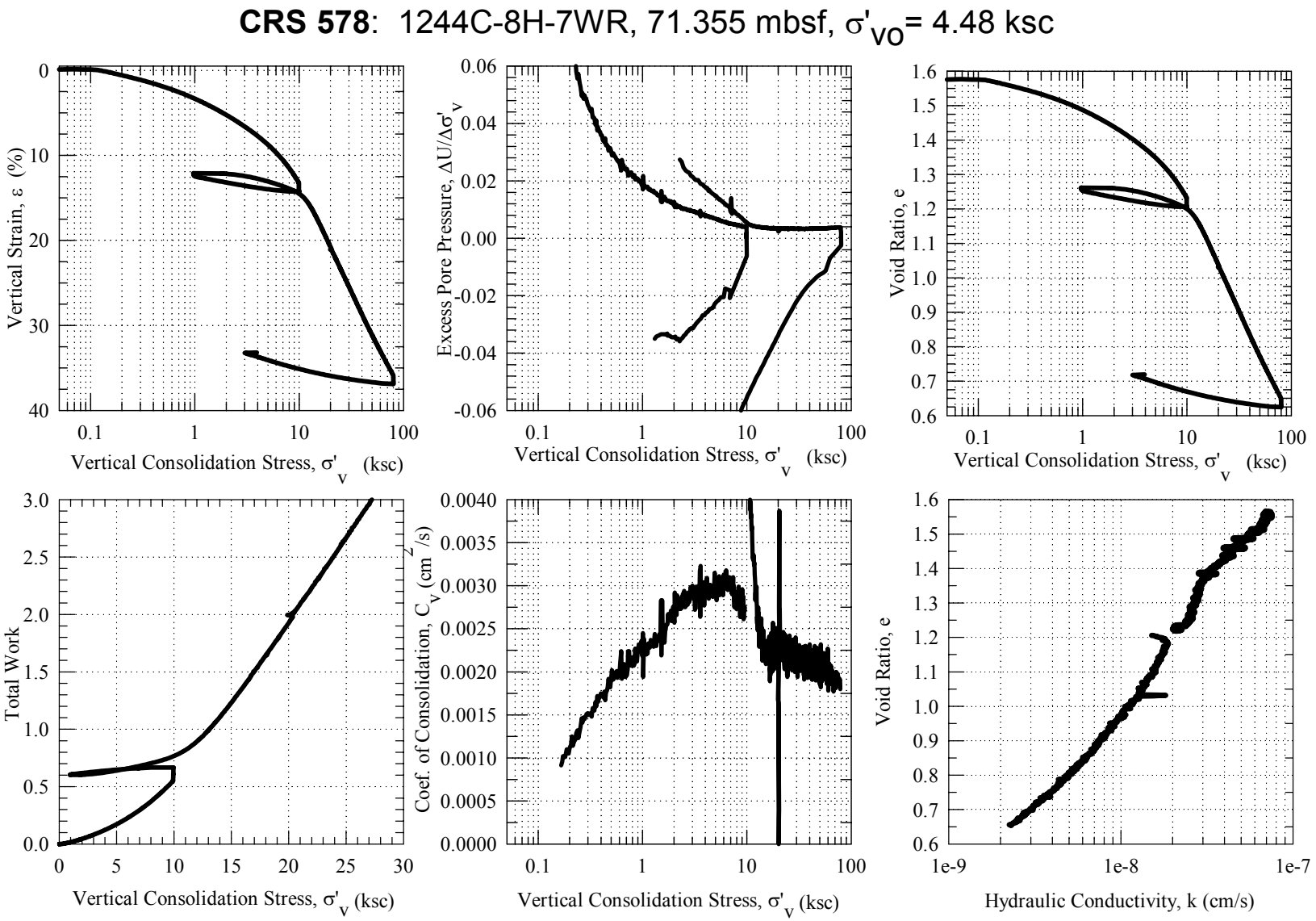

Figure 5.31: CRS 578

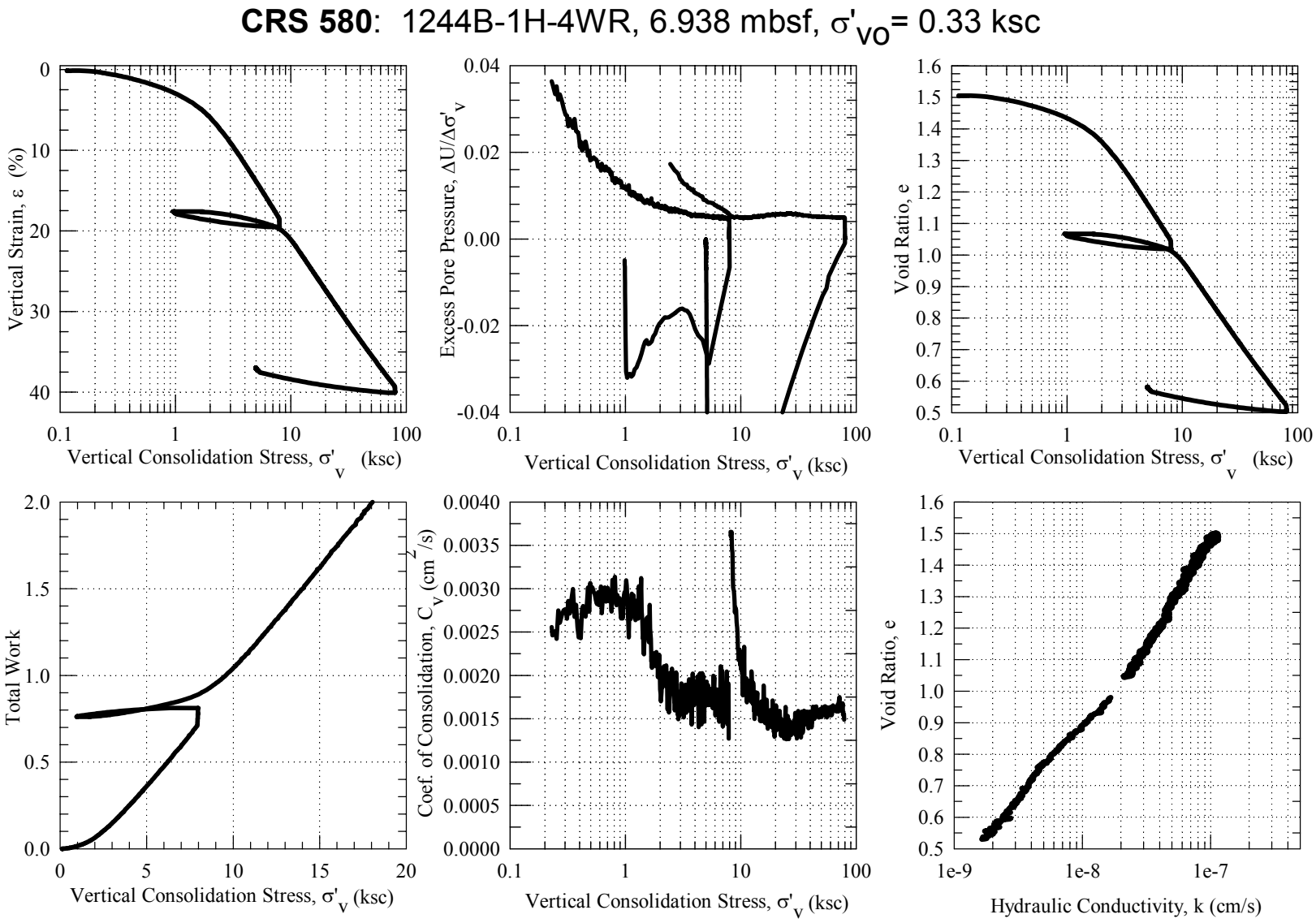

Figure 5.32: CRS 580

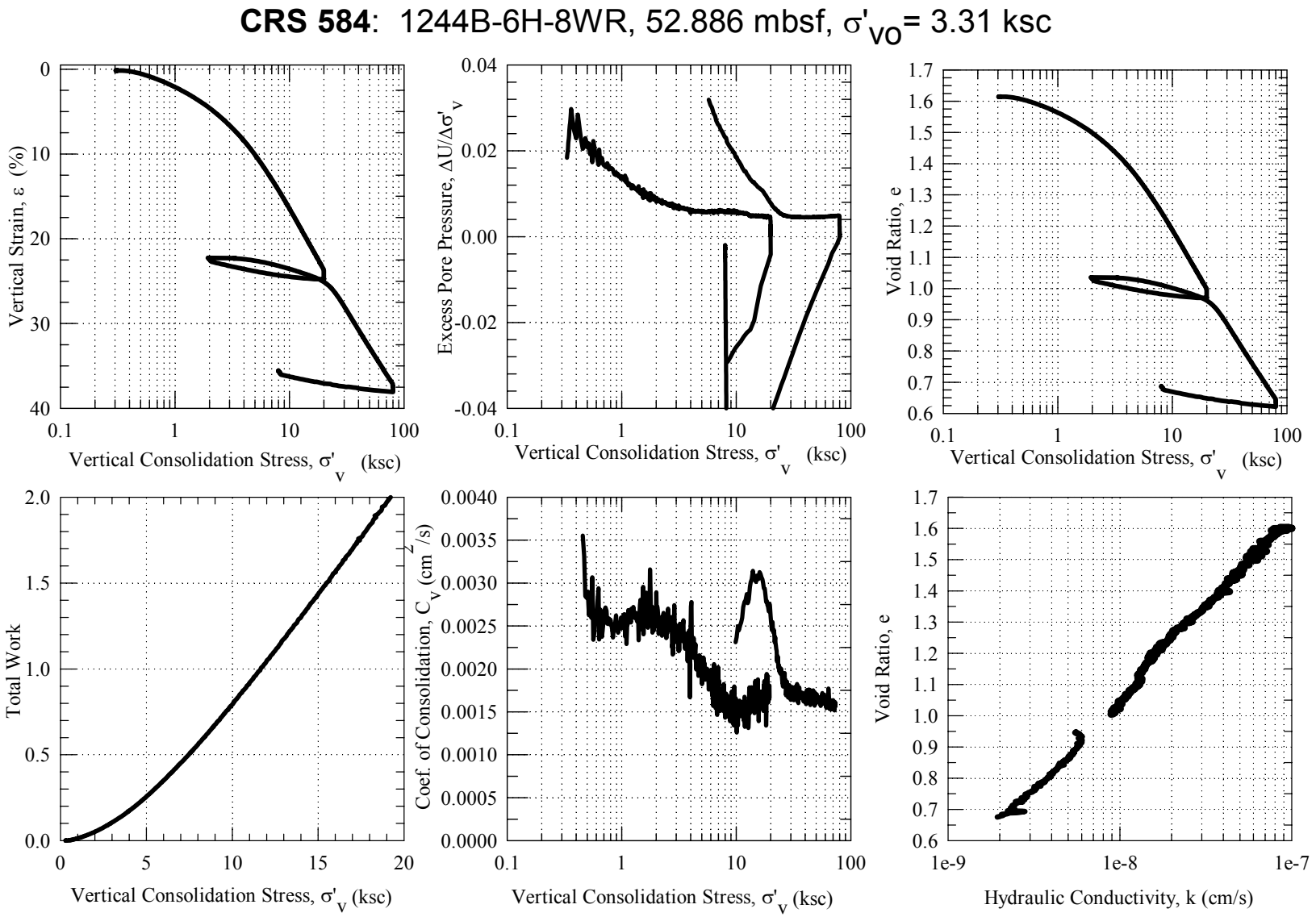

Figure 5.33: CRS 584

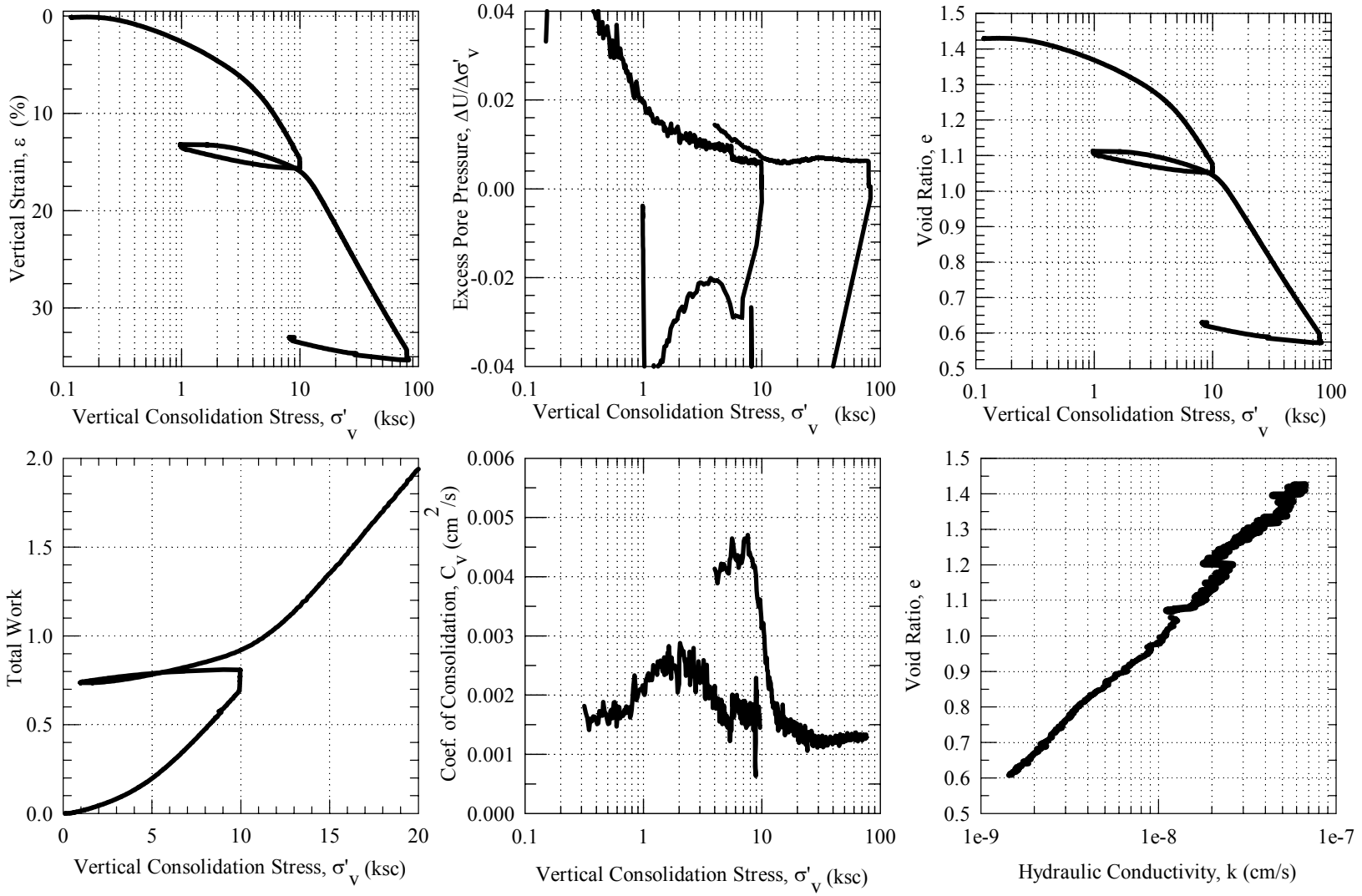

Figure 5.34: CRS 585

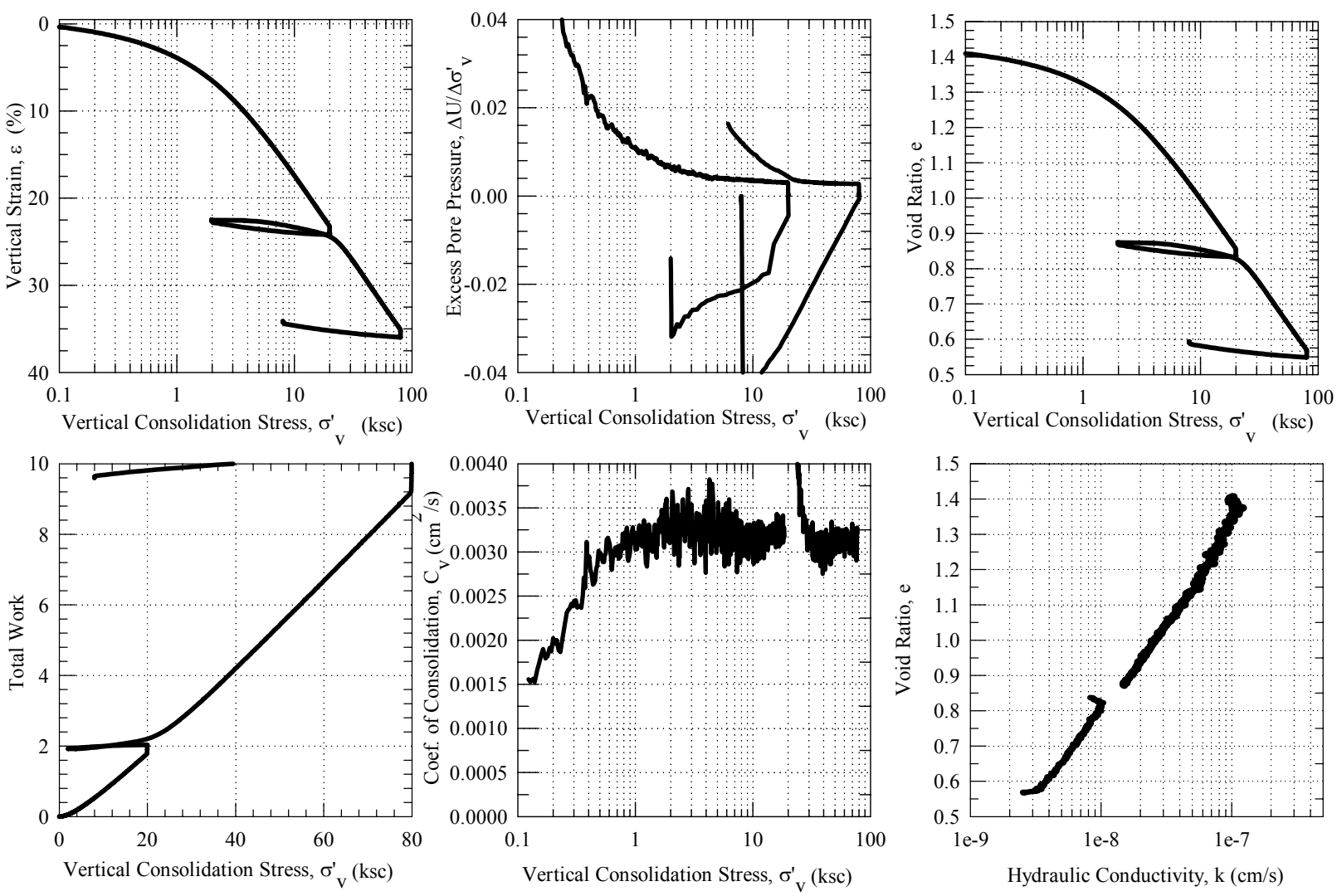

Figure 5.35: CRS 608

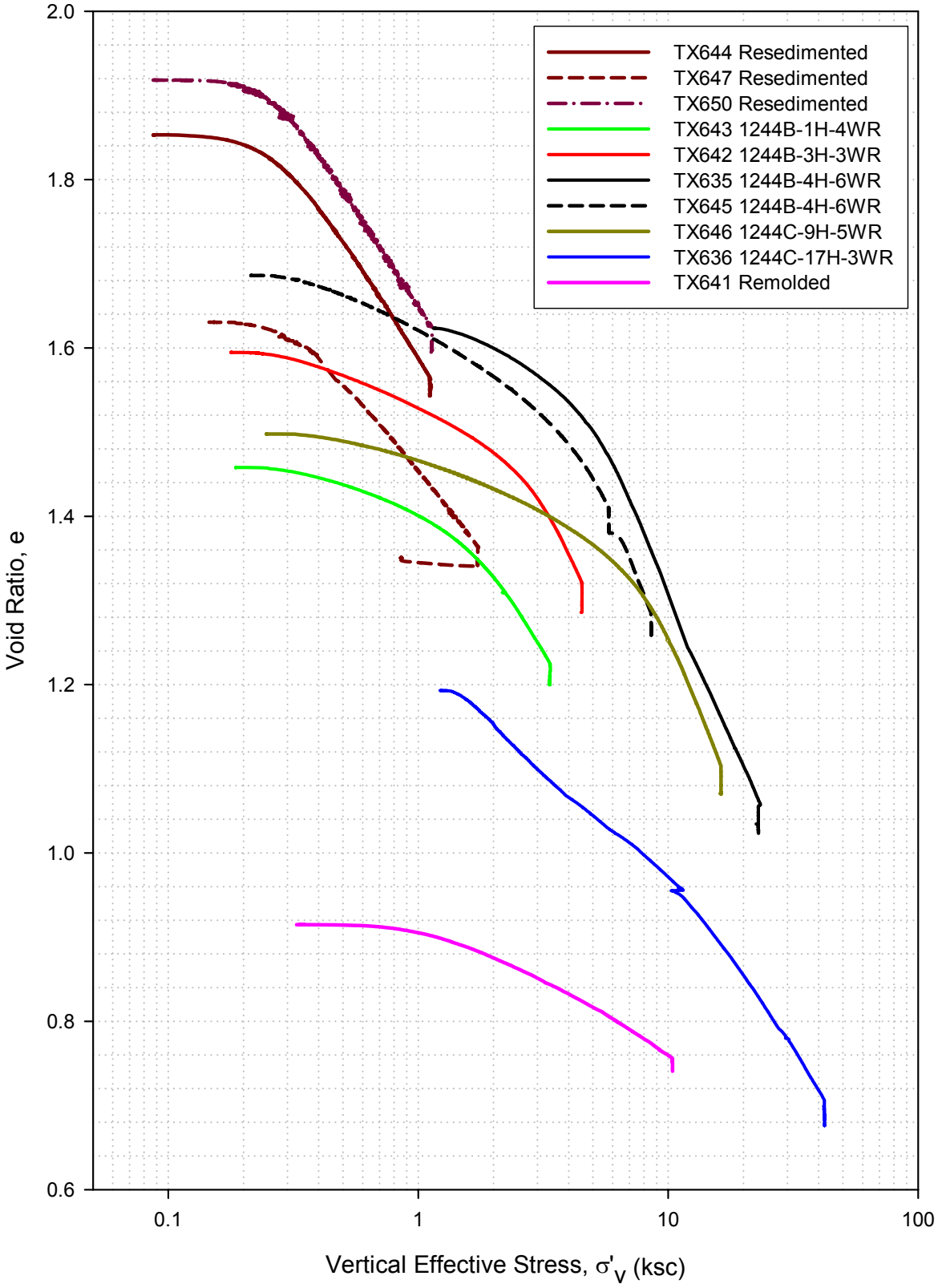

Figure 5.36: Summary of consolidation curves in e-logσ'_v space from CKoU tests

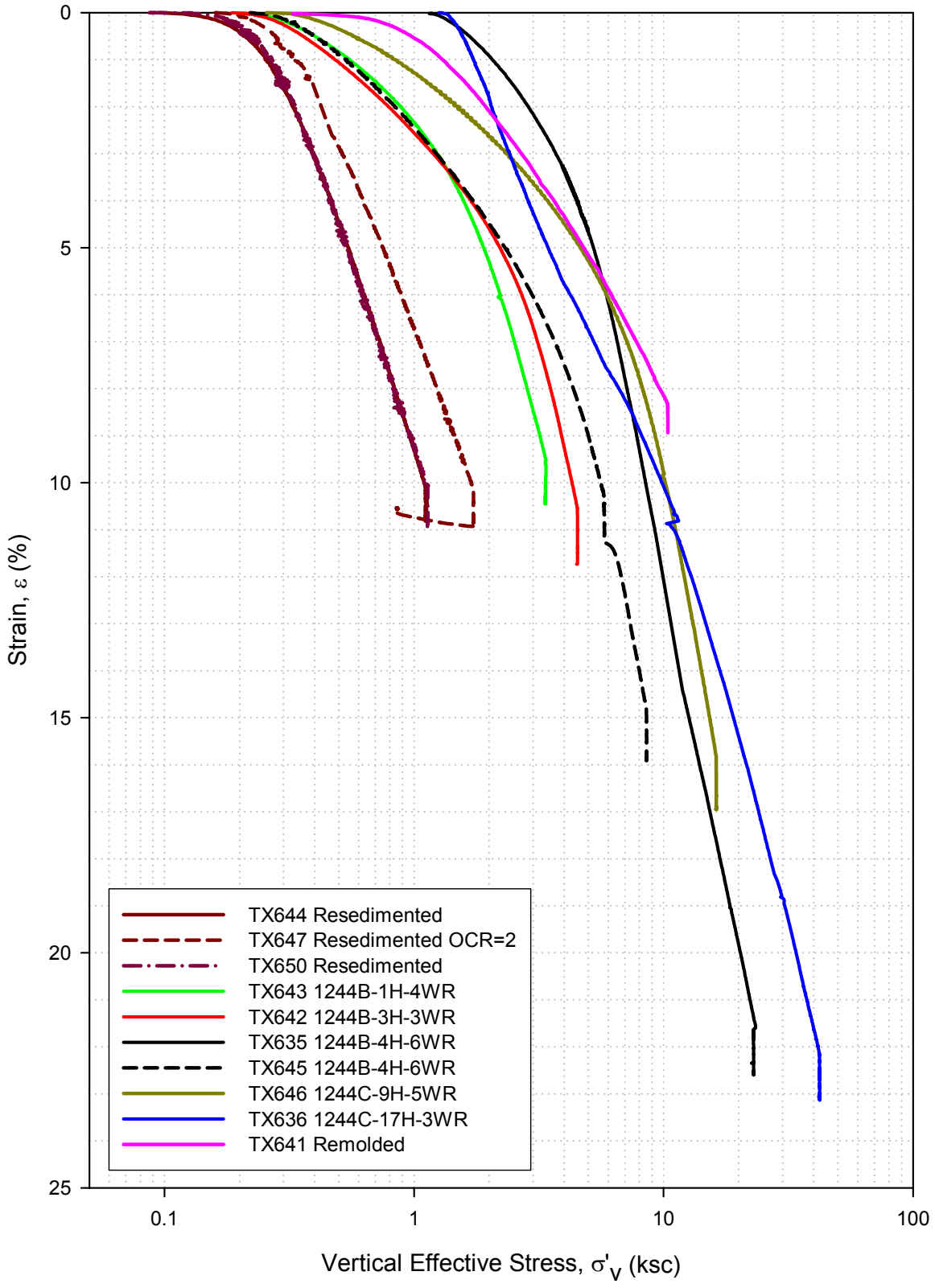

Figure 5.37: Summary of consolidation curves in ε-logσ'$_v$ space from CKoU tests

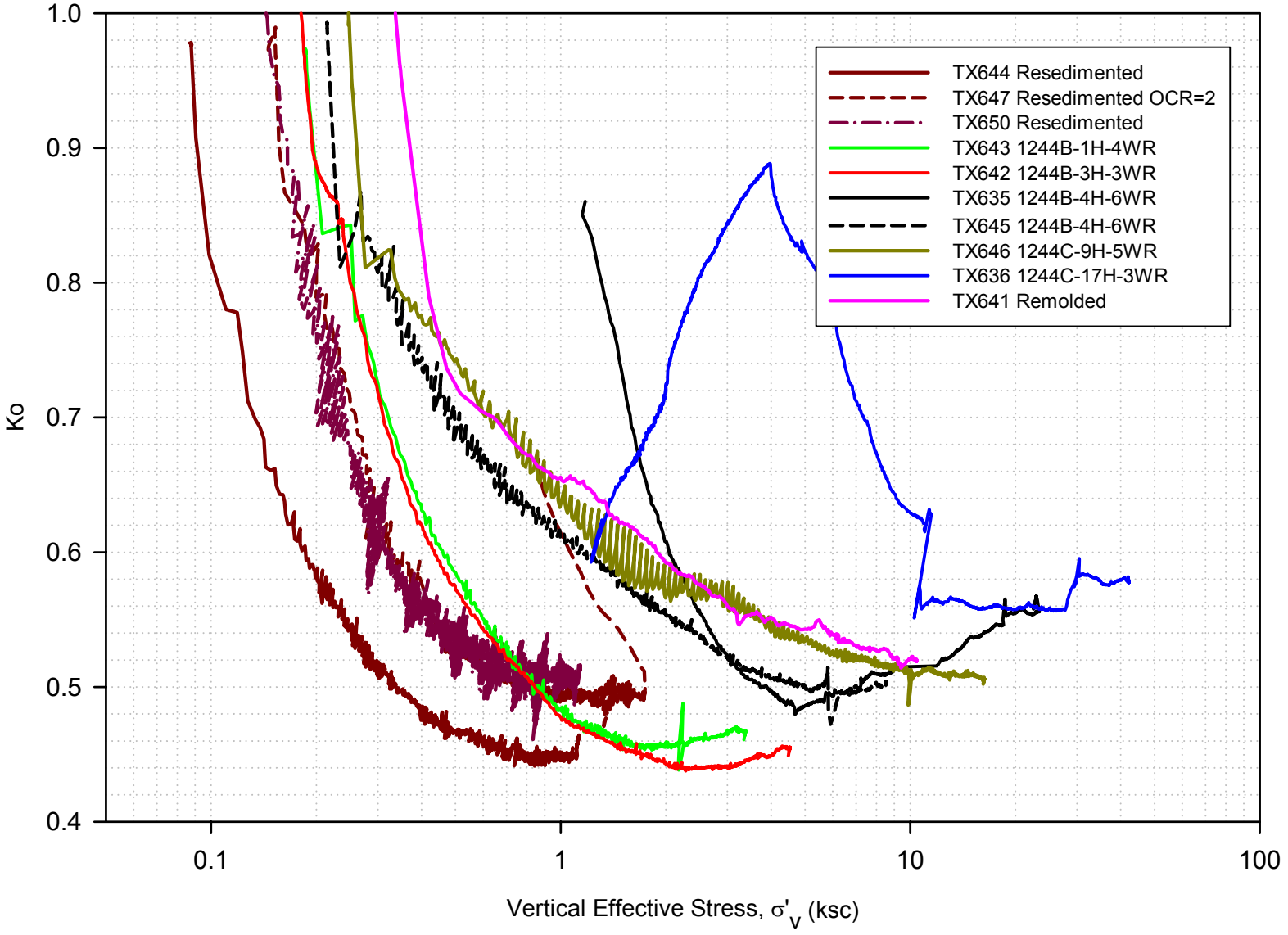

Figure 5.38: Summary of lateral stress ratio curves from CKoU tests

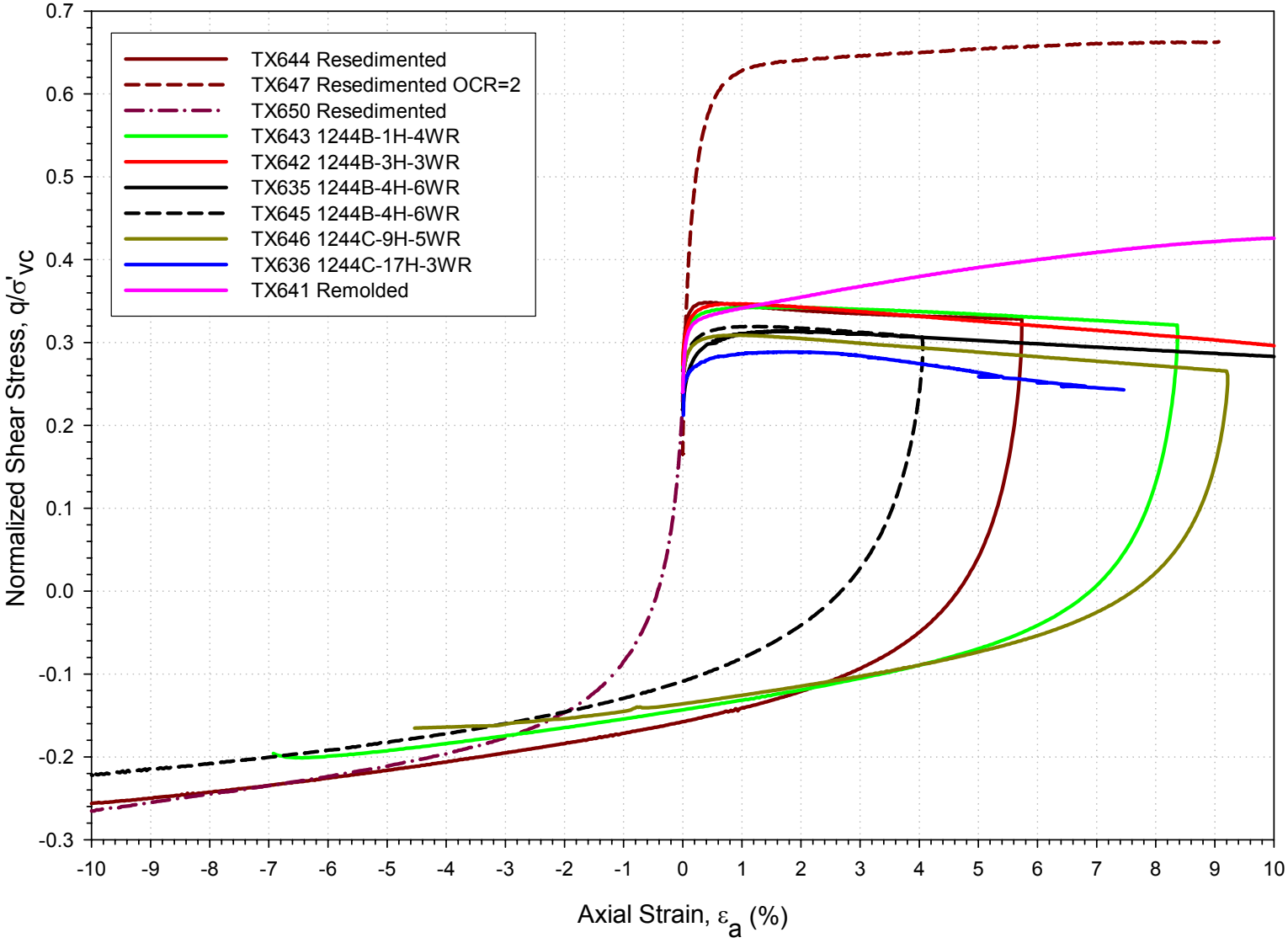

Figure 5.39: Summary of shear stress vs. strain curves from CKoU tests

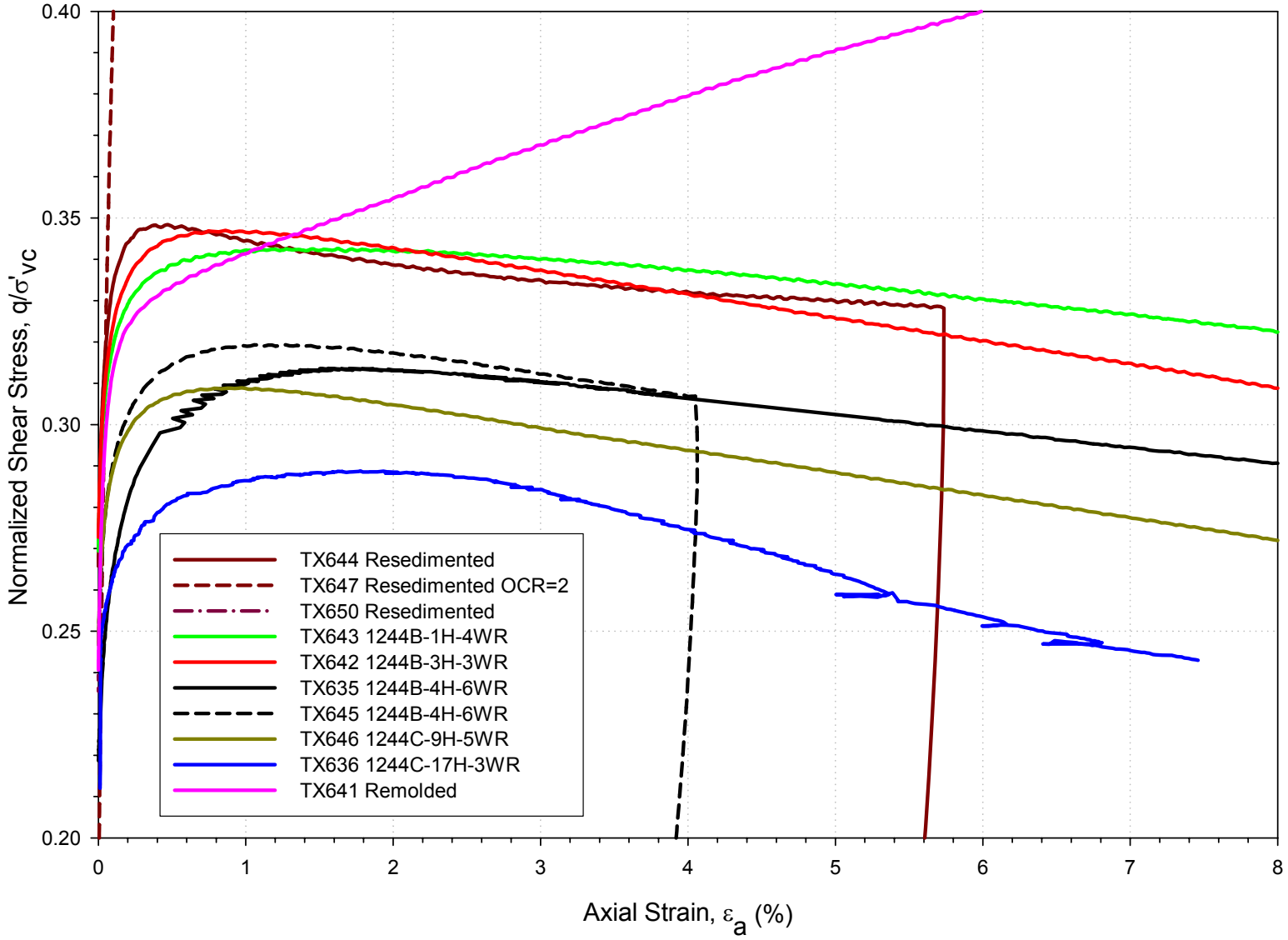

Figure 5.40: Summary of shear stress vs. strain curves from CKoU tests (compression only)

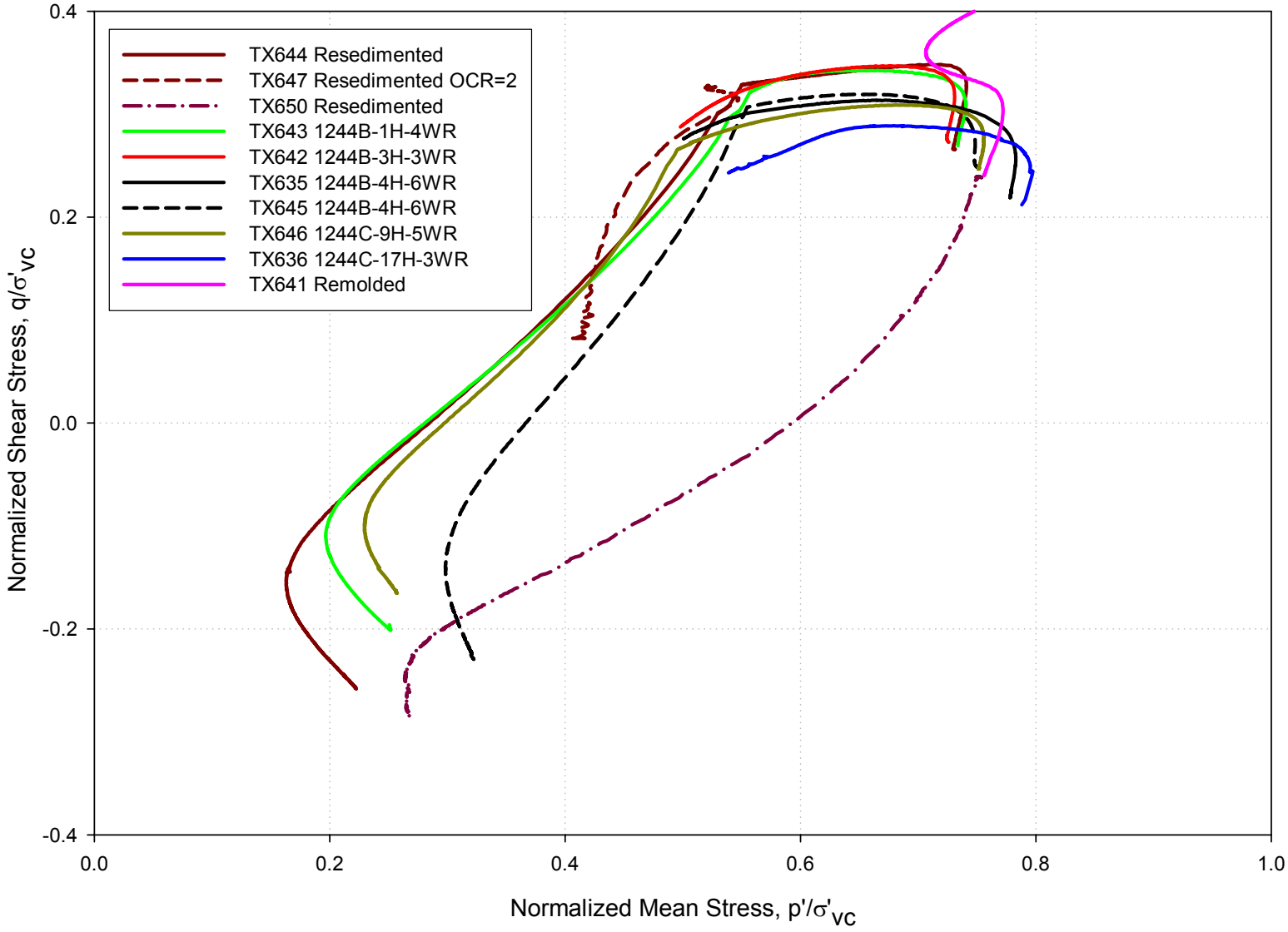

Figure 5.41: Summary of stress path plots from CKoU tests

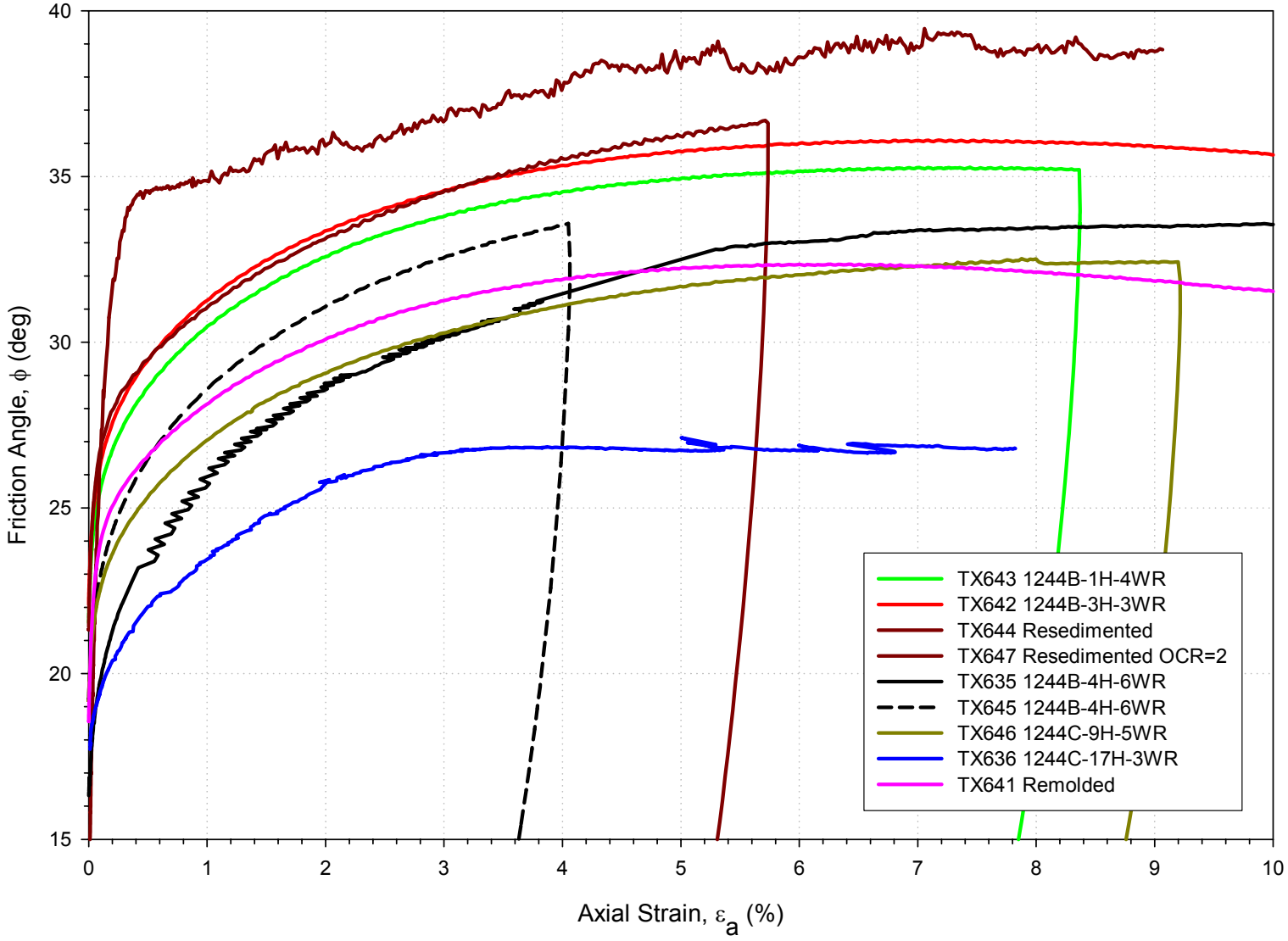

Figure 5.42: Summary of friction angle vs. strain curves from CKoU tests

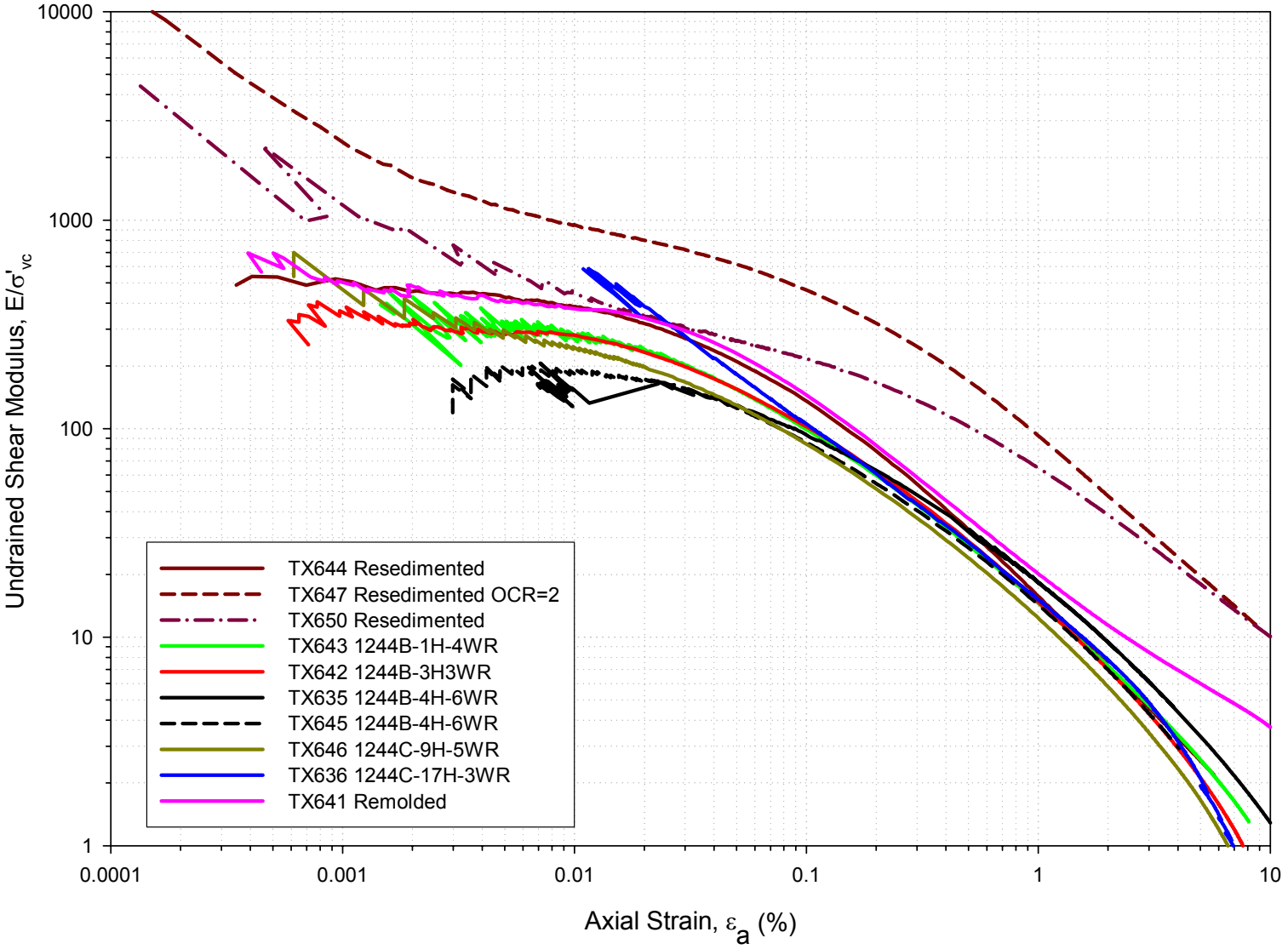

Figure 5.43: Summary of secant modulus vs. strain curves from CKoU tests

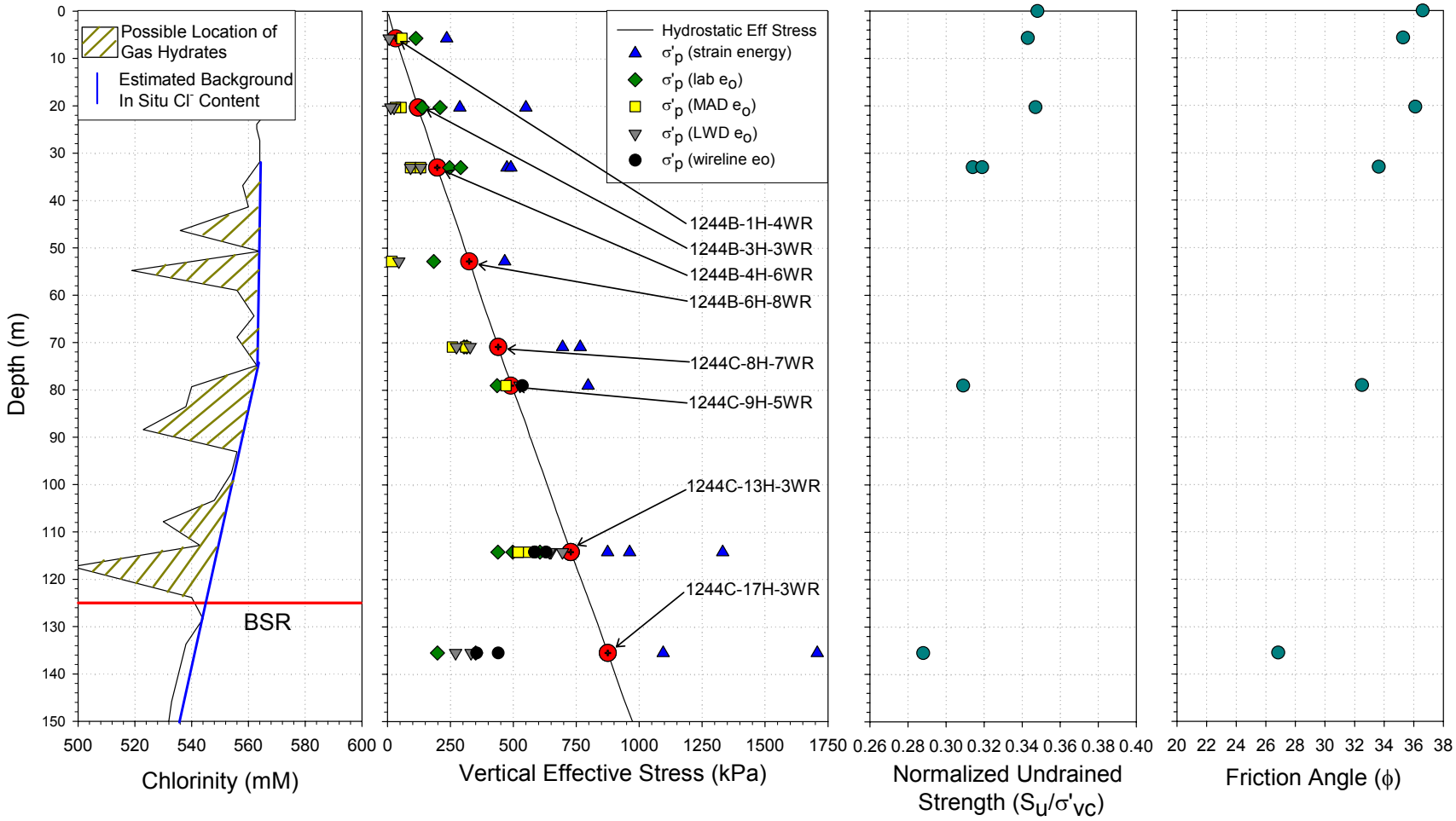

Figure 5.44: Undrained strength and friction angle profile

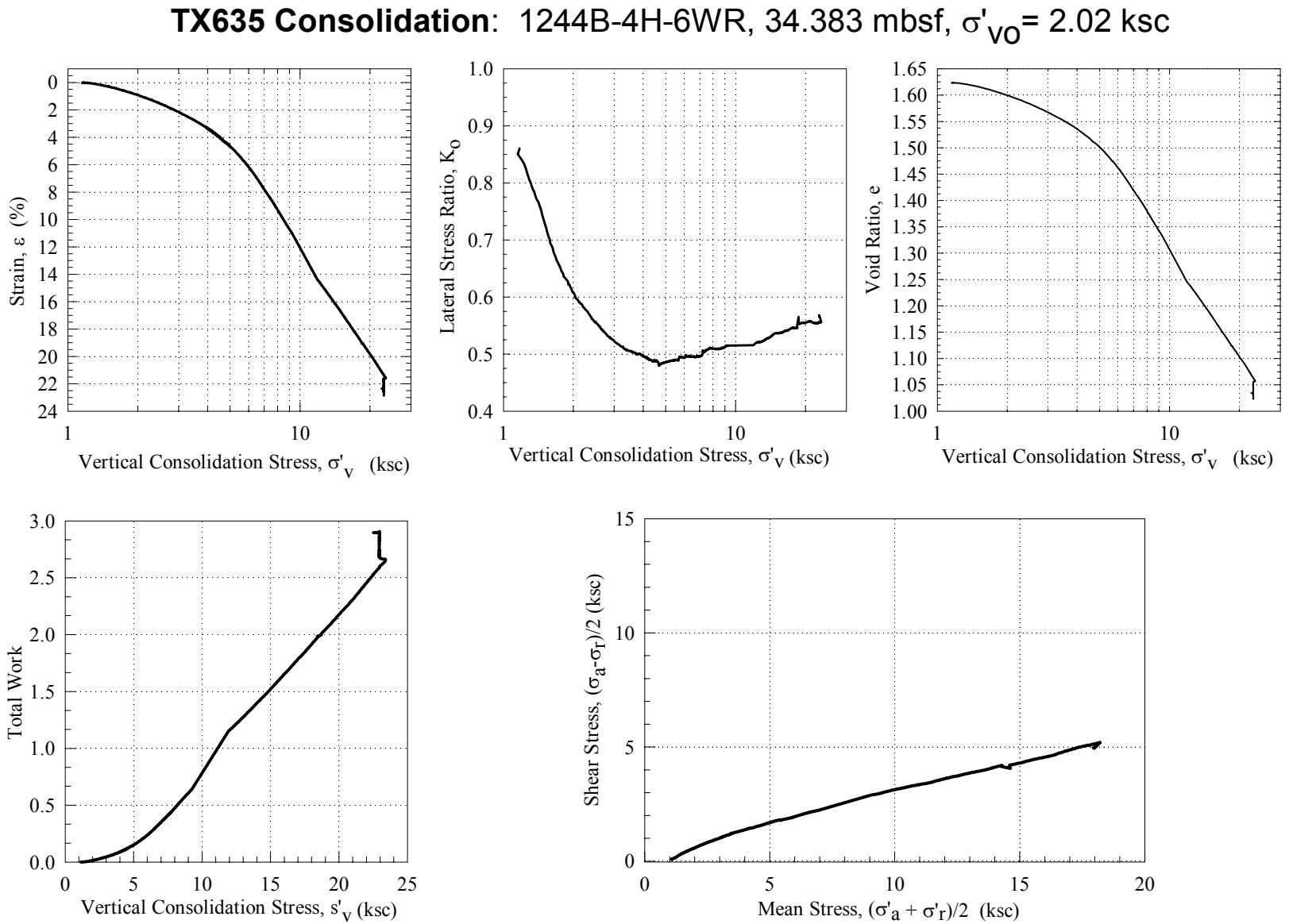

Figure 5.45: TX 635 Consolidation

TX635 Undrained Shear: 1244B-4H-6WR, 34.383 mbsf, σ'_{vo}= 2.02 ksc

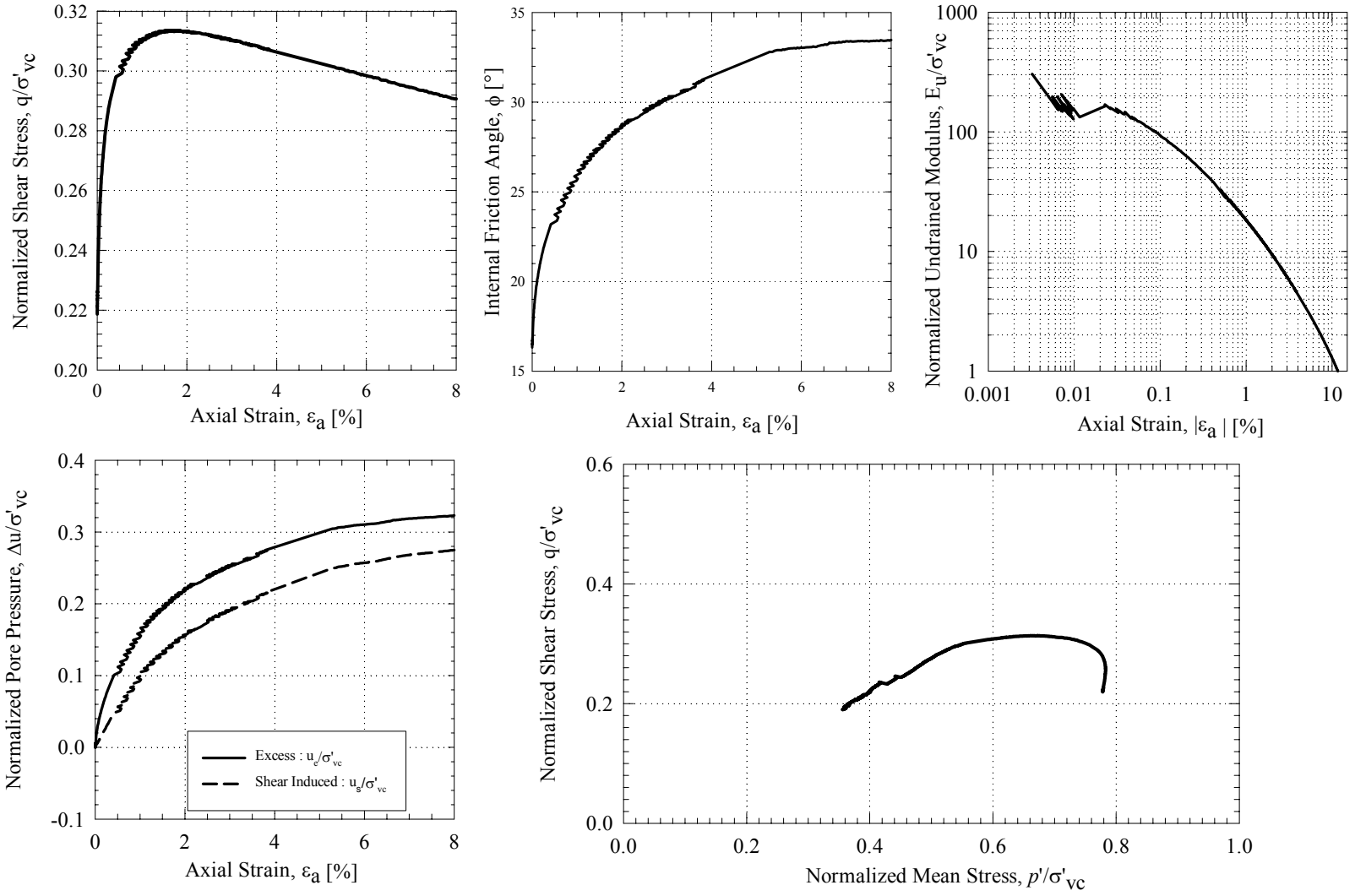

Figure 5.46: TX 635 Undrained Shear

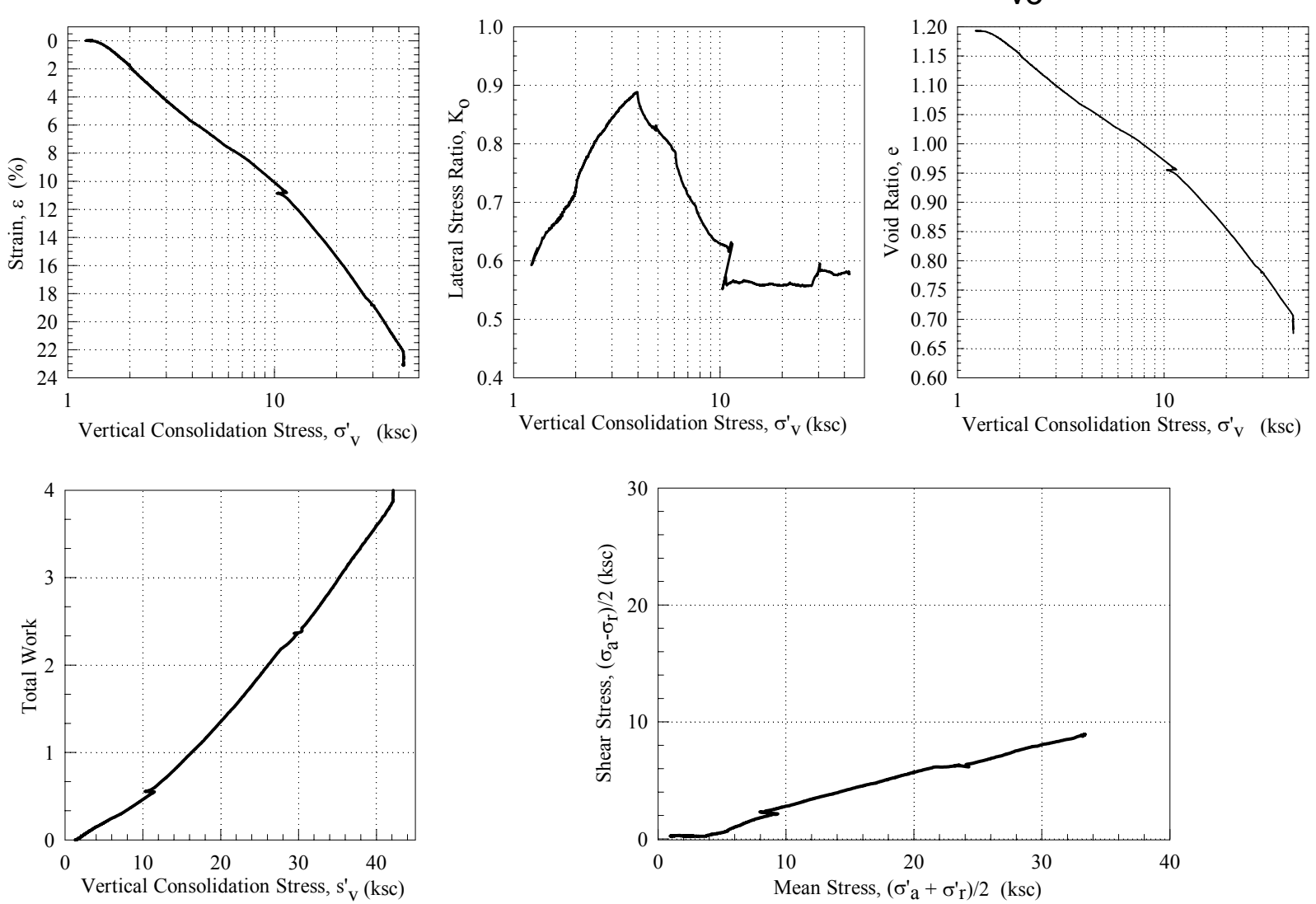

Figure 5.47: TX 636 Consolidation

TX636 Undrained Shear: 1244C-17H-3WR, 136.403 mbsf, σ'_{vo}= 8.92 ksc

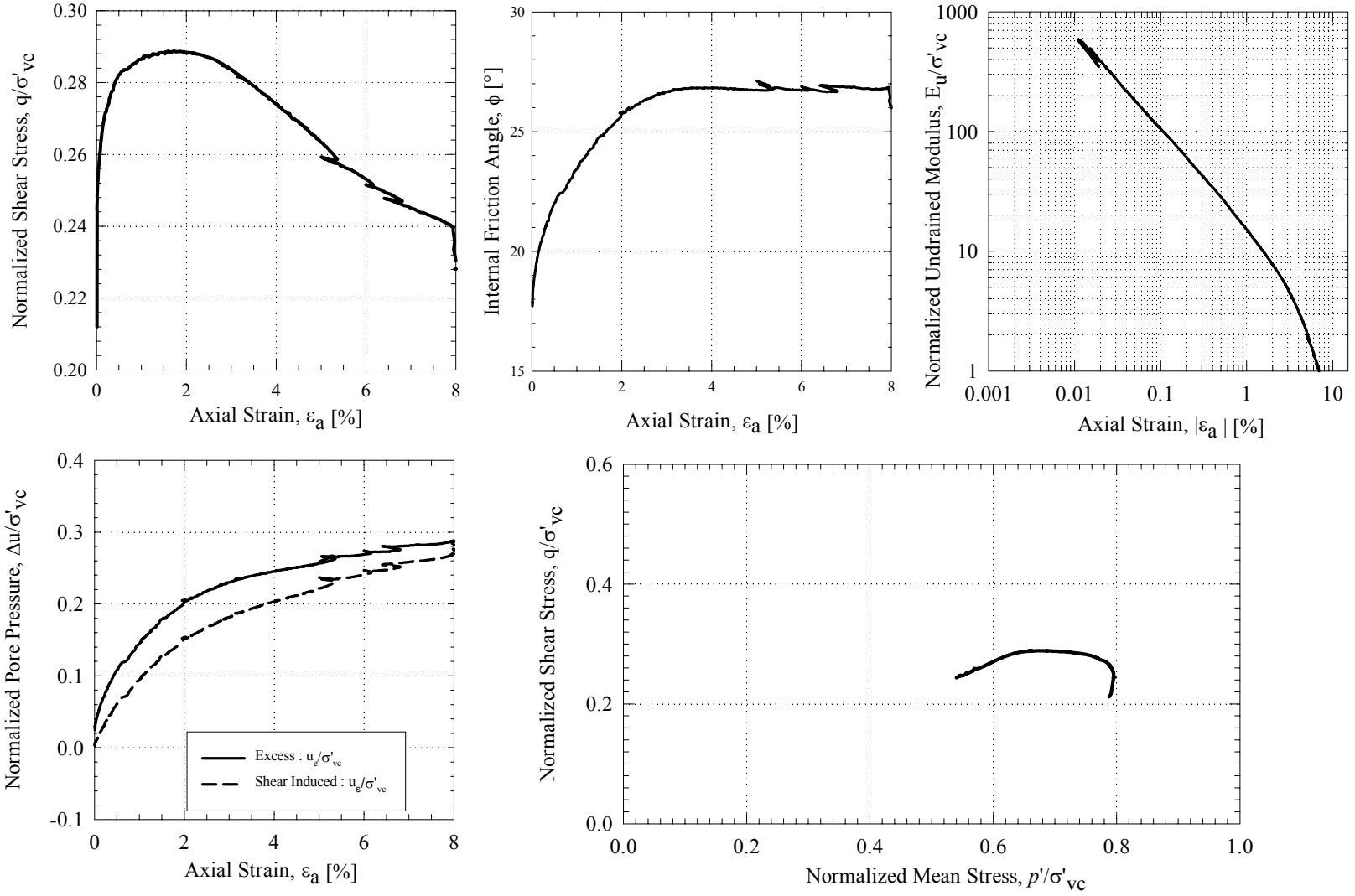

Figure 5.48: TX 636 Undrained Shear

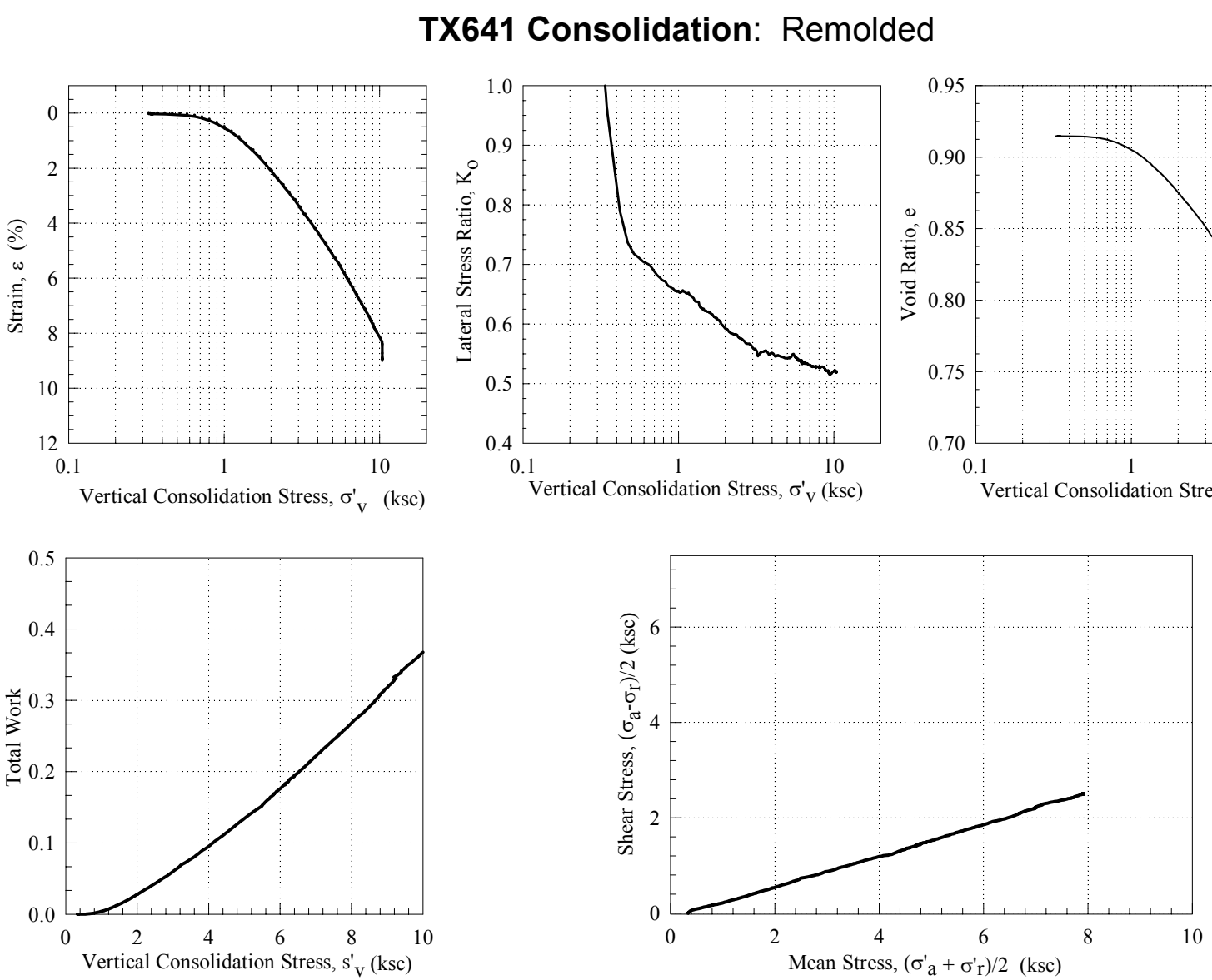

Figure 5.49: TX 641 Consolidation

TX641 Undrained Shear: Remolded

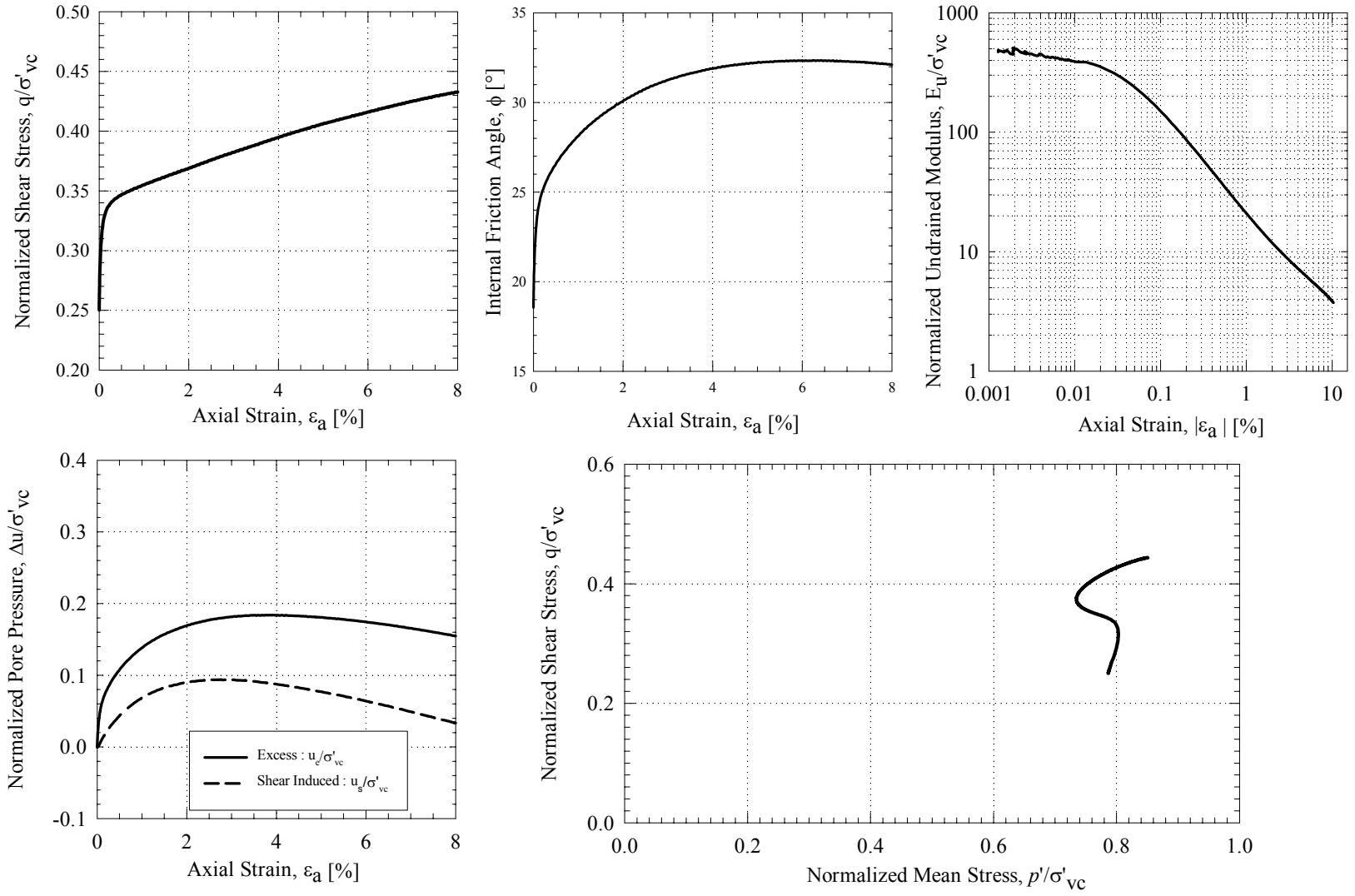

Figure 5.50: TX 641 Undrained Shear

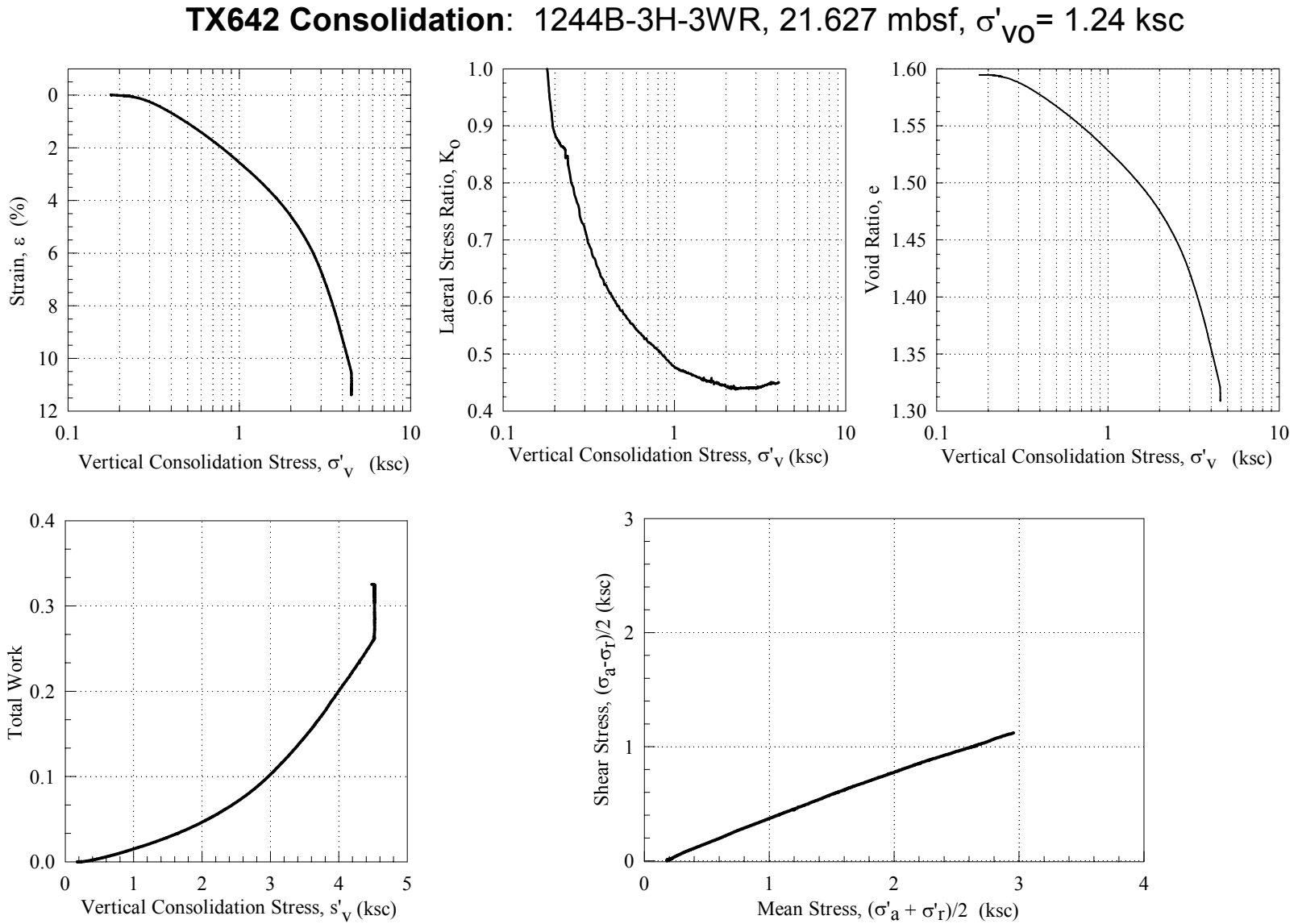

Figure 5.51: TX 642 Consolidation

TX642 Undrained Shear: 1244B-3H-3WR, 21.627 mbsf, σ'_{vo}= 1.24 ksc

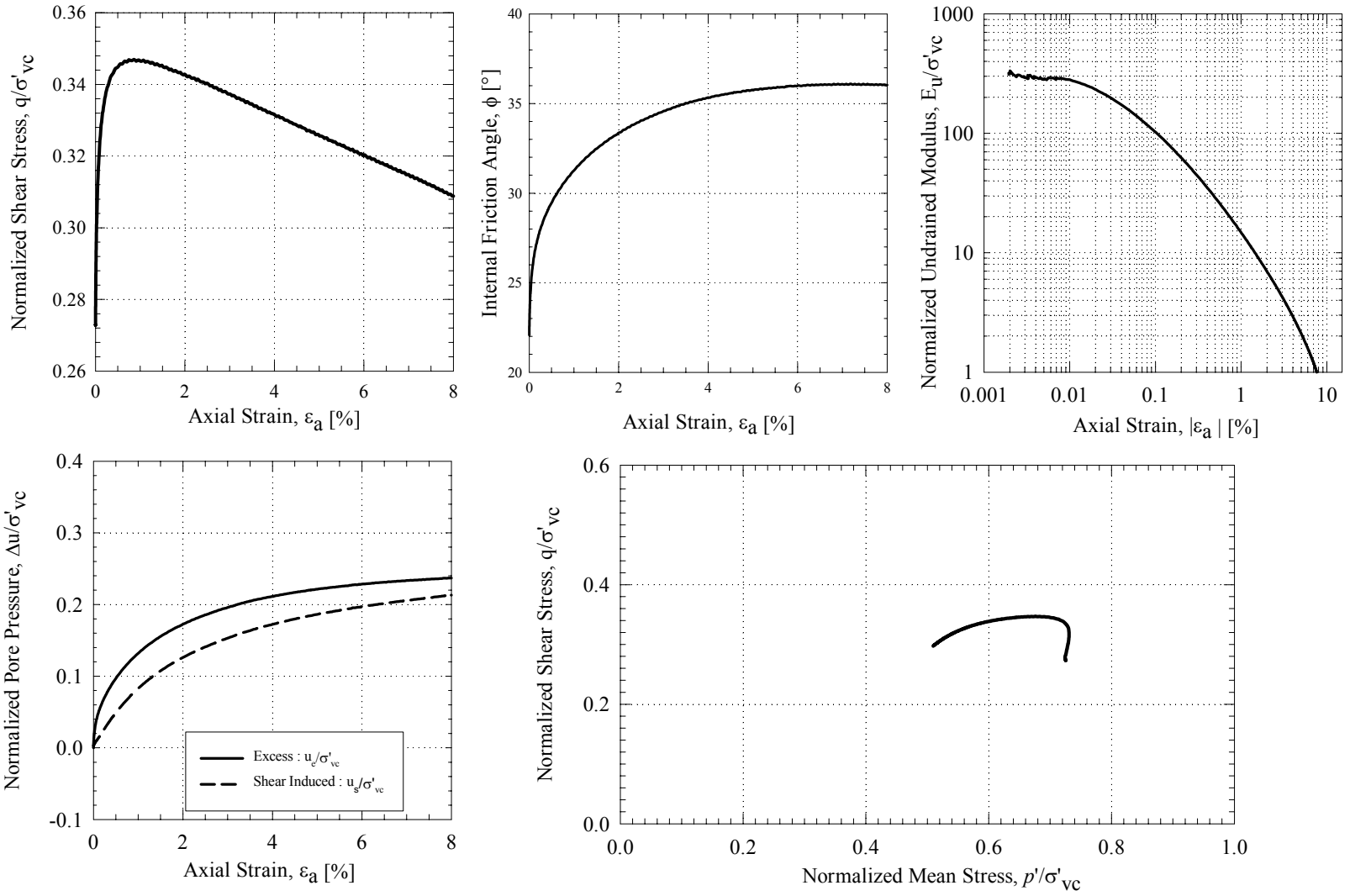

Figure 5.52: TX 642 Undrained Shear

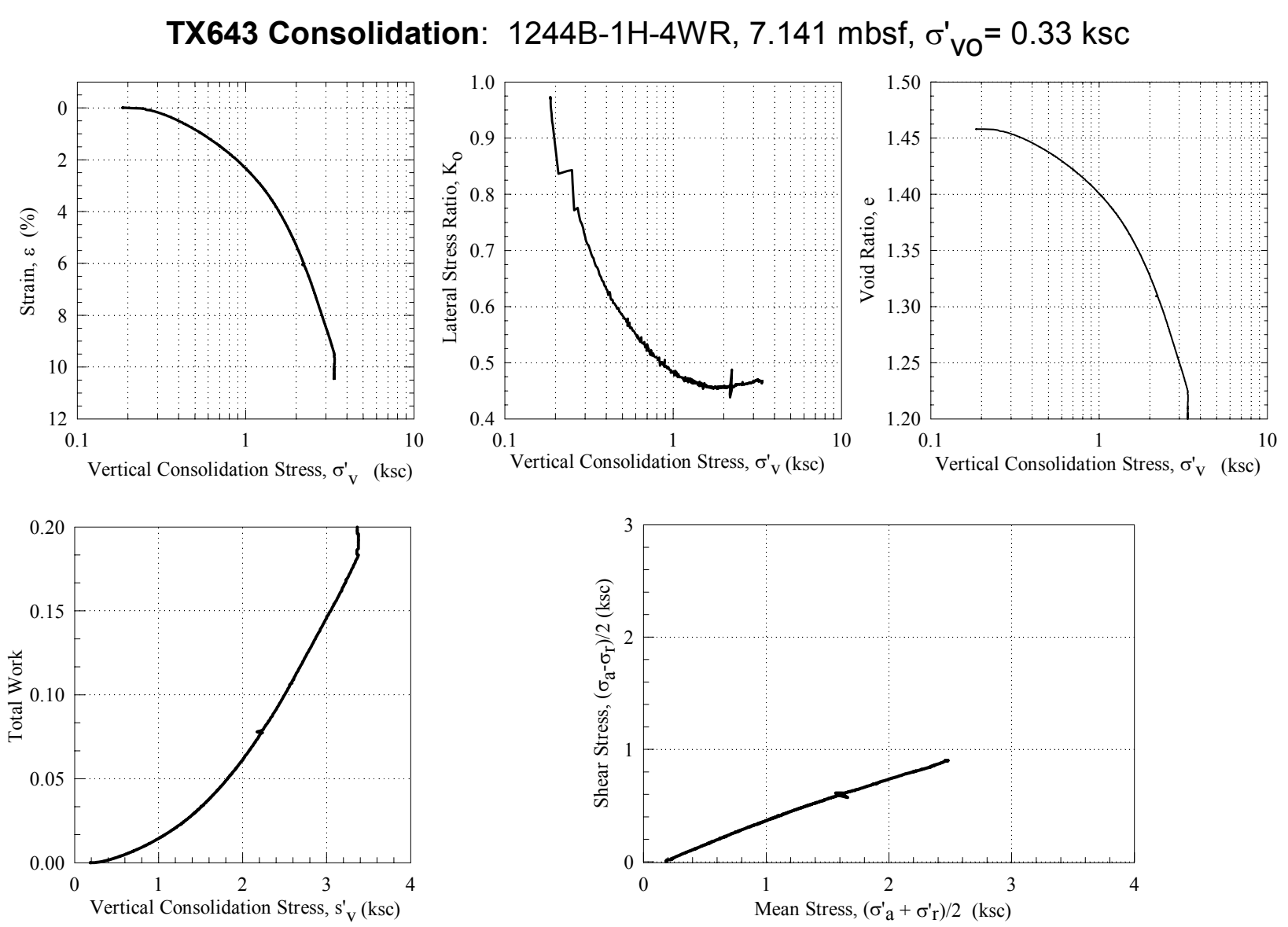

Figure 5.53: TX 643 Consolidation

TX643 Undrained Shear: 1244B-1H-4WR, 7.141 mbsf, σ'_{vo}= 0.33 ksc

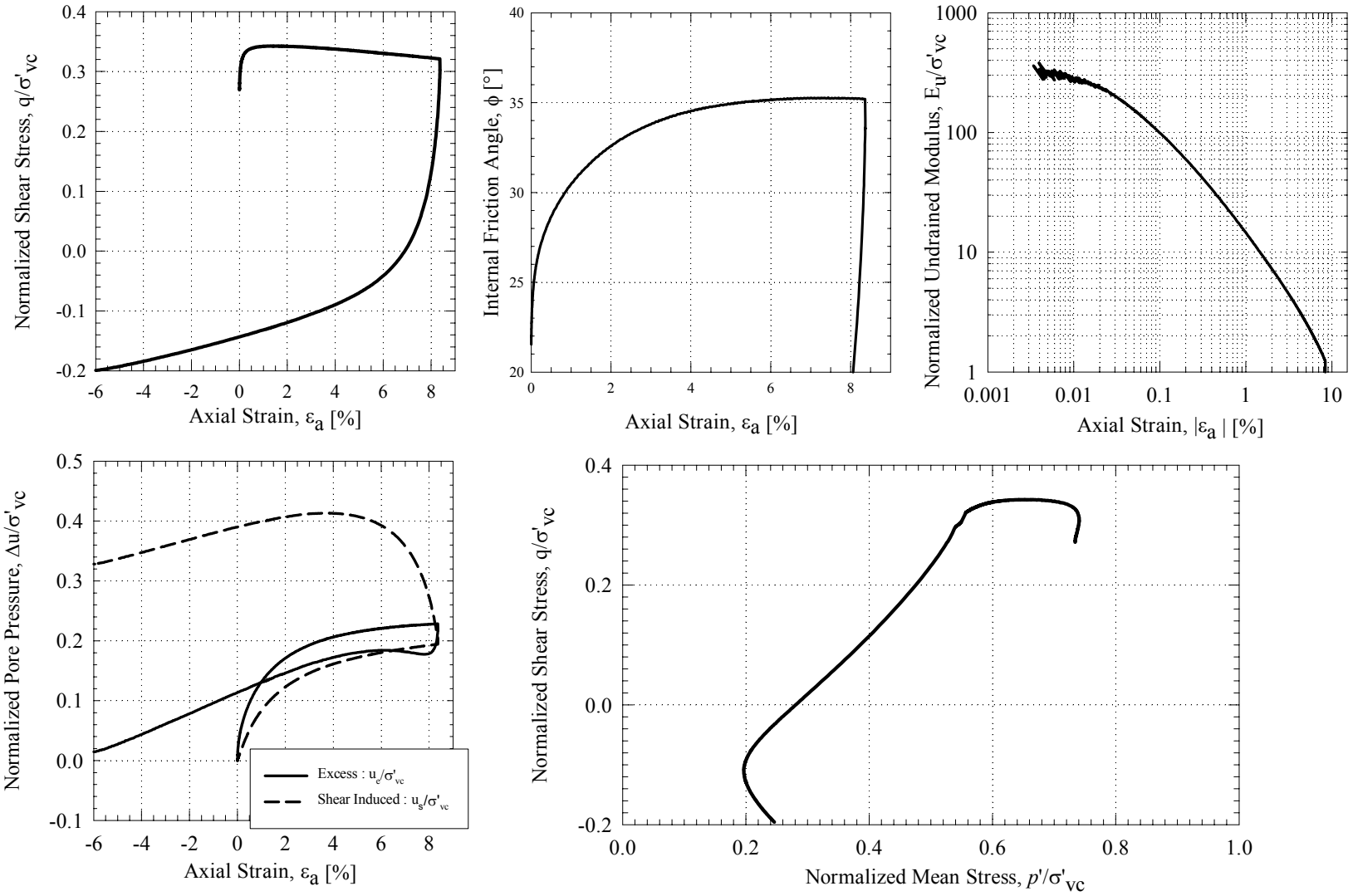

Figure 5.54: TX 643 Undrained Shear

TX644 Consolidation: Resedimented

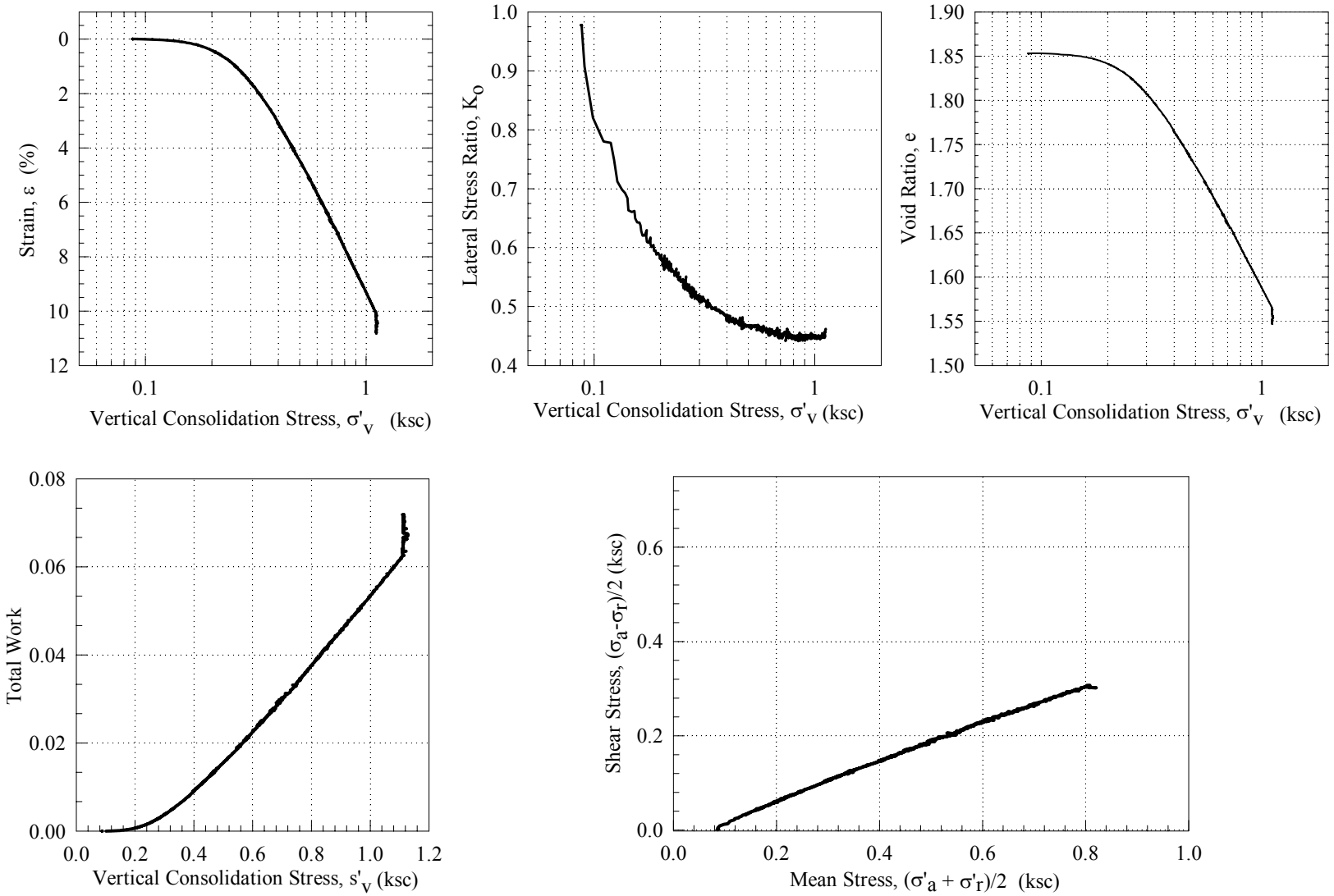

Figure 5.55: TX 644 Consolidation

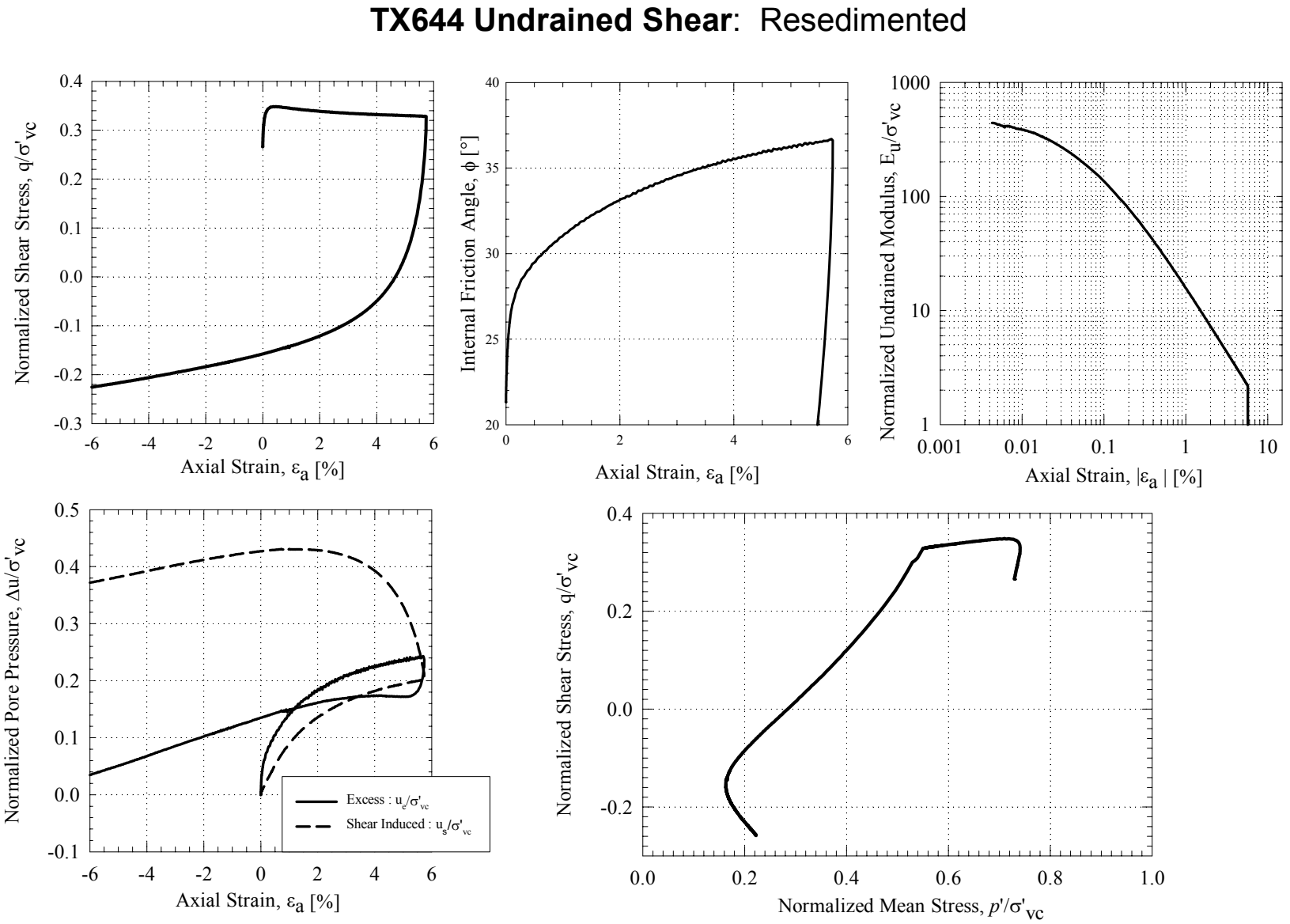

Figure 5.56: TX 644 Undrained Shear

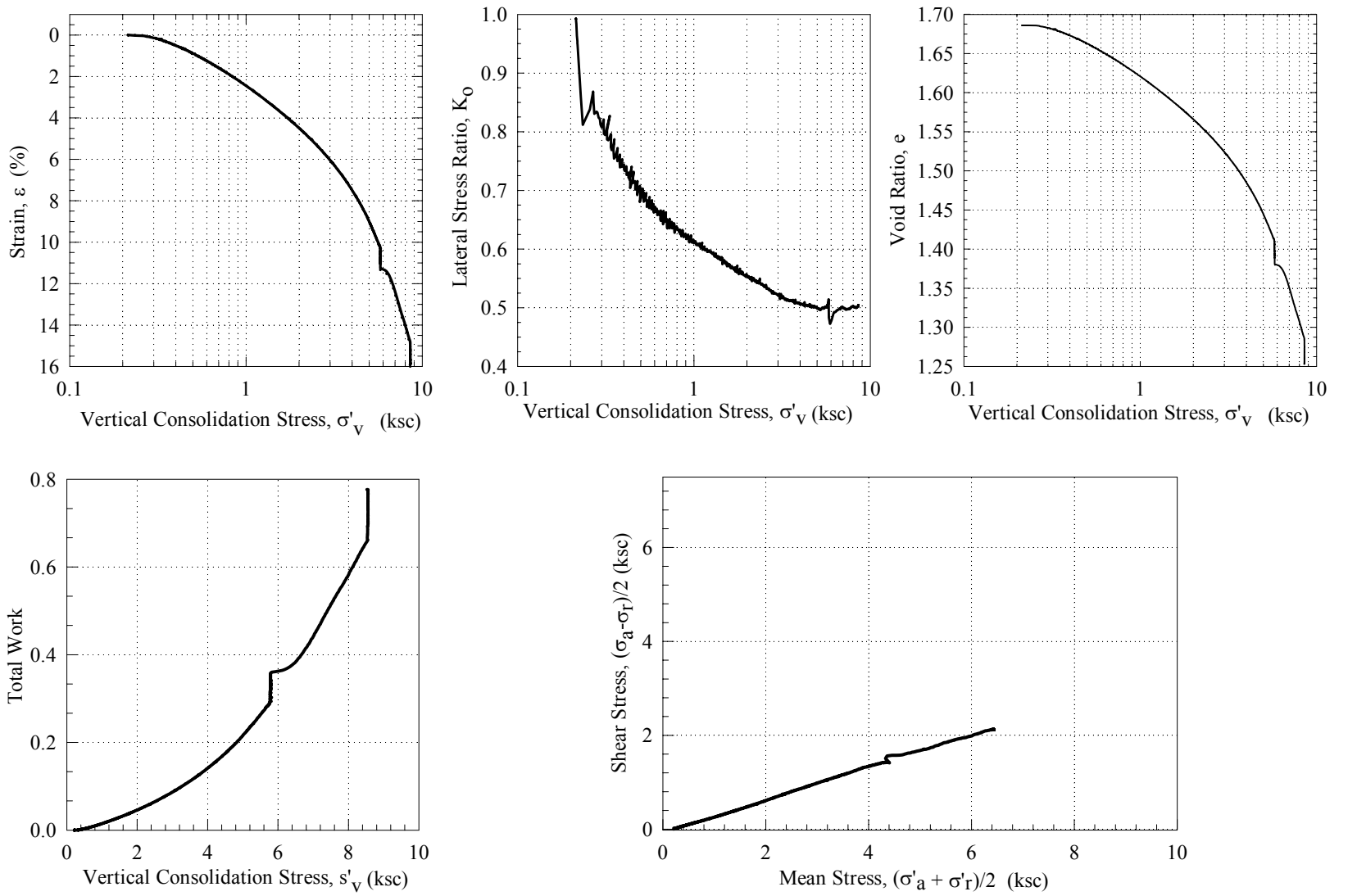

Figure 5.57: TX 645 Consolidation

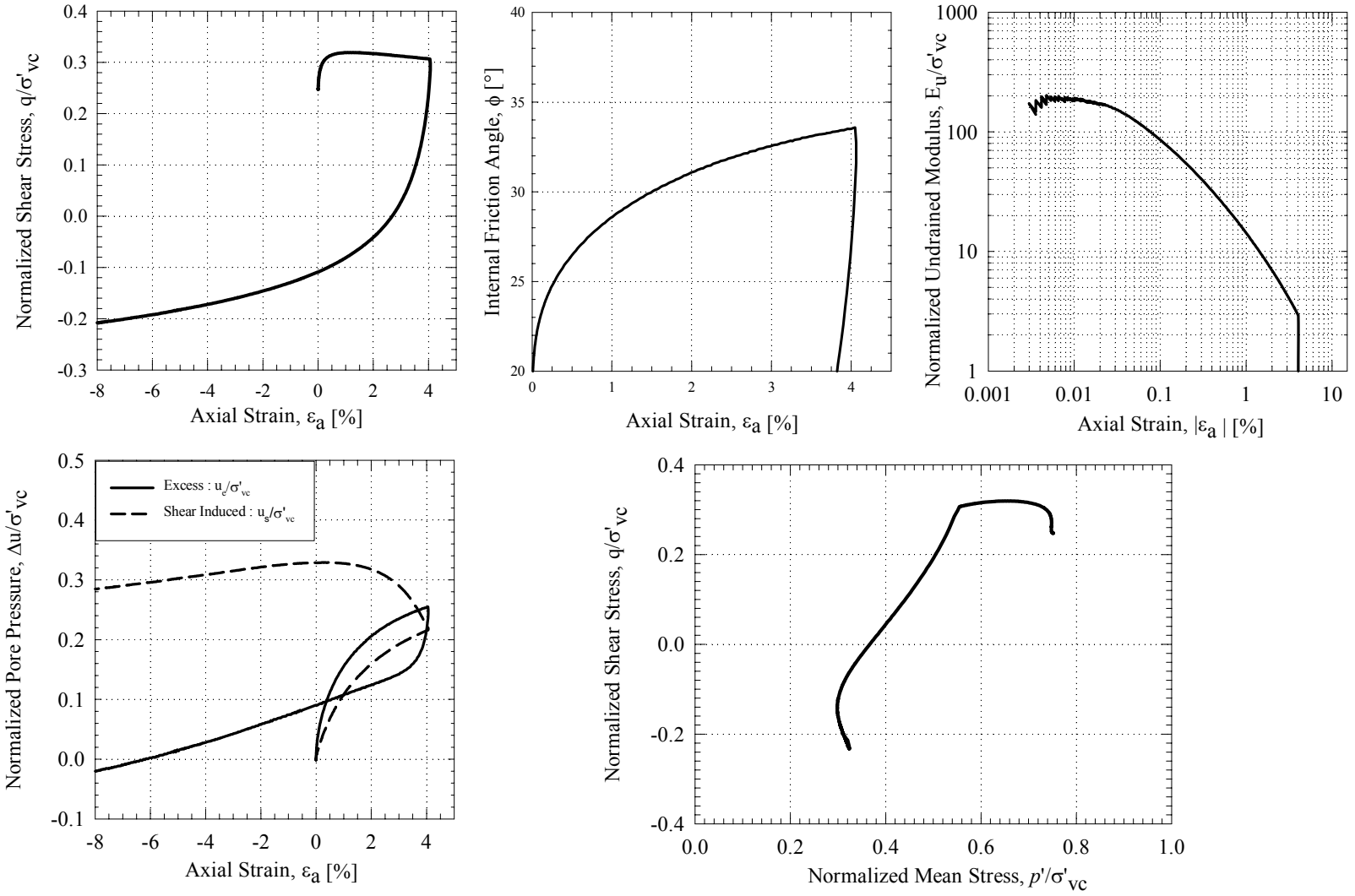

Figure 5.58: TX 645 Undrained Shear

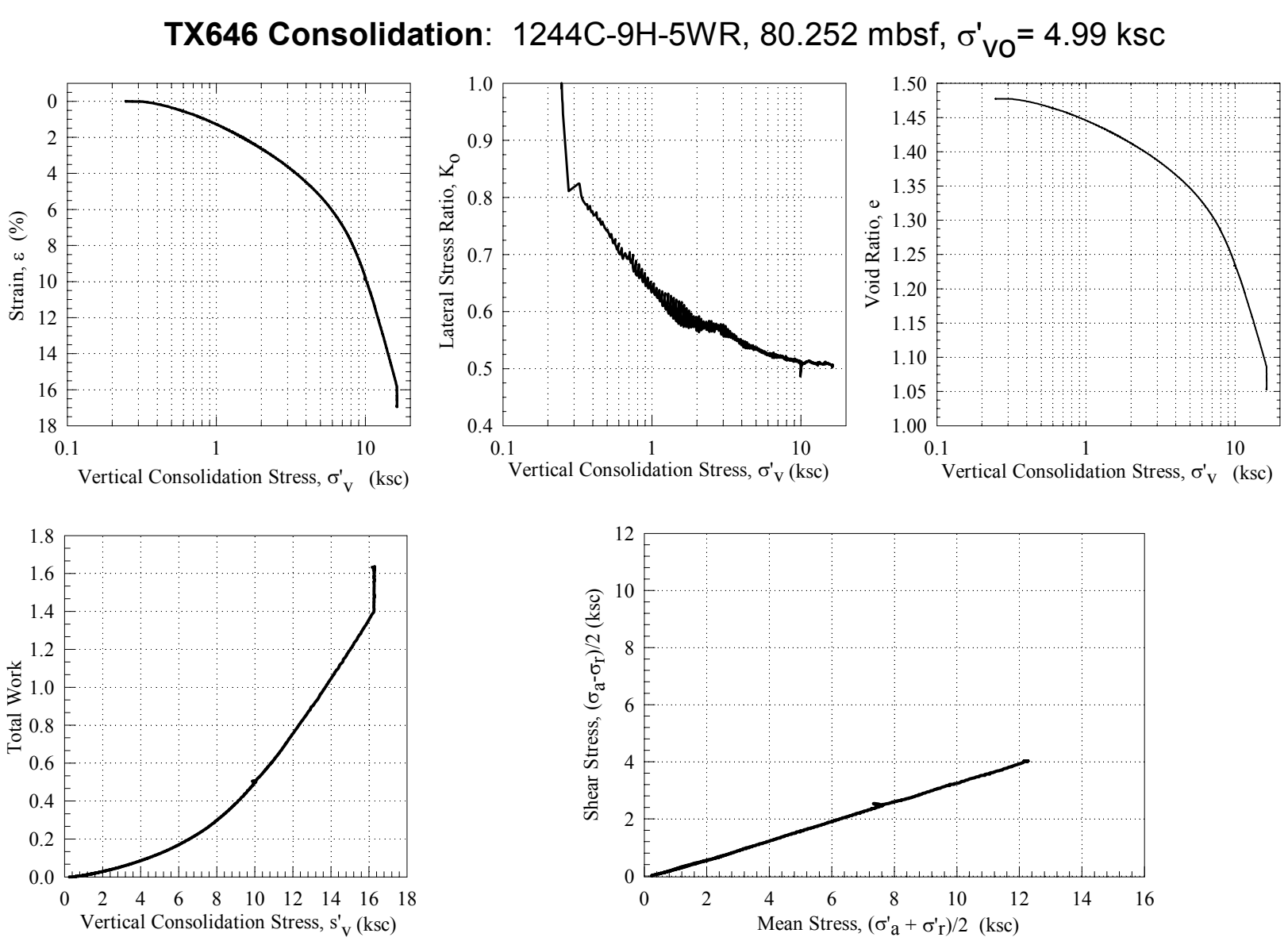

Figure 5.59: TX 646 Consolidation

TX646 Undrained Shear: 1244B-9H-5WR, 80.252 mbsf, σ'_{vo}= 4.99 ksc

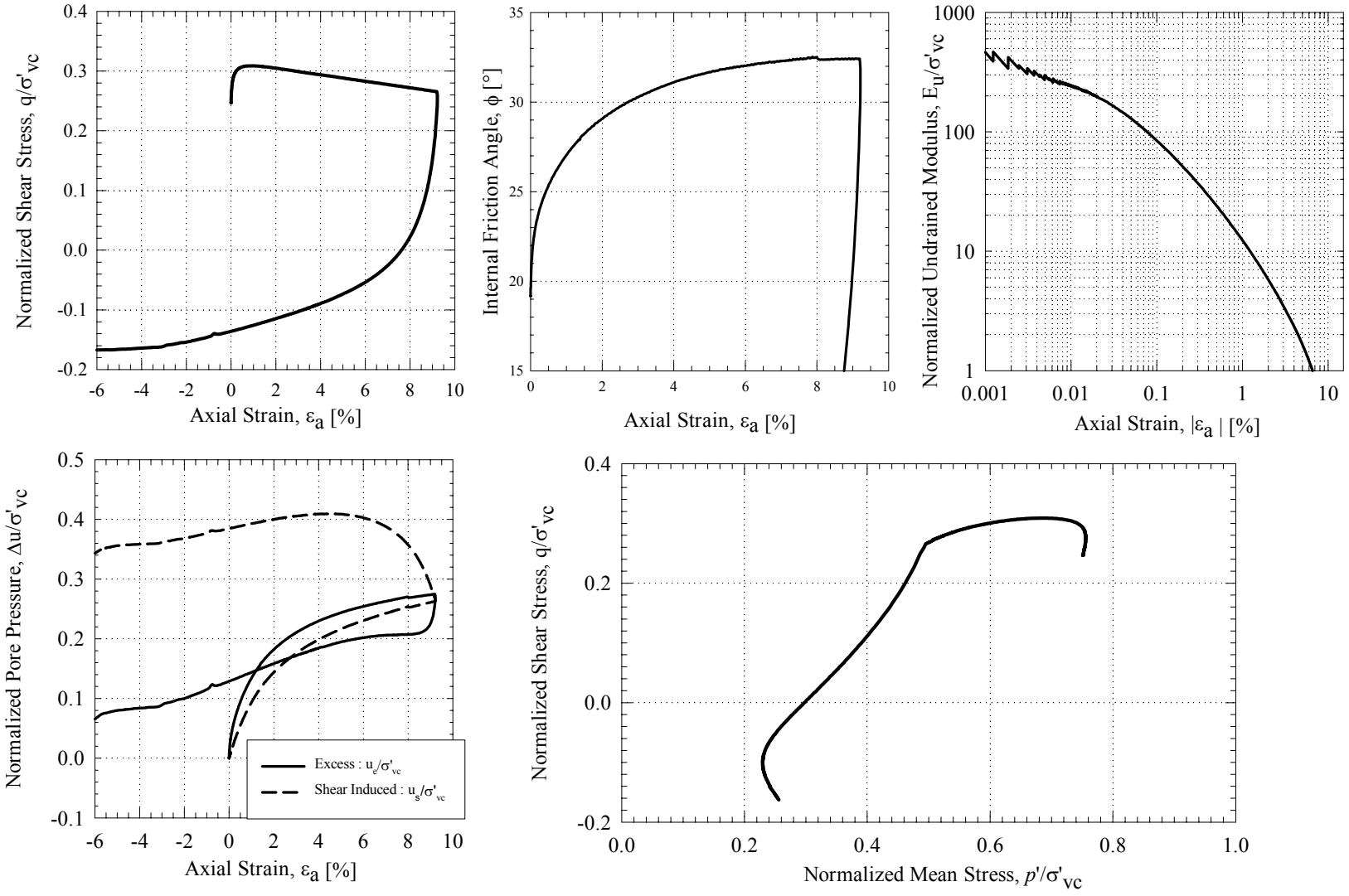

Figure 5.60: TX 646 Undrained Shear

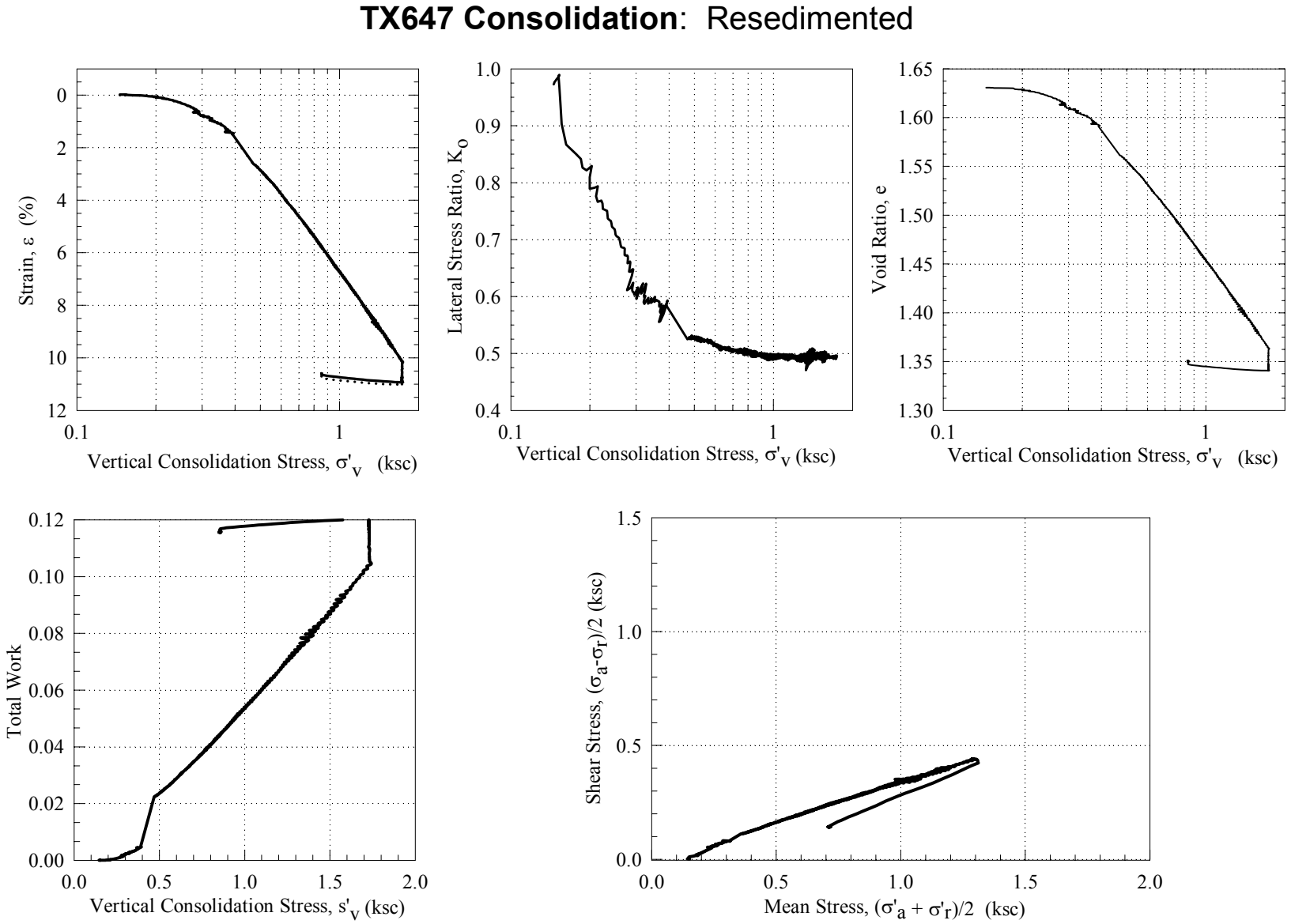

Figure 5.61: TX 647 Consolidation

TX647 Undrained Shear: Resedimented

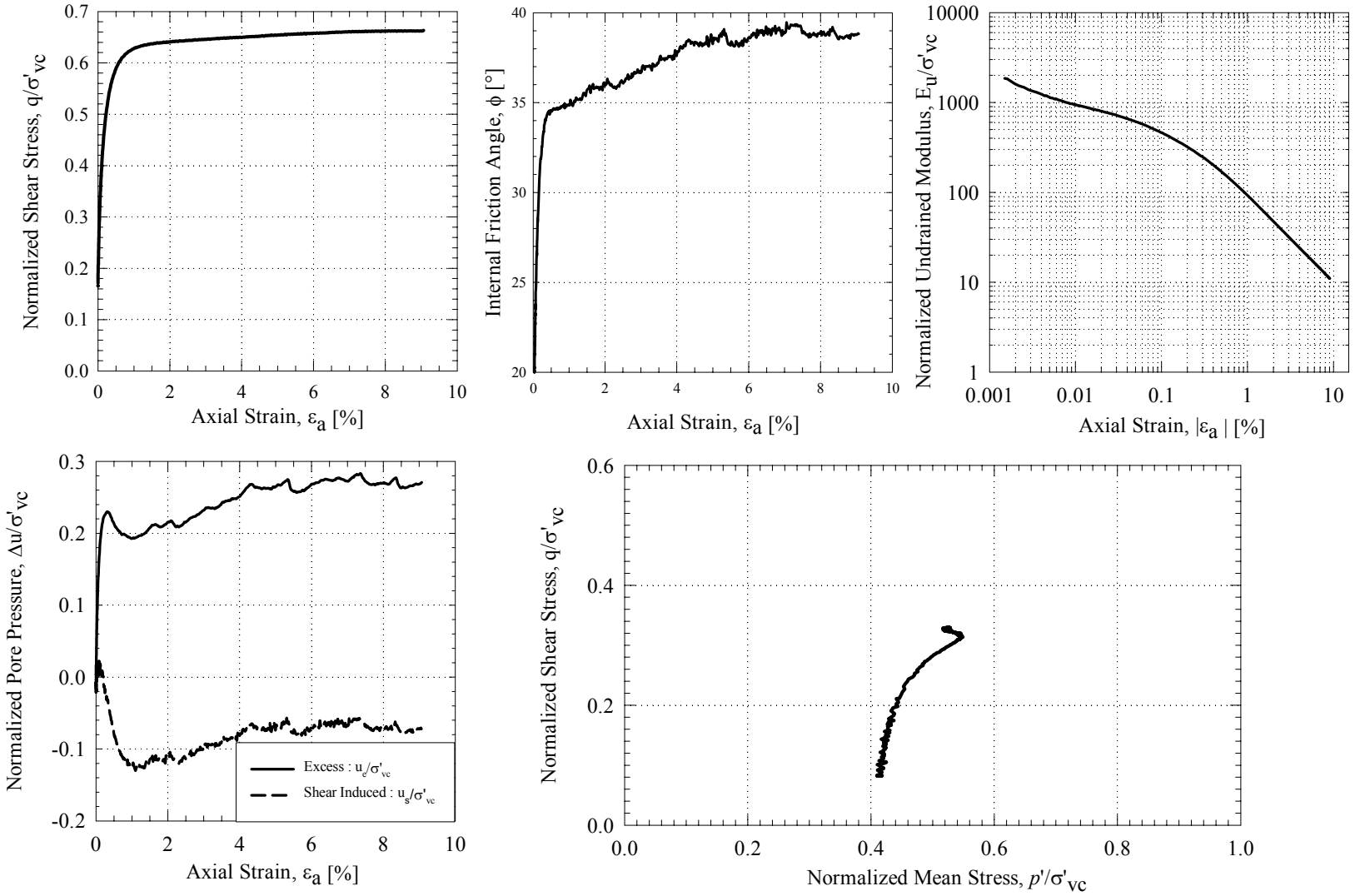

Figure 5.62: TX 647 Undrained Shear

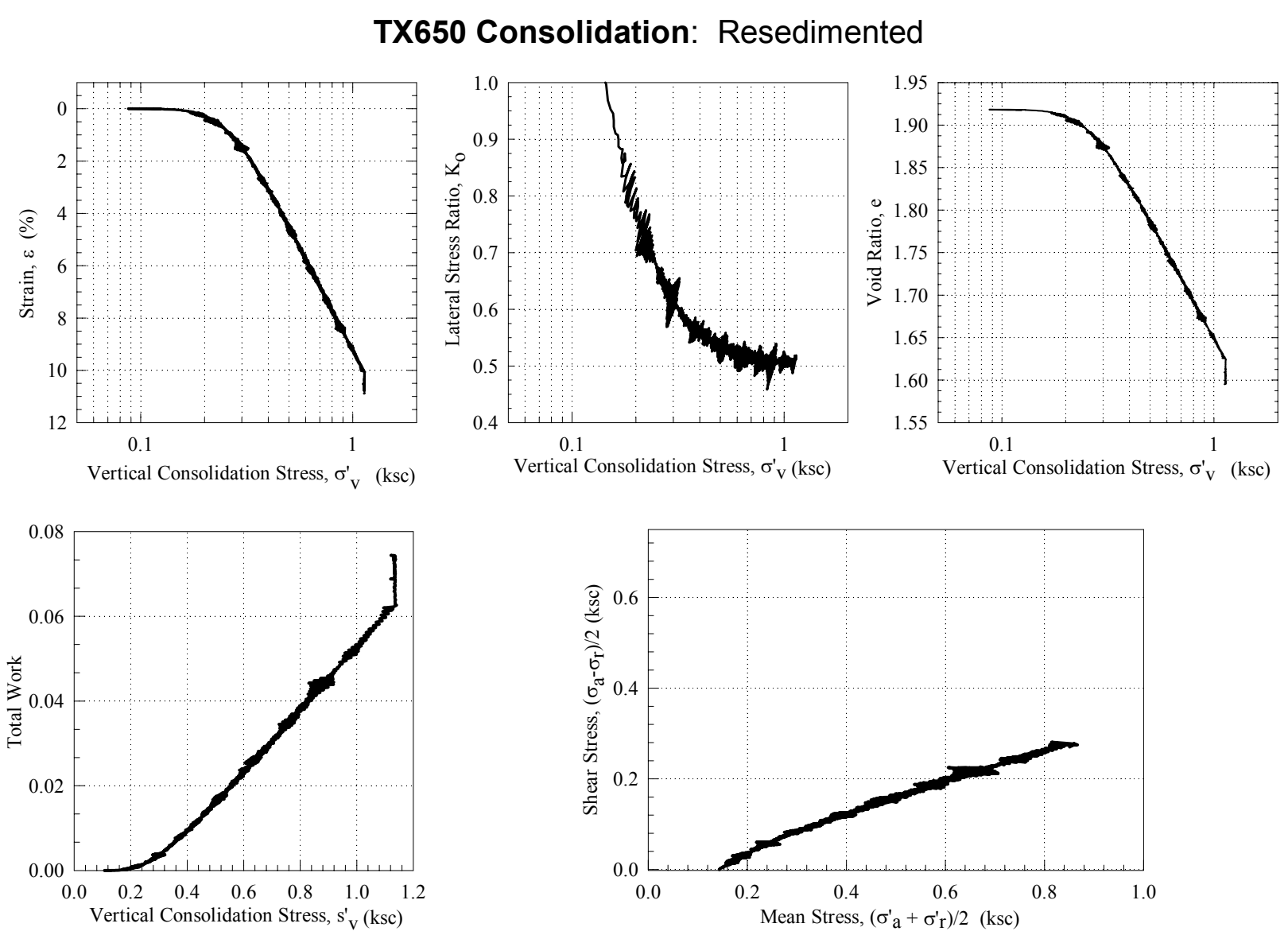

Figure 5.63: TX 650 Consolidation

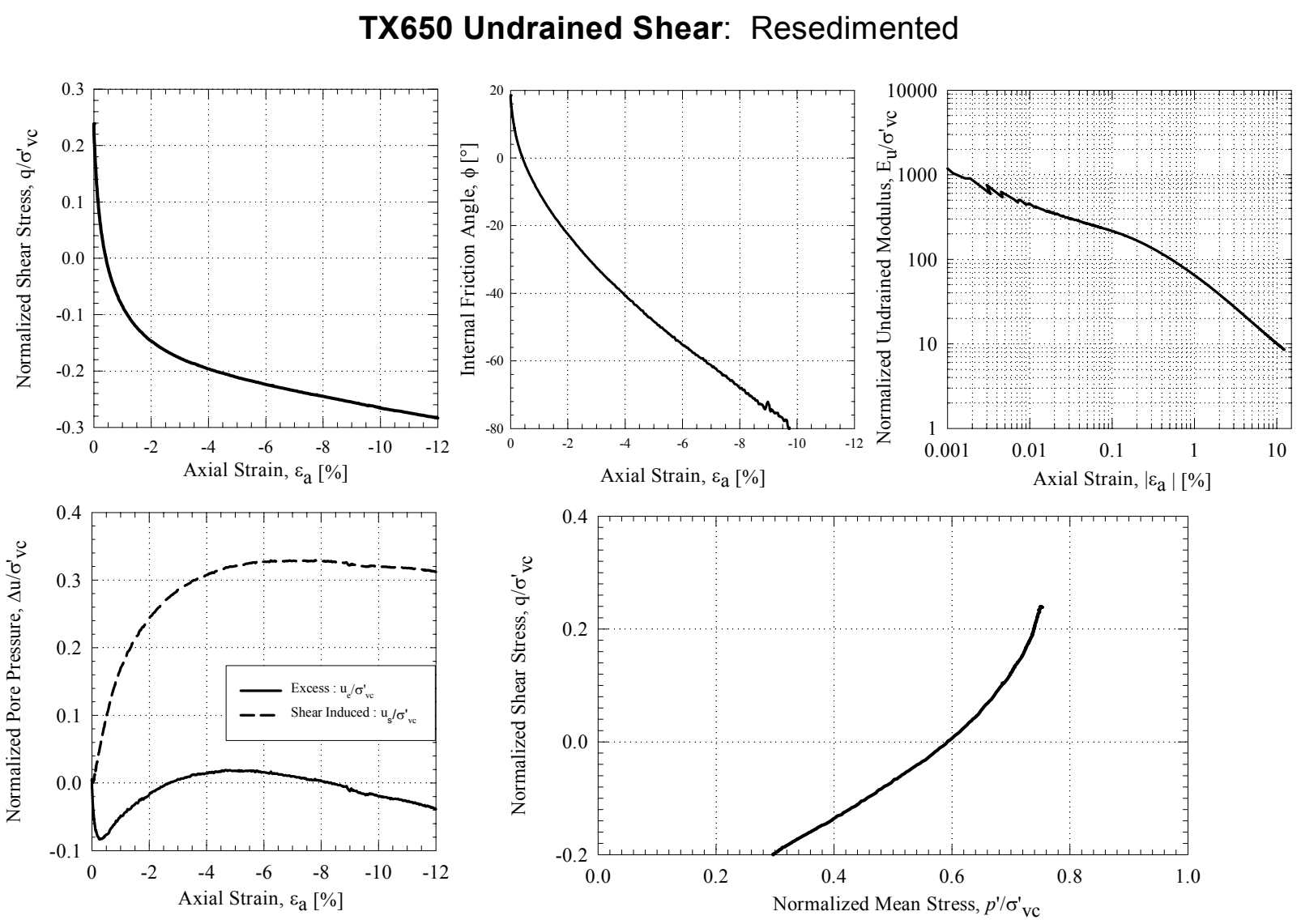

Figure 5.64: TX 650 Undrained Shear

Chapter 6: Interpretation of Laboratory Testing Results

Results from laboratory tests can be used and interpreted in a number of ways, depending on the purpose of the research. This chapter interprets the results of the laboratory tests described in Chapter 4 and Chapter 5. First to be discussed in this chapter will be the effect of sample disturbance, which plays a significant role in the interpretation of the laboratory results. Secondly, this chapter will give the stress history profile of the site. The next section will discuss the effect of the horizontal stress, as this plays in an important role in interpreting the stress history of the site. Fourth, the SHANSEP parameters of the soil will be estimated and will be used as a tool in determining the strength profile of ODP Site 1244. Lastly, the input parameters of a constitutive soil model will be derived. The soil model used in this study is the MIT E-3 soil model developed by Whittle (1987).

6.1 Sample Disturbance

As was mentioned in Section 2.2, sample disturbance can have a significant impact on the results of geotechnical laboratory tests. This section focuses on the effect of disturbance on the results of the CRSC and CKoU triaxial test by making comparisons to disturbance indices used for on-shore sampling. The general effect of sample disturbance on the consolidation data can be found in Section 2.2.2.

6.1.1. Sample Quality Indices

Sample quality indices are used to classify the quality of the soil sample. Terzaghi et al (1996) and Lunne et al (1997) have established criteria for evaluating the soil quality based on the strain to the plastic state. The criteria are described in Section 2.2.3. Table 6.1 gives the rating of the soil samples based on both criteria. It can be seen that the quality of the Hydrate Ridge soil is generally poor and decreases with depth. However, the difficulty with these two methods is they look solely at the slope of the initial loading, without considering what the true strain to the plastic state should be, i.e., what the slope of a reload cycle looks like.

Thus, in an attempt to more objectively classify the level of sample disturbance, a method comparing the slope of the initial loading to the slope of unload-reload cycle was developed. The following describes the steps used to perform this method (see Figure 6.1):

1) On the initial loading portion of the CRSC curve, locate the effective stress point that corresponds to a stress that is 4 times larger with respect to the initial point of the CRSC curve.
2) The void ratio corresponding to the effective stress point found in step one is subtracted from the initial void ratio to give Δe_i.
3) For the reload cycle, locate the effective stress point that corresponds to a stress increment of 4 with respect to the start of the reload cycle.
4) The void ratio corresponding to the effective stress point found in step three is subtracted from the void ratio at the start of the reload cycle to give Δe_r.
5) Then, the Δe_i is divided by Δe_r to give the Δe ratio.

The Δe ratio will indicate the degree of disturbance the sample has experienced. For a perfectly undisturbed sample, the ratio will equal 1. This method has yet to be tested widely; hence a scale that would classify the quality of the samples has not yet been developed. However, it is believed that a ratio ranging between 1 and 1.5 should indicate fair quality samples, while ratios greater than 1.5 would indicate poor quality samples. Figure 6.2 shows the Δe ratio for the CRSC tests with unload-reload cycles. It can be seen from the figure that only a few CRSC tests had Δe ratios that ranged from 1 to 1.5, which indicates some samples are of fair quality, with the rest being of poor quality. The CRSC samples that did not reach the normally consolidated state and whose unload-reload cycles did not occur in the normally consolidated state were not included. The reason for this exclusion is that the behavior of an unload-reload cycle that is not yet in the normally consolidated state differs from the behavior of an unload-reload cycle that has reached the normally consolidated state because the unload-reload cycle occurs within the yield surface and not on the yield surface. An important observation is the difference in soil quality between CRS 508 and CRS 563. It is unsure why there is a significant difference between the Δe ratio of the two tests, but looking at the consolidation curves (Figure 5.24 and Figure 5.26), it is evident that the initial loading of CRS 508 is similar to its unload-reload, while the initial loading of CRS 563 is different from its unload-reload. The other possibility is that the unload-reload cycle of CRS 508 does not fall in the normally consolidated, but slightly at the

border of the over and normally consolidated state. It is interesting to see that the sample with the best quality occurs at 79 mbsf. Furthermore, there is no sample quality trend with depth.

Also found in Figure 6.2 is the Δe ratio for CRS 316, which is a test that was run on a good quality BBC specimen. It can be seen in the figure that the Δe ratio for CRS 316 is about 1.3, which confirms that the sample is of good quality and verifies the validity of the Δe method.

6.2 Stress History

The behavior of a soil depends largely on the amount of overconsolidation that it has experienced. Hence, determining the preconsolidation pressure from consolidation tests is essential in gaining a better understanding of its behavior.

6.2.1. Strain Energy Method

Table 6.2 gives the values of the preconsolidation pressures estimated using the strain energy method, and Table 6.3 gives the overconsolidation ratio assuming hydrostatic in-situ water pressures. The strain energy method is discussed in detail in Section 2.2.4.2.

Figure 6.3 shows the stress history profile using the strain energy method. It can be seen from the profile that the deposit is overconsolidated based on this method. It can also be seen that the overconsolidation ratio decreases with depth for the mudline to about 40 mbsf and then is more or less constant with depth. Furthermore, the scatter increases with depth. Comparing this with the sample quality indices mentioned earlier, it can be seen that there is no direct trend between the sample disturbance indices and the preconsolidation pressure estimated using the strain energy method. A good example of this is the sample at 30 mbsf, which shows consistent estimated preconsolidation pressures, but poor soil quality with respect to the indices.

6.2.2. Extrapolation to In-Situ Void Ratio

An alternative method for determining the preconsolidation pressure was used in order to obtain a range of the possible values of the overconsolidation ratios. In this method, it was assumed that the preconsolidation pressure is located at the estimated in-situ void ratio, along the virgin compression line. The in-situ void ratios were taken from the following data:

1) *Laboratory void ratio.* The laboratory void ratio was estimated during each experiment by using phase relationship quantities such as the mass and height. The following equation was used in estimating the void ratio:

$$e_i = \frac{\left(G_s \cdot H_i \cdot A \cdot \rho_w - M_d\right)}{M_d} \tag{6.1}$$

where G_s is the specific gravity, H_i is the initial height, A is the area, ρ_w is the density of water, and M_d is the dry mass. The uncertainty with this estimate of the in-situ void ratio lies in the fact that the samples may have undergone drying and/or expansion during the time it was stored in the tubes. Also causing uncertainty is the presence of salt pore water.

2) *Moisture and Density (MAD) void ratio*. The MAD void ratio was measured by the ODP as part of their shipboard experiment program. Details of the MAD test are discussed in Section 3.1.4.1. It must also be noted that the MAD data assumes 100% saturation.

3) *Logging While Drilling (LWD) void ratio*. The LWD void ratio was measured in-situ during the drilling process. The details of LWD can be found in Section 3.1.3.1. Though the LWD should give the most reasonable void ratio estimate because of its true in-situ measurement, poor measurement conditions have resulted in uncertainties in the void ratio measurements.

4) *Wireline void ratio*. The wireline void ratio was measured in-situ after a hole had been drilled and the wireline tool lowered. Details of wireline measurements can be found in Section 3.1.3.2. The wireline data seem to give unreliable values of void ratio. It must be noted that wireline data is available only below 79.05 mbsf.

Table 6.4 gives the in-situ void ratios as estimated by different measurement methods for each sample. It is obvious that there is a significant variation in the estimated void ratio for each method. Figure 6.5 shows the distribution of the in-situ void ratios with depth for all four methods. It can be seen from the figure that below 53 mbsf, the void ratios from the different methods are in agreement. Above 53 mbsf, there is a significant difference in void ratio from the different methods. More noticeably, the lab void ratios above 53 mbsf are consistently lower than the other void ratios. One possible reason for this scatter is that the measurements up to 53 mbsf are from hole B, while measurements below 53 mbsf are from hole C. Furthermore, the

consistently lower laboratory void ratios may be due to drying of the material in storage. This result is unexpected and raises the possibility of sample alteration during storage of the samples. Also noticeable from the graph is a decreasing trend in the void ratio values below 53 mbsf.

The preconsolidation pressure by extrapolation was estimated as follows (see Figure 6.4):

1) *Projection of virgin compression line*. For each CRSC curve in e-logσ'_v, a line is drawn along the straight portion of the compression curve. This line corresponds to the virgin compression line. The line is then projected back and up, beyond the normally consolidated zone.
2) *In-situ void ratio*. A horizontal line corresponding to the in-situ void ratio estimated from any of the aforementioned methods is drawn on the curve.
3) *Estimation of the preconsolidation pressure*. The intersection of the virgin compression line and the in-situ void ratio line will give the value of the preconsolidation pressure.

The estimated preconsolidation pressures and corresponding OCRs from this method using all the aforementioned methods of estimating the in-situ void ratios can be found in Table 6.2 and Table 6.3 respectively.

Figure 6.5 shows the preconsolidation pressures as estimated from extrapolation, as well as the Δe sample quality index. It can be seen that the estimates of the void ratio-extrapolated-preconsolidation pressures from the sample at 53 mbsf are quite low and are scattered. When checking the Δe sample quality index, it can be seen that this sample has the poorest quality. It can also be seen from Figure 6.5 that the preconsolidation pressures from the sample at 79 mbsf are consistent. Nonetheless, this sample has the highest quality based on the Δe sample quality index. However, though these two samples show a relationship between the Δe sample quality index and the variability in preconsolidation pressures from the different methods, the other samples show otherwise. For example, the sample at 71 mbsf shows a low sample quality, but the estimated preconsolidation pressures are fairly consistent. Hence, the Δe, Terzaghi et al (1996), and Lunne et al (1997) sample quality indices do not have a relationship with the estimated preconsolidation pressures.

6.2.3. Stress History Profile

As seen in Table 6.2, there are significant variations in the estimation of the preconsolidation pressure depending on which method and which void ratio was used. Figure 6.6 gives the stress history profile as estimated from the two methods and for the lab and wireline void ratios. As mentioned earlier, the strain energy method predicts overconsolidation throughout the depth. Also, since it is believed that the laboratory void ratio may be low for the samples above 53 mbsf, the estimated preconsolidation pressure using this void ratio will be on the high side.

When comparing the strain energy and void ratio extrapolation methods, it is clearly illustrated that there is a large difference between the estimates of the preconsolidation pressure. However, it is fair to state that the value of the preconsolidation pressure from the strain energy method can be considered as an upper bound estimate, while the value from the extrapolation to the in-situ void ratio can be considered as a lower bound estimate.

6.2.4. Importance of In-situ Stress State

Hydrate Ridge is located in the Cascadia accretionary complex, which was formed by the subduction of the Juan de Fuca plate beneath North America. The geologic setting implies that the soil in the accretionary complex, and hence Hydrate Ridge, is undergoing passive loading, i.e., the soil is being pushed inwards laterally (Chevallier et al, 2003). Should this behavior be true, the shape of the yield surface would differ greatly from what is usually expected of a soil undergoing one-dimension vertical loading.

A CRSC test was conducted on a sample loaded along the horizontal direction in order to investigate the preconsolidation pressure anisotropy (see Table 6.2). The resulting preconsolidation pressure was greater than that of the preconsolidation pressure from the vertically-oriented tests. This finding supports the assumption that the soil experienced a greater horizontal stress than vertical stress, as a result of the soil being loaded passively, especially in the shallower section of the deposit.

The succeeding discussion attempts to describe the stress path behavior of the soil in MIT p'-q space. Furthermore, the discussion will attempt to describe the yield surface, i.e., transition from elastic to plastic state, thus explaining why the preconsolidation pressure is higher for the horizontally-oriented sample. The discussion will also include an explanation as to why the

shallow specimens exhibit high OCR when analyzed using the traditional geotechnical interpretation methods. Nonetheless, a best estimate of stress history will be developed. The following must be understood in order to thoroughly appreciate the discussion:

1) p' is the mean effective stress $(\sigma'_h+\sigma'_v)/2$, q is the shear stress $(\sigma_v-\sigma_h)/2$, and K is the lateral effective stress ratio (σ'_h/σ'_v).
2) In MIT p'-q space, the vertical effective stress is higher than the horizontal effective stress when q is positive, and the opposite occurs when q is negative.
3) The yield surface distinguishes between the plastic and elastic state.
4) When soil is loaded within the yield surface, it is assumed that the yield surface is stationary.
5) When a soil is loaded beyond the yield surface, the yield surface extends and rotates in the direction of the stress path.

Figure 6.7 describes the possible shape of the yield surface. The data from Figure 6.7 was taken from tests performed on samples from 1244B-1H-4WR, specifically, CRS580, CRS608, TX643, and TX650. The in-situ vertical effective stress assuming hydrostatic conditions was found to be 32 kPa (solid circle). Point A refers to the vertical preconsolidation pressure for the vertically-oriented specimen, which is equal to 235 kPa. The location of the stress point on the yield surface corresponding to the preconsolidation pressure within p'-q space lies between the K_o and K_a lines, and is bounded by a 45^o line from point A. The K_o-line was taken from the consolidation portion of TX643, and represents the lower limit of the preconsolidation pressure (point B). The K_a-line refers to the triaxial compression mode of failure from TX643, and represents the upper limit of the preconsolidation pressure (point C). Hence, the stress path is believed to occur between the dotted line and the dash-double-dot line.

CRS608 is a CRSC test on a horizontally-oriented sample. This sample is constrained in the vertical direction and loaded in the horizontal direction. It must be noted that this test ignores the effect of the intermediate principal stress (σ_2). The value of the horizontal preconsolidation pressure for CRS608 is 301 kPa, and is indicated by point D on the figure. The stress point on the yield surface corresponding to the horizontal σ'_p is bounded by a 45^o line from point D. The possible locations can be on the $1/K_o$, $1/K_a$, or K_p lines. The $1/K_o$ line is the absolute minimum and is believed to be too low. The $1/K_a$ line, which is taken from the triaxial compression friction angle, is assumed to be a reasonable minimum value. Hence, it was assumed that the

minimum stress path for CRS608 follows the $1/K_a$ line, as indicated by the thick dashed-line. Furthermore, the location of the preconsolidation pressure in p'-q space for this case is point E. This minimum stress path gives an upper limit of the vertical preconsolidation pressure for the horizontally-oriented specimen (point F). The $\sigma'_{pv\ (upper\ limit)}$ was found to be 76 kPa, giving an OCR of 2.38.

The K_p line refers to the triaxial extension mode of failure line, which was estimated from the extension portion of TX643 and the extension test TX650. This line represents the maximum possible stress path for CRS608 (thick dash-dot line). Based on this assumption, the location of the preconsolidation pressure in p'-q space is point G. This maximum stress path gives a lower limit of the vertical preconsolidation pressure for the horizontally-oriented specimen (point H). The $\sigma'_{pv\ (lower\ limit)}$ was found to be 33 kPa, giving an OCR of 1.03.

The two broken lines in Figure 6.7 represent the range of the possible locations of the yield surface. The resulting OCR range from the upper and lower limit estimates of the preconsolidation pressure is 1.03 to 2.38, which is reasonable and within the range that is expected. The implication of this finding is that the samples are being passively loaded in the shallow depth of the deposit. This explains why such a high OCR was measured using the vertically-oriented CRSC test. It is also consistent with the fact that extrapolation to the in-situ void ratio gives much lower σ'_p.

Dividing the $\sigma'_{pv\ (upper\ limit)}$ and $\sigma'_{pv\ (lower\ limit)}$ by the σ'_{pv} from CRS 580 gives 0.32 and 0.14, respectively. In the absence of extensive testing, these factors can be applied to the σ'_{pv} measured from the other CRSC tests, in order to give a more reasonable estimate of the preconsolidation pressure and OCR. Table 6.5 and Table 6.6 give the preconsolidation pressure and OCR with the upper and lower limit factors applied to the strain energy preconsolidation pressure estimates. Figure 6.8 shows the stress history profile with the upper and lower limit factors applied. The tables and figure show that the lower limit factor reduces the strain energy preconsolidation pressure drastically. In fact, below 5.7 mbsf, the lower limit factor causes underconsolidation. The upper limit factor also reduces the strain energy preconsolidation pressure, but to a lesser degree. Below 32.98 mbsf, the upper limit factor causes underconsolidation. This method predicts that the deposit has a generally constant OCR of 0.4 to 0.5 that is constant with depth below 20 mbsf.

If the stress path was assumed to follow the $1/K_o$ line instead of the $1/K_a$ (point I, Figure 6.7), the $\sigma'_{pv\ (1/Ko\ upper\ limit)}$ would be 139 kPa (point J, Figure 6.7). Thus, the $1/K_o$ upper limit factor would be equal to 0.59. Figure 6.9 shows the effect of the $1/K_o$ factor on the preconsolidation pressure. It can be seen from the figure that the $1/K_o$ factor reduces the strain energy preconsolidation pressure such that it is in the normally consolidated state. However, though this result is believed to be possible, it is unlikely because the deposition and formation conditions at the site suggest underconsolidation.

6.3 SHANSEP Parameters

Ladd and Foott (1974) theorized that a normally consolidated soil deposit of uniform mineralogical makeup will exhibit unique strength properties when normalized by the vertical effective consolidation stress. This theory led to the development of the *Stress History and Normalized Soil Engineering Properties* (SHANSEP) theory. Ladd went on to state that for overconsolidated soils, the value of the normalized strength varies with the value of the OCR raised to an experimentally determined factor. The resulting equation is as follows:

$$\frac{S_u}{\sigma'_{vc}} = S(OCR)^m \tag{6.2}$$

where S_u is the undrained strength, σ'_{vc} is the vertical effective consolidation stress, and *OCR* is the overconsolidation ratio. The parameters *S* and *m* are called the SHANSEP parameters. *S* is the value of the normalized undrained strength for a normally consolidated soil, while *m* is the factor that gives the normalized undrained strength for overconsolidated soil. These parameters are obtained from a series of SHANSEP CKoU triaxial tests, which were discussed in Section 4.5.3. It is important to understand that SHANSEP type triaxial tests involve one-dimensional consolidation to the normally consolidated state prior to shearing. The SHANSEP theory is discussed in better detail in Section 2.2.5.2.

As a result of differences in the normalized undrained strength profile, the hydrate ridge deposit was divided into 2 layers, as shown in Table 6.7 and Figure 6.10. Table 6.8 gives the recommended values of *S* and *m* for the Hydrate Ridge soil.

As a comparison, the values of *S* and *m* for Gulf of Mexico Clay (GMC), Boston Blue Clay (BBC), and for homogenous CL and CH sedimentary clays are also given in Table 6.8. Compared to the GMC, BBC, and CL/CH clays, the Hydrate Ridge soil has a higher m value.

This implies that the increase in strength of Hydrate Ridge due to an increase in OCR is higher compared to the other soils. Furthermore, the S value for the Hydrate Ridge soil is similar to BBC and is much higher than GMC and CL/CH clays. This means that the Hydrate Ridge soil has a normally consolidated undrained strength that is similar to BBC and higher than GMC and CL/CH clays.

6.4 Strength Profile

Once the SHANSEP parameters and stress history have been obtained, the strength profile of the deposit can be formulated using the SHANSEP equation. The following are the equations used to describe the strength profile:

Layer A:
$$\frac{s_u}{\sigma'_{vc}} = 0.35(OCR)^{0.94} \tag{6.3}$$

Layer B:
$$\frac{s_u}{\sigma'_{vc}} = 0.31(OCR)^{0.94} \tag{6.4}$$

Figure 6.11 gives the strength profile at the site based on equations 6.3 and 6.4. As shown in Section 6.2.4, the soil is believed to be underconsolidated. As such, the value for the OCR that was used in determining the strength profile was 1. Furthermore, the σ'_{vc} that was used was equal to the unfactored strain energy preconsolidation pressure.

Another method for determining the strength profile involves determining the relationship between the void ratio during shearing and the strength, then extrapolating an in-situ strength from the in-situ void ratio. Figure 6.12 shows the variation of undrained strength with the void ratio at shearing. The trend line gives the following equation:

Layer A:
$$\frac{q}{\sigma'_{vc}} = 0.0562e + 0.2513 \tag{6.5}$$

Layer B:
$$\frac{q}{\sigma'_{vc}} = 0.0444e + 0.2897 \tag{6.6}$$

The R^2 for the trend line of Layer A and B are 0.9675 and 1 respectively. Interestingly, this figure shows that the behavior of the soil deviates from the SHANSEP theory. In SHANSEP theory it is assumed that the normalized undrained strength is independent of the shearing void ratio, i.e., the points in Figure 6.12 should form a horizontal line. However, it is seen from the figure that the strength increases with increasing void ratio. This implies that the normalized undrained strength is also dependent on the stress at consolidation. This result has also been

noticed in DSS tests on offshore samples conducted by Quiros et al (2000). Their study has shown that the normalized undrained strength decreases with increasing consolidation stress. They propose a method by which the consolidation water content is taken into consideration when estimating the normalized undrained strength.

The laboratory measured void ratios were used in equation (6.5) and (6.6) to obtain an estimate of the strength. Figure 6.11 shows the results of this method compared to the strength estimated from the SHANSEP equation. It can be seen in the figure that the void ratio extrapolation gives slightly higher results.

On the issue of strength anisotropy, a look into the yield surface developed in section 6.2.4 will provide more insight. The strength measured in triaxial extension is the strength after significant consolidation (due to SHANSEP consolidation) and after the rotation of the yield surface. Hence, the measured strength is usually on the low side. However, analysis of the stress path history found in Figure 6.7 suggests that the strength in compression and extension loading will be similar (point E and G in Figure 6.7).

Another important strength parameter is the increment in stress required to cause failure. If it is assumed that the second horizontal stress, σ'_2, is defined as:

$$\sigma'_2 = \frac{\sigma'_1 + \sigma'_3}{2} \tag{6.7}$$

then the increment in stress to cause failure in this principal plane can be calculated. The following are the equations used to calculate the increment in stress to cause failure in each principal plane:

$$\Delta\sigma_{vf} = \sigma'_{hi} - \sigma'_{vi} + 2q_f \tag{6.8}$$

$$\Delta\sigma_{h1f} = 0 \tag{6.9}$$

$$\Delta\sigma'_{h2f} = \frac{\sigma'_{hi} - \sigma'_{vi}}{2} + q_f \tag{6.10}$$

The triaxial tests were consolidated under the K_o-condition. However, because the site is believed to be consolidated under passive conditions, the values of σ'_{hi} and σ'_{vi} from the triaxial test need to be adjusted to reflect the in-situ conditions. As such, the upper and lower limit factors are applied to the measured σ'_p to get σ'_{vi}. The factor that must be applied to σ'_p to get σ'_{hi} is equal to 1.28, which was obtained by dividing point D by point A in Figure 6.7. The increment in stress to cause failure in the first horizontal direction is assumed to be equal to zero.

This is because the material is at passive failure in the field. Figure 6.13 shows the increment in stress to cause failure in the vertical and horizontal (intermediate) direction with depth. It can be seen from the figure that the increments to failure in both the vertical and horizontal direction increase with depth.

6.5 MIT E-3 Parameters

MIT E-3 is a constitutive soil model developed at MIT by Whittle (1987). It is a complex soil model and requires fifteen input parameters (see Table 6.9). The model was developed to simulate the behavior of normally consolidated to lightly over-consolidated clay (OCR<8). The model formulation is based on three key elements:

1) incremental effective stress-strain relationship
2) hysteretic model
3) bounding surface model

Another important assumption of the MIT E-3 model is the assumption of rate independent behavior of clay, i.e. effects of creep are neglected.

The MIT E-3 parameters were obtained according to the framework suggested by Korchaiyapruk (2000). Figure 6.14 shows the framework for selection of the model input parameters for the MIT E-3 soil model. Basically, the process involved dividing the soil deposit into the necessary number of layers, which in this case were two. Then, the parameters that could be obtained from laboratory tests such as e_o, λ, K_{oNC}, $2G/K$, ϕ_{TC}, and ϕ_{TE} were averaged for each layer. For the h, C, n, c, ω, γ, κ_o, ψ_o, and S_t parameters, parametric studies were conducted in order to obtain the "best-fit" consolidation, undrained shear strength, shearing stress path, and undrained shear modulus curves. Figure 6.15, Figure 6.17, Figure 6.19, and Figure 6.21 give the best-fit consolidation, undrained shear strength, shearing stress path, and undrained shear modulus curves for Layer A, while Figure 6.16, Figure 6.18, Figure 6.20, and Figure 6.22 give the best-fit curves for Layer B. It can be seen from the figures that the selected parameters fit well with the laboratory curves. Table 6.10 gives the MIT E-3 parameters for both Layer A and Layer B of the hydrate ridge soil. Also included in this table are the MIT E-3 parameters for Boston Blue Clay (BBC) and Gulf of Mexico Clay (GMC).

Compared to the GMC, layer A of Hydrate Ridge is less compressible, has less strain softening and less strength, but has a higher friction angle and small strain stiffness. Layer B of

Hydrate Ridge has similar compressibility, less strain softening and less strength, but has a higher friction angle and small strain stiffness than the GMC. Compared to BBC, layer A and B is generally less compressible, has less strain softening, and similar friction angle and strength.

6.6 References

Baligh, M. M. (1985). "The Strain Path Method." *Journal of Geotechnical Engineering*, ASCE, 111(9), 1108-1136.

Becker, D. E., Crooks, J. H. A., Been, K., and Jefferies, M. G. (1987). "Work as a Criterion for Determining In Situ and Yield Stress in Clays." *Canadian Geotechnical Journal*, 24(4), 549-564

Casagrande, A. (1936) "The Determination of the Preconsolidation Load and Its Practical Significance." *Proceedings of the First International Conference on Soil Mechanics and Foundation Engineering*, Cambridge, MA, Vol. 3, 60-64

Chevallier, J., Trehu, A. M., Meyer, J., Johnson, J. E., Bangs, N. L., (2003). "Stratigraphic and Structural Evolution of South Hydrate Ridge." *Eos Trans. AGU* 84(46) Fall Meeting Supplement, Abstract OS51C-0870.

Korchaiyapruk, A. (1998). "Development of Framework for Soil Model Input Parameter Selection Procedures." S.M. thesis, Dept. of Civil Engineering, MIT, Cambridge, MA.

Ladd, C. C., and Foott, R. (1974). "New Design Procedure for Stability of Soft Clays." *Journal of Geotechnical Engineering*, 100(7), 763-786.

Ladd, C. C. (1991). "Stability Evaluation During Staged Construction." *Journal of Geotechnical Engineering*, 117(4), 537-615.

Lunne, T., Berre, T., And Strandvik, S. (1997). "Sample Disturbance Effects in Soft Low Plastic Norwegian Clay." in: *Almeida (ed.) Recent Developments in Soil and Pavement Mechanics,* Balkema, Rotterdam, 81-102

Quiros, G. W., Little, R. L., Garmon, S. (2000). "A Normalized Soil Parameter Procedure for Evaluating In-Situ Undrained Shear Strength." *2000 Offshore Technology Conference*, Houston, Texas

Santagata, M. C., and Germaine, J. T. (2002). "Sampling Disturbance Effects in Normally Consolidated Clays." *Journal of Geotechnical and Geoenvironmental Engineering*, 128(12), 997-1006

Sutabutr, T. (1999). "Analyses and Interpretation of Tapered Piezoprobe and Application to Offshore Pile Design." Sc.D. thesis, Dept. of Civil Engineering, MIT, Cambridge, MA.

Whittle, A. J. (1987). "A Constitutive Model for Overconsolidated Clays with Application to the Cyclic Loading of Friction Piles." Sc.D. thesis, Dept. of Civil Engineering, MIT, Cambridge, MA.

Whittle, A. J. (1993). "Evaluation of a Constitutive Model for Overconsolidated Clays." *Geotechnique*, 43(2), 289-313.

Hole	Test No.	Terzaghi et al.	Lunne et al.
B1H4WR	CRS580	A	VGE
	TX643	A	VGE
B3H3WR	CRS497	D	P
	CRS563	C	GF
	TX642	C	GF
B4H6WR	CRS508	D	P
	CRS585	C	GF
	TX635	C	GF
	TX645	D	P
B6H8WR	CRS584	D	P
C8H7WR	CRS504	D	P
	CRS578	E	P
C9H5WR	CRS569	D	P
	TX646	D	P
C13H3WR	CRS491	E	VP
	CRS493	E	VP
	CRS567	D	P
C17H3WR	CRS495	E	VP
	CRS564	E	VP
	TX636	E	VP

TPM: A (best quality) to E (poorest quality)
NGI: VGE-Very Good to Excellent
GF-Good to Fair
P-Poor
VP-Very Poor

Table 6.1: Sample quality indices

Test Name	Hole	Depth (mbsf)	σ'_{vo} (kPa)	σ'_p (kPa)				
				strain energy	lab e_o	MAD e_o	LWD e_o	wireline e_o
CRS580	1H-4WR	6.938	32	235	113	57	6	
CRS608	1H-4WR (H)	6.976	32	301	130	38	3	
TX643	1H-4WR	7.141	32	170				
CRS497	3H-3WR	21.779	122	287	138	54	26	
CRS585	3H-3WR	21.513	122	550	209	31	13	
TX642	3H-3WR	21.627	122	273				
CRS508	4H-6WR	34.205	198	475	247	91	92	
CRS563	4H-6WR	34.332	198	490	290	131	132	
TX635	4H-6WR	34.383	198	492				
TX645	4H-6WR	34.269	198	427				
CRS584	6H-8WR	52.886	325	466	183	17	45	
CRS504	8H-7WR	71.609	439	695	304	258	273	
CRS578	8H-7WR	71.355	439	766	315	311	329	
CRS569	9H-5WR	80.113	489	797	435	471	527	535
TX646	9H-5WR	80.252	489	788				
CRS491	13H-3WR	115.654	729	875	498	559	695	630
CRS493	13H-3WR	115.603	729	962	438	517	649	585
CRS567	13H-3WR	115.413	729	1332	606	520	643	584
CRS495	17H-3WR	136.556	875	1095	199		332	439
CRS564	17H-3WR	136.467	875	1707	351		271	354

Table 6.2: Estimated preconsolidation pressures

Test Name	Hole	Depth (mbsf)	OCR				
			strain energy	lab e_o	MAD e_o	LWD e_o	wireline e_o
CRS580	1H-4WR	6.938	7.27	3.49	1.75	0.20	
CRS608	1H-4WR (H)	6.976	9.30	4.02	1.18	0.10	
TX643	1H-4WR	7.141	5.23				
CRS497	3H-3WR	21.779	2.36	1.13	0.44	0.21	
CRS585	3H-3WR	21.513	4.52	1.72	0.26	0.11	
TX642	3H-3WR	21.627	2.24				
CRS508	4H-6WR	34.205	2.40	1.25	0.46	0.46	
CRS563	4H-6WR	34.332	2.48	1.47	0.66	0.67	
TX635	4H-6WR	34.383	2.49				
TX645	4H-6WR	34.269	2.15				
CRS584	6H-8WR	52.886	1.44	0.57	0.05	0.14	
CRS504	8H-7WR	71.609	1.58	0.69	0.59	0.62	
CRS578	8H-7WR	71.355	1.74	0.72	0.71	0.75	
CRS569	9H-5WR	80.113	1.63	0.89	0.96	1.08	1.09
TX646	9H-5WR	80.252	1.61				
CRS491	13H-3WR	115.654	1.20	0.68	0.77	0.95	0.86
CRS493	13H-3WR	115.603	1.32	0.60	0.71	0.89	0.80
CRS567	13H-3WR	115.413	1.83	0.83	0.71	0.88	0.80
CRS495	17H-3WR	136.556	1.25	0.23		0.38	0.50
CRS564	17H-3WR	136.467	1.95	0.40		0.31	0.40

Table 6.3: Estimated overconsolidation ratios (OCRs)

Test Name	Hole	Depth (mbsf)	in-situ void ratio			
			lab	MAD	LWD	wireline
CRS580	1H-4WR	6.938	1.566	1.671	2.179	
CRS608	1H-4WR (H)	6.976	1.418	1.671	2.179	
CRS497	3H-3WR	21.779	1.608	1.872	2.076	
CRS585	3H-3WR	21.513	1.433	1.872	2.076	
CRS508	4H-6WR	34.205	1.659	1.958	1.983	
CRS563	4H-6WR	34.332	1.715	1.958	1.956	
CRS584	6H-8WR	52.886	1.667	2.239	1.983	
CRS504	8H-7WR	71.609	1.532	1.577	1.561	
CRS578	8H-7WR	71.355	1.573	1.577	1.561	
CRS569	9H-5WR	80.113	1.510	1.488	1.456	1.451
CRS491	13H-3WR	115.654	1.402	1.372	1.319	1.343
CRS493	13H-3WR	115.603	1.414	1.372	1.319	1.343
CRS567	13H-3WR	115.413	1.334	1.372	1.319	1.343
CRS495	17H-3WR	136.556	1.377		1.280	1.227
CRS564	17H-3WR	136.467	1.229		1.280	1.227

Table 6.4: In-situ void ratios from different measurement methods

Test Name	Hole	Depth (mbsf)	σ'_{vo} (kPa)	σ'_p (kPa)				
				strain energy	strain energy upper lim.	strain energy lower lim.	lab e_o	wireline e_o
CRS580	1H-4WR	6.938	32	235	75	33	113	
TX643	1H-4WR	7.141	32	170	54	24		
CRS497	3H-3WR	21.779	122	287	92	40	138	
CRS585	3H-3WR	21.513	122	550	176	77	209	
TX642	3H-3WR	21.627	122	273	87	38		
CRS508	4H-6WR	34.205	198	475	152	66	247	
CRS563	4H-6WR	34.332	198	490	157	69	290	
TX635	4H-6WR	34.383	198	492	158	69		
TX645	4H-6WR	34.269	198	427	137	60		
CRS584	6H-8WR	52.886	325	466	149	65	183	
CRS504	8H-7WR	71.609	439	695	223	97	304	
CRS578	8H-7WR	71.355	439	766	245	107	315	
CRS569	9H-5WR	80.113	489	797	255	112	435	535
TX646	9H-5WR	80.252	489	788	252	110		
CRS491	13H-3WR	115.654	729	875	280	122	498	630
CRS493	13H-3WR	115.603	729	962	308	135	438	585
CRS567	13H-3WR	115.413	729	1332	426	186	606	584
CRS495	17H-3WR	136.556	875	1095	351	153	199	439
CRS564	17H-3WR	136.467	875	1707	546	239	351	354

Table 6.5: Preconsolidation pressures with upper and lower limit factors applied

Test Name	Hole	Depth (mbsf)	OCR				
			strain energy	strain energy upper lim.	strain energy lower lim.	lab e_o	wireline e_o
CRS580	1H-4WR	6.938	7.27	2.30	1.01	3.49	
TX643	1H-4WR	7.141	5.23	1.65	0.72		
CRS497	3H-3WR	21.779	2.36	0.76	0.33	1.13	
CRS585	3H-3WR	21.513	4.52	1.45	0.64	1.72	
TX642	3H-3WR	21.627	2.24	0.72	0.31		
CRS508	4H-6WR	34.205	2.40	0.77	0.34	1.25	
CRS563	4H-6WR	34.332	2.48	0.79	0.35	1.47	
TX635	4H-6WR	34.383	2.49	0.80	0.35		
TX645	4H-6WR	34.269	2.15	0.69	0.30		
CRS584	6H-8WR	52.886	1.44	0.46	0.20	0.57	
CRS504	8H-7WR	71.609	1.58	0.51	0.22	0.69	
CRS578	8H-7WR	71.355	1.74	0.56	0.24	0.72	
CRS569	9H-5WR	80.113	1.63	0.52	0.23	0.89	1.09
TX646	9H-5WR	80.252	1.61	0.52	0.23		
CRS491	13H-3WR	115.654	1.20	0.38	0.17	0.68	0.86
CRS493	13H-3WR	115.603	1.32	0.42	0.18	0.60	0.80
CRS567	13H-3WR	115.413	1.83	0.59	0.26	0.83	0.80
CRS495	17H-3WR	136.556	1.25	0.40	0.18	0.23	0.50
CRS564	17H-3WR	136.467	1.95	0.62	0.27	0.40	0.40

Table 6.6: Overconsolidation ratios with upper and lower limit factors applied

Soil Sample	Depth (mbsf)	Layer
1244B-1H-4WR	5.70	A
1244B-3H-3WR	20.30	
1244B-4H-6WR	32.98	B
1244B-6H-8WR	52.81	
1244C-8H-7WR	70.88	
1244C-9H-5WR	79.05	
1244C-13H-3WR	114.20	
1244C-17H-3WR	135.55	

Table 6.7: Hydrate Ridge deposit layer subdivision

	S	m
Hydrate Ridge-Layer A	0.35	0.94
Hydrate Ridge-Layer B	0.31	0.94
Homogenous CL/CH sedimentary clay (*Ladd, 1991*)	$0.2+0.05I_p$	$0.88(1-C_s/C_c)$
Gulf of Mexico Clay (*Sutabutr, 1999*)	0.25	
Boston Blue Clay (*Santagata, 2002)*	0.33	0.71

Table 6.8: SHANSEP parameters for Hydrate Ridge deposit and other soil types

Parameter	Physical Contribution/Meaning	Test Type
e_o	void ratio at reference stress on virgin compression line	consolidation tests (CRSC or oedometer)
λ	compressibility of virgin consolidated clays	
C	nonlinear volumetric swelling behavior	
n	nonlinear volumetric swelling behavior	
h	irrecoverable plastic strain	
K_{0NC}	K_0 for virgin consolidated clays	consolidation tests with horizontal stress measurements (Ko-oedometer or Ko-triaxial)
2G/K	ratio of elastic shear to bulk modulus (poisson's ratio for initial unload)	
ϕ'_{TC}	critical state friction angle in triaxial compression (large strain failure criterion)	undrained triaxial shear tests
ϕ'_{TE}	critical state friction angle in triaxial extension (large strain failure criterion)	
c	undrained shear strength (geometric of bounding surface)	
S_t	amount of postpeak strain softening in undrained triaxial compression	
ω	nonlinearity at small strains in undrained shear	
γ	shear-induced pore pressure for overconsolidated clay	
κ_o	small strain compressibility at load reversal	resonant column or cross-hole shear wave velocity type tests
ψ_o	rate of evolution of anisotropy (rotation and change in size of bounding surface)	drained triaxial shear tests

Table 6.9: MIT E-3 Soil Model Input Parameters

Characteristic	Parameter	Hydrate Ridge Layer A	Hydrate Ridge Layer B	Average Gulf Clay[1]	BBC Layer C[2]	BBC Layer D[2]	BBC Layer E[2]
Compression	λ	0.242	0.280	0.282	0.139	0.397	0.360
	e_o	1.671	1.917	1.490	1.333	1.833	2.167
	K_o	0.450	0.460	0.630	0.555	0.534	0.584
Swelling Characteristics	C	40.00	30.00	6.25	24.33	27.33	24.33
	n	1.55	1.55	1.53	1.53	1.60	1.60
Small Strain Stiffness	κ_o	0.0010	0.0010	0.0065	0.0009	0.0010	0.0010
	ω	1.00	3.00	0.39	1.17	1.20	1.30
	2G/K	1.4348	1.2000	0.9230	0.9811	1.0830	0.9155
Strength	ϕ_{TC}	35.69	33.07	25.6	32.17	34.86	36.71
	ϕ_{TE}	53.08	42.90	27.8	37.26	31.84	32.36
	c	0.670	0.600	0.785	0.697	0.677	0.703
	S_t	1.65	1.80	3.10	1.98	3.17	2.50
Bounding Plasticity	γ	0.30	0.50	0.50	0.30	0.15	0.11
	h	0.08	0.03	0.30	0.20	0.20	0.01
	ψ	60	60	100	60	35	21

[1]: Sutabutr, 1999
[2]: Korchaiyapruk, 1998

Table 6.10: Summary of MIT E-3 Input Parameters

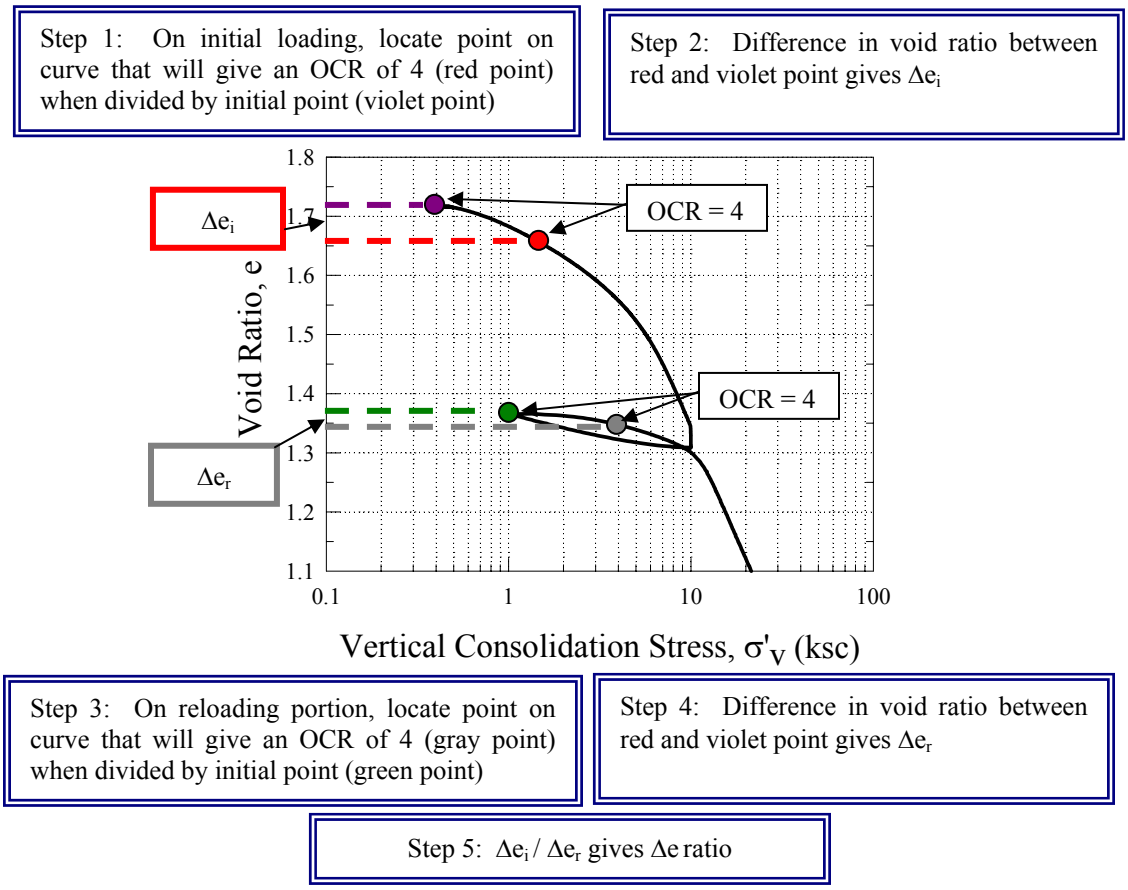

Figure 6.1: Steps for calculating Δe ratio

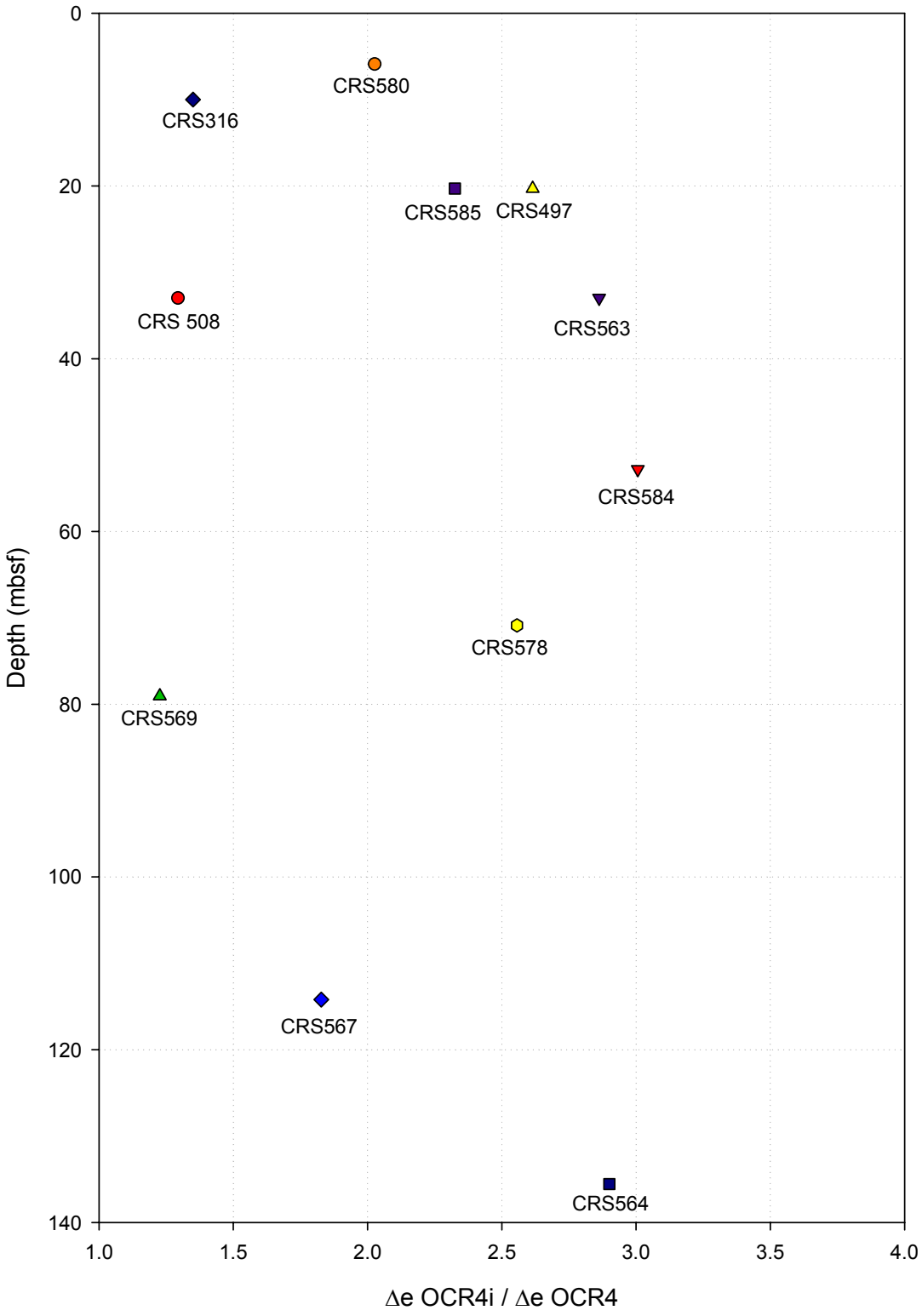

Figure 6.2: Δe ratio as an indicator of soil quality

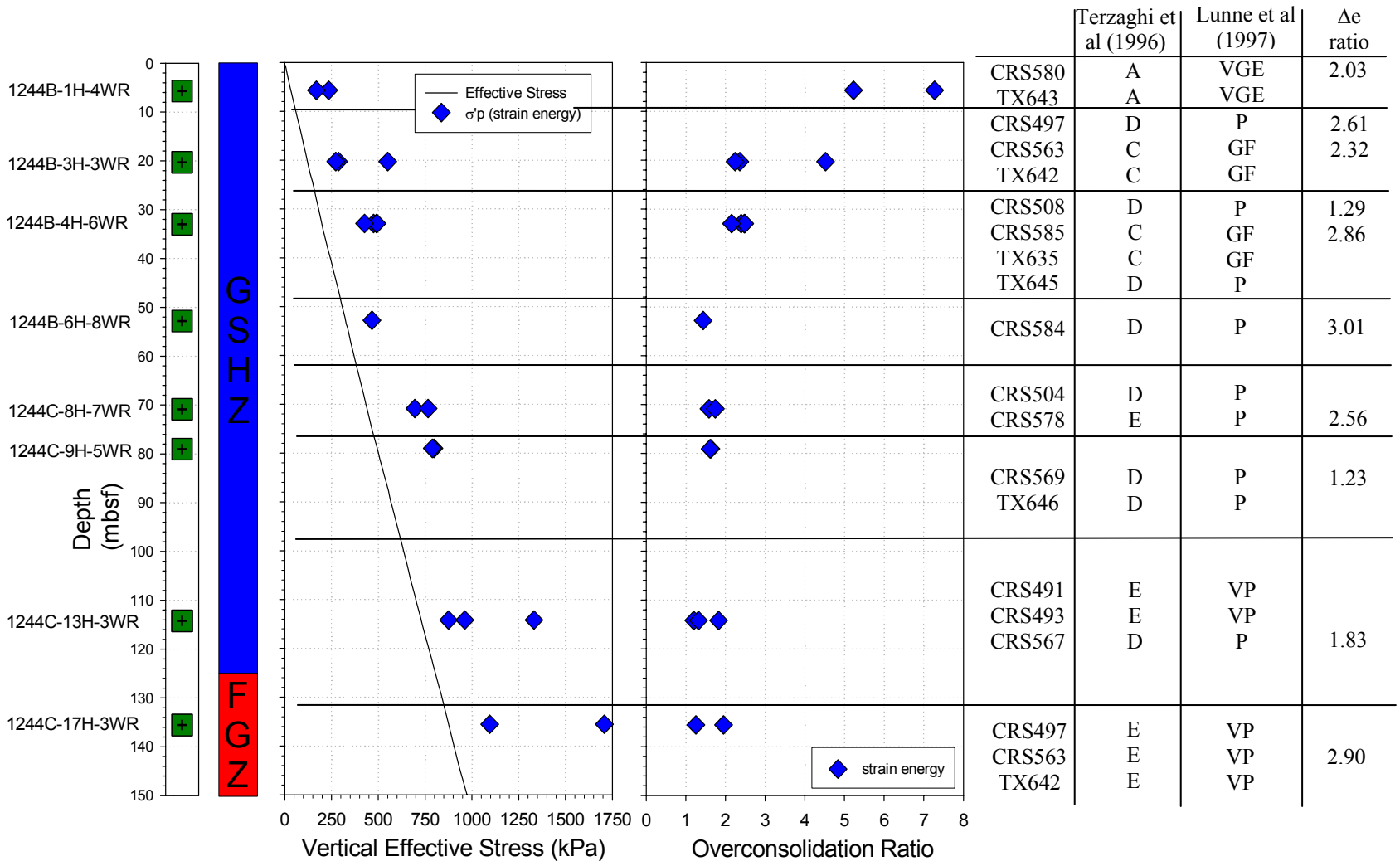

	Terzaghi et al (1996)	Lunne et al (1997)	Δe ratio
CRS580	A	VGE	2.03
TX643	A	VGE	
CRS497	D	P	2.61
CRS563	C	GF	2.32
TX642	C	GF	
CRS508	D	P	1.29
CRS585	C	GF	2.86
TX635	C	GF	
TX645	D	P	
CRS584	D	P	3.01
CRS504	D	P	
CRS578	E	P	2.56
CRS569	D	P	1.23
TX646	D	P	
CRS491	E	VP	
CRS493	E	VP	
CRS567	D	P	1.83
CRS497	E	VP	
CRS563	E	VP	2.90
TX642	E	VP	

Figure 6.3: Stress history profile based on strain energy method

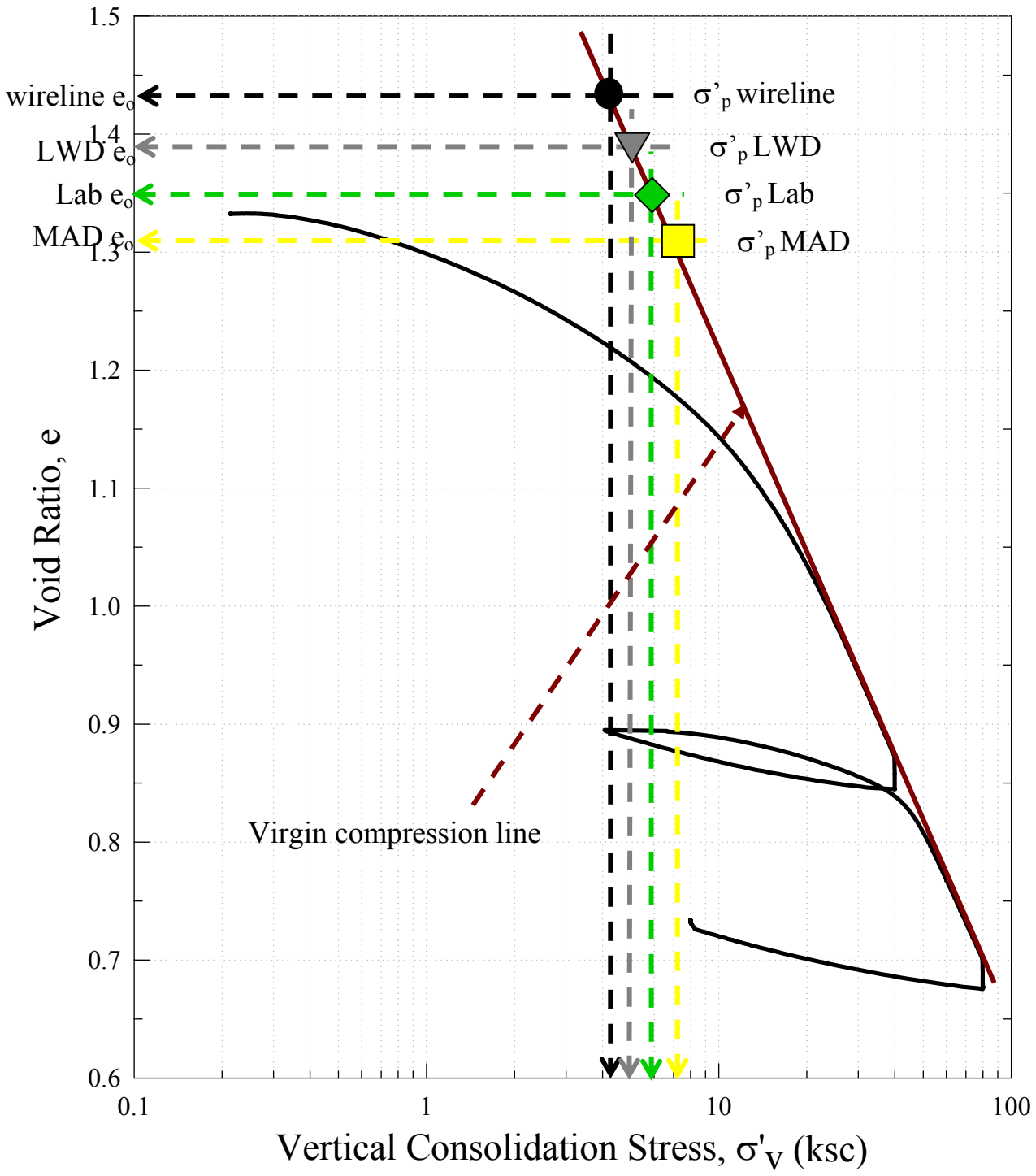

Figure 6.4: Extrapolation to initial void ratio to get preconsolidation pressure

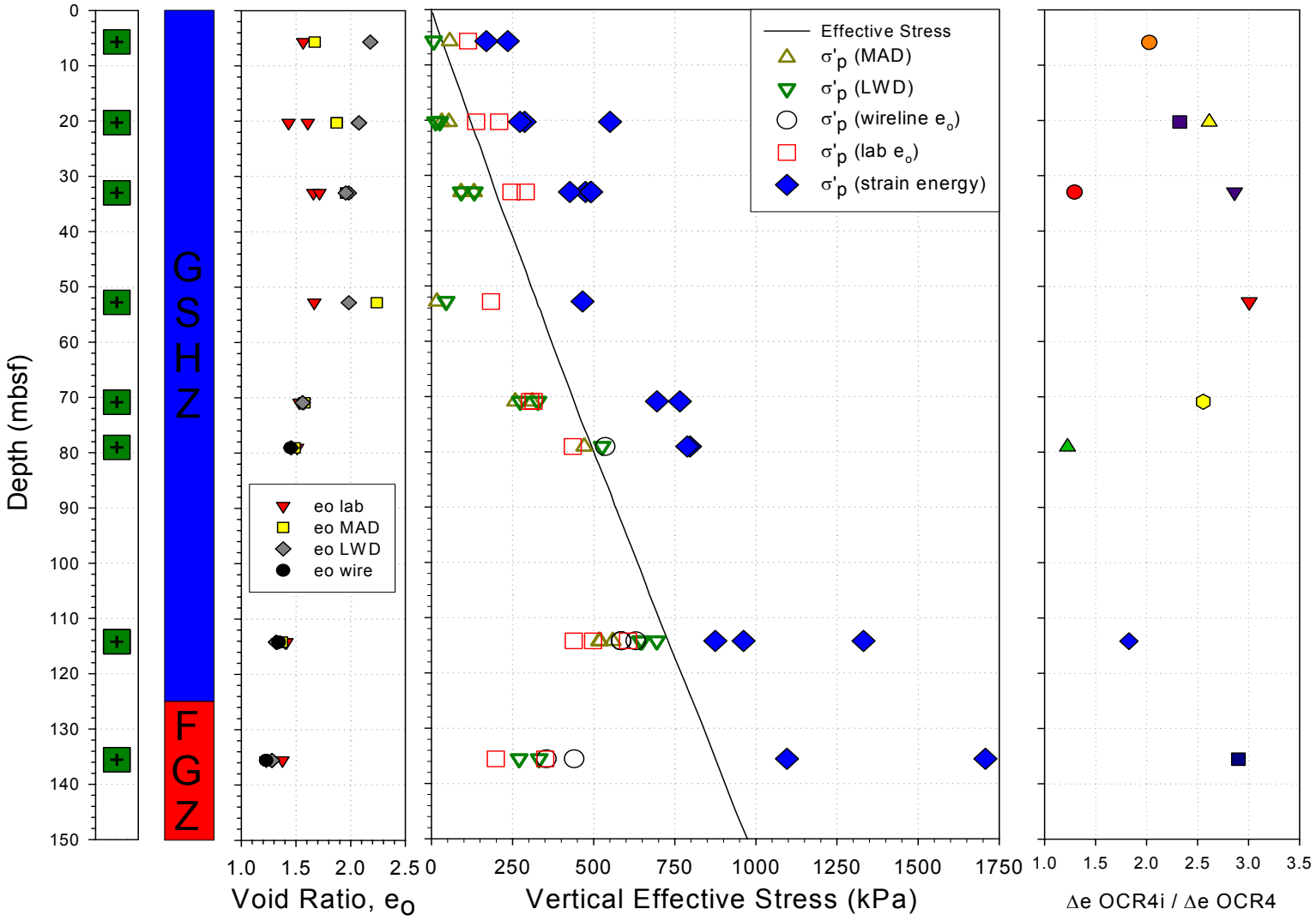

Figure 6.5: In-situ void ratios and extrapolated maximum past pressure

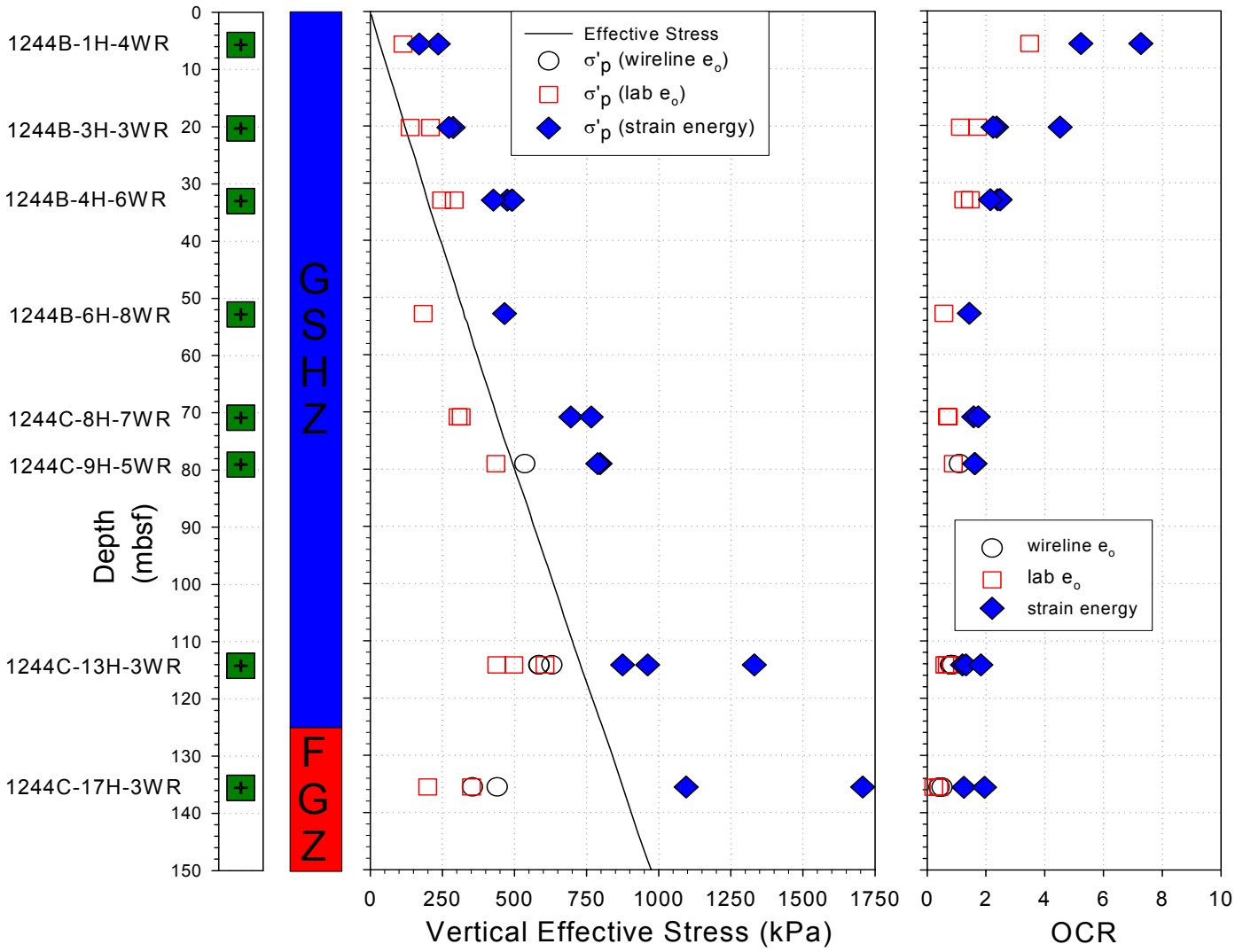

Figure 6.6: Stress history profile

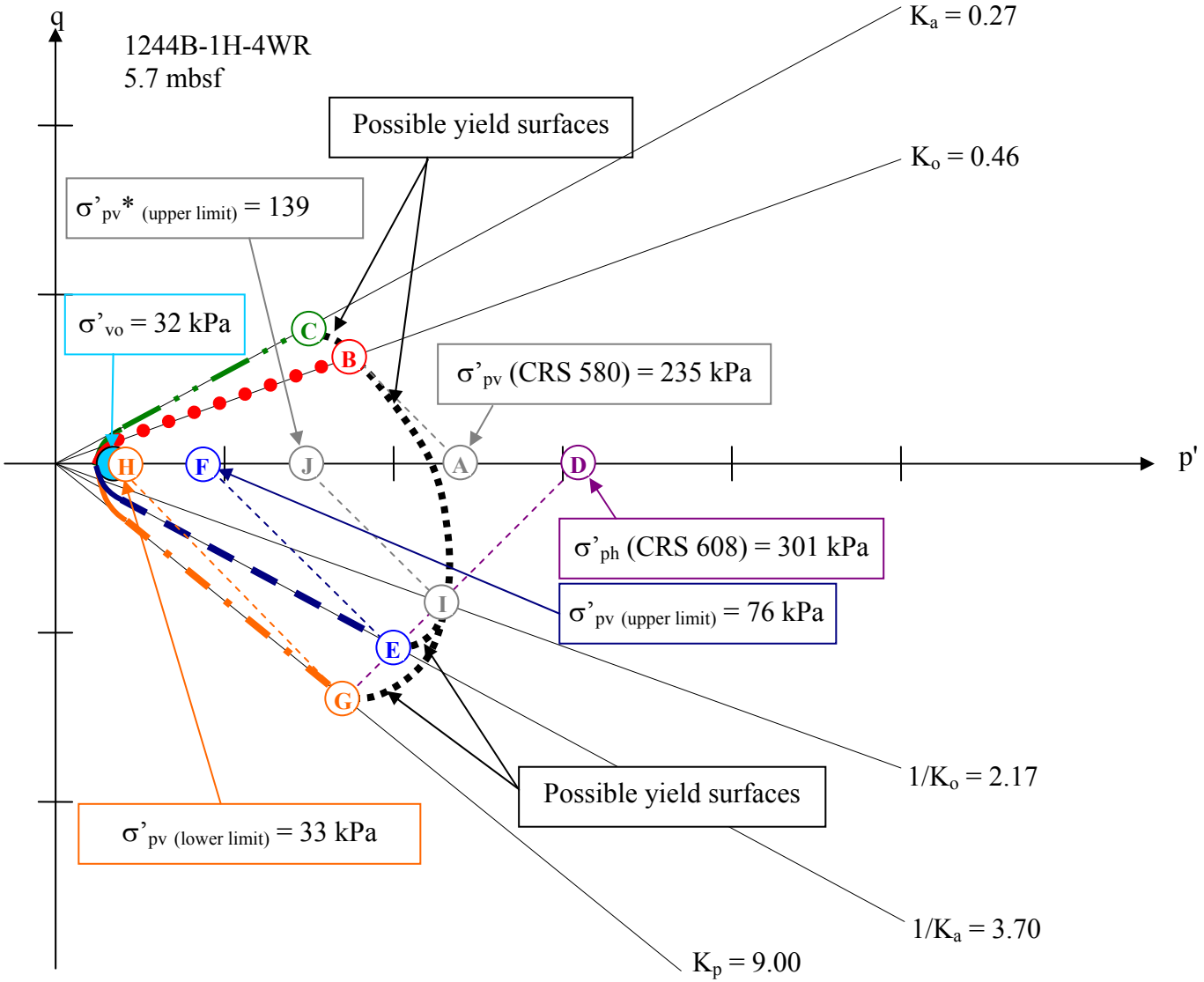

Figure 6.7: Possible shape of yield surface for samples from 1244B-1H-4WR

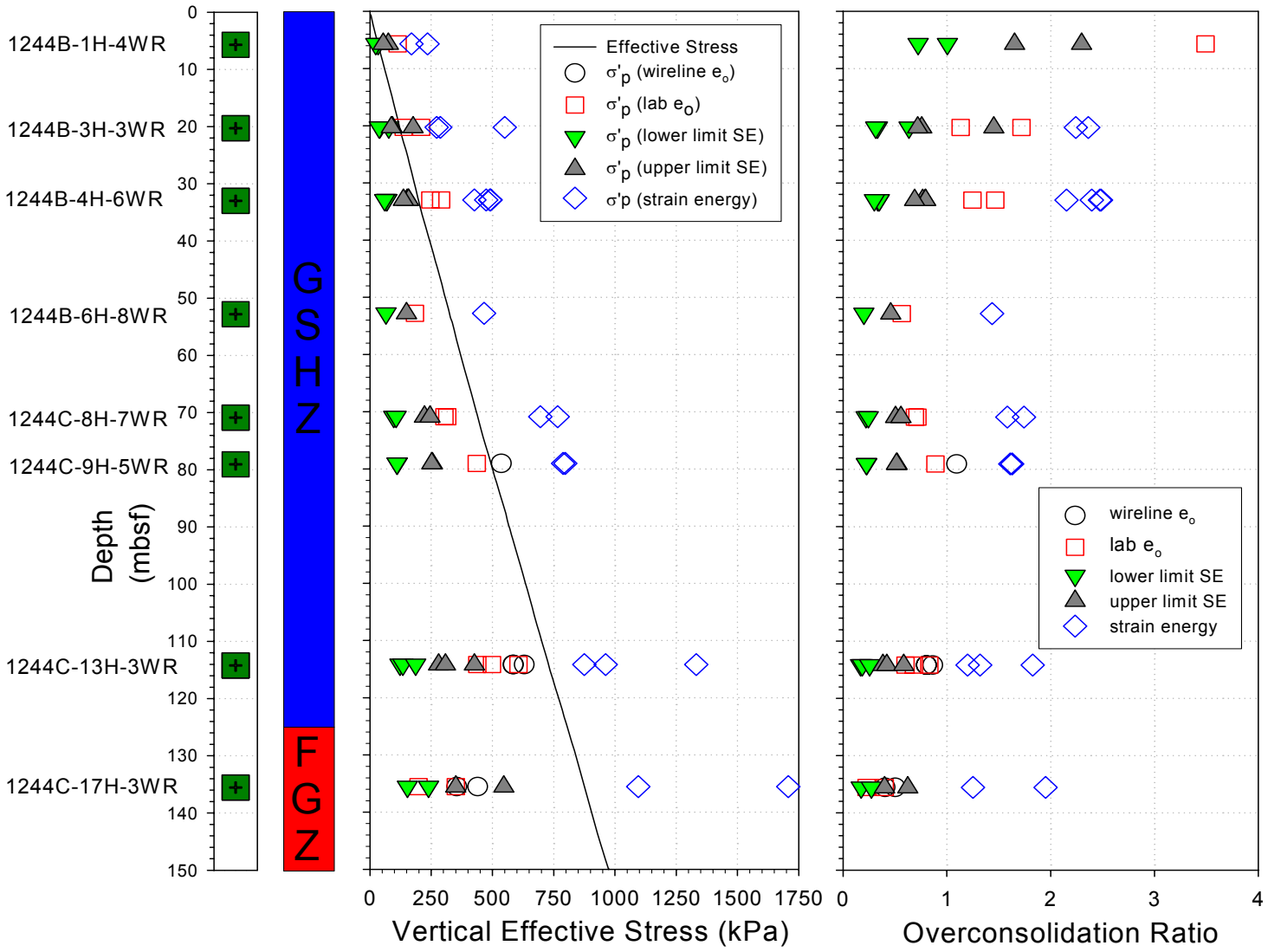

Figure 6.8: Stress history profile with upper and lower limit factors applied

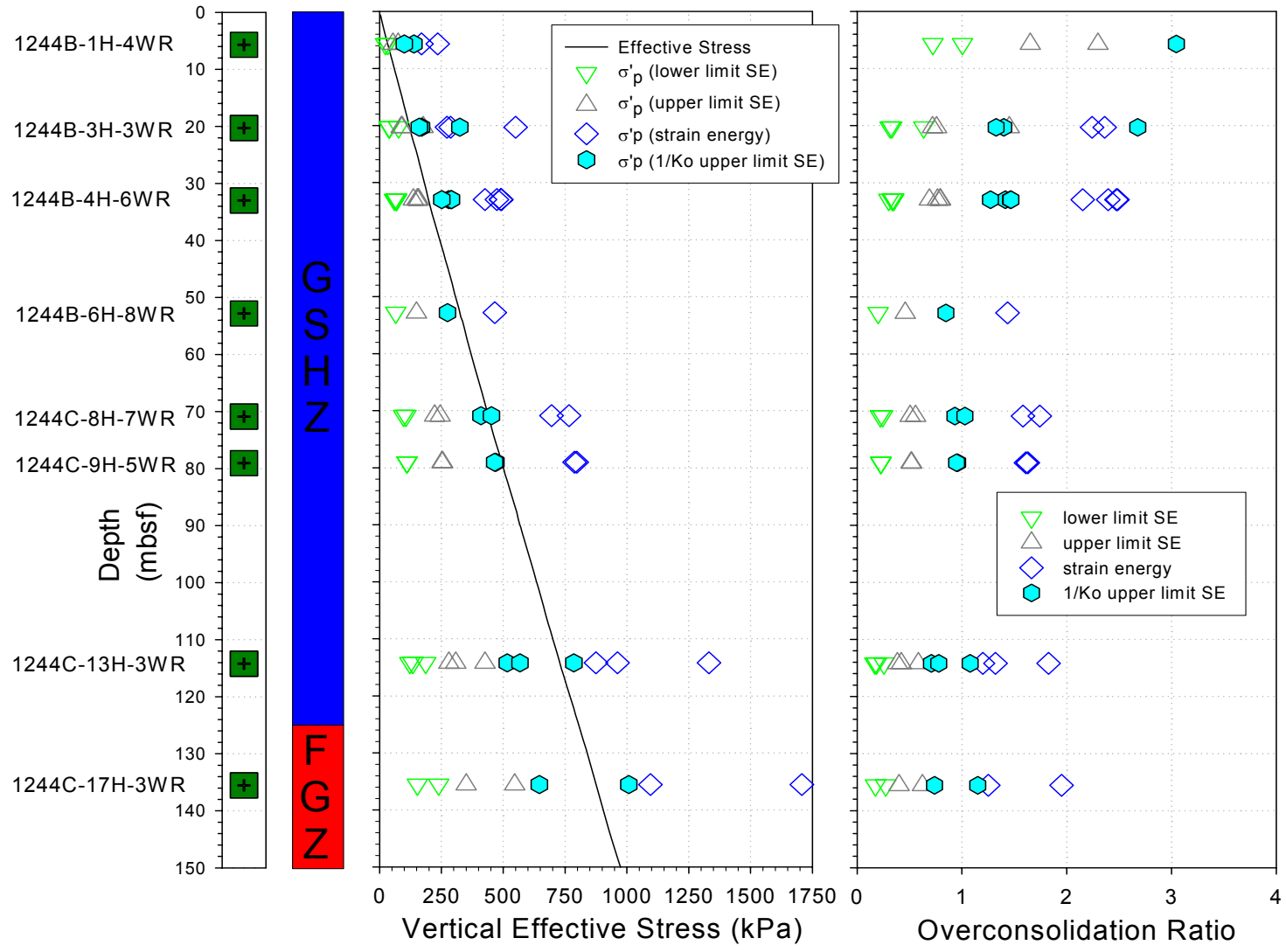

Figure 6.9: Stress history profile with $1/K_o$ upper limit factor applied

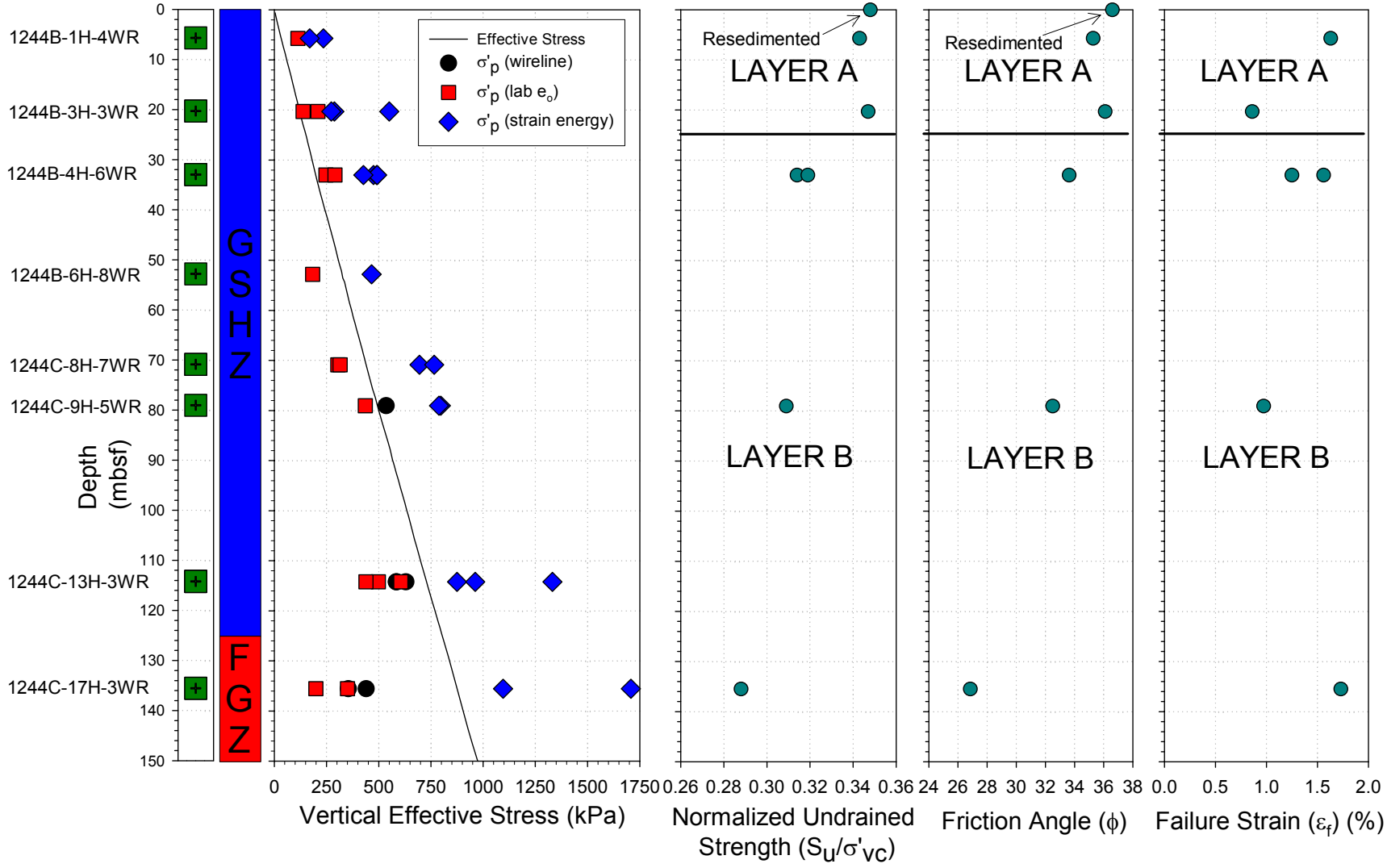

Figure 6.10: Layer division for Hydrate Ridge deposit

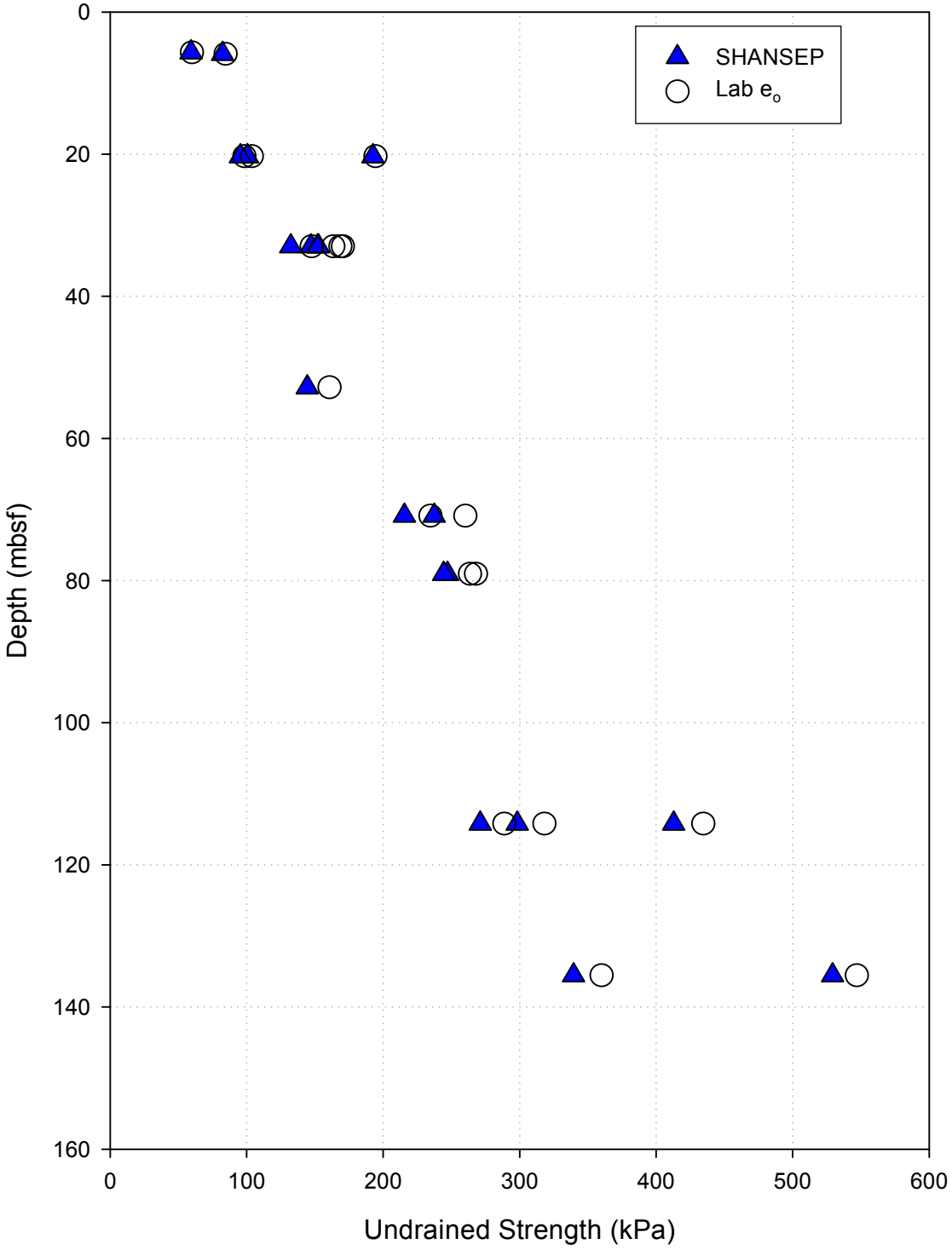

Figure 6.11: Undrained strength profile using the SHANSEP equation and void ratio extrapolation

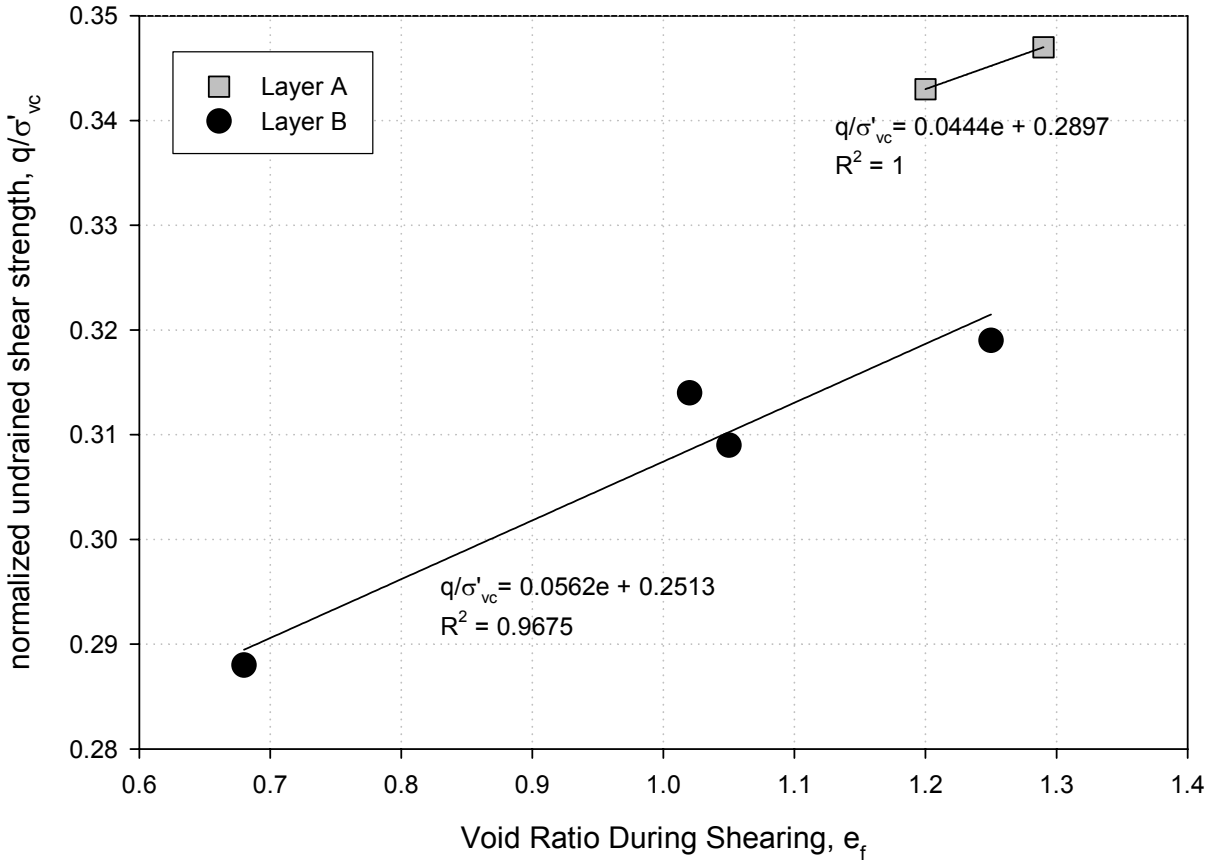

Figure 6.12: Void ratio during shearing vs. normalized undrained shear strength

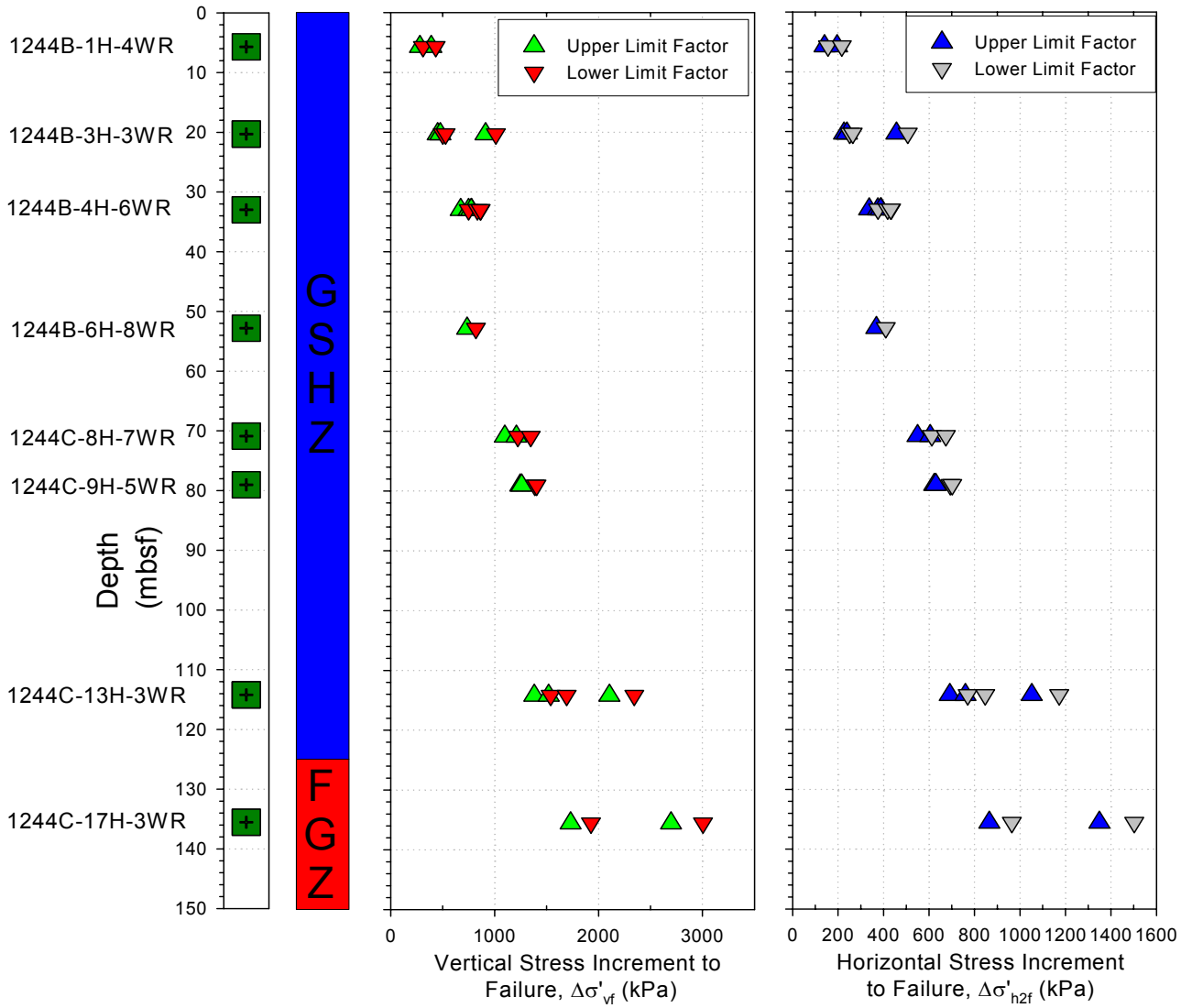

Figure 6.13: Stress increment to failure

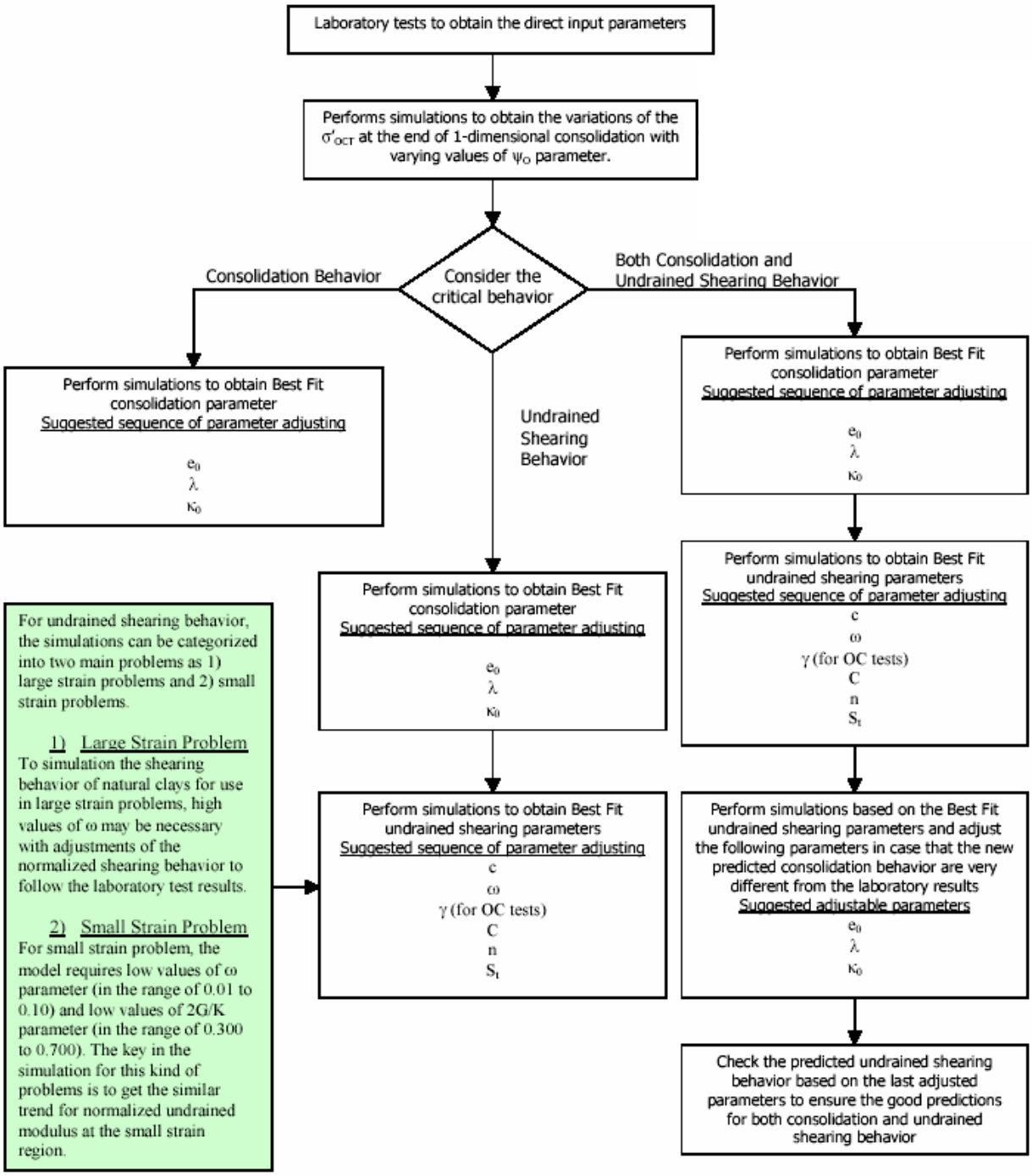

Figure 6.14: Flowchart showing the framework for selection of MIT E-3 model input parameters (*Korchaiyapruk, 2000*)

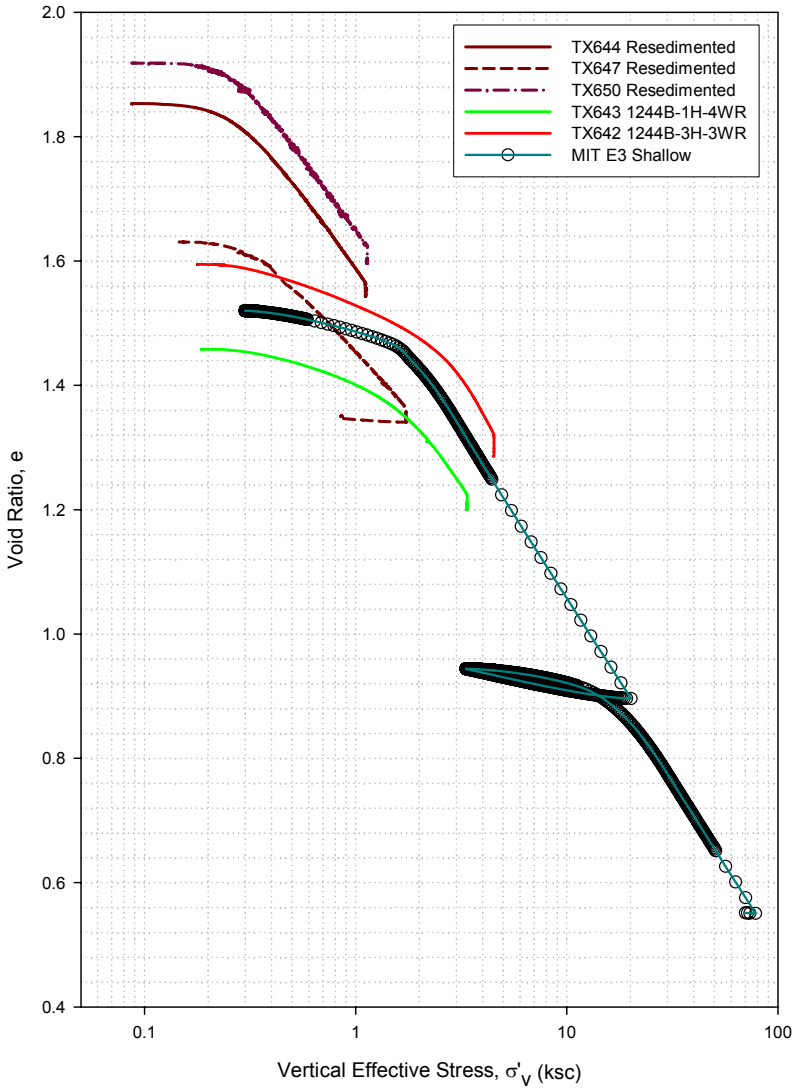

Figure 6.15: MIT E-3 best-fit consolidation curve—Layer A

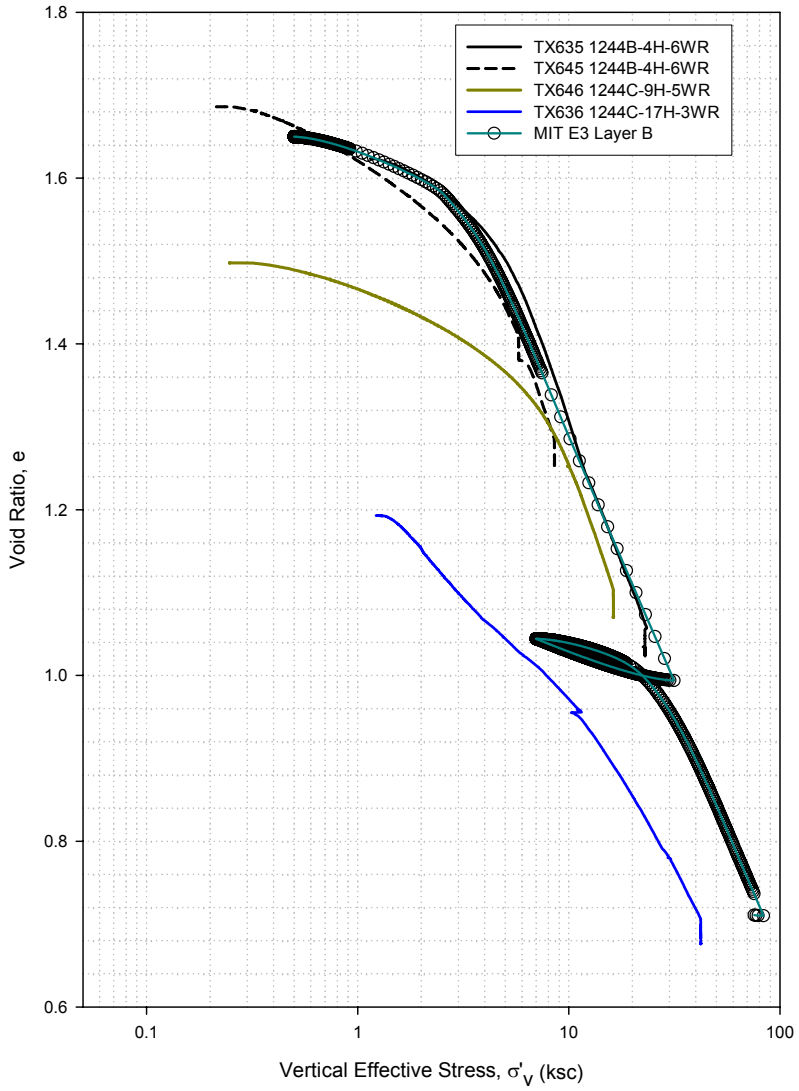

Figure 6.16: MIT E-3 best-fit consolidation curve—Layer B

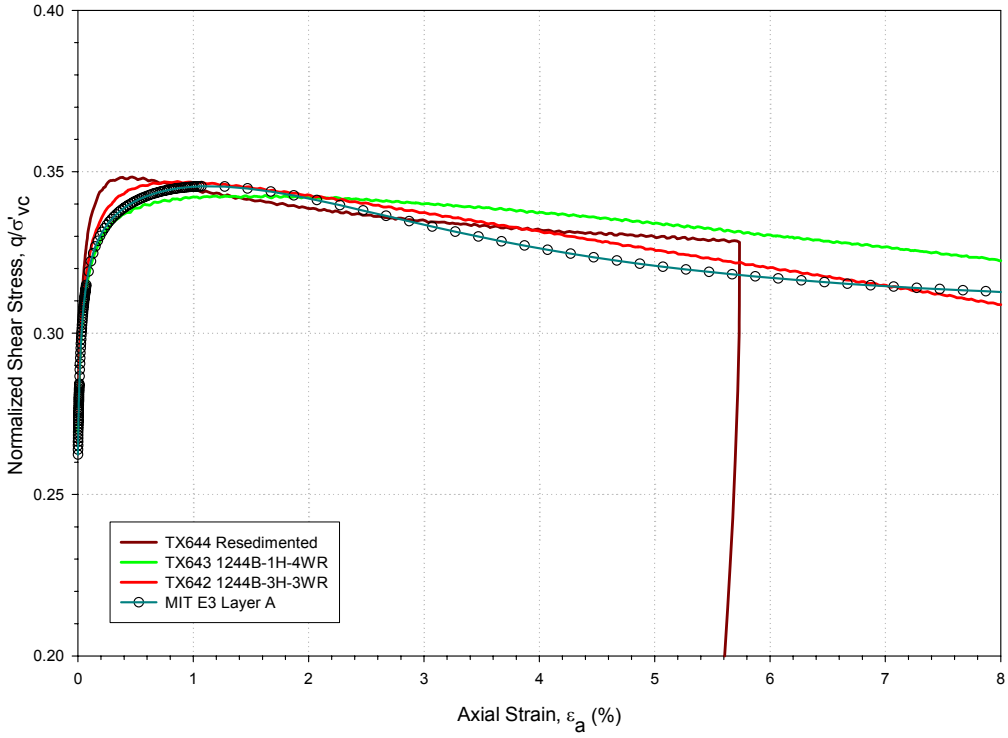

Figure 6.17: MIT E-3 best-fit stress-strain curve—Layer A

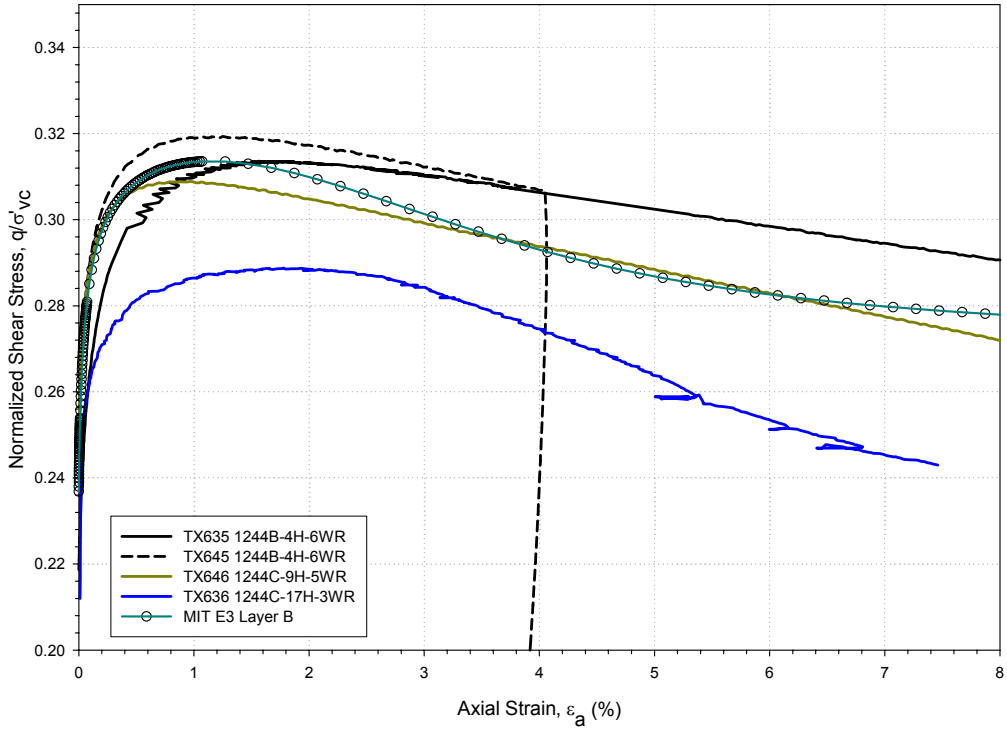

Figure 6.18: MIT E-3 best-fit stress-strain curve—Layer B

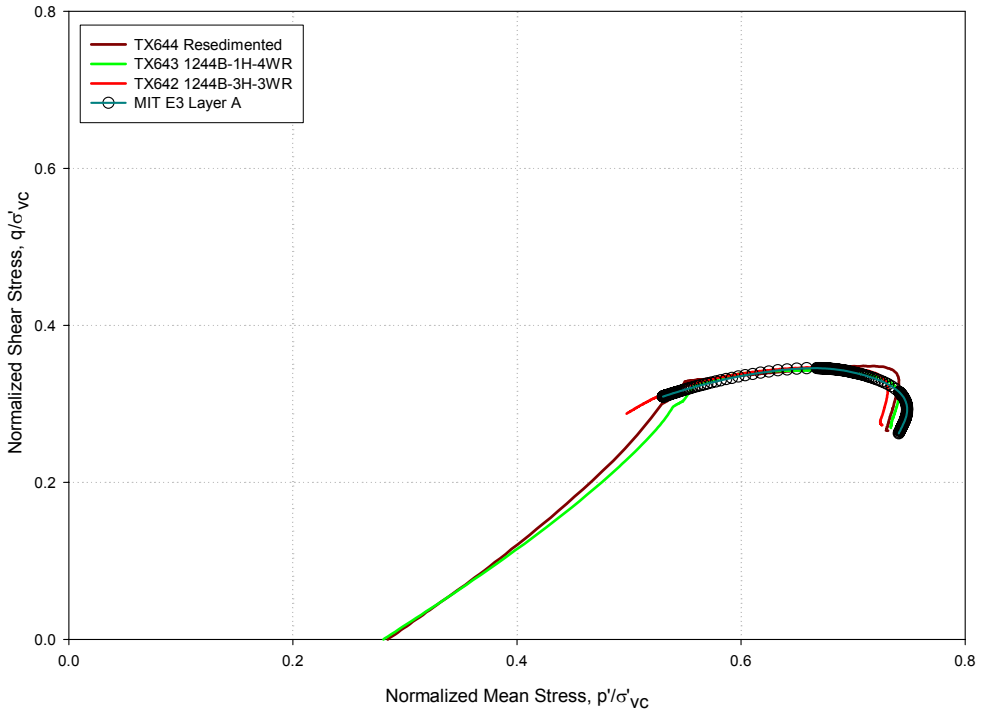

Figure 6.19: MIT E-3 best-fit shearing stress path—Layer A

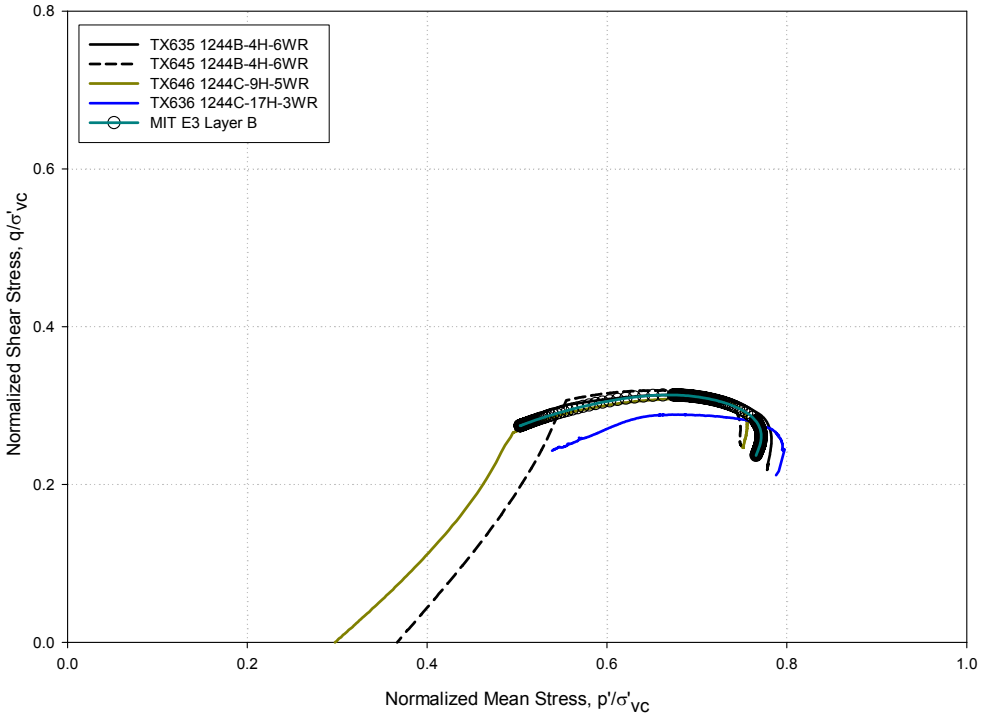

Figure 6.20: MIT E-3 best-fit shearing stress path—Layer B

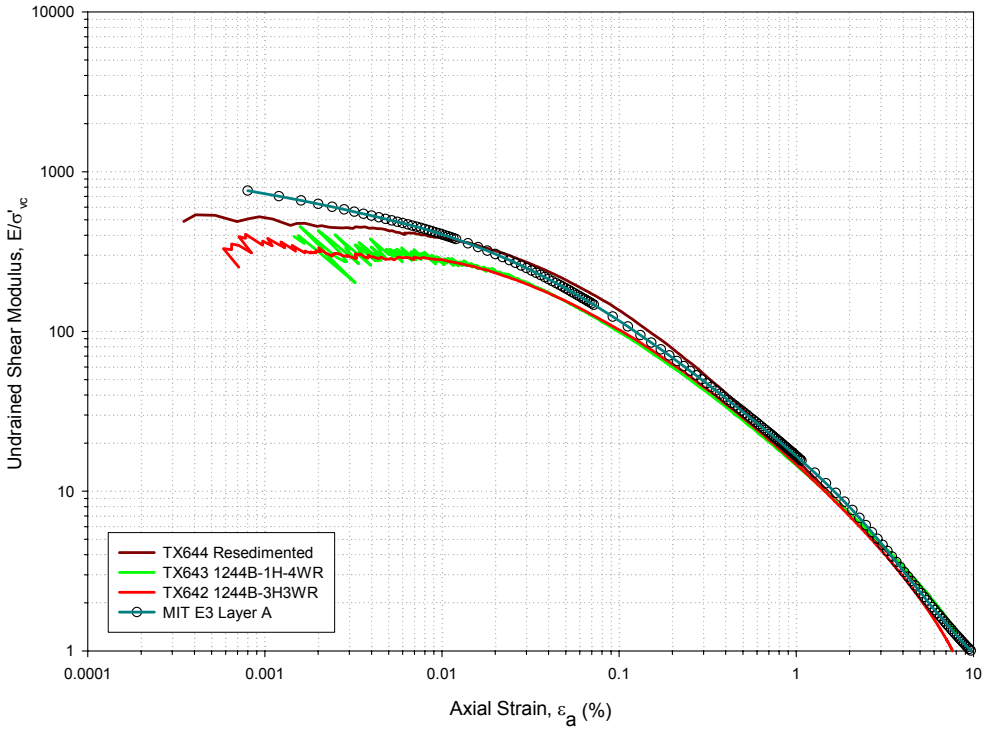

Figure 6.21: MIT E-3 best-fit undrained shear modulus curve—Layer A

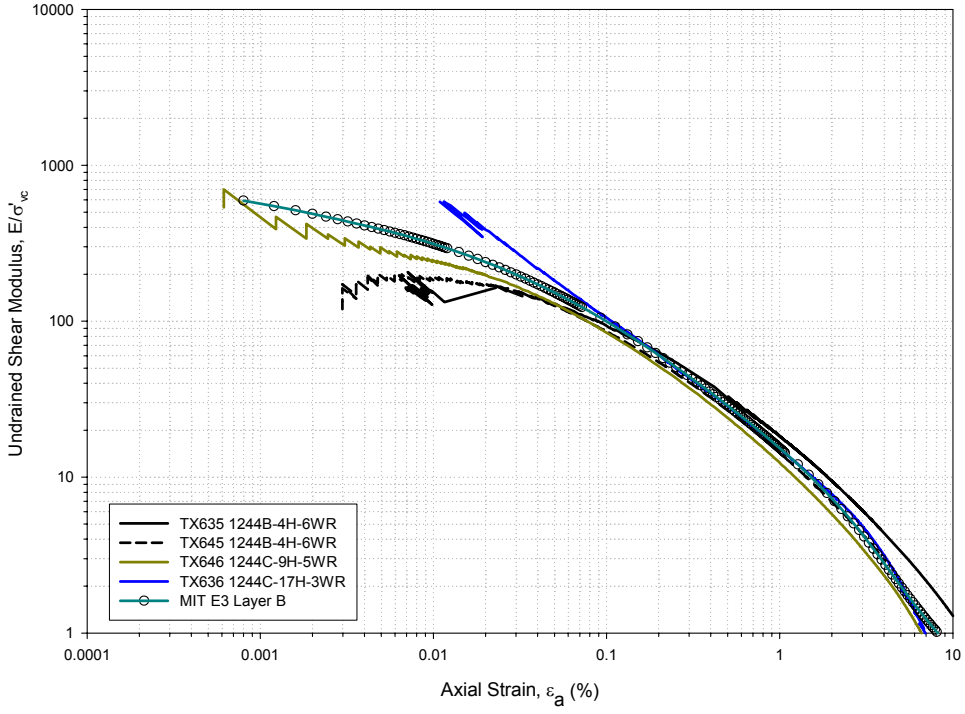

Figure 6.22: MIT E-3 best-fit undrained shear modulus curve—Layer B

Chapter 7: Conclusion

Eight whole care sediment samples obtained from Hydrate Ridge, Cascadia Continental Margin were provided to MIT in order to understand the stress history, consolidation behavior, and strength characteristics of the soil. To achieve this, a geotechnical testing program consisting of standard geotechnical laboratory tests was performed. The testing program included Atterberg limits and x-ray diffraction to classify the material, Constant Rate of Strain Consolidation (CRSC) tests to understand consolidation behavior, and K_o-Consolidated Undrained triaxial (CK_oU) tests to determine the strength characteristics.

The Atterberg limits have shown that the Hydrate Ridge soil is a dark greenish-gray, high plasticity silt (MH) based on USCS classification. The soil has been found to have 50% clay sized particles with an activity close to 1, which is typical of the clay mineral Illite. The soil exhibits an average liquid limit, plastic limit, and plasticity index of 82%, 38% and 44%, respectively. Performing atterberg limits on oven-dried samples dramatically affects the atterberg limits of the soil, as shown by the 17% reduction in the liquid limit for an oven-dried sample. This reduction in the liquid limit, together with an average loss on ignition of 5.45%, may indicate the presence of organic matter in the soil.

The samples provided by the ODP were highly disturbed, as shown by the cracks and voids in the tube x-rays. Further evidence of the poor soil quality is reflected in the rounded CRS consolidation curves. Application of the Terzaghi et al (1996) and Lunne et al (1997) criteria for classifying soil quality has confirmed that the soil is of poor quality. The only sample that exhibited good quality with respect to these two criteria is the shallowest sample. However, the difficulty with these two criteria is they are based on the strain to the in-situ stress without considering the shape of the undisturbed curve. As such a method involving comparison between the initial loading and unload-reload cycle was developed. This criterion, called the Δe ratio, has confirmed that most of the soil samples are highly disturbed. Interestingly, the Δe ratio does not agree with the two other criteria. As an example, the two criteria classify the shallowest sample as having good quality, but the Δe ratio classifies it as below average quality. Furthermore, the two criteria classify the sample at 79mbsf as poor quality, whereas the Δe ratio

considers this sample as the best among all the samples. Nonetheless, collectively, the criteria generally classify the soil as having poor quality. It must be noted however that these criteria are based on typical land-based application. It is not known though how these criteria would apply to oceanic sediments with high in-situ stress levels and varied consolidation conditions.

Because of the high level of disturbance and high in-situ stresses of the samples, the consolidation curves were very rounded and in most cases, the consolidation did not reach the normally consolidated state. In an attempt to obtain the complete consolidation curves, a small-diameter CRSC ring was used to be able to reach higher stresses. This proved successful as the normally consolidated state was reached for all but one sample (17H-3WR), thus allowing measurement of the consolidation properties. The in-situ hydraulic conductivity (k_o) is found to vary between $1.5x10^{-7}$ to $3x10^{-8}$ cm/s with no trend with depth. The compression ratio (C_c) ranges from 0.473 to 0.704 with an average of 0.600. C_c is fairly constant up to a depth of 79 mbsf, after which, C_c decreases.

Application of the strain energy method yield high preconsolidation pressures that indicate the soil is normally to slightly overconsolidated (1<OCR<2) in the deeper layers and overconsolidated (3<OCR<8) in the shallow layers. Due to concerns about the effect of disturbance on the estimated preconsolidation pressures using the strain energy method, an alternative method was used in order to provide a lower bound for the OCR estimate. This method involved extrapolating the virgin consolidation line to the in-situ void ratio to get a lower bound estimate of the preconsolidation pressure. Based on this method, the estimated OCRs is 1 ± 0.15, indicating that the deep deposit is normally to underconsolidated. However, this estimate is again based on normal land application context, i.e., K_o-condition.

A study by Chevallier et al (2003) has shown that Hydrate Ridge is undergoing passive loading, i.e., the deposit is being compressed laterally. If this were true, then it would be likely that the deposit is experiencing a higher horizontal stress than the vertical. As such, it was deemed necessary to examine the horizontal consolidation behavior. Therefore, a horizontally-oriented CRSC test was run in order to understand the in-situ stress state. The specimen was taken from the shallowest sample. The result of this test, coupled with an analysis of the predicted yield surface and stress path has shown that the horizontal effective stress is greater than the vertical effective stress. Though the stress path that the soil follows is not exactly known, it is believed to be bound by the $1/K_a$ and the K_p lines. The vertical effective stress from

the $1/K_a$ line provides an upper limit to the preconsolidation pressure, while the K_p line provides a lower limit. The result of this analysis implies that the estimated strain energy from the preconsolidation pressure is too high. By dividing the upper and lower limit of the preconsolidation pressure by the strain energy preconsolidation pressure for the shallowest specimen, an upper and lower limit factor is calculated that can be used to reduce the strain energy preconsolidation pressures. The result is a stress history profile that indicates underconsolidation. It is believe that the site is under a state of high lateral loading and underconsolidated because of the accretionary margin setting.

To reduce the effect of sample disturbance on the undrained strength properties, the SHANSEP testing methodology was used. This method involved K_o-consolidating the specimens to >10% strain, as prescribed by Ladd (1991). It has been proven that consolidation to this strain state is sufficient in minimizing the effect of sample disturbance on the undrained strength properties. Furthermore, the SHANSEP methodology was necessary to be able to use resedimented specimens for testing, which were essential due to the limited amount of good quality, "testable" soil. The soil for the resedimented specimens was taken from soil trimmings, highly disturbed samples, and previously tested specimens. The test results for the resedimented specimens exhibited good correlation with the shallow depth samples.

The results of the triaxial tests have shown that the Hydrate Ridge deposit may be divided into two layers; the shallow layer extends from the mudline to about 20mbsf and the deep layer extends below 20mbsf. The normally consolidated average normalized undrained strength for the shallow and deep layers are 0.35 and 0.31 respectively, which is similar to that of Boston Blue Clay. The average large strain friction angle in triaxial compression for the shallow layer is 36^o and 33^o for the deep layer.

The SHANSEP parameters were determined with S and m values of 0.35 and 0.94 respectively for the shallow layer, and S and m values of 0.31 and 0.94 respectively for the deep layer. Together with the site stress history, the SHANSEP parameters were used in the SHANSEP equation to estimate the strength profile of the site. Because the site is shown to be underconsolidated, the value of the OCR used is equal to 1.

The input parameters for the MIT E-3 soil model were determined for both layers using the "best-fit parameter" framework. These parameters may then be used in order to further understand the behavior of the soil. Furthermore, the soil model may be used to model the

behavior of a tool such as the tapered piezoprobe when inserted into the Hydrate Ridge soil. The model may also be used to analyze the strain path in order to understand the tube sampling disturbance.

Appendix A: Tube Radiographs

The following appendix contains positive prints of the x-ray negatives for each tube sample. Each print contains the date the tube was x-rayed, as well as the name of the tube. The first print gives the x-ray for the first nine inches (marker 0-9) of the tube, while the second print gives the x-ray for the next three inches, with a four inch overlap (5-C). A description of the x-ray procedures can be found in Section 3.2.

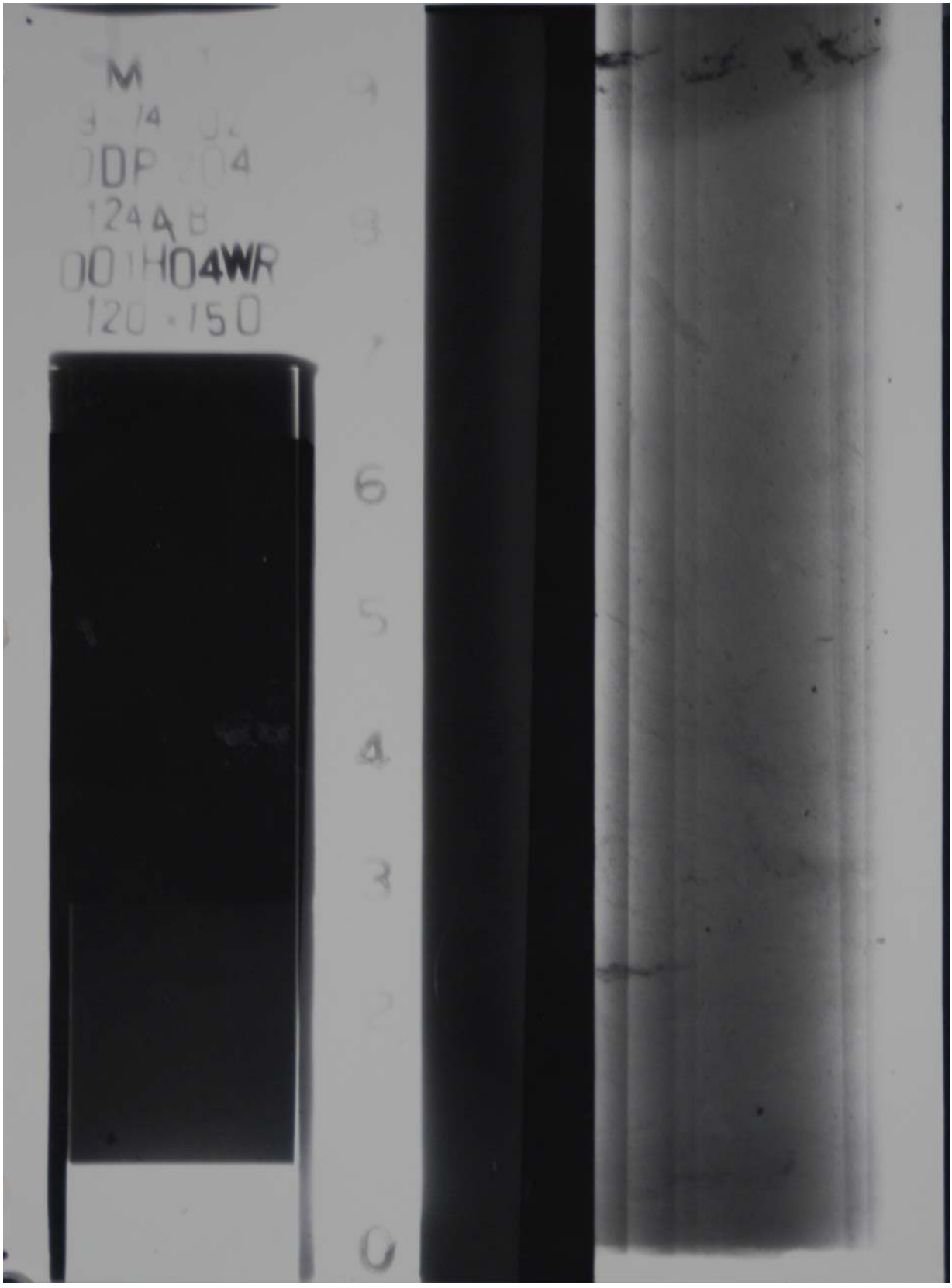

1244B-1H-4WR 1st Print

1244B-1H-4WR 2nd Print

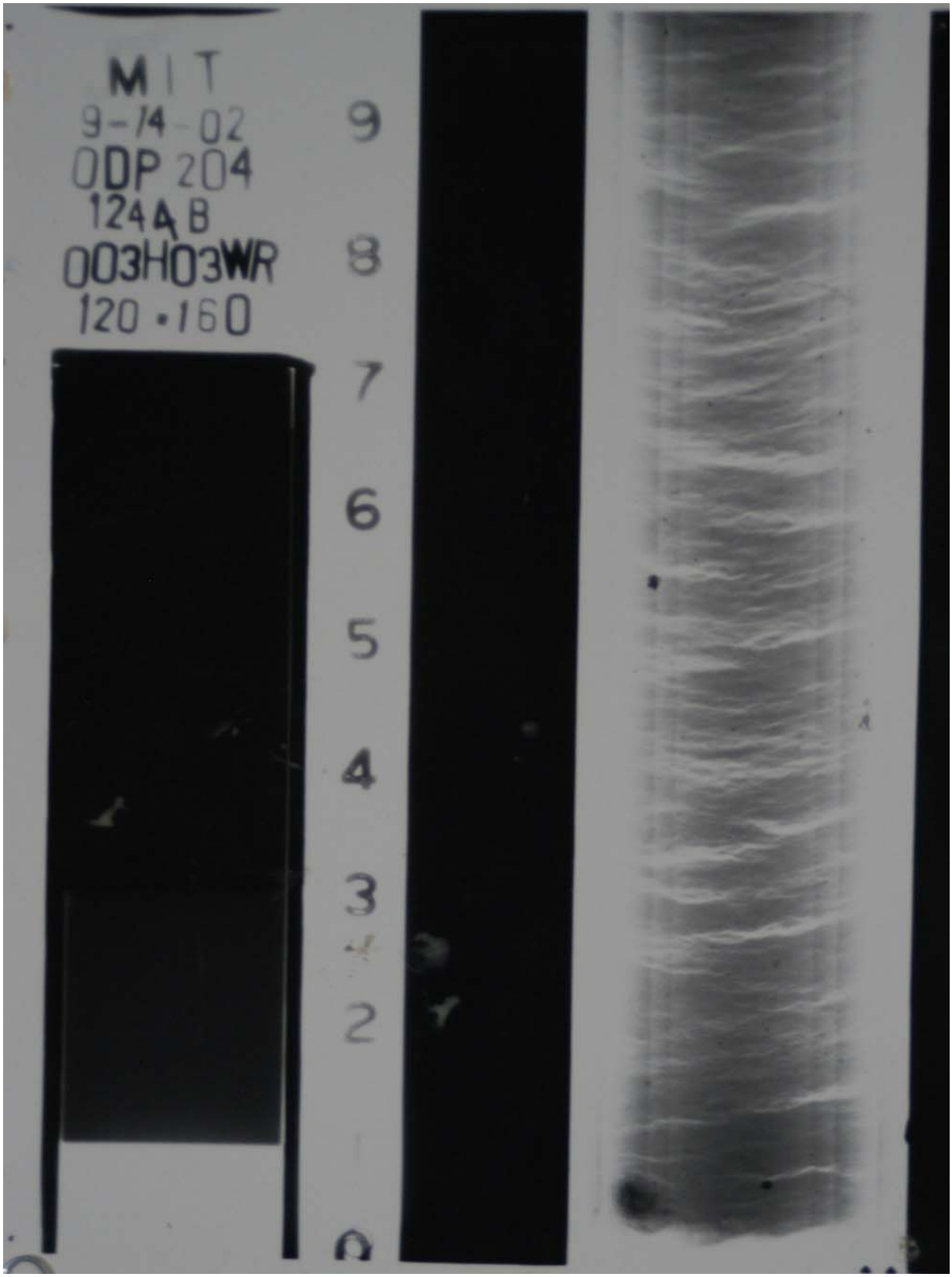

1244B-3H-3WR 1st Print

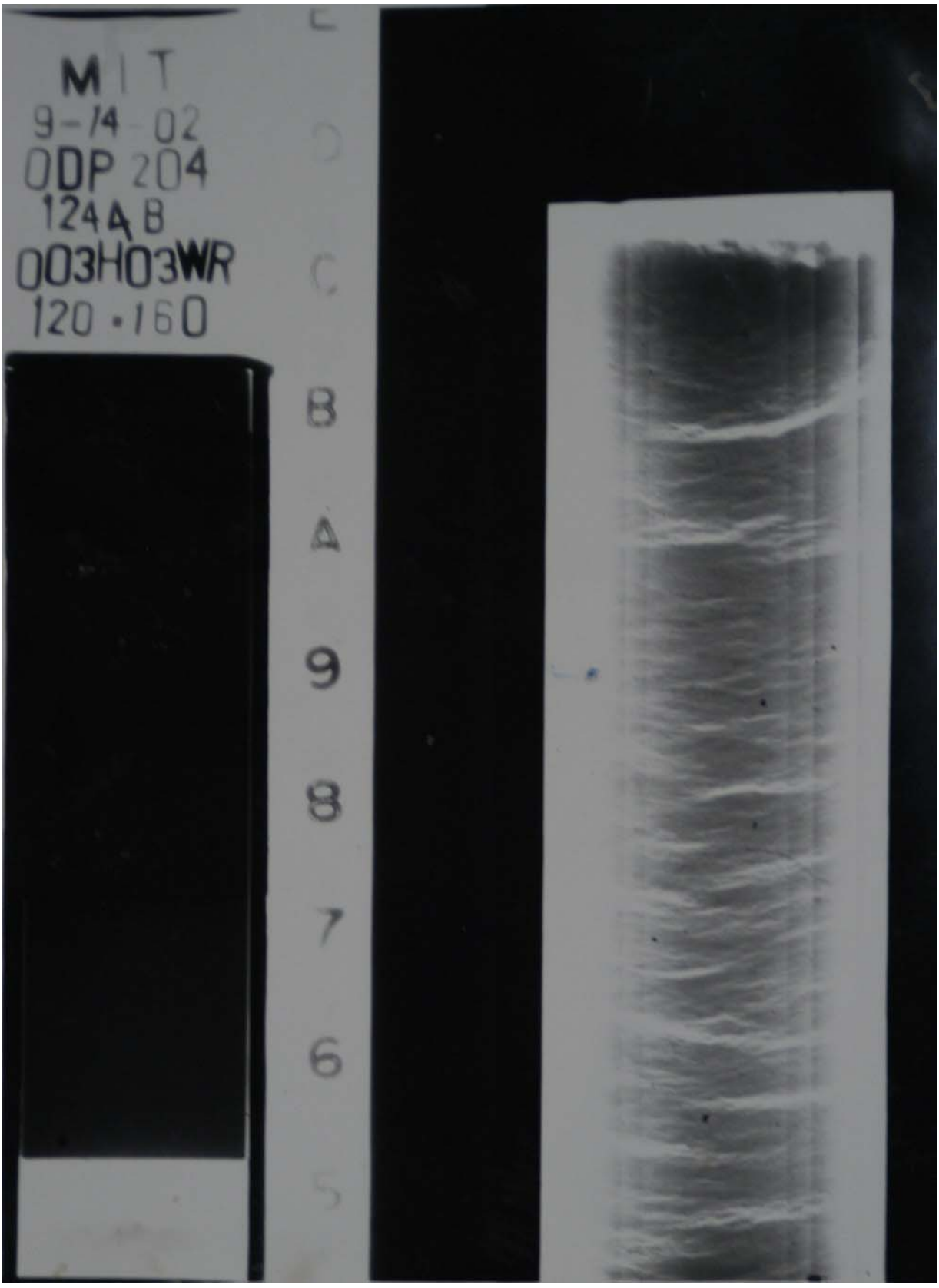

1244B-3H-3WR 2nd Print

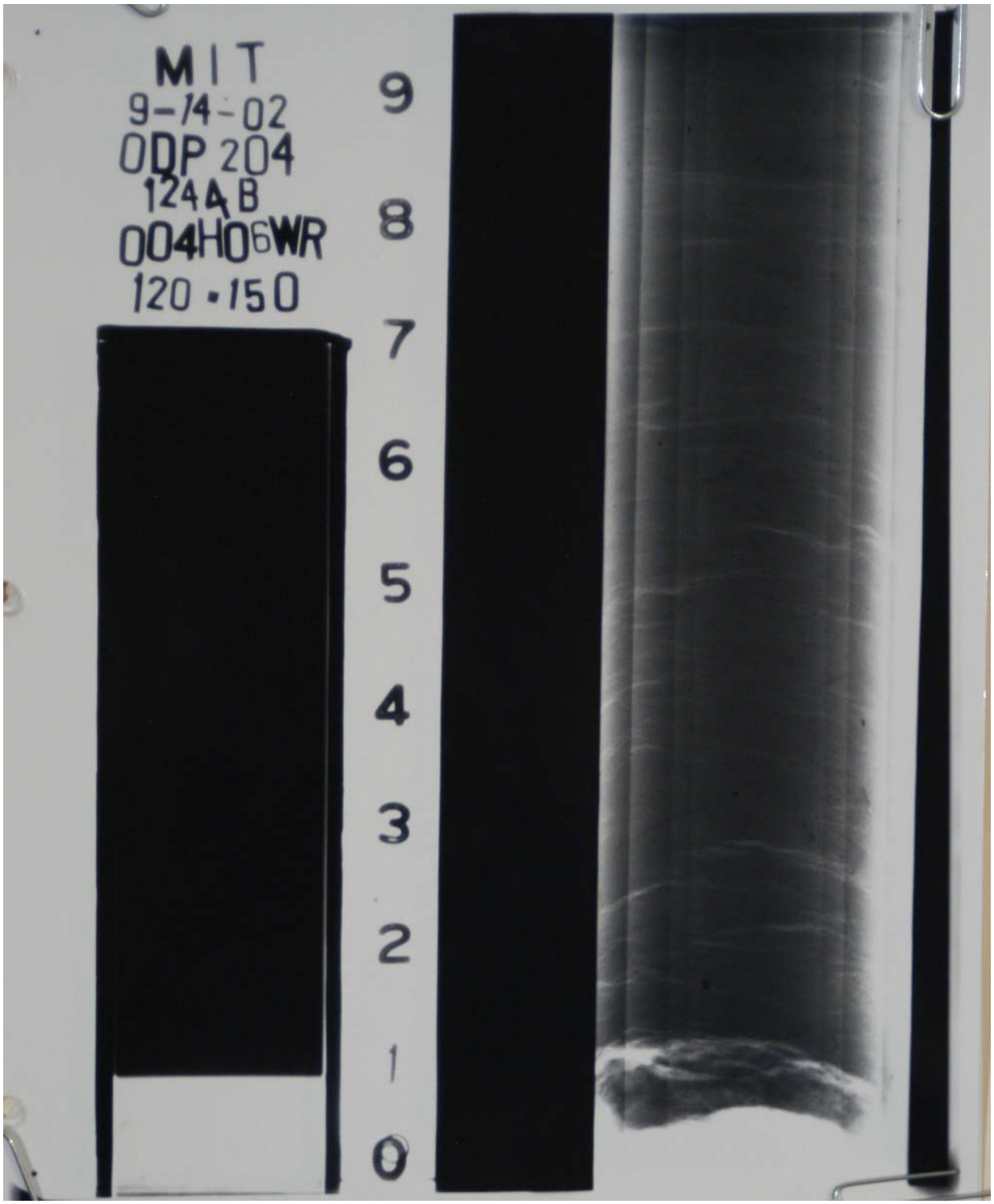

1244B-4H-6WR 1st Print

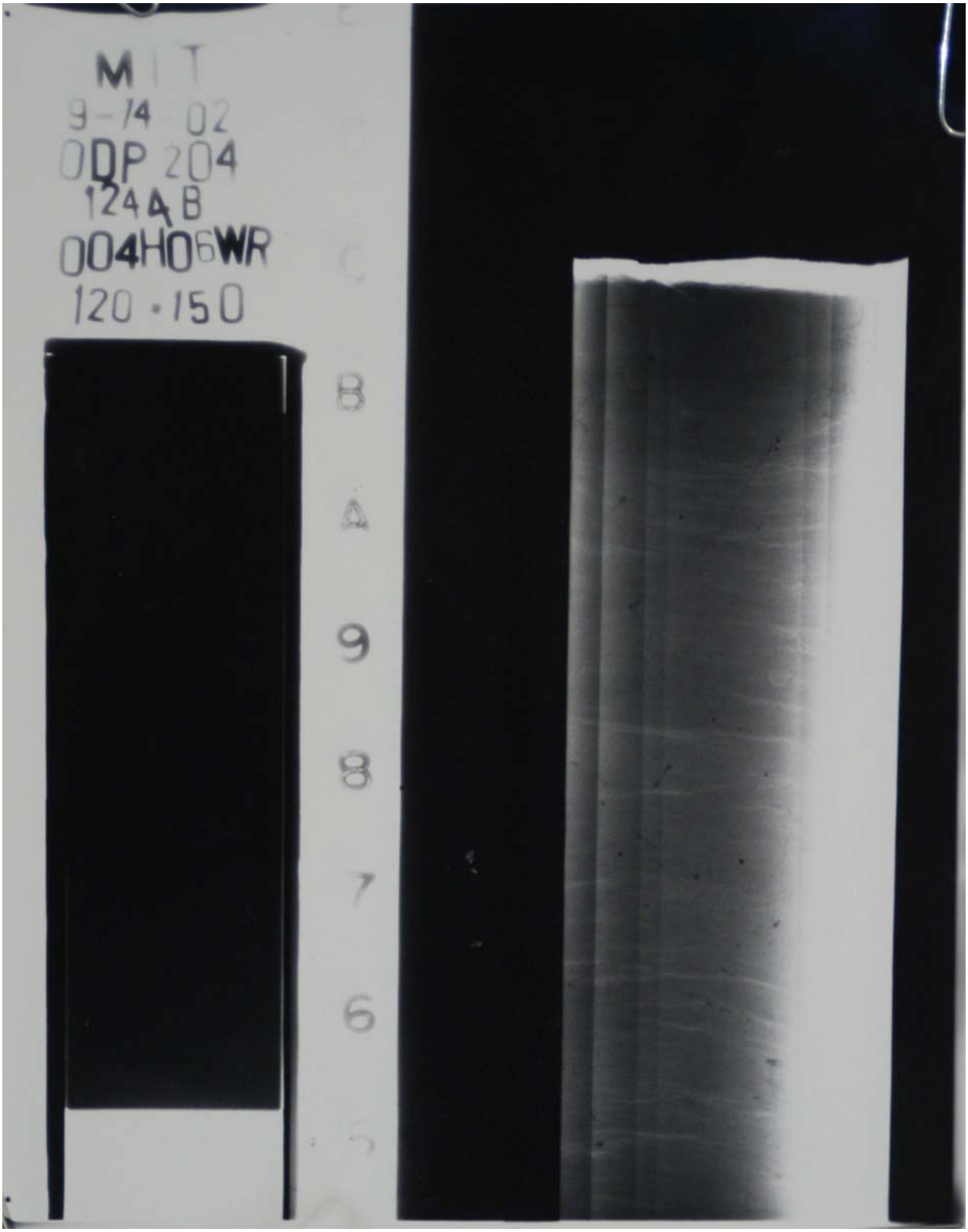

1244B-4H-6WR 2nd Print

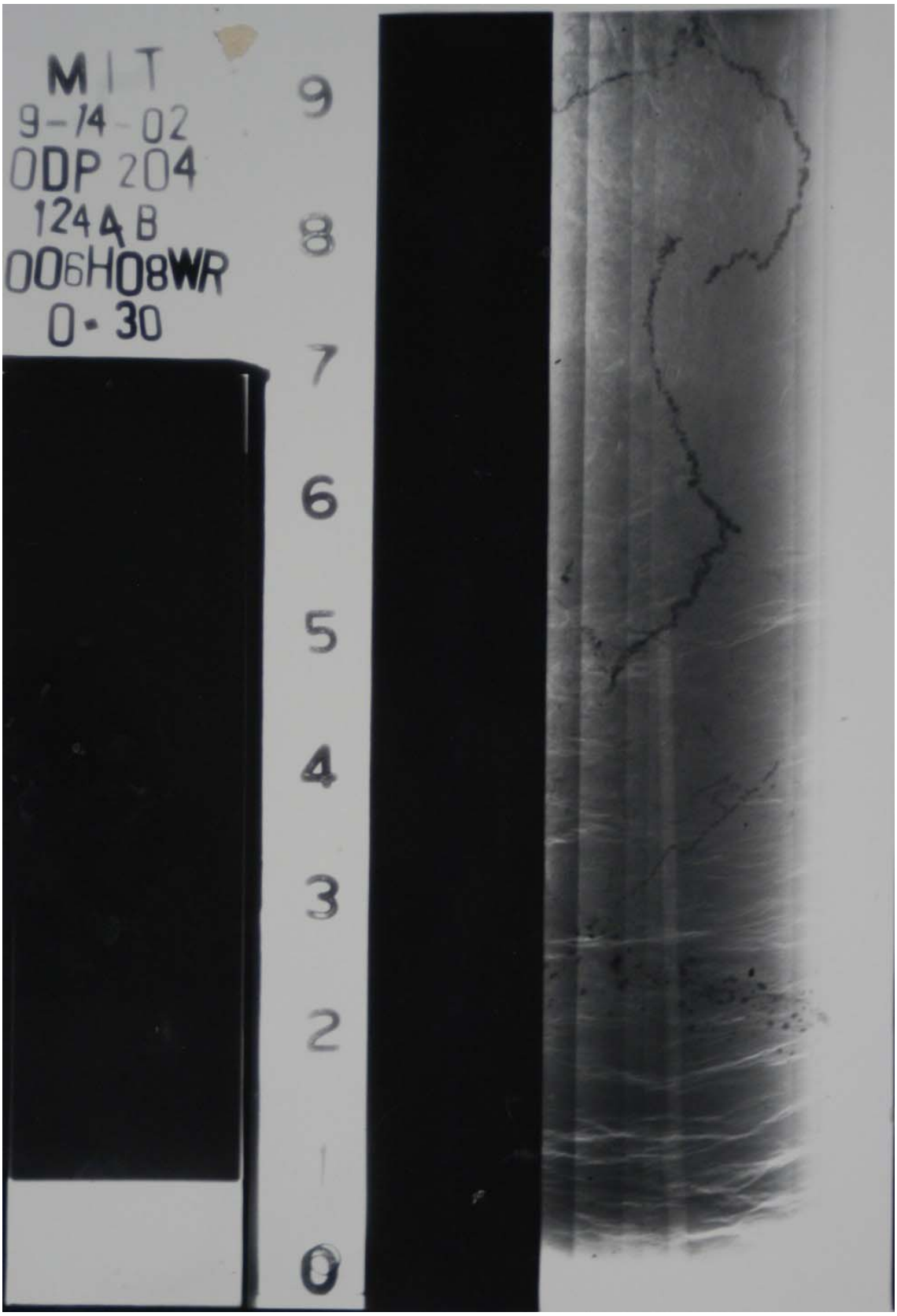

1244B-6H-8WR 1st Print

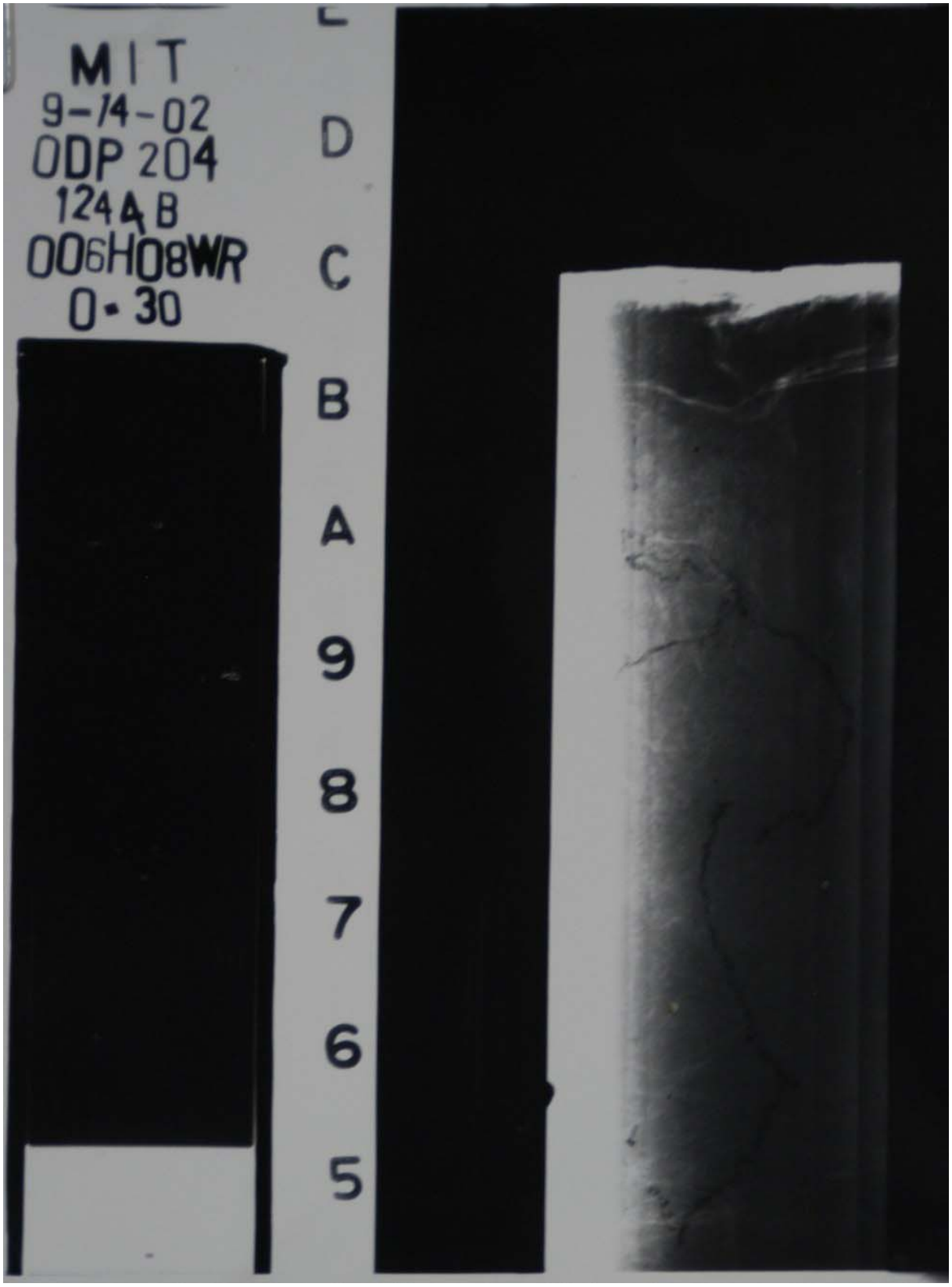

1244B-6H-8WR 2nd Print

1244C-8H-7WR 1st Print

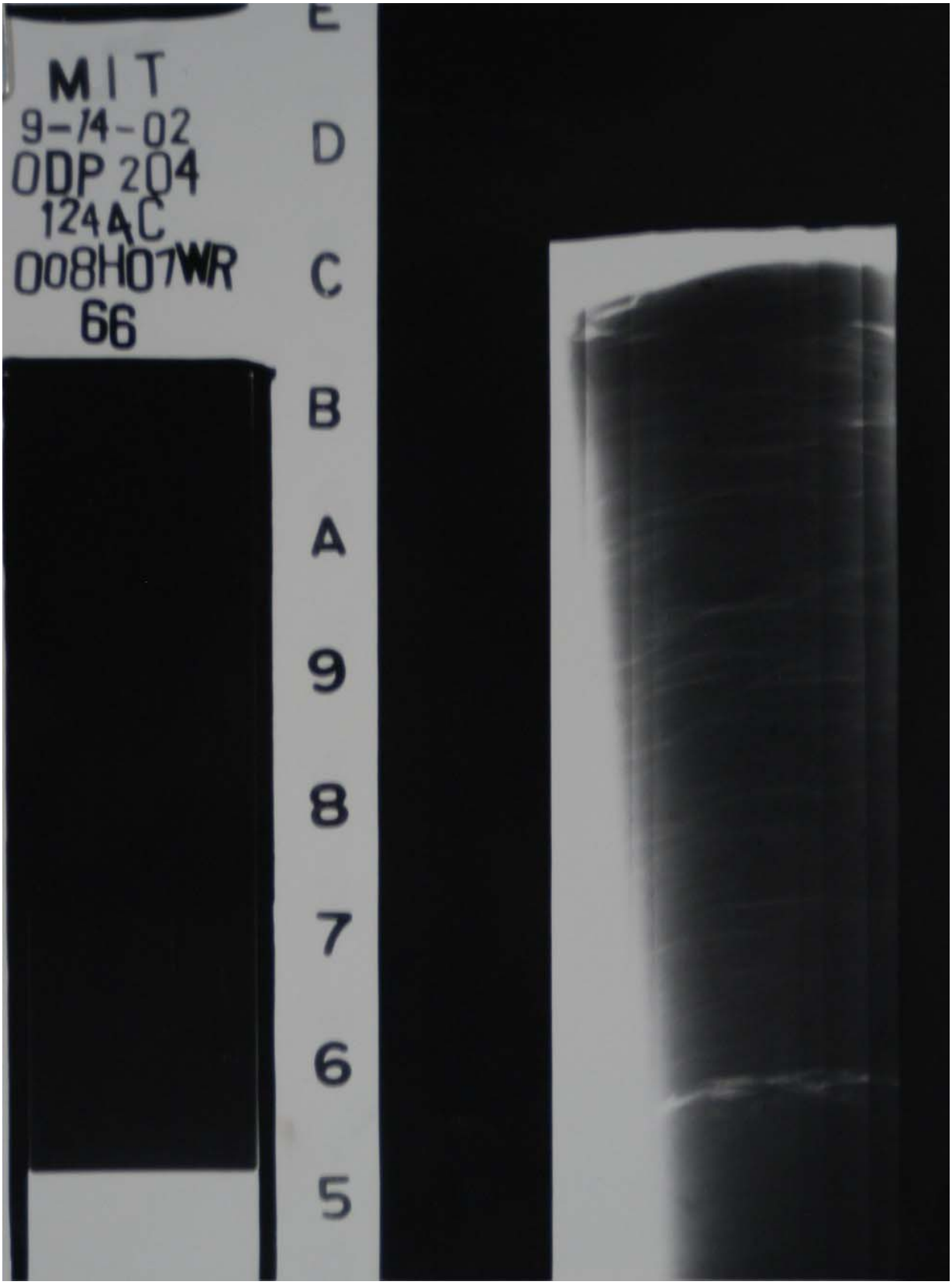

1244C-8H-7WR 2nd Print

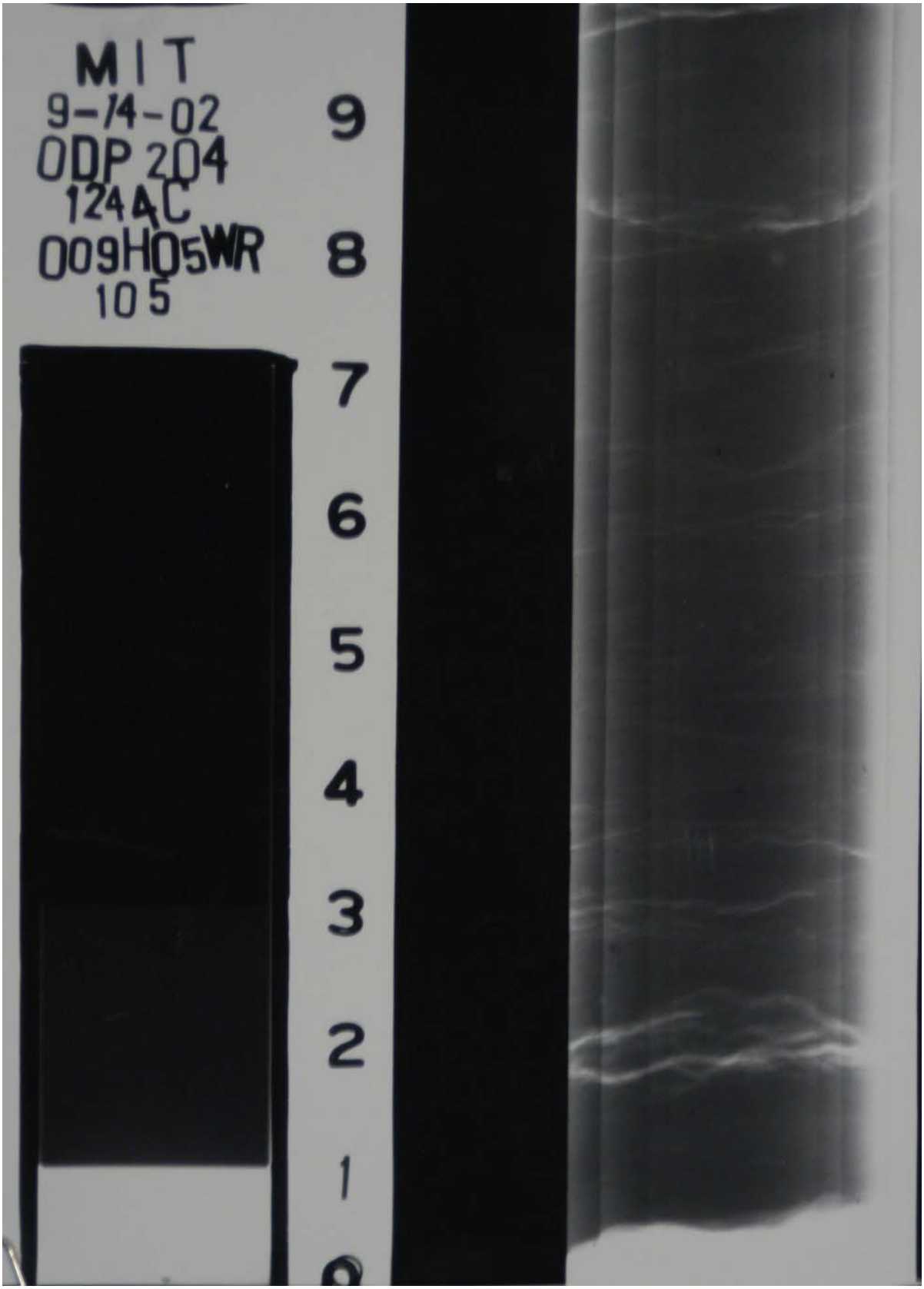

1244C-9H-5WR 1st Print

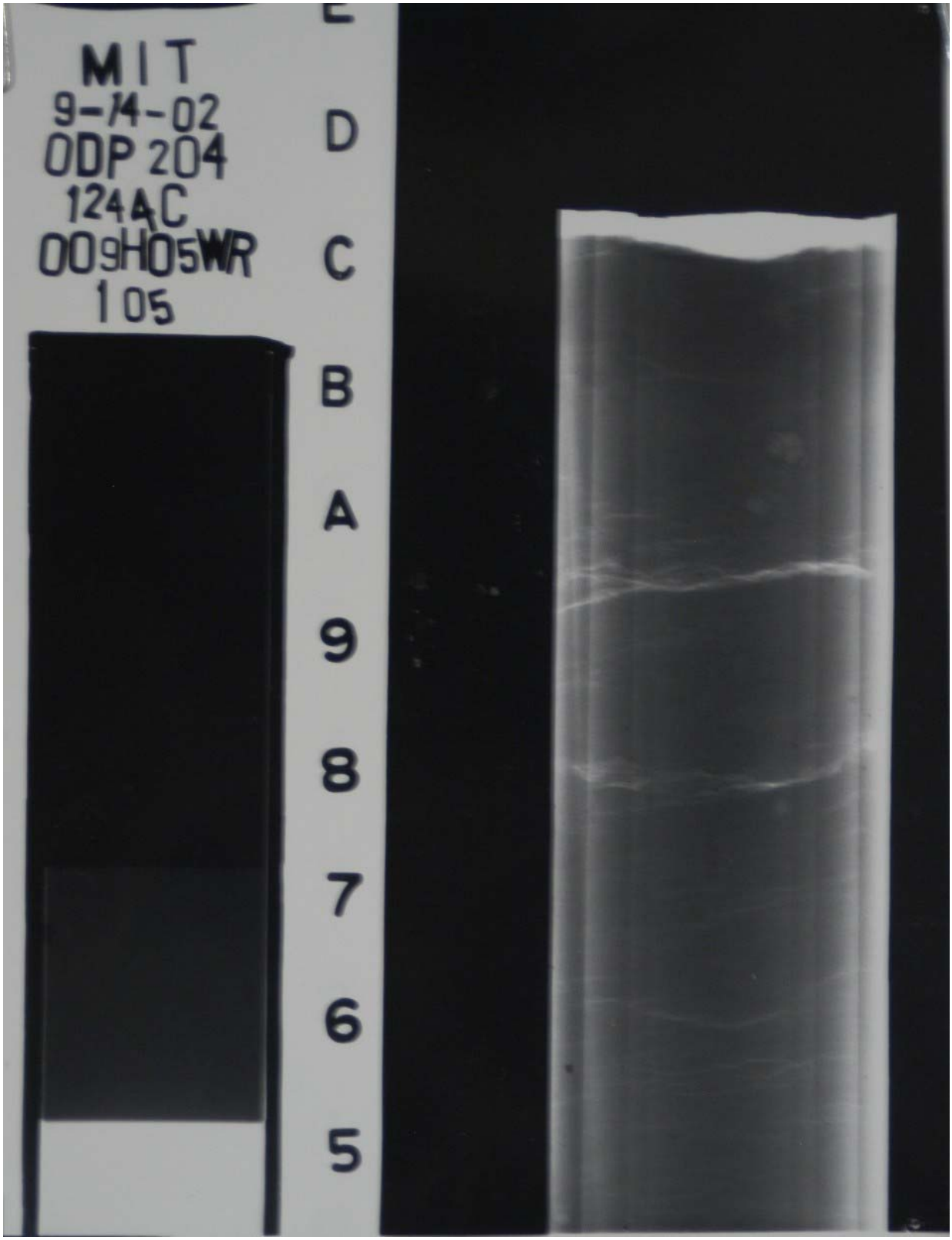

1244C-9H-5WR 2nd Print

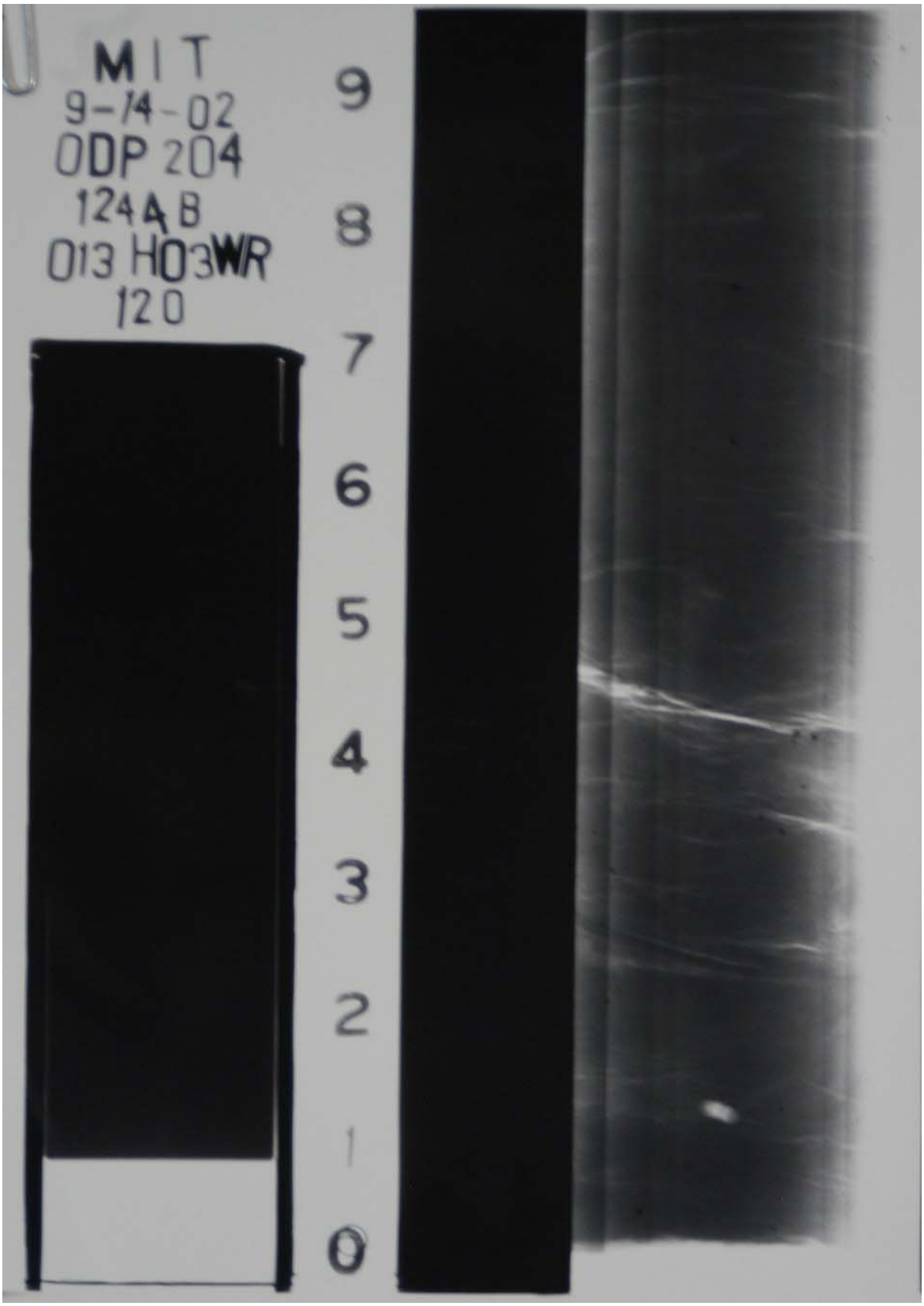

1244C-13H-3WR 1st Print

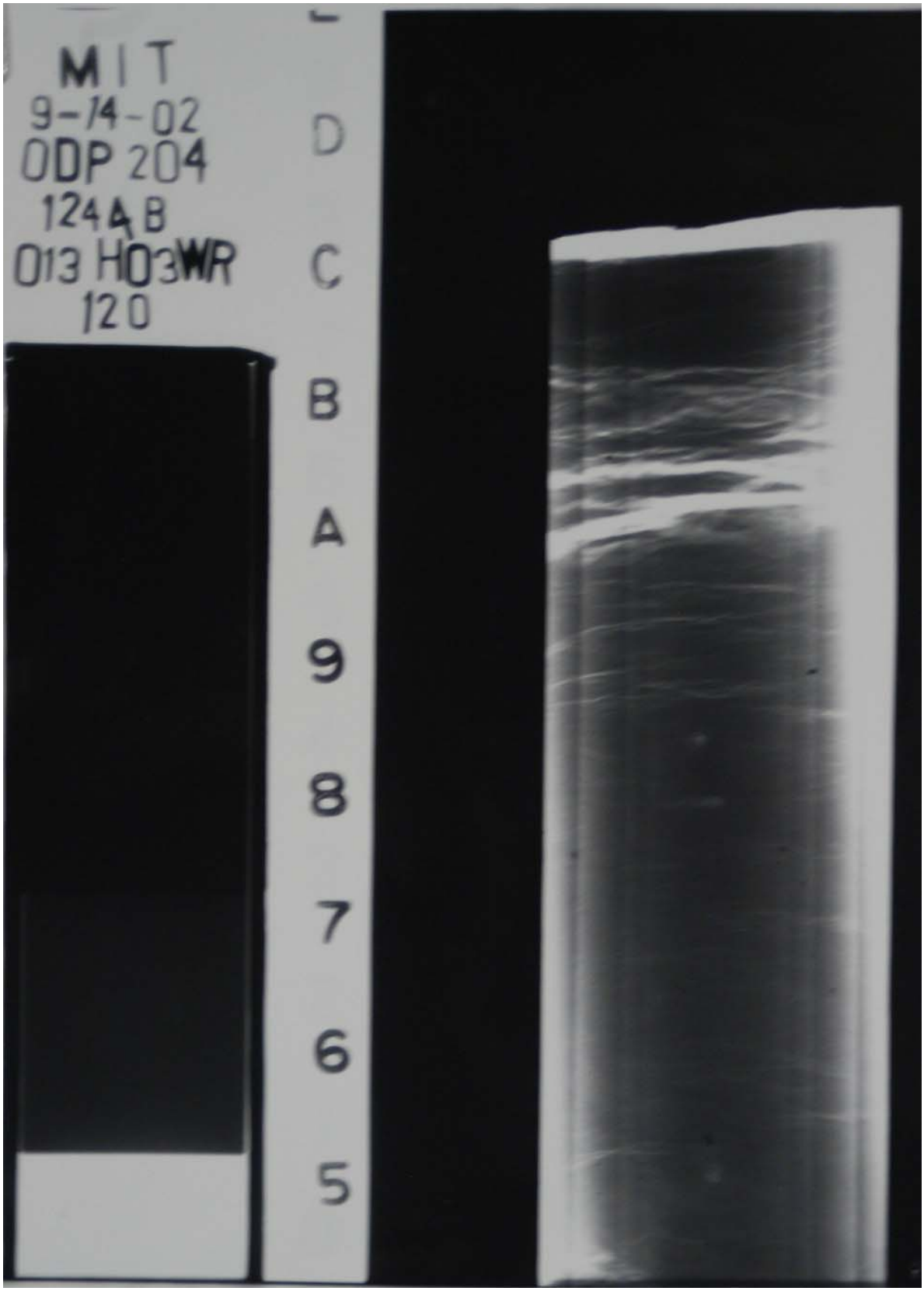

1244C-13H-3WR 2nd Print

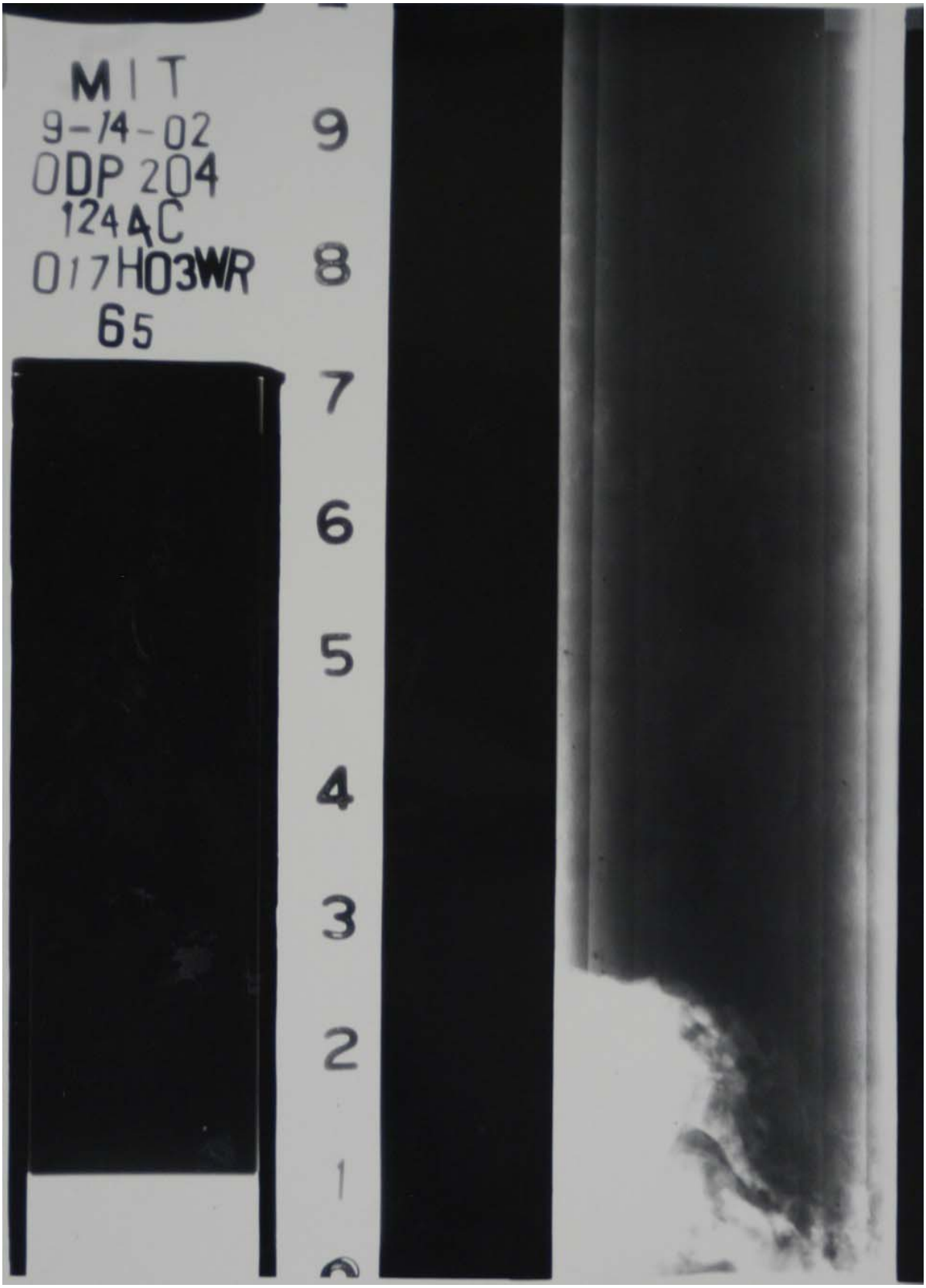

1244C-17H-3WR 1st Print

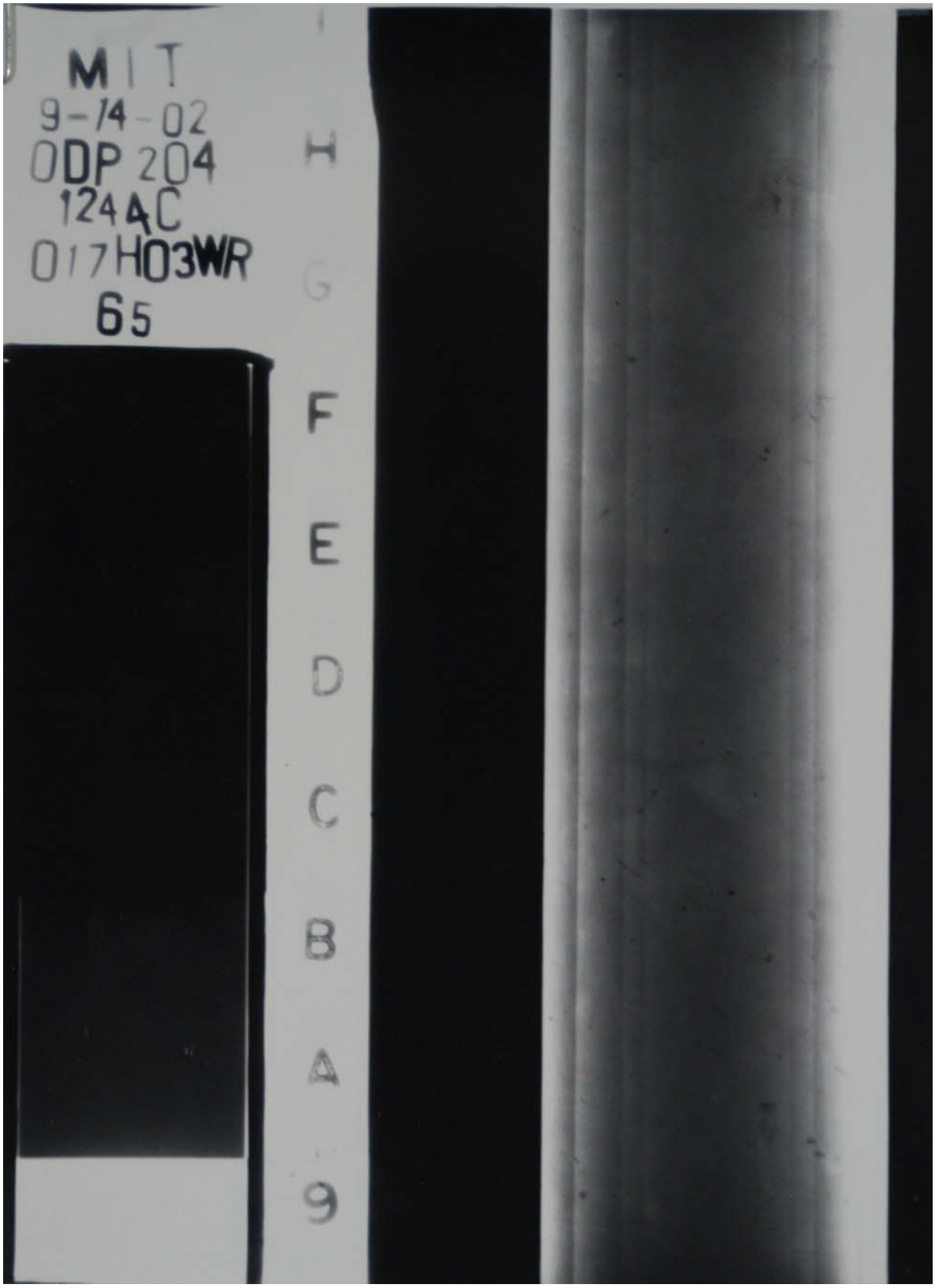

1244C-17H-3WR 2nd Print

Appendix B: Radiography Logs

The following appendix contains the radiography logs for each sampling tube. The top of the log contains the name of each tube as well as the location of the top portion of the tube within the coring section. The right-hand side of each log marks the specimen locations of the consolidation and triaxial tests performed on each tube. The left-hand side shows a brief description of the soil from the tube x-rays. Section 3.2 describes the purpose of the radiography logs.

RADIOGRAPHY LOG
MASSACHUSETTS INSTITUTE OF TECHNOLOGY

Project: Ocean Drilling Program - Leg 204 - Flemings
Sample No.: 1H 4WR
Depth: 120-150
Sample Type:
Boring No.: 1244 B
Depth @ 0":
Date:

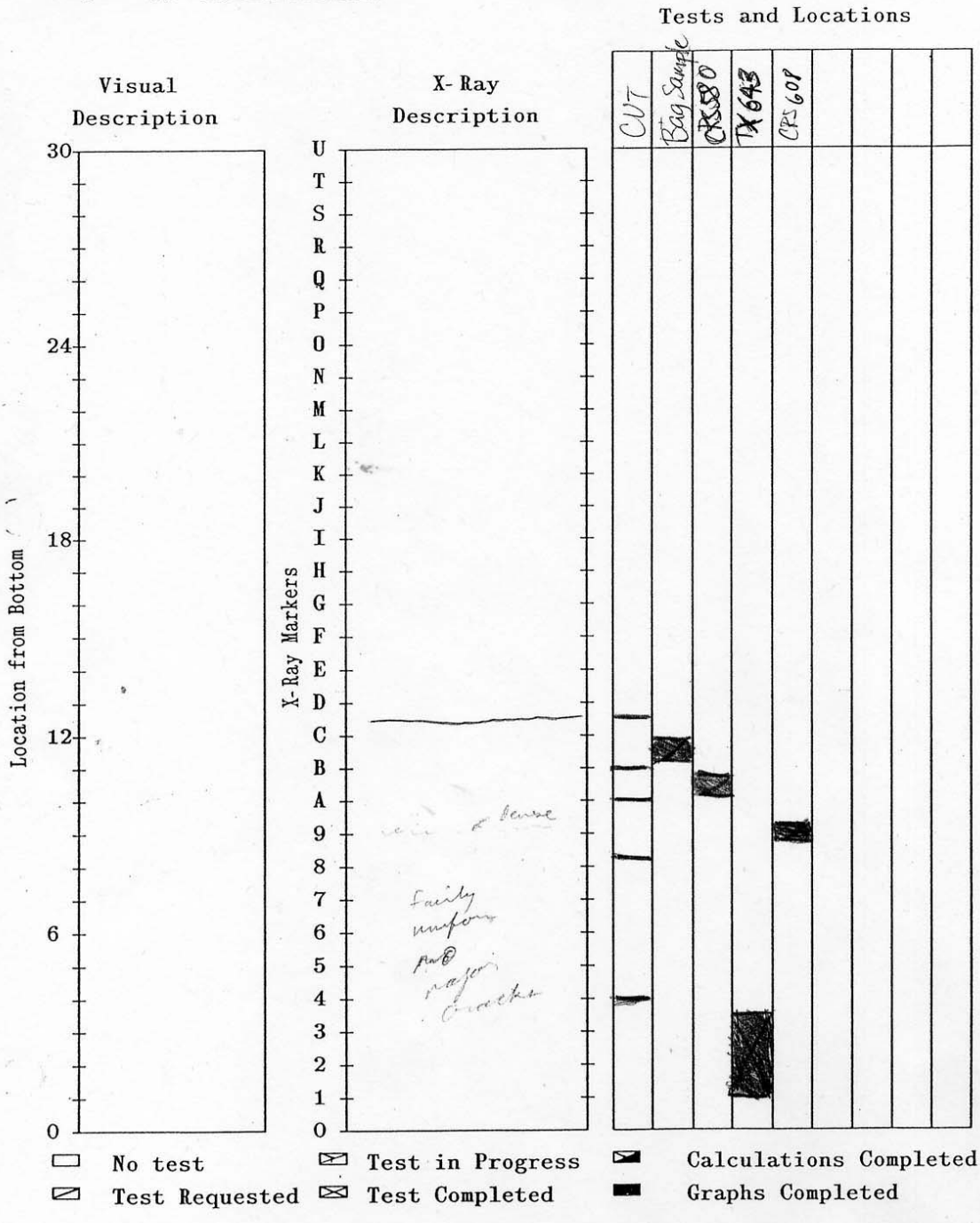

1244B-1H-4WR

35

RADIOGRAPHY LOG
MASSACHUSETTS INSTITUTE OF TECHNOLOGY

Project: ODP/TAMU Drilling Program - Leg 204 - Flemings
Sample No.: 3H3WR
Depth: 120-150
Sample Type:
Boring No.:
Depth @ 0":
Date:

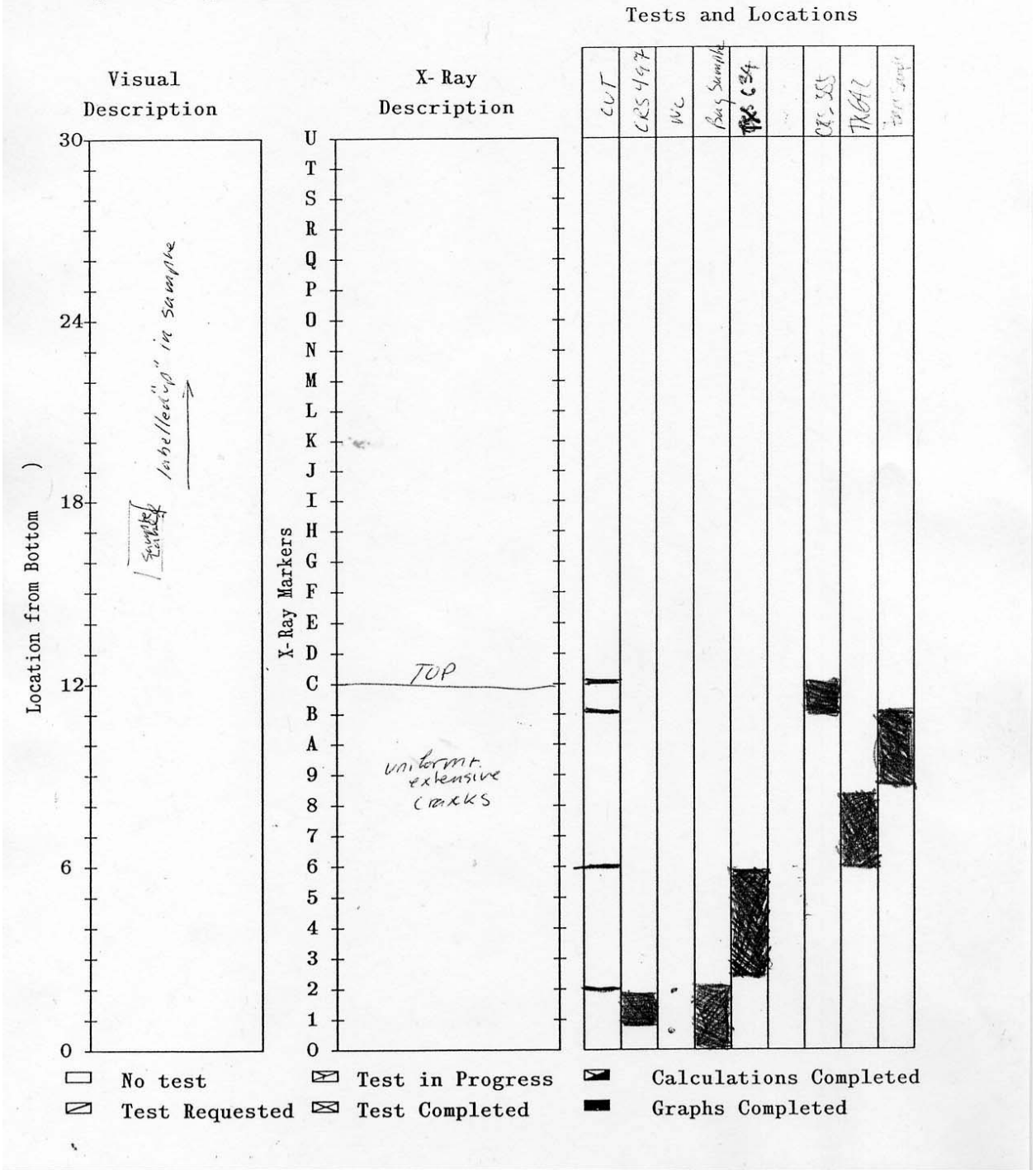

1244B-3H-3WR

39

RADIOGRAPHY LOG
MASSACHUSETTS INSTITUTE OF TECHNOLOGY

Project Ocean Drilling Program - Leg 204 - Flemings
Sample No. 4H 6WR
Depth 120-150
Sample Type
Boring No. 1244B
Depth @ 0"
Date

Tests and Locations

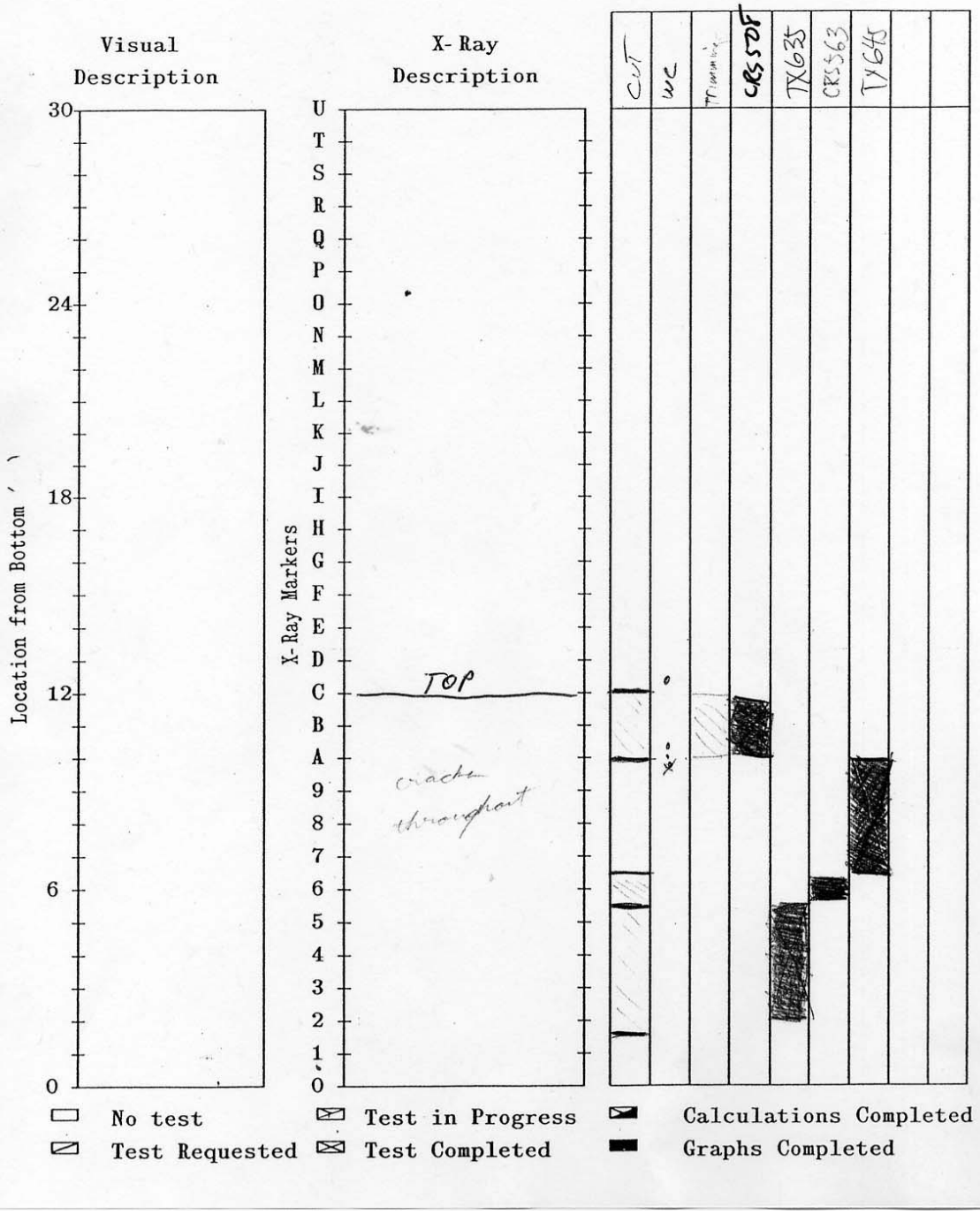

1244B-4H-6WR

RADIOGRAPHY LOG
MASSACHUSETTS INSTITUTE OF TECHNOLOGY

Project: Ocean Drilling Program - Leg 204 - Flemings
Sample No.: 6H 8WR
Depth: 0-30
Sample Type:
Boring No.: 1244 B
Depth @ 0":
Date:

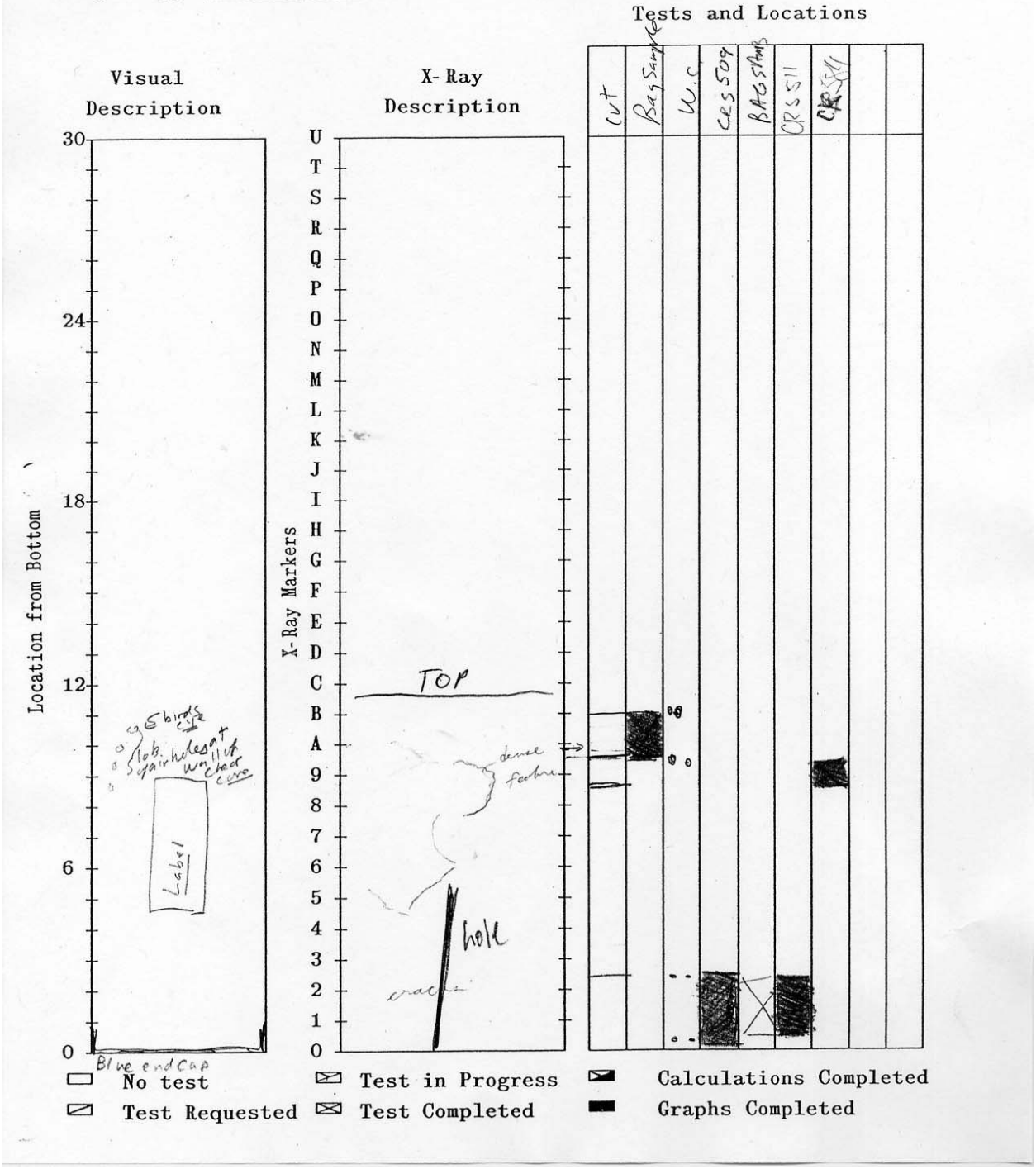

1244B-6H-8WR

45

RADIOGRAPHY LOG
MASSACHUSETTS INSTITUTE OF TECHNOLOGY

Project: Ocean Drilling Program - Leg 204 - Flemings
Sample No.: 8H 7WR
Depth: 66
Sample Type:
Boring No.: 1244 C
Depth @ 0":
Date:

Tests and Locations

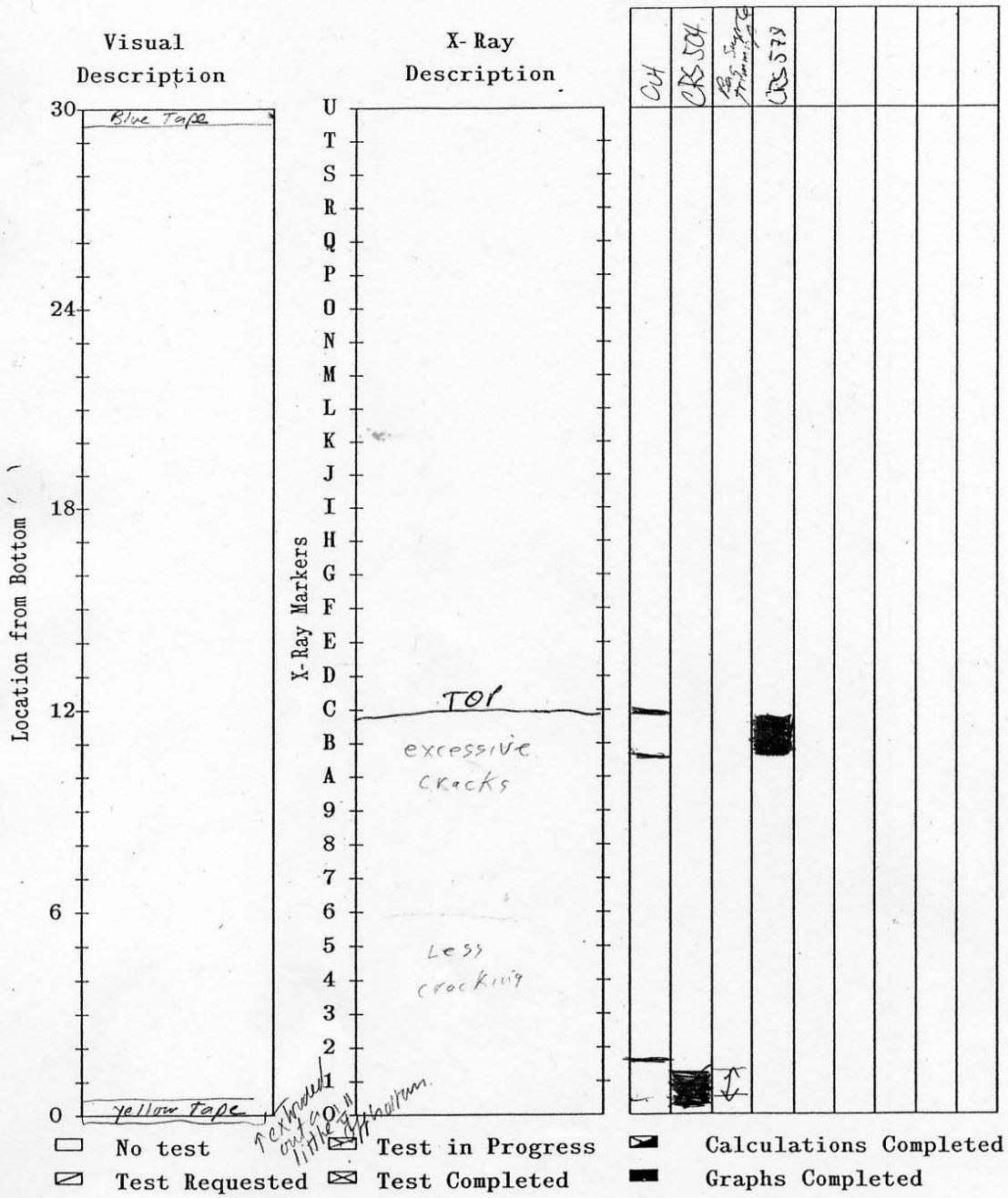

1244C-8H-7WR

50

RADIOGRAPHY LOG
MASSACHUSETTS INSTITUTE OF TECHNOLOGY

Project Ocean Drilling Program - Leg 204 - Flemings
Sample No. 9H 5WR
Depth 105
Sample Type
Boring No. 1244 C
Depth @ 0"
Date

Tests and Locations

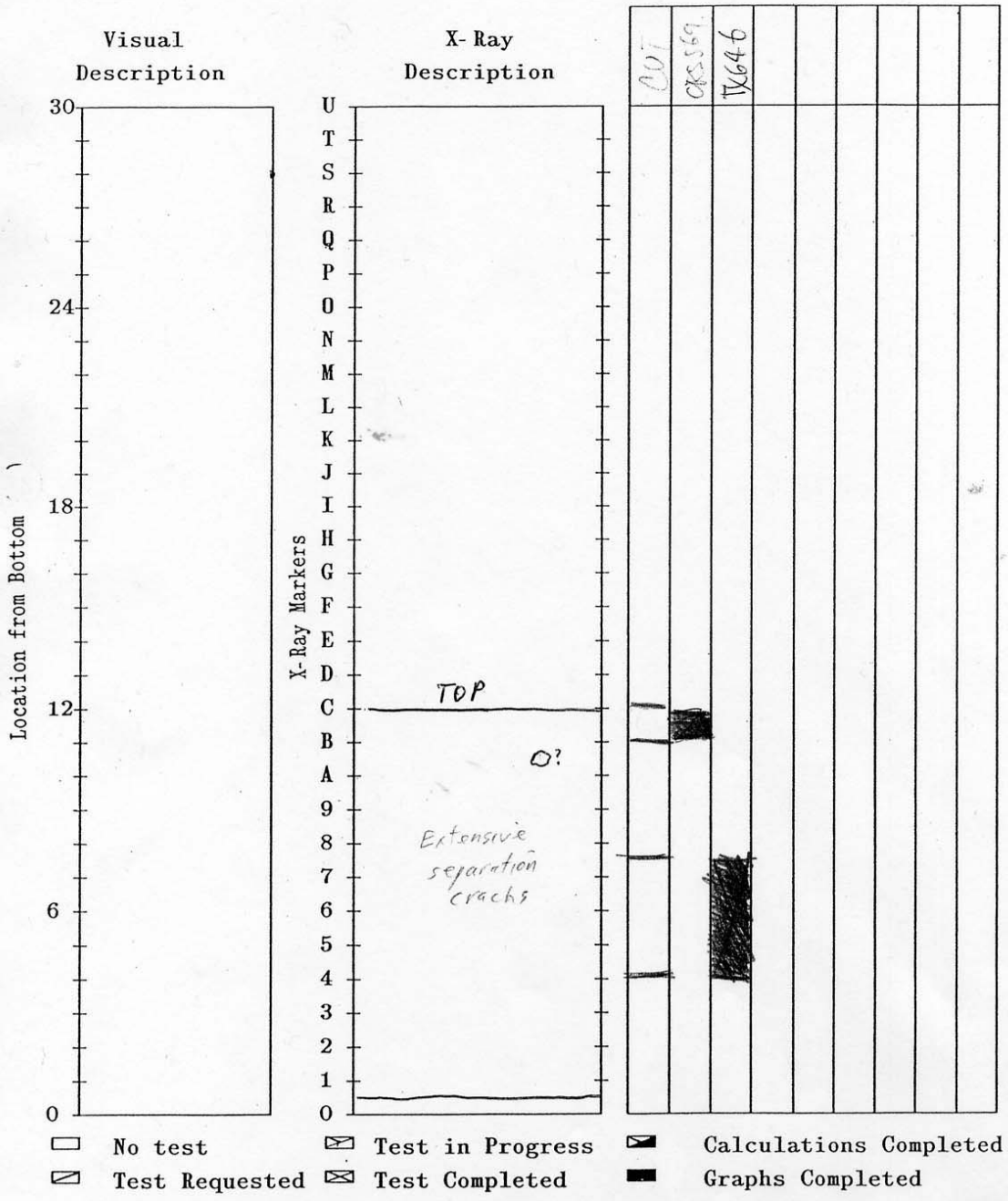

1244C-9H-5WR

55

RADIOGRAPHY LOG
MASSACHUSETTS INSTITUTE OF TECHNOLOGY

Project: Ocean Drilling Program - Leg 204 - Flemings
Sample No.: 13H 3WR
Depth: 120
Sample Type:
Boring No.: 1244B C
Depth @ 0":
Date:

Leg	Site	Hole	Core	Type	Sec	
204	1244	C	13	H	3	114.2 mbsf

Tests and Locations

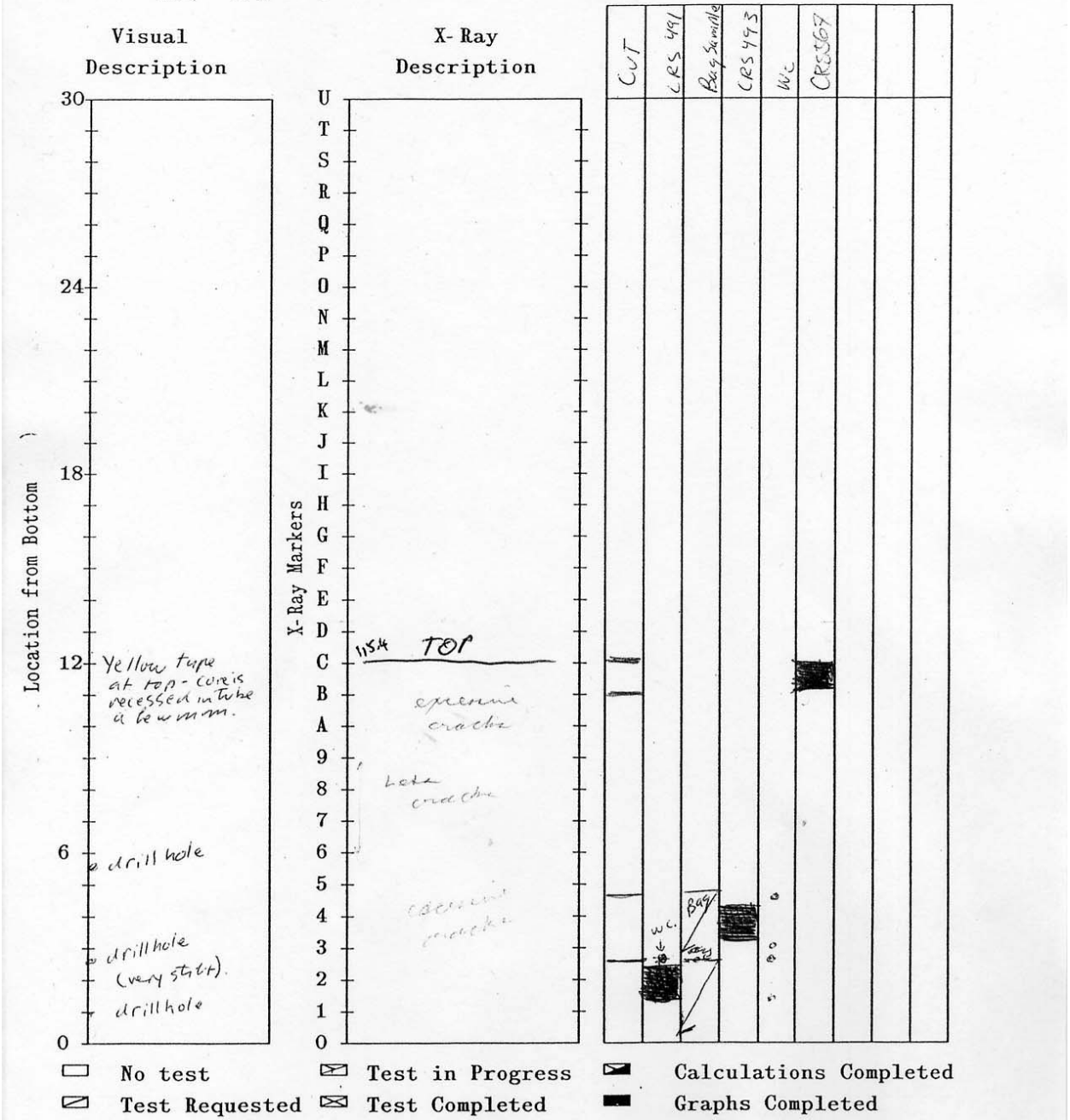

1244C-13H-3WR

RADIOGRAPHY LOG
MASSACHUSETTS INSTITUTE OF TECHNOLOGY

Project: Ocean Drilling Program - Leg 204 - Flemings
Sample No.: 17H 3WR
Depth: 65
Sample Type:
Boring No.: 1244C
Depth @ 0":
Date:

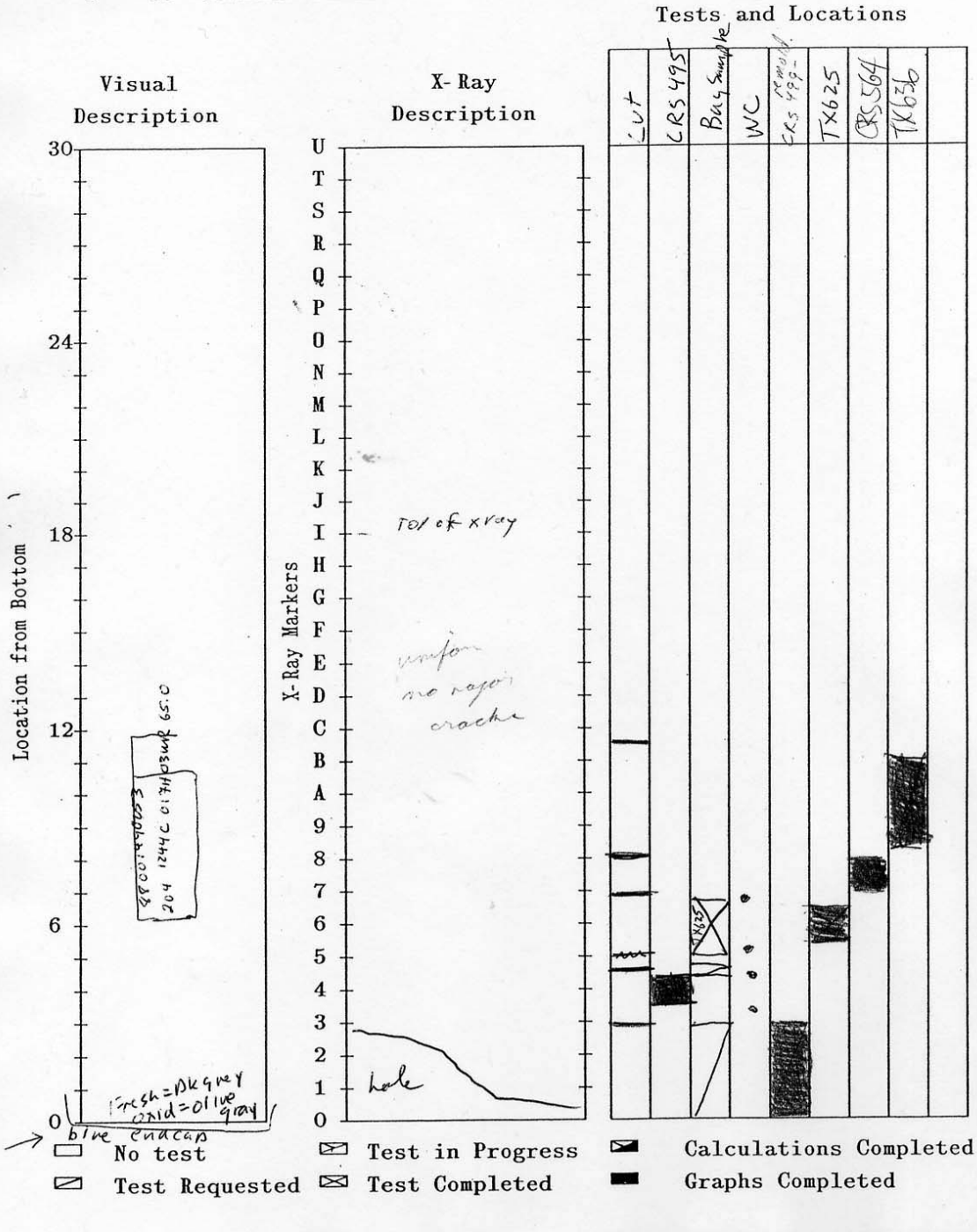

1244C-17H-3WR